Recent Advances of Knowledge Discovery Assisted Clinical Diagnosis

Lead Guest Editor: Hangjun Che
Guest Editors: Man Fai Leung, Wenming Cao, Cheng Liu, and Zheng Yan

Recent Advances of Knowledge Discovery Assisted Clinical Diagnosis

Recent Advances of Knowledge Discovery Assisted Clinical Diagnosis

Lead Guest Editor: Hangjun Che
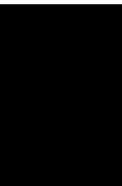Guest Editors: Man Fai Leung, Wenming Cao, Cheng Liu, and Zheng Yan

Contents

Contents

Research Article

ECG-Based Multiclass Arrhythmia Classification Using Beat-Level Fusion Network

Junyuan Jing [ID],[1] **Jing Zhang** [ID],[1] **Aiping Liu** [ID],[1] **Min Gao** [ID],[2] **Ruobing Qian,**[3] **and Xun Chen**[3]

[1]*School of Information Science and Technology, University of Science and Technology of China, Hefei 230027, China*
[2]*Department of Electrocardiogram, The First Affiliated Hospital of USTC, Division of Life Sciences and Medicine, University of Science and Technology of China, Hefei 230001, Anhui, China*
[3]*Department of Neurosurgery, The First Affiliated Hospital of USTC, Division of Life Sciences and Medicine, University of Science and Technology of China, Hefei 230001, Anhui, China*

Correspondence should be addressed to Junyuan Jing; lzyjjy@mail.ustc.edu.cn

Cardiovascular disease (CVD) is one of the most severe diseases threatening human life. Electrocardiogram (ECG) is an effective way to detect CVD. In recent years, many methods have been proposed to detect arrhythmia using 12-lead ECG. In particular, deep learning methods have been proven to be effective and have been widely used. The attention mechanism has attracted extensive attention in many fields in a series of deep learning methods. Off-the-shelf solutions based on deep learning and attention mechanism for ECG classification mostly give weights to time points. None of the existing methods were considered using the attention mechanism dealing with ECG signals at the level of heartbeats. In this paper, we propose a beat-level fusion net (BLF-Net) for multiclass arrhythmia classification by assigning weights at the heartbeat level, according to the contribution of the heartbeat to diagnostic results. This algorithm consists of three steps: (1) segmenting the long ECG signal into short beats; (2) using a neural network to extract features from heartbeats; and (3) assigning weights to features extracted from heartbeats using an attention mechanism. We test our algorithm on the PTB-XL database and have superiority over state-of-the-art performance on six classification tasks. Besides, the principle of this architecture is clarified by visualizing the weight of the attention mechanism. The proposed BLF-Net is shown to be useful and automatically provides an effective network structure for arrhythmia classification, which is capable of aiding cardiologists in arrhythmia diagnosis.

1. Introduction

Cardiovascular disease (CVD) is at high risk of leading to death. According to the World Health Organization (WHO), in 2019, an estimated 17.9 million individuals died from CVDs, representing 32% of global deaths [1]. In particular, sudden cardiac deaths account for roughly 50% of all fatalities due to cardiovascular disease, with cardiac arrhythmias accounting for about 80% of them [2]. Electrocardiogram (ECG) is widely used for recording the heart's electrical activities, which can reflect the physical condition of humans. ECG is noninvasive and inexpensive. It is obtained by electrodes attached to the skin. The standard ECG has 12 leads, namely, I, II, III, avR, avL, avF, V1, V2, V3, V4,

V5, and V6. Automatic arrhythmia detection using ECG has become increasingly important. It can assist doctors in treating patients and provide helpful information about heart conditions for ordinary people with wearable devices.

ECG signal has its periodicity due to the regular electrical activity of the heart. A typical ECG signal record is composed of several heartbeats. These heartbeats are closely related physiologically and temporally. On the one hand, each beat of the ECG signal can be divided into PRQST waves according to different physiological meanings. Depolarization of the right atrium is responsible for the first half of the P wave, while depolarization of the left atrium is responsible for the second half. Depolarization of the middle of the left side of the interventricular septum causes the QRS

complex's initial 0.01 second. Depolarization of the endo-cardium of both ventricles produces the next few milliseconds of the QRS complex. Depolarization of a smaller portion of the right ventricle and a larger portion of the left ventricle follows. The final few milliseconds of the QRS complex are caused by depolarization of the basilar region of the left ventricle. The T wave is created by the ventricles repolarizing [3].

In the past few decades, a large number of arrhythmia classification methods have been proposed. Technically, a typical method includes preprocessing, feature extraction, and feature classification. Feature extraction is the most sophisticated step because we need to choose a set of features manually. Therefore, ECG classification based on deep neural networks (DNNs), which have the capability of automatic feature extraction, has attracted much attention and many DNN-based arrhythmia classification works have been proposed.

Since each beat has the same structure, a novel method using the beat-level attention fusion network for multiclass arrhythmia classification is proposed by exploiting this feature. Our method can be divided into three steps: (1) segmentation, (2) beat-level feature extraction, and (3) interbeat feature fusion. The segmentation module transforms ECG signals into different heartbeats. Beat-level feature extraction module extracts features from heartbeats. Interbeat feature fusion module fuses beat-level features into global features that incorporate information about the whole ECG signal by considering the contribution of the heartbeat to diagnostic results. The main contributions of our algorithm are stated as follows. The model BLF-Net is proposed by utilizing the attention mechanism at the level of heartbeat instead of the time point. The attention mechanism gives weights for different beats in an ECG signal. The purpose is to focus on the informative beats and suppress less useful beats among one ECG signal. This model outperforms the state-of-the-art models in terms of arrhythmia detection. Besides, this model provides a new perspective for arrhythmia detection. That is, an ECG signal can be dealt with the level of heartbeats and attention can be utilized to fuse features extracted from each beat.

2. Related Works

Traditional methods are required to extract features manually. Typical features extracted manually are statistical features [4], morphological features [5, 6], P-QRS-T features [7, 8], and wavelet features [9, 10]. Also, dimensionality reduction methods can be exploited for extracting useful information, such as principal component analysis (PCA) [11], independent component analysis (ICA) [12, 13], and linear discriminant analysis (LDA) [14, 15]. After extracting features, there are varieties of classifiers to be chosen from. Commonly used techniques are support vector machine (SVM) [16, 17], artificial neural network (ANN) [18], decision tree [9, 12], and bayesian classifier [6, 13].

A set of well-designed hand-crafted features is necessary and important for high performance and robustness in traditional methods, while it costs a lot of labor to design

manual features. How to design features usually depends on the researchers' work experience. As a consequence, methods based on the deep neural network [19] have gradually become mainstream in ECG classification due to the ability to extract features automatically. Convolutional neural networks (CNNs) are widely employed because of their ability to extract features effectively. A patient-specific ECG heartbeat classification using an adaptive CNN was developed by Kiranyaz et al. [20], which is a single structure that integrates feature extraction and classification. The continuous wavelet transform was utilized by Al Rahhal et al. [21] to convert ECG into images, which were then input into a CNN network pretrained on ImageNet. For identifying supraventricular and ventricular ectopic beats, this approach performed well. A 34-layer residual CNN presented by Hannun et al. [22] reached expert-level performance in detecting cardiac arrhythmias. In some studies, the ECG signal was regarded as a time-series and they deployed recurrent neural network (RNN) which is designed for dealing with sequential data. Long short-term memory (LSTM) and gated recurrent unit (GRU) are two representative variants of RNN. Based on several LSTMs and wavelet transform, a real-time heartbeat classification method was developed by Saadatnejad et al. [23] for personal wearable gadgets. For classifying biometric ECG signals, a deep bidirectional GRU network was developed by Lynn et al. [24]. Besides all that, many studies have proposed multilayer networks by combining CNN and RNN. By combining a residual CNN with a bidirectional LSTM, He et al. [25] achieved good results for arrhythmia classification. Yao et al. [26] used a model composed of VGGNet and LSTMs to classify multiclass arrhythmias. This model is effective in recognizing paroxysmal arrhythmias and supports varied-length inputs. Recently, a number of works [27, 28] have exploited the attention mechanism to take into account the fact that different parts of ECG signals contribute dissimilarly to the diagnosis. There are many variants of the attentional mechanism [29–31]. Zhang et al. [32] used the spatio-temporal attention mechanism to deal with the ECG classification by assigning weights in the spatio-temporal dimension of ECG. These works exploited the attention mechanism to assign weights to ECG signals at the level of time point (i.e., temporal attention mechanism). The temporal attention mechanism can focus on which signal points are more important in the temporal dimension and which signal points do not have a sufficiently prominent contribution to the result. However, the ECG signal is composed of heartbeats; so another practicable alternative is to exploit the attention mechanism to assign weights at the level of ECG heartbeat. Considering the use of the attention mechanism from the perspective of the heartbeat allows the attention mechanism to take the heartbeat as a whole and pay attention to how much the heartbeat contributes to the result. That is to say, beats that contribute more to the result are assigned higher weights. This provides a new perspective to treat and process ECG signals. In other words, extracting features from each beat and fusing these features deserves further research.

3. Method

3.1. Problem Formulation.

The multiclass and multilabel 12-lead ECG dataset is defined as

$$X = \left\{\left(x^{(1)}, y^{(1)}\right), \left(x^{(2)}, y^{(2)}\right), \ldots, \left(x^{(n)}, y^{(n)}\right)\right\}, \quad (1)$$

where $x^{(i)} \in \mathbb{R}^{L \times D}$ is the ECG signal, L refers to the length of the signal, and D refers to the signal dimension (i.e., the number of leads). $y^{(i)} \in \mathbb{F}_2^C$, C refers to the number of categories and $\mathbb{F}_2 = \{0, 1\}$ is a set containing only 0 and 1.

The goal of the arrhythmia classification is to construct a model to automatically identify the categories of arrhythmia based on the ECG signal. The model takes 12-lead ECG signals as input and outputs predicted labels. The model needs to learn the mapping relationship $\mathcal{H}(\cdot)$ from the input $x^{(i)}$ to the output $z^{(i)}$ of the output layer, which is defined as

$$z^{(i)} = \mathcal{H}\left(x^{(i)}; \theta\right), \quad (2)$$

where θ refers to the network parameters of the model. During training, the goal of the model is to minimize the binary cross entropy loss (BCE Loss) of the predicted probability relative to its reference label, defined as

$$L(X; \mathcal{H}) = -\sum_{k=1}^{C} \left(y_k^{(i)} \log z_k^{(i)} + \left(1 - y_k^{(i)}\right) \log\left(1 - z_k^{(i)}\right)\right). \quad (3)$$

3.2. Model Overview.

The proposed BLF-Net includes 3 parts illustrated in Figure 1: (1) segmentation used for segmenting ECG signal into heartbeats; (2) beat-level feature extraction used for extracting features from beats; (3) interbeat feature fusion used for synthesizing features extracted by beat-level feature extraction module.

Specifically, in our model, the ECG signal is first fed into the segmentation module, and several segmented beats are obtained. The segmented beats are sent to the beat-level feature extraction module to obtain the encoded features of each beat. These features are then fed into the interbeat feature fusion module, where the features are fused using an attention mechanism to assign different weights to emphasize useful beats and suppress the less useful ones. Finally, a two-layer fully connected layer is used as a classifier to output the probability of classification.

The ECG signal is a periodic and multibeat signal. The heartbeat is the basic component of the ECG signal. A typical ECG signal consists of a P wave, QRS complex, and other waves. Different heartbeats are temporally and physiologically correlated with each other. On the one hand, the heartbeat can be divided into P, QRS, T waves, etc., according to the physiological process of the heart, which corresponds to the occurrence of different changes in the heart and is expressed as a complete cycle; on the other hand, when pathological changes occur, there may be irregular changes between different beats of one ECG signal. Such changes are expressed as the variability between different beats. According to the above-given two points, pathological changes in the heart can be reflected by the individual beat

characteristics of the ECG signal. Therefore, each heartbeat should be emphasized, and the method used for automatic arrhythmia detection should have the ability to extract features from individual heartbeats.

3.3. Segmentation.

Let $X \in \mathbb{R}^{L \times D}$ be an original ECG signal, where L is the length of the original ECG signal and D is the number of leads. Then, we adopt a classical R-peak detection algorithm proposed by Pan et al. [33]. This algorithm comprises the following steps: (1) bandpass filter, (2) differentiator, (3) squaring process, (4) moving-window integration, and (5) thresholding. After this, we get a sequence of R-peaks.

According to the positions of the detected R-peaks, we segment the original ECG signal into heartbeats. The first L_f points and the last L_k points of an R-peak are considered as one heartbeat. Finally, we have a series of beats denoted as $B = (b_1, b_2, \ldots, b_s)$ where $b_i \in \mathbb{R}^{L_b \times D}, i \in 1, 2, \ldots, s$, $L_b = L_f + L_k$ is the length of a heartbeat.

3.4. Beat-Level Feature Extraction.

Beat-level feature extraction module is composed of CNN and RNN. Hence, the procedure for this part can be formulated as

$$
\begin{aligned}
f_{CNN} &= CNN(B) = CNN(b_1, b_2, \ldots, b_s) \\
&= (CNN(b_1), CNN(b_2), \ldots, CNN(b_s)) \\
&= \left(f_{CNN_1}, f_{CNN_2}, \ldots, f_{CNN_s}\right), \\
f_{RNN} &= RNN(f_{CNN}) \\
&= RNN\left(f_{CNN_1}, f_{CNN_2}, \ldots, f_{CNN_s}\right) \\
&= \left(RNN\left(f_{CNN_1}\right), \ldots, RNN\left(f_{CNN_s}\right)\right) \\
&= (f_1, f_2, \ldots, f_s).
\end{aligned} \quad (4)
$$

3.4.1. Convolutional Neural Network.

A convolutional neural network contains 6 1-dimension (1-D) convolution layers, as shown in Figure 1. "Conv1d 3×64, 2" means that the kernel size of the convolution layer is 3, the number of kernels is 64, and the stride for the cross-correlation is 2. "Conv1d 3×64" means that the stride for the cross-correlation is 1. Other similar expressions have similar meanings. A batch normalization (BN) layer together with a rectified linear unit (ReLU) function follows each convolution layer. BN [34] normalizes each batch during training, which is used for accelerating the convergence. ReLU [35] is a common function used for activating output values and avoiding the vanishing gradient to a certain extent. Dropout [36] follows every two convolution layers to prevent overfitting.

3.4.2. Recurrent Neural Network.

Following the convolutional neural network, the recurrent neural network (RNN) is utilized. More specifically, GRU [37], a kind of RNN, is adopted here. GRU uses gate mechanisms to modulate the information flow, similar to LSTM, but the hidden state is
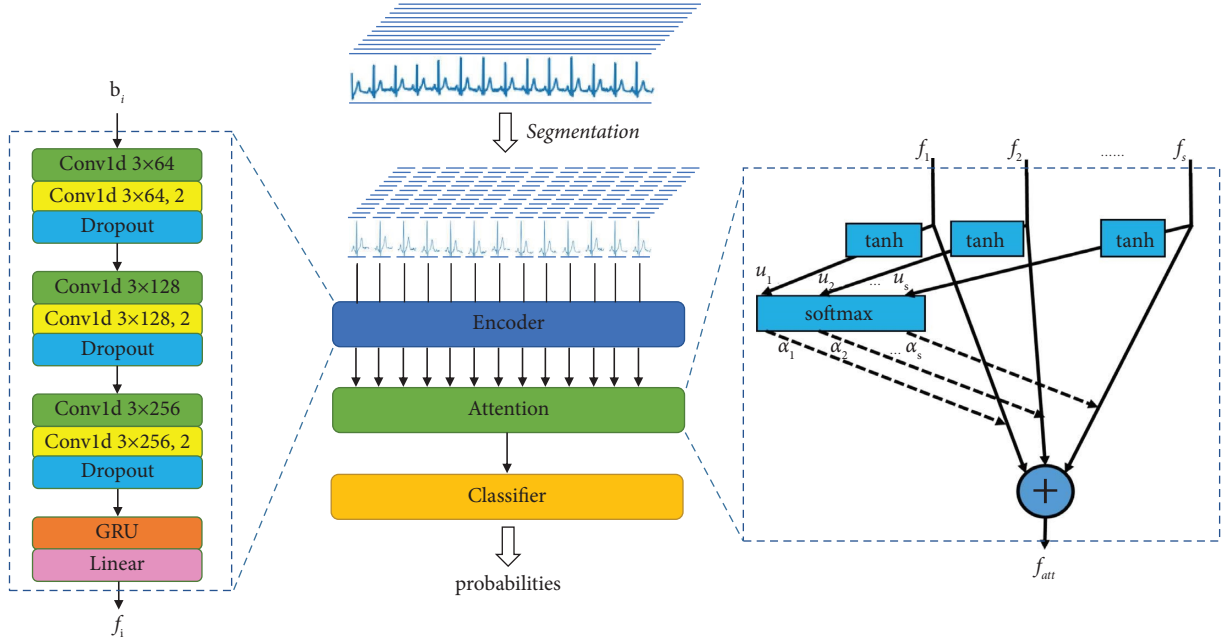
FIGURE 1: The framework of our method.

utilized to convey information instead of the cell state. We use a bidirectional GRU which is a combination of a forward GRU layer and a backward GRU layer.

$$y_t = f\left(W_z x_t + U_z \odot h_{t-1}\right), \tag{5a}$$

$$r_t = f\left(W_r x_t + U_r h_{t-1}\right), \tag{5b}$$

$$\widetilde{h}_t = \tanh\left(W x_t + U\left(r_t h_{t-1}\right)\right), \tag{5c}$$

$$h_t = \left(1 - y_t\right)h_{t-1} + y_t \widetilde{h}_t. \tag{5d}$$

Here, the sigmoid function is denoted by the symbol f. $\odot$ stands for element-by-element multiplication. The update and reset gates, y_t and r_t, determine the extent to which the activation h_t is updated and the extent to which the prior activation h_{t-1} is forgotten, respectively. W_z, U_z, W, U, W_r and U_r are the trainable parameters. The activation h_t is the weighted sum of the prior activation h_{t-1} and the candidate's activation $\widetilde{h}_t$.

3.5. Interbeat Feature Fusion.
For learning features from several beats and putting different weights on the features of different beats, we utilize the attention mechanism [38] to fuse features extracted from different beats. Considering that the number of heartbeats may not be consistent for each segmented record, the masking technique is used. After using the masking technique, the attention mechanism actually performs assigning weights to the heartbeats that the record actually has. First, we concatenate the features extracted previously. Let $f_1, f_2, \ldots, f_s$ refer to features. Here, $f_i \in \mathbb{R}^n$, n is the number of features after passing through the beat-level feature extraction module. After

passing the concatenation layer, we obtain the following output:

$$f_o = Cat\left(f_1, f_2, \ldots, f_s\right). \tag{6}$$

Then, the concatenated features f_o is fed through an attention layer i.e.,

$$f_{att} = Attention\left(f_o\right). \tag{7}$$

This algorithm is formulated as

$$u_i = \tanh\left(W f_i + b\right), \tag{8a}$$

$$\alpha_i = \frac{\exp\left(u_i^T u\right)}{\sum_i \exp\left(u_i^T u\right)}, \tag{8b}$$

$$f_{att} = \sum_i \alpha_i f_i. \tag{8c}$$

Here, $i \in 1, 2, \ldots, s$. This procedure is illustrated in Figure 1. Weights are assigned to beats in an ECG signal by the attention mechanism in order to emphasize those that are more related to arrhythmia detection. In the attention mechanism, we first compute scores using the input of attention layer f_i. Specifically, W and b here are trainable parameters. We compute the linear mapping of f_i and then it is activated by nonlinear function $\tanh(\cdot)$. tanh shown in Figure 1 represents this process. In order to get the weight in the interval [0, 1], the softmax function is applied to the scores we get previously. softmax shown in Figure 1 represents this step. Finally, the output of the attention layer is obtained by using different weight factors in the input features f_i to achieve the weighted average. The intersection of the dashed line and the solid line represents a

multiplication of scalars and vectors, and the plus sign in the circle means the addition of a vector.

4. Experimental Studies and Results

4.1. Environment. Python 3.7 and Pytorch 1.2.0 are used to implement the proposed approach. In this study, all of the experiments were carried out on a server using 128 GB of RAM, a Xeon E5 2620 processor, and four GeForce RTX 2080 graphics cards.

4.2. Data Description. The PTB-XL dataset [39] consists of 21837 clinical 12-lead ECG records from 18885 patients, each lasting 10 seconds. The annotation of ECG statements follows the SCP-ECG standard [40], and each record can have several statements. The ECG statements in the dataset are divided into 71 different classes. There are 44 diagnostic statements, 19 form statements, and 12 rhythm statements in these categories. The statements are nonexclusive at three levels, and the diagnostic statements comprise four form rhythm statements. Furthermore, diagnostic statements are divided into five superclasses (CD: conduction disturbance, HYP: hypertrophy, MI: myocardial infarction, NORM: normal ECG, and STTC: ST/T change) and 23 subclasses. The number of ECG records and the descriptions of different classes for superclasses of diagnostic statements are shown in Table 1. This study employed a sampling rate of 100 Hz.

4.3. Evaluation Metric. We use area under curve (AUC) to evaluate how our model performs on arrhythmia classification. AUC refers to the area under a receiver operating characteristic curve [41]. Let n be the number of samples, M refers to the number of positive samples, and N refers to the number of negative samples; here, $n = M + N$. First, the samples are sorted in descending order by score. Then, the rank corresponding to the sample with the largest score is set as n, and the rank corresponding to the sample with the second-largest score is set as $n - 1$, and so on. Then, we add up the ranks of all the positive samples, subtract $M(1 + M)/2$, and then divide by $M \times N$. To sum up, AUC is defined as

$$AUC = \frac{\sum_{i \in positiveClass} rank_i - M(1 + M)/2}{M \times N}. \quad (9)$$

The Mann–Whitney U, which determines whether negatives are rated lower than positives, is found to be closely related to the AUC. The Wilcoxon test of ranks [42] is another name for it.

4.4. Training Setting

4.4.1. Model Optimization. Mini-batch is used for saving memory and accelerating training. The batch size is set to 256 samples. The Xavier uniform initializer [43] is used to initialize the weights of convolutional layers, while the orthogonal initializer is used to initialize the weights of the bidirectional GRU. We also employ the Adam optimizer [44] to iteratively update the parameters due to its potential

Table 1: List of the distribution and the description for superclasses of diagnostic statements.

#Records	Superclass	Description
9528	NORM	Normal ECG
5486	MI	Myocardial infarction
5250	STTC	ST/T change
4907	CD	Conduction disturbance
2655	HYP	Hypertrophy

to speed up the convergence of the network. The rate of learning is set at 3e-4.

4.4.2. Regularization Strategies. Because the neural network has huge amounts of parameters, to avoid overfitting, we need to apply regularization on the loss function to impose a cost on the optimization function to make the optimal solution smooth. Specifically, L_2 regularization is utilized in our model. L_2 regularization is the most common regularization technique. L_2 regularization limits the magnitude of the parameters by adding a penalty term to the loss function. With w representing the parameters of the model, L_2 regularization is expressed as

$$L_2(\theta) = \|\theta\|_2^2 = \sum_i \theta_i^2. \quad (10)$$

The loss function with L_2 regularization term is expressed as

$$L_R(X; \mathscr{H}) = L(X; \mathscr{H}) + L_2(\theta). \quad (11)$$

Here, $L_R(X; \mathscr{H})$ is the loss function used in our model, $L(X; \mathscr{H})$ is the BCE loss as noted in equation (3).

4.4.3. Cross Validation. The PTB-XL dataset was divided into ten parts by reference [39]. The tenth part serves as the test set and the rest of the nine parts serve as the training set. For the remaining nine parts, we follow the recommendation and use 9-fold cross-validation to make use of the training set thoroughly in consideration of the small size of the training set. We divide the training set into nine equal parts using this strategy. Each of the nine parts takes turns as the validation data, and the training data is made up of the remaining subsets. In the end, the final probabilities are calculated by averaging the output of nine models.

4.5. Experimental Process. The input shape of the network is (256, 12, 1000). The first dimension is the batch size for the mini-batch, here is 256. The second dimension refers to the channel number (i.e., the number of leads). The third dimension here is the length of the signal whose sampling frequency is 100 Hz and duration is 10 s.

After passing the segmentation module, the dimensions are turned into (256, 20, 12, and 80). Here, the first dimension is still the batch size and the third dimension is the channel number. The second dimension is the number of beats and the fourth dimension is the length of beat, which is set to 25 before R-peak and 55 after R-peak. Then, these

segmented ECG signals are fed into the beat-level feature extraction module. Since one out of every two convolutional layers is set to stride 2, the output of the convolutional block is with dimensions (256, 20, 256, and 10). The first and the second dimensions are the same as before and the third dimension is the kernel number of the last layer. These feature maps are flowed into a GRU and a linear layer to get features with dimensions (256, 20, 64, and 10).

Next, these features are put into the interbeat feature fusion module to fuse features extracted from the beat-level feature extraction module along the dimension of different beats. The input of the beat-level feature fusion module is reshaped into (256, 20, 640). That is, we merge the last two dimensions as features of a certain beat. All these features are fed into the attention layer to obtain the fusion features with dimensions (256, 640). Finally, a fully connected layer is adopted as a classifier to transform these features into probabilities of different kinds of arrhythmias. Here, the sigmoid function is utilized to compress the output of the model into probabilities between 0 and 1. Adam optimizer is adopted to iteratively update network parameters.

5. Result & Discussion

5.1. Classification Performance. With the above-given experimental setup, the experiments were conducted. We followed the recommendations of [45] and compared them with 7 previous works at 6 annotation levels. Table 2 compares the proposed method with 7 previous works [45] on six classification tasks based on macro-AUC scores. As shown in Table 2, our algorithm has superiority over the works listed in [45]. Compared to the wavelet + NN algorithm, macro-AUC scores are improved by 9.2%, 9.7%, 9.5%, 7.1%, 17.7%, and 8.9% in the six classification tasks, respectively. The number of parameters in our model is better than that of methods with similar performance, as will be discussed later. This demonstrates that the proposed algorithm produces a significant improvement in detecting most arrhythmias, suggesting that it is a competitive method in detecting arrhythmias when compared to state-of-the-art methods. And, the confusion matrices are shown in Figure 2.

5.2. Ablation Studies. To explain the effectiveness of BLF-Net and investigate the influence of hyperparameters in model performance, ablation studies are applied. In this process, we deploy the same experimental settings as before. That is, the same evaluation metric and training settings are adopted.

5.2.1. Comparison between Backbone Network and BLF-Net. To illustrate the validity of BLF-Net, we make experiments to compare the performance between the backbone network and BLF-Net. The backbone network is the same structure as the beat-level feature extraction module shown in Figure 1, which is followed by a fully connected layer as a classifier. There is no beat-level fusion structure in the backbone network. That is, we send the original ECG signal to the backbone network without segmentation and interbeat

Table 2: Comparing our work with the previous works in terms of classification performance.

Models	Macro-AUC scores					
	All	Diag.	Sub-diag.	Super-diag.	Form	Rhythm
Lstm[1]	0.907	0.927	0.928	0.927	0.851	0.953
Inception1d[1]	0.925	0.931	0.930	0.921	**0.899**	0.953
Lstm_bidir[1]	0.914	0.932	0.923	0.921	0.876	0.949
Resnet1d_wang[1]	0.919	0.936	0.928	0.930	0.880	0.946
Fcn_wang[1]	0.918	0.926	0.927	0.925	0.869	0.931
Wavelet + NN[1]	0.849	0.855	0.859	0.874	0.757	0.890
Xresnet1d101[1]	0.925	0.937	0.929	0.928	0.896	0.957
Ours	**0.927**	**0.938**	**0.941**	**0.936**	0.891	**0.969**

[1]These models are stated in detail in [45]. The best performance is highlighted in bold.

Figure 2: The confusion matrices of BLF-net on superdiagnostic. The first subfigure shows an example of a subfigure. TN, FP, FN, and TP represent true negative, false positive, false negative and true positive, respectively.

feature fusion. By contrast, we deploy the model with segmentation and feature fusion i.e., BLF-Net. Table 3 shows the macro-AUC score of the backbone network and BLF-Net in classifying multi-class cardiac arrhythmias based on the PTB-XL dataset.

This experiment demonstrates the introduction of the beat-level fusion module can effectively improve the accuracy of arrhythmia detection by contrast with a simple feature extraction module. As shown in Table 3, BLF-Net outperforms BackboneNet based on the macro-AUC score of all different criteria in detecting multiclass cardiac arrhythmias.

5.2.2. Comparison between Temporal Attention Module and with Interbeat Feature Fusion Module. To verify the effectiveness of the interbeat feature fusion module, we make another experiment to compare the performance between the temporal attention module and the interbeat feature fusion module. In this experiment, we remove the segmentation module of BLF-Net and feed the original ECG signal into the neural network. Then, the interbeat feature fusion module is changed to the temporal attention module. The modified model is named temporal attention network, and we compare the results of this model with BLF-Net. The

TABLE 3: Comparing our work with the branch network in terms of classification performance.

Models	Macro-AUC scores					
	All	Diag.	Sub-diag.	Super-diag.	Form	Rhythm
BackboneNet	0.908	0.924	0.921	0.919	0.828	0.946
BLF-net	**0.927**	**0.938**	**0.941**	**0.936**	**0.891**	**0.969**

The best performance is highlighted in bold.

structure of the temporal attention network consists of the backbone network and the temporal attention module. The backbone network is the same configuration as the BLF-Net, which is followed by the temporal attention module used for assigning weights to the features temporally. A fully connected classifier is employed here and the number of output categories is denoted as n_c. The result is shown in Table 4. This experiment is conducted to demonstrate that the attention module applied among beats outperforms that applied among time points. The temporal attention module assigns weights temporally. This means that the attention module focuses on the microlevel, which is less likely to capture global information and focuses more on local changes. While the interbeat feature fusion module focuses on the beat level, this allows for a better fusion of features extracted from each beat.

5.2.3. Analysis of Segmentation Length. The heartbeat length L_b in this experiment is set to 80 points. This hyperparameter can be regarded as a window size for a beat-level feature extraction module to observe heartbeats. Here, experiments were conducted to analyse the effect of this hyperparameter on the model. We chose different heartbeat length L_b to repeat the experiments of arrhythmias detection based on the PTB-XL dataset. Table 5 shows the result of these experiments. It can be seen that among the rhythm $L_b = 160$ reachs the highest score and among the form $L_b = 80$ reaches the highest score. From here, we can get a conclusion, the greater the heartbeat length we set, the better score among the rhythm we get. And, the smaller heartbeat length we set, the better score among the form we get. we can infer that a greater heartbeat length will catch more information about rhythm and a smaller heartbeat length will catch less.

An explanation is given for the decrease in macro-AUC scores as the heartbeat length is reduced. A shorter heartbeat length means a smaller observation window for the ECG signal. The signal acquired by a single heartbeat becomes less. Unlike morphological judgments, rhythm is inferred by comparing similar signals at the time before and after. While morphology is judged by the amplitude at the same time. For shorter time windows, we have less signal to observe and less signal to compare back and forth. For longer time windows, more signals can be observed and more signals can be compared back and forth to determine rhythm-related information, so the larger the observation window, the more accurate the rhythm-related judgments. Longer signals mean that it is easier to determine the rhythm of the heartbeat.

5.3. Performance Analysis. ECG signal is composed of beats, each heartbeat reflects the same electrical activity (i.e., from depolarization to repolarization). One cycle of the electrical activity of the heart can be denoted as a random signal $X(t)$. Beat in the sample can be regarded as the observed signal $x(t)$ of random signal $X(t)$. Beats that come from the same ECG signal have the same physiological meanings and individuals, so they can be considered as an identical distribution. Therefore, a series of continuous beats can be dealt with the same network due to identical distribution. In this paper, a module named beat-level feature extraction is deployed to extract features from beats. Our beat-level feature extraction module extract features from beats with the same structure. Then, features extracted by the beat-level feature extraction module are fed into the interbeat feature fusion module to focus more on the representative beats. Take the STTC as an example. The ST segment myocardial infarction (STEMI) is reflected in ST elevation [46]. ST elevation is linked to infarction and can be preceded by changes indicating ischemia, such as ST depression or the T waves inversion, according to [47]. In this case, our model will assign higher weights to those heartbeats that show the morphological characteristic of ST elevation.

5.4. Attention Weights. To illustrate how the interbeat feature fusion module works, we show the weights assigned by the attention layer, as shown in Figure 3. The upper parts in Figures 3(a)–3(d) show the waveform of lead II, and the lower parts show the weights assigned by our interbeat feature fusion module. The higher weight assigned to a beat, the more contribution this beat has to the result. As shown in Figure 3, our model gives higher weights to the abnormal heartbeats, suggesting that these abnormal heartbeats are paid more attention to in our method. In clinical practice, abnormal heartbeats define the diagnostic results for the ECG signal. Therefore, we can consider that the proposed method well learns the important features from ECG signals and reasonably explains the classification results.

5.5. Parameter Size. We make a comparison in terms of the number of parameters between the proposed BLF-Net and four previous works in this subsection, as shown in Table 6. It can be seen that the proposed model does not have a large number of parameters but achieves optimal performance. Compared to "inception1d" and "resnet1d_wang," our model outperforms on the macro-AUC score. And, as shown in Table 2, our model surpasses the performance of other models on subdiagnostic and superdiagnostic significantly. Although the performance of the model "xresnet1d101" is comparable to ours, the number of parameters in our model is much less than this works. The experiment result shows that a decrease in convolutional layers doesn't sacrifice the ability of models to learn compared with other models. In addition, fewer parameters are less likely to overfit, contributing to better generalization and less memory-consuming.

TABLE 4: Comparing our work with the temporal attention network in terms of classification performance.

Models	Macro-AUC scores					
	All	Diag.	Sub-diag.	Super-diag.	Form	Rhythm
Temporal attention network	0.921	0.920	0.923	0.930	0.855	0.953
BLF-net	**0.927**	**0.938**	**0.941**	**0.936**	**0.891**	**0.969**

TABLE 5: Comparison of BLF-Net with different heartbeat lengths in terms of classification performance.

Lengths	Macro-AUC scores					
	All	Diag.	Sub-diag.	Super-diag.	Form	Rhythm
$L_b = 160$	0.925	0.937	0.931	0.933	0.887	**0.969**
$L_b = 120$	0.923	**0.938**	0.934	0.931	0.890	0.961
$L_b = 80$	**0.927**	0.937	**0.941**	**0.936**	**0.891**	0.954

The best performance is highlighted in bold.
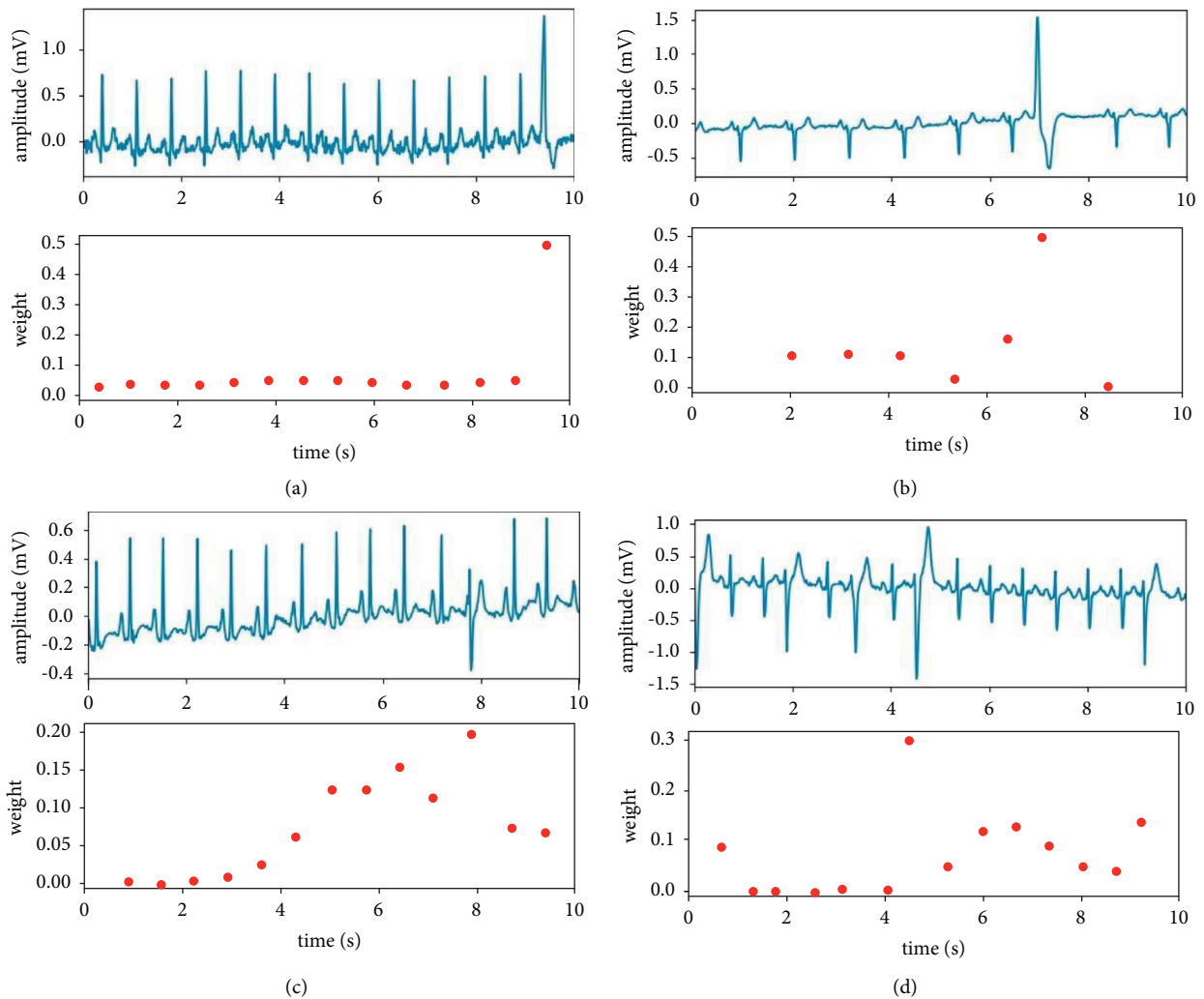
FIGURE 3: The heartbeat-level weights assigned by the proposed interbeat feature fusion module for different ECG classes including (a) myocardial Infarction, (b) conduction disturbance and myocardial infarction, (c) myocardial infarction and ST/T change, and (d) conduction disturbance and hypertrophy and myocardial Infarction. The upper subfigures in (a)–(d) show the original ECG signal from lead II. The lower subfigures show the corresponding heartbeat-level weights.

TABLE 6: Comparison of the number of parameters of previous works and the proposed BLF-Net.

Models	The number of parameters
Inception1d[1]	507653
Resnet1d_wang[1]	473349
Fcn_wang[1]	309765
Xresnet1d101[1]	3642501
Ours	569373

[1]These models are stated in detail in [45].

6. Conclusion

BLF-Net, an end-to-end multiclass arrhythmia classification model utilizing 12-lead ECG records, is proposed in this study. The attention mechanism is used by BLF-Net to focus on the informative features while suppressing the unimportant ones. Experiments show that when compared to off-the-shelf methods, BLF-Net achieves state-of-the-art performance. And, BLF-Net is both lightweight and effective. BLF-Net, the proposed model for arrhythmia classification, has the promise of aiding cardiologists in their clinical practice.

Data Availability

The PTB-XL database used to support the findings of this study is publicly available and can be downloaded at https://physionet.org/files/ptb-xl/1.0.1/.

Conflicts of Interest

The authors declare that they have no conflicts of interest.

Acknowledgments

References

[1] World Health Organization, "Cardiovascular diseases (cvds)," 2021, https://www.who.int/news-room/fact-sheets/detail/cardiovascular-diseases-(cvds.

[2] R. Mehra, "Global public health problem of sudden cardiac death," *Journal of Electrocardiology*, vol. 40, no. 6, pp. S118–S122, 2007.

[3] J W. Hurst, "Naming of the waves in the ecg, with a brief account of their genesis," *Circulation*, vol. 98, no. 18, pp. 1937–1942, 1998.

[4] T. Adjei, W. Von Rosenberg, V. Goverdovsky et al., "Pain prediction from ecg in vascular surgery," *IEEE journal of Translational Engineering in Health and Medicine*, vol. 5, no. 1–10, pp. 1–10, 2017.

[5] Y. Kutlu, D. Kuntalp, and D. Kuntalp, "A multi-stage automatic arrhythmia recognition and classification system," *Computers in Biology and Medicine*, vol. 41, no. 1, pp. 37–45, 2011.

[6] Z Zhang, J. Dong, X Luo et al., "Heartbeat classification using disease-specific feature selection," *Computers in Biology and Medicine*, vol. 46, pp. 79–89, 2014.

[7] H. H. Haseena, A. T. Mathew, J K. Paul, T. Mathew, and J. K. Paul, "Fuzzy clustered probabilistic and multi layered feed forward neural networks for electrocardiogram arrhythmia classification," *Journal of Medical Systems*, vol. 35, no. 2, pp. 179–188, 2011.

[8] G M Lin, K. M. Liu, and K. Liu, "An electrocardiographic system with anthropometrics via machine learning to screen left ventricular hypertrophy among young adults," *IEEE Journal of Translational Engineering in Health and Medicine*, vol. 8, no. 1–11, pp. 1–11, 2020.

[9] M. Seera, C. P. Lim, W S Liew et al., "Classification of electrocardiogram and auscultatory blood pressure signals using machine learning models," *Expert Systems with Applications*, vol. 42, no. 7, pp. 3643–3652, 2015.

[10] F A Elhaj, N. Salim, A R Harris et al., "Arrhythmia recognition and classification using combined linear and nonlinear features of ecg signals," *Computer Methods and Programs in Biomedicine*, vol. 127, pp. 52–63, 2016.

[11] T. Ince, S. Kiranyaz, G. M. Kiranyaz, and M. Gabbouj, "A generic and robust system for automated patient-specific classification of ecg signals," *IEEE Transactions on Biomedical Engineering*, vol. 56, no. 5, pp. 1415–1426, 2009.

[12] R. J. Martis, U. R. Acharya, H. Prasad et al., "Application of higher order statistics for atrial arrhythmia classification," *Biomedical Signal Processing and Control*, vol. 8, no. 6, pp. 888–900, 2013.

[13] R. J. Martis, U Acharya, H. Prasad et al., "Automated detection of atrial fibrillation using bayesian paradigm," *Knowledge-Based Systems*, vol. 54, pp. 269–275, 2013.

[14] R. J. Martis, U. R. Acharya, L. Min, C. Rajendra Acharya, and L. C. Min, "Ecg beat classification using pca, lda, ica and discrete wavelet transform," *Biomedical Signal Processing and Control*, vol. 8, no. 5, pp. 437–448, 2013.

[15] J S Wang, W. C. Chiang, Y L Hsu et al., "Ecg arrhythmia classification using a probabilistic neural network with a feature reduction method," *Neurocomputing*, vol. 116, pp. 38–45, 2013.

[16] H. Khorrami, M. Moavenian, and M. Moavenian, "A comparative study of dwt, cwt and dct transformations in ecg arrhythmias classification," *Expert Systems with Applications*, vol. 37, no. 8, pp. 5751–5757, 2010.

[17] G. M. Lin and H. H. S. Lu, "A 12-lead ecg-based system with physiological parameters and machine learning to identify right ventricular hypertrophy in young adults," *IEEE Journal of Translational Engineering in Health and Medicine*, vol. 8, no. 1–10, pp. 1–10, 2020.

[18] Y. Özbay, "A new approach to detection of ecg arrhythmias: A New Approach to Detection of ECG Arrhythmias: Complex Discrete Wavelet Transform Based Complex Valued Artificial Neural Networkomplex discrete wavelet transform based complex valued artificial neural network," *Journal of Medical Systems*, vol. 33, no. 6, pp. 435–445, 2009.

[19] R. J. Ka Naz and P. Niyas, "Deep neural network based multiclass arrhythmia classification," *Intelligent Systems, Technologies and Applications: Proceedings of Sixth ISTA 2020*, pp. 223–235, India, 2021.

[20] S. Kiranyaz, T. Ince, M. Gabbouj, T. Ince, and M. Gabbouj, "Real-time patient-specific ecg classification by 1-d convolutional neural networks," *IEEE Transactions on Biomedical Engineering*, vol. 63, no. 3, pp. 664–675, 2016.

[21] M M Al Rahhal, Y. Bazi, M. Al Zuair et al., "Convolutional neural networks for electrocardiogram classification," *Journal of Medical and Biological Engineering*, vol. 38, no. 6, pp. 1014–1025, 2018.

[22] A Y. Hannun, P. Rajpurkar, M. Haghpanahi et al., "Cardiologist-level arrhythmia detection and classification in ambulatory electrocardiograms using a deep neural network," *Nature Medicine*, vol. 25, no. 1, pp. 65–69, 2019.

[23] S Saadatnejad, M Oveisi, M Hashemi, M. Oveisi, and M. Hashemi, "Lstm-based ecg classification for continuous monitoring on personal wearable devices," *IEEE journal of biomedical and health informatics*, vol. 24, no. 2, pp. 515–523, 2020.

[24] H. M. Lynn, S B Pan, P. Kim, and P. Kim, "A deep bidirectional gru network model for biometric electrocardiogram classification based on recurrent neural networks," *IEEE Access*, vol. 7, pp. 145395–145405, 2019.

[25] R. He, Y. Liu, K Wang et al., "Automatic cardiac arrhythmia classification using combination of deep residual network and bidirectional lstm," *IEEE Access*, vol. 7, pp. 102119–102135, 2019.

[26] Q. Yao, X. Fan, Y. Cai, R Wang, L Yin, and Y Li, "Time-incremental convolutional neural network for arrhythmia detection in varied-length electrocardiogram," in *Proceedings of the 2018 IEEE 16th Intl Conf on Dependable, Autonomic and Secure Computing, 16th Intl Conf on Pervasive Intelligence and Computing, 4th Intl Conf on Big Data Intelligence and Computing and Cyber Science and Technology Congress (DASC/PiCom/DataCom/CyberSciTech)*, IEEE, Athens, Greece, Auguest 2018.

[27] Q. Yao, R. Wang, X. Fan et al., "Multi-class arrhythmia detection from 12-lead varied-length ecg using attention-based time-incremental convolutional neural network," *Information Fusion*, vol. 53, pp. 174–182, 2020.

[28] M. Jiang, J. Gu, Li Yang et al., "HADLN: hybrid attention-based deep learning network for automated arrhythmia classification," *Frontiers in Physiology*, vol. 12, 2021.

[29] D. Bahdanau, K. H. Cho, and Y. Bengio, "Neural machine translation by jointly learning to align and translate," in *Proceedings of the The 3rd International Conference on Learning Representations(ICLR)*, San Diego, CA, USA, May 2015.

[30] A. Vaswani, N. Shazeer, N. Parmar et al., "Attention is all you need," *Advances in Neural Information Processing Systems*, vol. 30, 2017.

[31] W. Jin, H. Yu, and X. Luo, "Cvt-assd: convolutional vision-transformer based attentive single shot multibox detector," in *Proceedings of the 2021 IEEE 33rd International Conference on Tools with Artificial Intelligence (ICTAI)*, pp. 736–744, IEEE, Washington, DC, USA, November 2021.

[32] J. Zhang, A. Liu, M. Gao et al., "Ecg-based multi-class arrhythmia detection using spatio-temporal attention-based convolutional recurrent neural network," *Artificial Intelligence in Medicine*, vol. 106, Article ID 101856, 2020.

[33] J. Pan, W. Tompkins, J. Pan, and W. J. Tompkins, "A real-time qrs detection algorithm," *IEEE Transactions on Biomedical Engineering*, vol. 3, pp. 230–236, 1985.

[34] S. Ioffe and C. Szegedy, "Batch normalization: accelerating deep network training by reducing internal covariate shift," in *Proceedings of the International Conference on Machine Learning*, pp. 448–456, PMLR, Miami, Florida, USA, July 2015.

[35] V. Nair and G. E. Hinton, "Rectified Linear Units Improve Restricted Boltzmann Machines," in *Proceedings of the 27th International Conference on International Conference on Machine Learning*, Haifa Israel, June 2010.

[36] N. Srivastava, G. Hinton, A. Krizhevsky, I. Sutskever, and R. Salakhutdinov, "Dropout: a simple way to prevent neural networks from overfitting," *Journal of Machine Learning Research*, vol. 15, no. 1, pp. 1929–1958, 2014.

[37] K. Cho, B. Van Merriënboer, C. Gulcehre et al., "Learning phrase representations using rnn encoder-decoder for statistical machine translation," 2014, https://arxiv.org/abs/1406.1078.

[38] Z. Yang, D. Yang, C. Dyer, X. He, A. Smola, and E. Hovy, "Hierarchical attention networks for document classification," in *Proceedings of the 2016 Conference of the North American Chapter of the Association for Computational Linguistics: Human Language Technologies*, San Diego, CA, USA, June 2016.

[39] P. Wagner, N. Strodthoff, R. D. Bousseljot et al., "PTB-XL, a large publicly available electrocardiography dataset," *Scientific Data*, vol. 7, no. 1, 2020.

[40] ISO Central Secretary, *Health Informatics — Standard Communication Protocol — Part 91064: Computer-Assisted Electrocardiography*, International Organization for Standardization, Geneva, CH, Switzerland, 2009.

[41] F. T. Fawcett, "An introduction to ROC analysis," *Pattern Recognition Letters*, vol. 27, no. 8, pp. 861–874, 2006.

[42] S J Mason, N. E. Graham, J. Mason, and N. E. Graham, "Areas beneath the relative operating characteristics (roc) and relative operating levels (rol) curves: Areas beneath the relative operating characteristics (ROC) and relative operating levels (ROL) curves: Statistical significance and interpretationtatistical significance and interpretation," *Quarterly Journal of the Royal Meteorological Society*, vol. 128, no. 584, pp. 2145–2166, 2002.

[43] X. Glorot and Y. Bengio, "Understanding the difficulty of training deep feedforward neural networks," in *Proceedings of the 13th International Conference on Artificial Intelligence and Statistics*, pp. 249–256, Sardinia, Italy, May 2010.

[44] D. P. Kingma and B. Jimmy, "Adam: a method for stochastic optimization," 2014, https://arxiv.org/abs/1412.6980.

[45] N. Strodthoff, P. Wagner, T Schaeffter, W. Samek, S. Tobias, and W. Samek, "Deep learning for ecg analysis: Deep Learning for ECG Analysis: Benchmarks and Insights from PTB-XLenchmarks and insights from ptb-xl," *IEEE Journal of Biomedical and Health Informatics*, vol. 25, no. 5, pp. 1519–1528, 2021.

[46] J. Jeroen, "Third universal definition of myocardial infarction"," *Journal of the American College of Cardiology*, vol. 60, no. 16, pp. 1581–1598, 2012.

[47] B. R. Walker and N. R. Colledge, *Davidson's Principles and Practice of Medicine E-Book*, Elsevier Health Sciences, Amsterdam, Netherlands, 2013.

Retraction

Retracted: U-Net-Based Medical Image Segmentation

Journal of Healthcare Engineering

This article has been retracted by Hindawi following an investigation undertaken by the publisher [1]. This investigation has uncovered evidence of one or more of the following indicators of systematic manipulation of the publication process:

(1) Discrepancies in scope

(2) Discrepancies in the description of the research reported

(3) Discrepancies between the availability of data and the research described

(4) Inappropriate citations

(5) Incoherent, meaningless and/or irrelevant content included in the article

(6) Peer-review manipulation

The presence of these indicators undermines our confidence in the integrity of the article's content and we cannot, therefore, vouch for its reliability. Please note that this notice is intended solely to alert readers that the content of this article is unreliable. We have not investigated whether authors were aware of or involved in the systematic manipulation of the publication process.

Wiley and Hindawi regrets that the usual quality checks did not identify these issues before publication and have since put additional measures in place to safeguard research integrity.

We wish to credit our own Research Integrity and Research Publishing teams and anonymous and named external researchers and research integrity experts for contributing to this investigation.

The corresponding author, as the representative of all authors, has been given the opportunity to register their agreement or disagreement to this retraction. We have kept a record of any response received.

References

[1] X. Yin, L. Sun, Y. Fu, R. Lu, and Y. Zhang, "U-Net-Based Medical Image Segmentation," *Journal of Healthcare Engineering*, vol. 2022, Article ID 4189781, 16 pages, 2022.

Retraction

Retracted: Effects of the Femoral Nerve Block and Adductor Canal Block on Tourniquet Response and Postoperative Analgesia in Total Knee Arthroplasty

Journal of Healthcare Engineering

This article has been retracted by Hindawi following an investigation undertaken by the publisher [1]. This investigation has uncovered evidence of one or more of the following indicators of systematic manipulation of the publication process:

(1) Discrepancies in scope

(2) Discrepancies in the description of the research reported

(3) Discrepancies between the availability of data and the research described

(4) Inappropriate citations

(5) Incoherent, meaningless and/or irrelevant content included in the article

(6) Peer-review manipulation

The presence of these indicators undermines our confidence in the integrity of the article's content and we cannot, therefore, vouch for its reliability. Please note that this notice is intended solely to alert readers that the content of this article is unreliable. We have not investigated whether authors were aware of or involved in the systematic manipulation of the publication process.

In addition, our investigation has also shown that one or more of the following human-subject reporting requirements has not been met in this article: ethical approval by an Institutional Review Board (IRB) committee or equivalent, patient/participant consent to participate, and/or agreement to publish patient/participant details (where relevant).

Wiley and Hindawi regrets that the usual quality checks did not identify these issues before publication and have since put additional measures in place to safeguard research integrity.

We wish to credit our own Research Integrity and Research Publishing teams and anonymous and named external researchers and research integrity experts for contributing to this investigation.

The corresponding author, as the representative of all authors, has been given the opportunity to register their agreement or disagreement to this retraction. We have kept a record of any response received.

References

[1] D. Jin, Y. Zhu, F. Ji, and X. Kong, "Effects of the Femoral Nerve Block and Adductor Canal Block on Tourniquet Response and Postoperative Analgesia in Total Knee Arthroplasty," *Journal of Healthcare Engineering*, vol. 2022, Article ID 2327753, 6 pages, 2022.

Retraction

Retracted: Impact of High-Flux Hemodialysis on Chronic Inflammation, Antioxidant Capacity, Body Temperature, and Immune Function in Patients with Chronic Renal Failure

Journal of Healthcare Engineering

This article has been retracted by Hindawi following an investigation undertaken by the publisher [1]. This investigation has uncovered evidence of one or more of the following indicators of systematic manipulation of the publication process:

(1) Discrepancies in scope

(2) Discrepancies in the description of the research reported

(3) Discrepancies between the availability of data and the research described

(4) Inappropriate citations

(5) Incoherent, meaningless and/or irrelevant content included in the article

(6) Peer-review manipulation

The presence of these indicators undermines our confidence in the integrity of the article's content and we cannot, therefore, vouch for its reliability. Please note that this notice is intended solely to alert readers that the content of this article is unreliable. We have not investigated whether authors were aware of or involved in the systematic manipulation of the publication process.

Wiley and Hindawi regrets that the usual quality checks did not identify these issues before publication and have since put additional measures in place to safeguard research integrity.

We wish to credit our own Research Integrity and Research Publishing teams and anonymous and named external researchers and research integrity experts for contributing to this investigation.

The corresponding author, as the representative of all authors, has been given the opportunity to register their agreement or disagreement to this retraction. We have kept a record of any response received.

References

[1] S. Li, H. Li, J. Wang, and L. Yin, "Impact of High-Flux Hemodialysis on Chronic Inflammation, Antioxidant Capacity, Body Temperature, and Immune Function in Patients with Chronic Renal Failure," *Journal of Healthcare Engineering*, vol. 2022, Article ID 7375006, 7 pages, 2022.

Retraction

Retracted: Knowledge-Based Discovery of the Role and Mechanism of Resveratrol in Improving Glomerular Tether Cell Proliferation and Apoptosis in Diabetic Nephropathy

Journal of Healthcare Engineering

This article has been retracted by Hindawi following an investigation undertaken by the publisher [1]. This investigation has uncovered evidence of one or more of the following indicators of systematic manipulation of the publication process:

(1) Discrepancies in scope

(2) Discrepancies in the description of the research reported

(3) Discrepancies between the availability of data and the research described

(4) Inappropriate citations

(5) Incoherent, meaningless and/or irrelevant content included in the article

(6) Peer-review manipulation

The presence of these indicators undermines our confidence in the integrity of the article's content and we cannot, therefore, vouch for its reliability. Please note that this notice is intended solely to alert readers that the content of this article is unreliable. We have not investigated whether authors were aware of or involved in the systematic manipulation of the publication process.

In addition, our investigation has also shown that one or more of the following human-subject reporting requirements has not been met in this article: ethical approval by an Institutional Review Board (IRB) committee or equivalent, patient/participant consent to participate, and/or agreement to publish patient/participant details (where relevant).

Wiley and Hindawi regrets that the usual quality checks did not identify these issues before publication and have since put additional measures in place to safeguard research integrity.

We wish to credit our own Research Integrity and Research Publishing teams and anonymous and named external researchers and research integrity experts for contributing to this investigation.

The corresponding author, as the representative of all authors, has been given the opportunity to register their agreement or disagreement to this retraction. We have kept a record of any response received.

References

[1] Y. Chi, S. Liu, X. Wu et al., "Knowledge-Based Discovery of the Role and Mechanism of Resveratrol in Improving Glomerular Tether Cell Proliferation and Apoptosis in Diabetic Nephropathy," *Journal of Healthcare Engineering*, vol. 2022, Article ID 9705144, 8 pages, 2022.

Retraction

Retracted: Knowledge Discovery-Based Analysis of Health Factors of Urinary Infections in Elderly Cardiology Inpatients

Journal of Healthcare Engineering

This article has been retracted by Hindawi following an investigation undertaken by the publisher [1]. This investigation has uncovered evidence of one or more of the following indicators of systematic manipulation of the publication process:

(1) Discrepancies in scope

(2) Discrepancies in the description of the research reported

(3) Discrepancies between the availability of data and the research described

(4) Inappropriate citations

(5) Incoherent, meaningless and/or irrelevant content included in the article

(6) Peer-review manipulation

The presence of these indicators undermines our confidence in the integrity of the article's content and we cannot, therefore, vouch for its reliability. Please note that this notice is intended solely to alert readers that the content of this article is unreliable. We have not investigated whether authors were aware of or involved in the systematic manipulation of the publication process.

In addition, our investigation has also shown that one or more of the following human-subject reporting requirements has not been met in this article: ethical approval by an Institutional Review Board (IRB) committee or equivalent, patient/participant consent to participate, and/or agreement to publish patient/participant details (where relevant).

Wiley and Hindawi regrets that the usual quality checks did not identify these issues before publication and have since put additional measures in place to safeguard research integrity.

We wish to credit our own Research Integrity and Research Publishing teams and anonymous and named external researchers and research integrity experts for contributing to this investigation.

The corresponding author, as the representative of all authors, has been given the opportunity to register their agreement or disagreement to this retraction. We have kept a record of any response received.

References

[1] M. Zhao, Y. Pi, and L. Zhang, "Knowledge Discovery-Based Analysis of Health Factors of Urinary Infections in Elderly Cardiology Inpatients," *Journal of Healthcare Engineering*, vol. 2022, Article ID 7037037, 8 pages, 2022.

Hindawi

Retraction

Retracted: Study of Subfascial Endoscopic Perforator Surgery Combined with Endovenous Laser Treatment in the Treatment of Great Saphenous Varicose Veins

Journal of Healthcare Engineering

This article has been retracted by Hindawi following an investigation undertaken by the publisher [1]. This investigation has uncovered evidence of one or more of the following indicators of systematic manipulation of the publication process:

(1) Discrepancies in scope

(2) Discrepancies in the description of the research reported

(3) Discrepancies between the availability of data and the research described

(4) Inappropriate citations

(5) Incoherent, meaningless and/or irrelevant content included in the article

(6) Peer-review manipulation

The presence of these indicators undermines our confidence in the integrity of the article's content and we cannot, therefore, vouch for its reliability. Please note that this notice is intended solely to alert readers that the content of this article is unreliable. We have not investigated whether authors were aware of or involved in the systematic manipulation of the publication process.

In addition, our investigation has also shown that one or more of the following human-subject reporting requirements has not been met in this article: ethical approval by an Institutional Review Board (IRB) committee or equivalent, patient/participant consent to participate, and/or agreement to publish patient/participant details (where relevant).

Wiley and Hindawi regrets that the usual quality checks did not identify these issues before publication and have since put additional measures in place to safeguard research integrity.

We wish to credit our own Research Integrity and Research Publishing teams and anonymous and named external researchers and research integrity experts for contributing to this investigation.

The corresponding author, as the representative of all authors, has been given the opportunity to register their agreement or disagreement to this retraction. We have kept a record of any response received.

References

[1] L. Wang, J. Du, and H. Zhang, "Study of Subfascial Endoscopic Perforator Surgery Combined with Endovenous Laser Treatment in the Treatment of Great Saphenous Varicose Veins," *Journal of Healthcare Engineering*, vol. 2022, Article ID 1801099, 7 pages, 2022.

Retraction

Retracted: Random Forest and LightGBM-Based Human Health Check for Medical Device Fault Detection

Journal of Healthcare Engineering

This article has been retracted by Hindawi following an investigation undertaken by the publisher [1]. This investigation has uncovered evidence of one or more of the following indicators of systematic manipulation of the publication process:

(1) Discrepancies in scope

(2) Discrepancies in the description of the research reported

(3) Discrepancies between the availability of data and the research described

(4) Inappropriate citations

(5) Incoherent, meaningless and/or irrelevant content included in the article

(6) Peer-review manipulation

The presence of these indicators undermines our confidence in the integrity of the article's content and we cannot, therefore, vouch for its reliability. Please note that this notice is intended solely to alert readers that the content of this article is unreliable. We have not investigated whether authors were aware of or involved in the systematic manipulation of the publication process.

Wiley and Hindawi regrets that the usual quality checks did not identify these issues before publication and have since put additional measures in place to safeguard research integrity.

We wish to credit our own Research Integrity and Research Publishing teams and anonymous and named external researchers and research integrity experts for contributing to this investigation.

The corresponding author, as the representative of all authors, has been given the opportunity to register their agreement or disagreement to this retraction. We have kept a record of any response received.

References

[1] W. Wang, "Random Forest and LightGBM-Based Human Health Check for Medical Device Fault Detection," *Journal of Healthcare Engineering*, vol. 2022, Article ID 2847112, 7 pages, 2022.

Retraction

Retracted: The Impact of a Knowledge Discovery-Based Psychoanalytic Intervention in the Treatment of Tuberculosis in University Students with Different Doses of Isoniazid

Journal of Healthcare Engineering

This article has been retracted by Hindawi following an investigation undertaken by the publisher [1]. This investigation has uncovered evidence of one or more of the following indicators of systematic manipulation of the publication process:

(1) Discrepancies in scope

(2) Discrepancies in the description of the research reported

(3) Discrepancies between the availability of data and the research described

(4) Inappropriate citations

(5) Incoherent, meaningless and/or irrelevant content included in the article

(6) Peer-review manipulation

The presence of these indicators undermines our confidence in the integrity of the article's content and we cannot, therefore, vouch for its reliability. Please note that this notice is intended solely to alert readers that the content of this article is unreliable. We have not investigated whether authors were aware of or involved in the systematic manipulation of the publication process.

In addition, our investigation has also shown that one or more of the following human-subject reporting requirements has not been met in this article: ethical approval by an Institutional Review Board (IRB) committee or equivalent, patient/participant consent to participate, and/or agreement to publish patient/participant details (where relevant).

Wiley and Hindawi regrets that the usual quality checks did not identify these issues before publication and have since put additional measures in place to safeguard research integrity.

We wish to credit our own Research Integrity and Research Publishing teams and anonymous and named external researchers and research integrity experts for contributing to this investigation.

The corresponding author, as the representative of all authors, has been given the opportunity to register their agreement or disagreement to this retraction. We have kept a record of any response received.

References

[1] Z. Xia, Y. Tan, and Y. Yang, "The Impact of a Knowledge Discovery-Based Psychoanalytic Intervention in the Treatment of Tuberculosis in University Students with Different Doses of Isoniazid," *Journal of Healthcare Engineering*, vol. 2022, Article ID 5610469, 8 pages, 2022.

Retraction

Retracted: An Association between EMX2 Variations and Mayer-Rokitansky-Küster-Hauser Syndrome: A Case-Control Study of Chinese Women

Journal of Healthcare Engineering

This article has been retracted by Hindawi following an investigation undertaken by the publisher [1]. This investigation has uncovered evidence of one or more of the following indicators of systematic manipulation of the publication process:

(1) Discrepancies in scope

(2) Discrepancies in the description of the research reported

(3) Discrepancies between the availability of data and the research described

(4) Inappropriate citations

(5) Incoherent, meaningless and/or irrelevant content included in the article

(6) Peer-review manipulation

The presence of these indicators undermines our confidence in the integrity of the article's content and we cannot, therefore, vouch for its reliability. Please note that this notice is intended solely to alert readers that the content of this article is unreliable. We have not investigated whether authors were aware of or involved in the systematic manipulation of the publication process.

Wiley and Hindawi regrets that the usual quality checks did not identify these issues before publication and have since put additional measures in place to safeguard research integrity.

We wish to credit our own Research Integrity and Research Publishing teams and anonymous and named external researchers and research integrity experts for contributing to this investigation.

The corresponding author, as the representative of all authors, has been given the opportunity to register their agreement or disagreement to this retraction. We have kept a record of any response received.

References

[1] H. Li, S. Liao, G. Luo et al., "An Association between EMX2 Variations and Mayer-Rokitansky-Küster-Hauser Syndrome: A Case-Control Study of Chinese Women," *Journal of Healthcare Engineering*, vol. 2022, Article ID 9975369, 6 pages, 2022.

Retraction

Retracted: Application of a Nursing Data-Driven Model for Continuous Improvement of PICC Care Quality

Journal of Healthcare Engineering

This article has been retracted by Hindawi following an investigation undertaken by the publisher [1]. This investigation has uncovered evidence of one or more of the following indicators of systematic manipulation of the publication process:

(1) Discrepancies in scope

(2) Discrepancies in the description of the research reported

(3) Discrepancies between the availability of data and the research described

(4) Inappropriate citations

(5) Incoherent, meaningless and/or irrelevant content included in the article

(6) Peer-review manipulation

The presence of these indicators undermines our confidence in the integrity of the article's content and we cannot, therefore, vouch for its reliability. Please note that this notice is intended solely to alert readers that the content of this article is unreliable. We have not investigated whether authors were aware of or involved in the systematic manipulation of the publication process.

In addition, our investigation has also shown that one or more of the following human-subject reporting requirements has not been met in this article: ethical approval by an Institutional Review Board (IRB) committee or equivalent, patient/participant consent to participate, and/or agreement to publish patient/participant details (where relevant).

Wiley and Hindawi regrets that the usual quality checks did not identify these issues before publication and have since put additional measures in place to safeguard research integrity.

We wish to credit our own Research Integrity and Research Publishing teams and anonymous and named external researchers and research integrity experts for contributing to this investigation.

The corresponding author, as the representative of all authors, has been given the opportunity to register their agreement or disagreement to this retraction. We have kept a record of any response received.

References

[1] J. Zhou and L. Wang, "Application of a Nursing Data-Driven Model for Continuous Improvement of PICC Care Quality," *Journal of Healthcare Engineering*, vol. 2022, Article ID 7982261, 8 pages, 2022.

Research Article

Segmentation of Brain Tissues from MRI Images Using Multitask Fuzzy Clustering Algorithm

Yunlan Zhao,[1] Zhiyong Huang [ID],[1] Hangjun Che [ID],[2] Fang Xie,[1] Man Liu,[1] Mengyao Wang,[1] and Daming Sun[3]

[1]*School of Microelectronics and Communication Engineering, Chongqing University, Chongqing 400044, China*
[2]*School of Electronics and Information Engineering, Southwest University, Chongqing 400715, China*
[3]*Chongqing Engineering Research Center of Medical Electronics and Information Technology,*
 Chongqing University of Posts and Telecommunications, Chongqing 400065, China

Correspondence should be addressed to Zhiyong Huang; zyhuang@cqu.edu.cn and Hangjun Che; hjche123@swu.edu.cn

In recent years, brain magnetic resonance imaging (MRI) image segmentation has drawn considerable attention. MRI image segmentation result provides a basis for medical diagnosis. The segmentation result influences the clinical treatment directly. Nevertheless, MRI images have shortcomings such as noise and the inhomogeneity of grayscale. The performance of traditional segmentation algorithms still needs further improvement. In this paper, we propose a novel brain MRI image segmentation algorithm based on fuzzy C-means (FCM) clustering algorithm to improve the segmentation accuracy. First, we introduce multitask learning strategy into FCM to extract public information among different segmentation tasks. It combines the advantages of the two algorithms. The algorithm enables to utilize both public information among different tasks and individual information within tasks. Then, we design an adaptive task weight learning mechanism, and a weighted multitask fuzzy C-means (WMT-FCM) clustering algorithm is proposed. Under the adaptive task weight learning mechanism, each task obtains the optimal weight and achieves better clustering performance. Simulated MRI images from McConnell BrainWeb have been used to evaluate the proposed algorithm. Experimental results demonstrate that the proposed method provides more accurate and stable segmentation results than its competitors on the MRI images with various noise and intensity inhomogeneity.

1. Introduction

With the increasing demand for medical services, medical imaging technology continues to be improved. Technology plays a major role in computer-assisted medicine. There are multimodal medical imaging technologies, such as magnetic resonance imaging (MRI), positron emission tomography (PET) scanning, and computed tomography (CT) scanning. MRI has the advantages of a high data rate, no radiation, and high soft-tissue contrast [1]. MRI is generally used to visualize the structure and tissue of a patient [2].

With the great number of medical images increasing in number, manual interpretation of image information becomes an impossible challenge. Experts have different experiences and knowledge. It is impossible to obtain uniform

and precise segmentation results [3]. Computer-assisted medical image processing plays a more and more important role. Image segmentation is an indispensable part of medical image processing [4]. The different tissues classification of the image provides a reference for doctors in disease diagnosis and intervention decisions. It helps improve diagnostic accuracy and efficiency. Hence, the research has great clinical significance in medical image segmentation.

Traditional image segmentation methods are divided into distinct categories according to their principles, such as threshold, clustering, region-based, and edge-based methods [5]. The fuzzy C-means (FCM) algorithm was first proposed by Bezdek et al. [6]. The FCM is widely used owing to its applicability and simplicity [7]. The FCM algorithm provides

the ability to describe the fuzziness of the images. Therefore, the fuzzy clustering algorithm is appropriate for MRI images. Nevertheless, the performance of traditional FCM still needs further improvement [8]. The core problem is sensitive to noise and the initialization of cluster centroids in brain MRI image segmentation. To solve the problem, many improved FCM algorithms have been proposed. Enhancements have been tried to improve algorithm performance by introducing local spatial information [7, 9], integrating bioinspired algorithms [10–12], and enhancing the image [13]. Ji et al. [9] introduced a method called RSCFCM for brain MRI image segmentation by introducing a factor for the spatial direction to deal with noise. The algorithm improved the segmentation accuracy. Meena Prakash et al. [14] employed a brain MRI segmentation algorithm integrated with spatial information and contrast enhancement based on FCM, but the clustering performance of the algorithm is not much improved compared with the original FCM algorithm. Pham et al. [7] integrated the PSO algorithm and kernelized fuzzy entropy clustering with spatial information and bias correction algorithm, called the PSO-KFECSB algorithm, which improved the robustness to noise and initializations, but the computational cost of the algorithm increased. Vinurajkumar and Anandhavelu [13] proposed an enhanced fuzzy segmentation framework for extracting white matter, which exhibited low values of computational time, but the segmentation results are sensitive to the initialization of the fuzzy partition matrix.

MRI images of different subjects have much common information. The related information could improve the segmentation performance. Classical FCM only deals with a single task. The algorithm pays no attention to the related tasks and only utilizes limited information [15]. To overcome the limitation, many multitask-related algorithms have been proposed, such as transfer-learning clustering algorithms [16], multitask clustering algorithms [15, 17, 18], multiview clustering algorithms [3, 19], collaborative clustering algorithms [20], and subspace clustering algorithms. Multitask learning learns related tasks simultaneously and shares useful information, such as representation and parameters among related tasks. Multitask learning strategy improves the clustering performance and obtains higher accuracy [21]. Hua et al. [3] designed a multiview fuzzy clustering algorithm to extract multiple feature data from the original image. Experimental results prove that the segmentation method optimizes the segmentation effect. Jiang et al. [18] proposed a distributed multitask fuzzy C-means (DMFCM) clustering algorithm for MRI image segmentation, which can extract common and individual information among different clustering tasks. The public cluster centroids represent the common information of different tasks. DMFCM significantly outperforms traditional FCM. However, because the common information is obtained directly from the original pixel data, the computational complexity greatly increases.

Generally, the current brain MRI image segmentation algorithms suffer from the shortcomings such as the sensitivity to the cluster initialization, lack of robustness to noise, and high computational complexity. In this study,

a new fuzzy clustering algorithm is to be explored for better improvement of the aforementioned problems. Based on the traditional FCM algorithm, we integrate multitask learning strategy and propose a weighted multitask fuzzy C-means clustering algorithm (WMT-FCM). WMT-FCM learns multiple different but related tasks simultaneously to extract public information. By introducing the adaptive weight learning mechanism, tasks are assigned optimal weights and can be adaptively learned to achieve a better clustering effect.

The summary of contributions in this research is as follows:

(1) We integrate the traditional FCM algorithm and multitask learning strategy with a new objective function and propose an improved fuzzy clustering method to enhance the accuracy of brain MRI image segmentation.

(2) We design an adaptive weight learning mechanism to obtain optimal weights for all tasks. Under the weight mechanism, the public information extracted from different tasks is more accurate, and each task can achieve better clustering effects.

(3) We regard the public cluster centroids as the public information of different tasks. Taking into account a large amount of pixel data in the images, we capture public information from cluster centroids instead of raw pixel data. It contributes to reducing computational complexity.

2. Related Work

2.1. Fuzzy C-Means Algorithm. In 1965, Zadeh published a paper on fuzzy sets. This paper used "Fuzzy" to describe the uncertainty of the classification. A membership function was proposed to indicate the fuzzy degree of elements [22]. Compared with classical set theory, elements in fuzzy sets have no strict boundaries. In fuzzy theory, elements are assigned membership values instead of clear categories.

Bezdek et al. introduced fuzzy theory the into hard C-means (HCM) algorithm and proposed FCM [6]. The FCM algorithm divides targets into numerous subcategories according to the uncertainty. The idea of FCM is to assign each data instance to all clusters with membership values [23, 24]. It is an unsupervised fuzzy clustering algorithm with no requirement for human intervention in the implementation of the algorithm [25]. In addition, there is no requirement for setting a threshold in advance. HCM is a hard partitioning method, and the result is either 1 or 0. Compared with HCM, FCM is more suitable for dealing with fuzzy and uncertain problems [26].

The fuzzy clustering algorithm is widely applied to medical image processing. Militello et al. [27] proposed a semiautomated and interactive approach based on the spatial fuzzy C-means algorithm to segment masses on dynamic contrast-enhanced breast MRI. Al-Saeed et al. [28] proposed a fast-generalized fuzzy C-means algorithm and used the unsupervised algorithm to segment the liver from the rest of the abdomen organs on CT scans. Zhao et al. [29] integrated a deep belief network and FCM unsupervised

deep clustering for lung cancer patient classification from lung CT images. Militello et al. [30] applied FCM to enhance automatic cell colony detection. Navaei Lavasani et al. [31] used the fuzzy C-means algorithm to segment prostate lesions on prostate dynamic contrast-enhanced MRI and obtained the diagnostic credibility increase. Rundo et al. [32] integrated T1w and T2w MRI image structural information based on the fuzzy C-means algorithm to enhance prostate gland segmentation.

Table 1 shows the symbols used in the FCM algorithm. Assume the input dataset with N data instances is $\mathbf{X} = \{x_1, x_2, \ldots \ldots x_N\}$, $\mathbf{V} = \{v_1, v_2, \ldots \ldots v_C\}$ is the cluster center vector, $\mathbf{U} = [u_{ij}]_{C \times N}$ is the membership matrix, u_{ij} is the membership value of the ith data sample to the jth cluster, and $C(1 < C < N)$ is the number of subcategories. The objective function of the FCM algorithm [6] is as follows:

$$J_{\text{FCM}} = \sum_{i=1}^{N} \sum_{j=1}^{C} u_{ij}^m \left\| x_i - v_j \right\|^2. \tag{1}$$

Regarding the objective function J_{FCM}, the constant m ($m > 1$) indicates the degree of ambiguity. When the value of m is larger, the fuzziness of clustering is higher. Therefore, a large value is not conducive to reduce the fuzziness. When the value of m equals 1, it is equivalent to the clustering result of the HCM algorithm. Usually, the value of m is assigned to 2 [2, 3, 24]. $\left\| x_i - v_i \right\|^2$ is the Euclidean distance between data sample x_i and cluster v_j. The constraints of the membership value are as follows:

$$\sum_{j=1}^{C} u_{ij} = 1, 0 \leq \sum_{i=1}^{N} u_{ij} \leq N, u_{ij} \in [0, 1]. \tag{2}$$

The FCM algorithm minimizes the objective function by iteratively calculating the membership degree and cluster centers. The Lagrange multiplier method is used to solve the objective function. The cluster centers and membership values can be iteratively updated by the following equations:

$$u_{ij} = \frac{\left(\left\| x_i - v_j \right\|^2 \right)^{-1/m-1}}{\sum_{l=1}^{C} \left(\left\| x_i - v_j \right\|^2 \right)^{-1/m-1}}, \tag{3}$$

$$v_j = \frac{\sum_{i=1}^{N} u_{ij}^m x_i}{\sum_{i=1}^{N} u_{ij}^m}. \tag{4}$$

Considering the uncertainty and unclearness of brain tissue boundaries, the fuzzy clustering algorithm can be employed in image segmentation. The input dataset $\mathbf{X} = \{x_1, x_2, \ldots \ldots x_N\}$ is the image pixel dataset, where x_i represents the grayscale of the ith pixel of the image. The segmentation of images is transformed into a clustering problem. That is, dividing N pixels into C cluster centers according to the final membership matrix.

The steps of segmentation images using the FCM algorithm are summarized as follows: (1) set the iteration stop threshold ε, the number of clusters C, fuzzy index m; (2) initialize the cluster centers randomly; (3) update the

TABLE 1: Description of symbols in FCM.

Symbol	Description
$\mathbf{X}$	Input dataset
$\mathbf{V}$	Cluster centers vector
$\mathbf{U}$	Membership matrix
C	Number of the clusters
N	Total number of samples
x_i	The ith sample
v_j	The jth cluster center
u_{ij}	The membership degree of x_i to v_j
M	Fuzzy factor

membership matrix and cluster centers according to equations (3) and (4); (4). Calculate the objective function; (5) If the objective function value converges, the algorithm stops, otherwise, it goes to step 3).

2.2. Multitask Learning Strategy. Multitask learning refers to performing multiple related tasks at the same time. Multitask learning uses the relationship between these tasks to enhance the clustering performance of a single task [33]. The definition of multitask learning is as follows: Assume learning tasks is $\mathbf{T} = \{t_1, t_2, \ldots t_T, \}$, all tasks are related but different. Multitask learning is aimed at improving the learning performance of each task by using public knowledge [34]. Multitask learning is applied to natural language processing, disease prediction, computer vision, etc. [35]. The information contained in each task helps other tasks learn better. Because different tasks usually have different noises, learning together will offset some noises to some extent. Multitask learning strategy has better generalization performance than single-task learning. In addition, it has better performance and robustness.

3. Brain MRI Images Segmentation Based on Multitask Fuzzy *C*-Means Algorithm

3.1. WMT-FCM. FCM is a fuzzy clustering method based on the objective function. Essentially, solving the objective function is an iterative optimization process. Therefore, the algorithm is easily affected by noise and random initialization of cluster centers and falls into a local optimum. In the clustering process, different MRI images have very similar cluster centers. The cluster centroids represent related information of different tasks. This related information helps to converge the objective function and avoids the negative effect of noise in MRI images [18]. It benefits the improvement of cluster analysis. However, the traditional single-task FCM is only suitable for a single-task scenario and exploits limited information. It cannot mine public information between different tasks.

Multitask technology has the advantage of mining public information contained in multiple tasks. To utilize the public information and improve the segmentation performance, we introduce multitask technology into the traditional FCM algorithm. Multitask clustering algorithm enables the collaborative learning of different tasks in the clustering process. It makes maximum use of the data information of each

task. Because different segmentation tasks usually have different noises, we cannot directly assign the same weight to each task. The task with a better clustering effect should give a higher contribution to the public information. Therefore, a weighted multitask fuzzy C-means (WMT-FCM)

algorithm with adaptive adjustment capability is proposed in this paper. Figure 1 is the schematic diagram of the WMT-FCM algorithm.

Assuming a dataset contains T tasks, and each task has N_t pixels. The objective function is proposed as follows:

$$J_{\text{WMT-FCM}} = \sum_{t=1}^{T} \sum_{i=1}^{N_t} \sum_{j=1}^{C_t} u_{ij,t}^m \left\| x_{i,t} - v_{j,t} \right\|^2 + \lambda \sum_{t=1}^{T} \sum_{d=1}^{D} \sum_{j=1}^{C_t} w_{d,t} p_{jd,t}^m \left\| v_{j,t} - z_d \right\|^2 + \gamma \sum_{t=1}^{T} \sum_{d=1}^{D} w_{d,t} \log(w_{d,t}). \quad (5)$$

The objective function constraints are as follows:

$$\begin{cases} \displaystyle\sum_{j=1}^{C_t} u_{ij,t} = 1, & 1 \le i \le N, u_{ij,t} \in [0,1], \\[3mm] \displaystyle\sum_{d=1}^{D} p_{jd,t} = 1, & 1 \le j \le C_t, 1 \le t \le T, \\[3mm] \displaystyle\sum_{t=1}^{T} w_{d,t} = 1, & 1 \le d \le D. \end{cases} \quad (6)$$

Where $x_{i,t}$ is the ith data sample of the tth task, $v_{j,t}$ is the jth private cluster center of the tth task, and $\mathbf{Z} = \{z_1, z_2, \ldots, z_D\}$ is the public cluster center vector of all tasks. $\mathbf{U}^{(t)} = [u_{ij,t}]_{C_t \times N_t}$ is the private membership matrix of the tth task. $p_{jd,t}$ represents the membership value of private cluster center $v_{j,t}$ to the dth public cluster center z_d. D is the number of public cluster centers. λ is a balance parameter to control the influence of the public clustering term. γ is used to adjust the penalty corresponding to the weights of each task. $\mathbf{W}^{(t)} = \{w_{1,t}, w_{2,t}, \ldots, w_{D,t}\}$ is the weight vector of the tth task. $w_{d,t}$ represents the importance of the tth task to the dth public cluster.

The first part of the objective function contains T-independent FCM clustering tasks. The first part aims to learn the within-task partition matrix and cluster centers. The second part aims to learn public information about all tasks. It uses the FCM objective function to learn the public partition matrix and public cluster centers. The third part is the regularization term. We introduce the Shannon entropy as the regularizer. The third part aims to identify the optimal weights of each task.

Although there is public information about different tasks, the difference also exists between all tasks. For

example, each task is affected by varying levels of noise and has different clustering effectiveness. Therefore, the influence of different tasks should be adjusted according to the actual situation instead of keeping it consistent. Considering the difference between separate tasks, we introduce the adaptive weight $w_{d,t}$. $w_{d,t}$ controls the impact of the tth task on the dth public cluster centers. If the relationship is clearer between the private cluster centers and the public clustering centers, a higher weight value is given. That means the task has a greater contribution to the public cluster centers. Conversely, if the relationship is fuzzier with public cluster centers, a lower weight parameter is given. The algorithm can utilize the effective public information of different tasks to the greatest extent and improve the clustering performance through adaptive weight adjustment.

3.2. Optimization. The Lagrange multiplier method is used to obtain the minimization of equation (5). According to the corresponding constraints, the objective Lagrangian function is defined as follows:

$$J_{\text{WMT-FCM}} = \sum_{t=1}^{T} \sum_{i=1}^{N_t} \sum_{j=1}^{C_t} u_{ij,t}^m \left\| x_{i,t} - v_{j,t} \right\|^2 + \lambda \sum_{t=1}^{T} \sum_{d=1}^{D} \sum_{j=1}^{C_t} w_{d,t} p_{jd,t}^m \left\| v_{j,t} - z_d \right\|^2 + \gamma \sum_{t=1}^{T} \sum_{d=1}^{D} w_{d,t} \log(w_{d,t}) + \sum_{t=1}^{T} \sum_{i=1}^{N_t} a_{i,t} \left(1 - \sum_{j=1}^{C_t} u_{ij,t} \right)$$

$$+ \sum_{t=1}^{T} \sum_{j=1}^{C_t} b_{j,t} \left(1 - \sum_{d=1}^{D} p_{jd,t} \right) + \sum_{d=1}^{D} c_d \left(1 - \sum_{t=1}^{T} w_{d,t} \right), \quad (7)$$
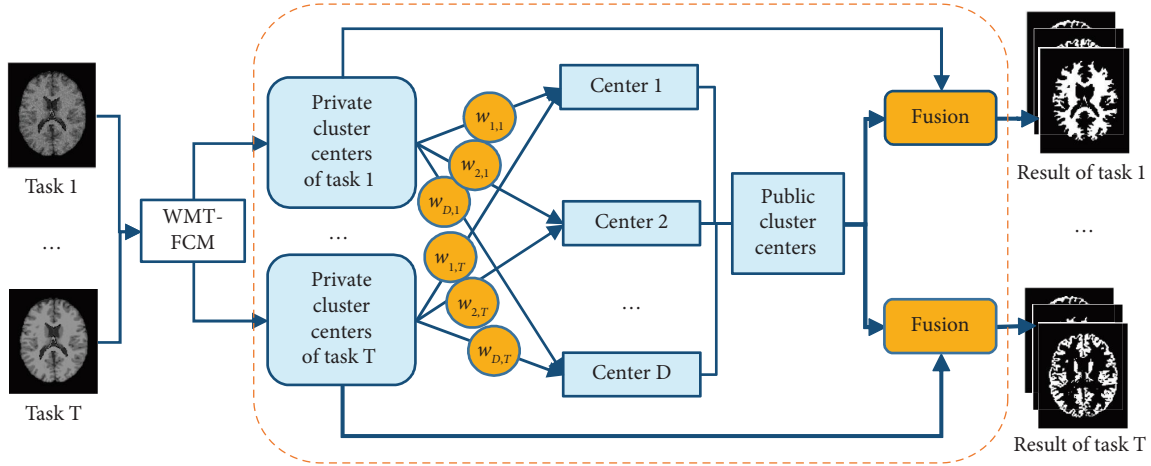
FIGURE 1: The schematic diagram of the WMT-FCM algorithm.

where $a_{i,t}$, $b_{j,t}$, and c_d are the Lagrange multipliers corresponding to the constraints ($\forall i \in \{1, 2, \ldots, N_t\}$, $\forall j \in \{1, 2, \ldots, C_t\}$, $\forall d \in \{1, 2, \ldots, D\}$, $\forall t \in \{1, 2, \ldots, T\}$).

3.2.1. Optimizing Membership Matrix. Taking the derivative of $J_{\text{WMT-FCM}}$ with respect to $u_{ij,t}$ and setting it to zero, we obtain

$$\frac{\partial J_{\text{WMT-FCM}}}{\partial u_{ij,t}} = u_{ij,t}^{m-1} \left\| x_{i,t} - v_{j,t} \right\|^2 - a_{i,t}.$$
$$= 0. \tag{8}$$

From equation (8), $u_{ij,t}$ is calculated as follows:

$$u_{ij,t} = \frac{a_{i,t}^{1/m-1}}{\left(\left\| x_{i,t} - v_{j,t} \right\|^2 \right)^{1/m-1}}. \tag{9}$$

According to $\sum_{l=1}^{C_t} u_{il,t} = 1$ and equation (9), $a_{i,t}$ can be obtained as follows after the necessary calculations:

$$a_{i,t} = \frac{1}{\left[\sum_{l=1}^{C_t} \left(\left\| x_{i,t} - v_{l,t} \right\|^2 \right)^{-1/m-1} \right]^{1/m-1}}. \tag{10}$$

By substituting equation (10) into equation (9), the iterative formulate of private membership value $u_{ij,t}$ for tth task is as follows:

$$u_{ij,t} = \frac{\left(\left\| x_{i,t} - v_{j,t} \right\|^2 \right)^{-(1/m-1)}}{\sum_{l=1}^{C_t} \left(\left\| x_{i,t} - v_{j,t} \right\|^2 \right)^{-(1/m-1)}}. \tag{11}$$

Similarly, the updating equation of the membership value $p_{jd,t}$ is as follows:

$$p_{jd,t} = \frac{\left(w_{d,t} \left\| v_{j,t} - z_d \right\|^2 \right)^{-(1/m-1)}}{\sum_{l=1}^{D} \left(w_{l,t} \left\| v_{j,t} - z_l \right\|^2 \right)^{-(1/m-1)}}. \tag{12}$$

3.2.2. Optimizing Cluster Centroid. Taking the derivative of $J_{\text{WMT-FCM}}$ with respect to $v_{j,t}$ and setting it to zero, we obtain

$$\frac{\partial J_{\text{WMT-FCM}}}{\partial v_{j,t}} = -\sum_{i=1}^{N_t} u_{ij,t}^m \left(x_{i,t} - v_{j,t} \right) + \lambda \sum_{d=1}^{D} w_{d,t} p_{jd,t}^m \left(v_{j,t} - z_d \right)$$
$$= 0. \tag{13}$$

According to equation (13), private clustering centroid $v_{j,t}$ is obtained as following after necessary calculations:

$$v_{j,t} = \frac{\sum_{i=1}^{N_t} u_{ij,t}^m x_{i,t} + \lambda \sum_{d=1}^{D} w_{d,t} p_{jd,t}^m z_d}{\sum_{i=1}^{N_t} u_{ij,t}^m + \lambda \sum_{d=1}^{D} w_{d,t} p_{jd,t}^m}. \tag{14}$$

Similarly, the updating equation of the public clustering centroid z_d is as follows:

$$z_d = \frac{\sum_{t=1}^{T} \sum_{j=1}^{C_t} w_{d,t} p_{jd,t}^m v_{j,t}}{\sum_{t=1}^{T} \sum_{j=1}^{C_t} w_{d,t} p_{jd,t}^m}. \tag{15}$$

3.2.3. Optimizing Weight. To derive the optimal weights, taking the derivative of the Lagrangian function with respect to $w_{d,t}$ and setting it to zero as follows:

$$\frac{\partial J_{\text{WMT-FCM}}}{\partial w_{d,t}} = \lambda \sum_{j=1}^{C_t} p_{jd,t}^m \left\| v_{j,t} - z_d \right\|^2 + \gamma \left(1 + \ln w_{d,t} \right) - c_d$$

$$= 0. \tag{16}$$

According to $\sum_{t=1}^{T} w_{d,t} = 1$ and equation (16), we can obtain the optimal weight $w_{d,t}$ using steps similar to optimize the membership matrix as follows:

$$w_{d,t} = \frac{\exp\left(-\lambda \sum_{j=1}^{C_t} p_{jd,t}^m \left\| v_{j,t} - z_d \right\|^2 / \gamma\right)}{\sum_{h=1}^{T} \exp\left(-\lambda \sum_{j=1}^{C_t} p_{jd,t}^m \left\| v_{j,t} - z_d \right\|^2 / \gamma\right)}. \quad (17)$$

The specific steps of WMT-FCM are summarized in Algorithm 1.

4. Experimental Results

4.1. The Experimental Dataset. To demonstrate the improvement of the proposed algorithm, the traditional FCM and DMFCM [18] are selected as comparison algorithms. The dataset of this study is downloaded from BrainWeb. The BrainWeb is acquired from the McConnell Brain Imaging Center of the Montreal Neurological Institute, McGill University [36]. This database contains a set of realistic MRI data produced by an MRI simulator. The BrainWeb simulates 3-dimensional data volumes using three sequences ($T1$, $T2$, and PD weighted). The simulated volumes contain a variety of slice thicknesses, noise levels, and intensity nonuniformity (INU) levels. The ground truth of the cerebral spinal fluid (CSF), the gray matter (GM), the white matter (WM), and the background are available.

The BrainWeb dataset in our work consists of 9 $T1$-weighted MRI images (slice 90) with 181217 pixels. The MRI images are corrupted with different levels of noise and INU. Details are shown in Table 2. These images are randomly combined as task groups. The ground truth images of the brain MRI images are shown in Figure 2.

4.2. Parameters Setting. λ and γ of the objective function influence the cluster centers and weight vectors according to equations (8) and (11). In this study, the optimal parameters of the proposed algorithm are obtained by the grid search strategy. λ and γ are set from two grids {20, 40, 60, 80,100, 120} and {0.2, 0.4, 0.6, 0.8, 1, 1.2}, respectively. In addition, all experiments are conducted with the maximum number of iterations $K = 100$, termination parameter $\varepsilon = 0.0001$, cluster index $m = 2$.

4.3. Evaluation Index. The quantitative performance comparison is performed using the Dice similarity coefficient (DSC) [37] and segmentation accuracy (SA) [38].

(1) Dice Similarity Coefficient. DSC measures the similarity between the ground truth and segmentation results. According to equation (12), S_1 represents the segmentation results. S_2 represents the ground truth for a single class. Here

the DSC measures the similarity of CSF, GM, WM, and background. The larger value of DSC indicates the better performance of the algorithm.

$$\text{DSC} = \frac{2|S_1 \cap S_2|}{|S_1| + |S_2|}. \quad (18)$$

(2) Average Dice Similarity Coefficient. The average Dice similarity coefficient [39] of WM, GM, and CSF is described as equation (13). Considering the nonbrain tissue background, we exclude it during the average DSC (DSC_{av}) calculating.

$$\text{DSC}_{av} = \frac{2\left(\left|S_1^{CSF} \cap S_2^{CSF}\right| + \left|S_1^{GM} \cap S_2^{GM}\right| + \left|S_1^{WM} \cap S_2^{WM}\right|\right)}{\left|S_1^{CSF}\right| + \left|S_2^{CSF}\right| + \left|S_1^{GM}\right| + \left|S_2^{GM}\right| + \left|S_1^{WM}\right| + \left|S_2^{WM}\right|}. \quad (19)$$

(3) Segmentation Accuracy. SA index measures the accuracy of the algorithm. Given in equation (14), where A_i is the pixel set of the ith cluster belonging to segmented results, B_i is the pixel set belongs to ground truth, and K is the number of clusters. The closer SA to 1 indicates better segmentation performance. The evaluation metric is defined as follows:

$$\text{SA} = \frac{\sum_{i=1}^{C} A_i \cap B_i}{\sum_{l=1}^{C} B_l}. \quad (20)$$

The metrics are an average of ten repeated experiments since the performance of FCM depends on the random initialization of the cluster centroids. Select 3 images with different levels of noise and intensity nonuniformity as a task group randomly. The inputs are segmented into the following four clusters: background, CSF, GM, and WM. All experiments are conducted on MATLAB 2019a and executed with a PC configured with a 1.50 GHz CPU and 16G memory Intel Core i7 processor, Windows 10.

5. Results and Discussion

To verify the stability and the antinoise ability improvement of the WMT-FCM algorithm, this section gives a comparison with classical FCM and DMFCM. There are nine MRI images from BrainWeb, as shown in Table 2.

Figure 3 shows the original images of 9 simulated MRI brain images (slice 90) as well as the corresponding segmentation results of the WMT-FCM algorithm. Segmented images include the entire image and individual tissues. Figure 2 displays the ground truth images of simulated MRI images (slice 90). Figure 3 qualitatively reveals that the WMT-FCM algorithm could partition different tissues. The segmented images overlap well with the ground truth on all tested images.

Initialization: set the number of tasks T, the number C_t of private centers, the number D of public centers, the termination threshold ε, fuzzy index m, the maximum number K of iterations, and the parameters λ and γ.
 Results: the final partition matrix and cluster centers for each task.
for $t = 1, \ldots, T$ **do**
       Randomly initialize cluster centroids and weights for the tth task;
end
Randomly initialize public clustering centroids;
for $k = 1, \ldots, K$ **do**
       Update $u_{ij,t}$ for each task using equation (11)
       Update $v_{j,t}$ for each task using equation (14)
       Update $p_{jd,t}$ using equation (12)
       Update z_d using equation (15)
       Update $w_{d,t}$ using equation (17)
       Calculate the fitness $J_{\mathrm{WMT-FCM}}{}^{(k)}$ using equation (5)
       if $|J_{\mathrm{WMT-FCM}}{}^{(k)} - J_{\mathrm{WMT-FCM}}{}^{(k-1)}| < \varepsilon$ **then**
              break
       end if
end

ALGORITHM 1: WMT-FCM.

TABLE 2: Information about the simulated MRI images.

	Image 1 (%)	Image 2 (%)	Image 3 (%)	Image 4 (%)	Image 5 (%)	Image 6 (%)	Image 7 (%)	Image 8 (%)	Image 9 (%)
Noise	1	5	7	1	7	9	3	3	5
INU	20	20	0	0	20	20	20	0	0

Table 3 shows the experimental results of the following three different algorithms: FCM, DMFCM, and the proposed WMT-FCM. The results include the mean values of the SA, $\mathrm{DSC_{av}}$ of all tissues. The WMT-FCM segmentation performance is significantly better than FCM. This shows It confirms that the introduction of multitask learning mechanism mines public information from multiple tasks. Compared with DMFCM, the segmentation effect of the WMT-FCM algorithm in this study is better. This demonstrates the effectiveness of the task weight learning mechanism. To archive the results, the single task execution time of FCM, WMT-FCM, and DMFCM is about 1 second, 6 seconds, and 600 seconds. The execution time of multitask algorithms is higher than classical FCM since the public partition matrix and the public cluster center learning require more time. However, even if the execution time is increased, the execution time of the WMT-FCM algorithm is still much shorter than DMFCM.

To further compare segmentation performance, the Dice similarity coefficient of each tissue is calculated. The result is presented in Table 4. WMT-FCM provides better results than FCM and DMFCM in WM, GM, and CSF generally. Among the three tissues, the performance of WMT-FCM is the best in WM and relatively poor in GM. However, even though the WMT-FCM segmentation performance is slightly inferior in GM. It is still significantly superior to FCM and DMFCM. FCM and DMFCM always fail to distinguish CSF accurately.

5.1. Robustness to Noise. Figure 4 shows SA and $\mathrm{DSC_{av}}$ of the algorithms on the images with 20% INU and different noise levels. As the images with a higher noise level, the clustering performance of both clustering algorithms is lower. The WMT-FCM clustering performance is better than the comparison algorithms, even if each algorithm's performance is declining with the noise level increasing. In addition, with the noise increasing, the WMT-FCM clustering performance decreases less than FCM and DMFCM, which indicates that WMT-FCM is more robust to noise.

5.2. Sensitivity to Initialization. Figure 5 displays the SA variations in repeated trials on image 3. The SA of FCM changed dramatically in different trials. Since the initialization of the clustering centroids is random, the FCM clustering performance depends on the initial values of cluster centers. Therefore, the results of the fuzzy clustering-based algorithm are usually inconsistent in repeated trials. However, the segmentation results of WMT-FCM are almost unchanged. In addition, SA values of WMT-FCM are higher than FCM and DMFCM in almost all trials. Repeated trials indicate that WMT-FCM is more robust to the initialization compared with FCM and DMFCM and generates consistent excellent segmentation performance.

To compare the algorithms' performance more visually, the visual results are shown in Figures 6 and 7. Figure 6 displays the segmented images of the first to fourth trials on

(a)

(b)

(c)

(d)
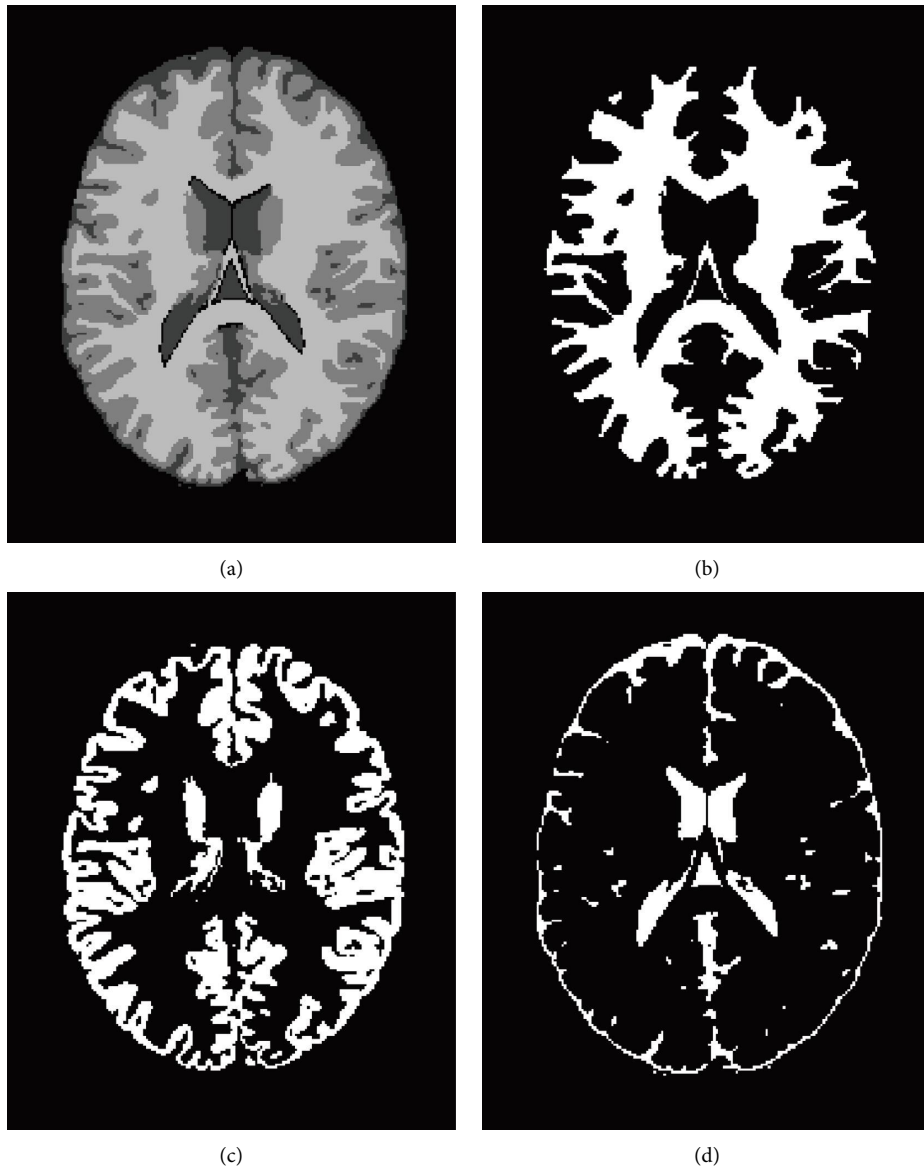
FIGURE 2: Ground truth images of the simulated brain MRI images: (a) total; (b) WM; (c) GM; (d) CSF.
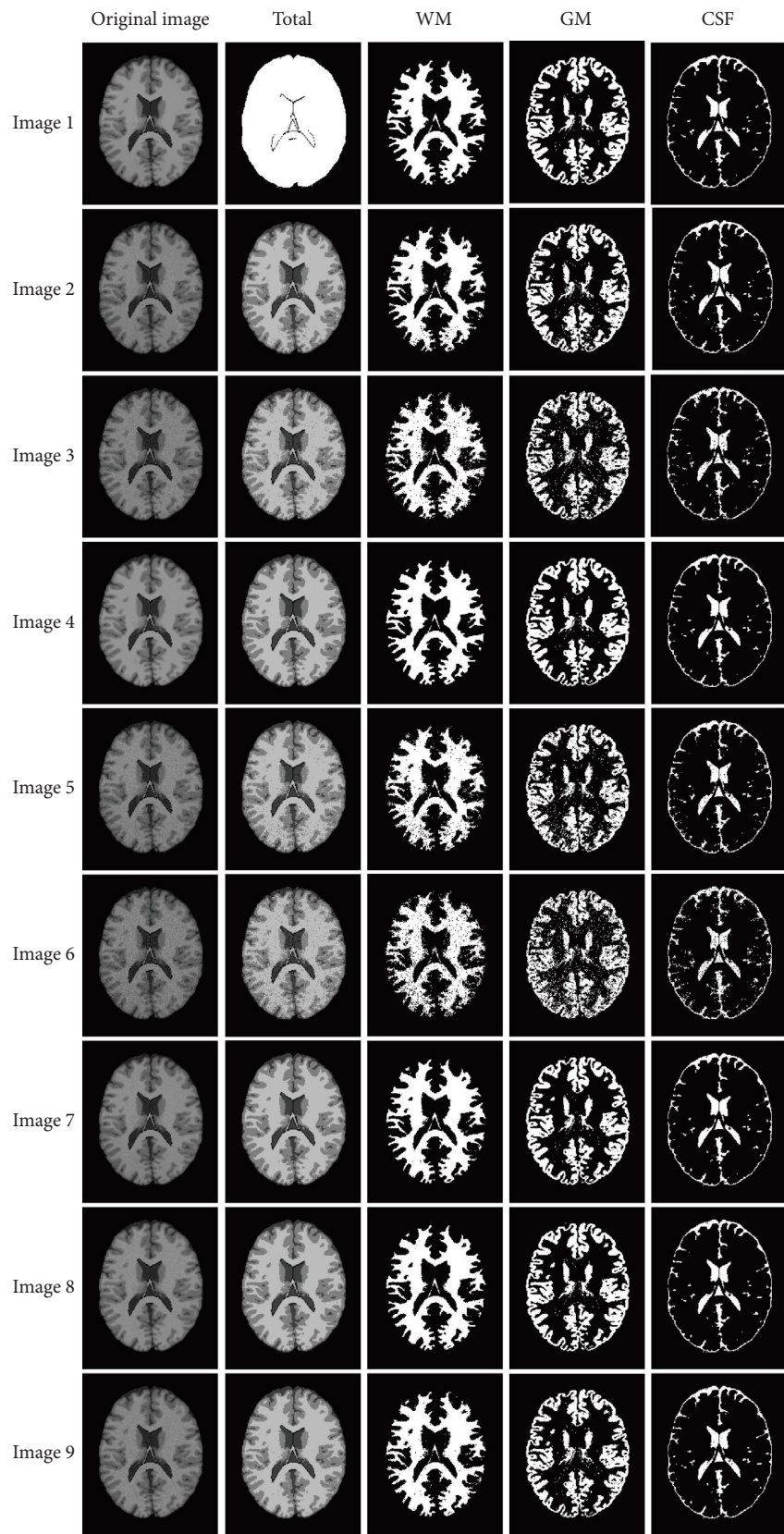
FIGURE 3: Segmentation results of simulated MRI brain images (slice 90) with different noises and INU in the WMT-FCM algorithm.

TABLE 3: The average values in terms of segmentation accuracy and average Dice similarity coefficient on simulated MRI brain images.

Image	SA			DSC$_{av}$		
	FCM	DMFCM	WMT-FCM	FCM	DMFCM	WMT-FCM
Image 1	0.8943	0.9531	0.9870	0.8059	0.9230	0.9737
Image 2	0.8668	0.9131	0.9705	0.7425	0.8366	0.9408
Image 3	0.8289	0.8765	0.9537	0.6705	0.7716	0.9081
Image 4	0.9142	0.9630	0.9914	0.8469	0.9390	0.9826
Image 5	0.8268	0.8686	0.9543	0.6752	0.7541	0.9090
Image 6	0.7979	0.8618	0.9237	0.6107	0.7415	0.8495
Image 7	0.8781	0.9164	0.9818	0.7789	0.8521	0.9632
Image 8	0.8905	0.8865	0.9845	0.8089	0.7932	0.9688
Image 9	0.8712	0.8778	0.9737	0.7572	0.7677	0.9472

TABLE 4: The average values in terms of the Dice similarity coefficient for a single tissue, including WM, GM, and CSF.

Image	WM			GM			CSF		
	FCM	DMFCM	WMT-FCM	FCM	DMFCM	WMT-FCM	FCM	DMFCM	WMT-FCM
Image 1	0.8989	0.9791	0.9801	0.6555	0.9317	0.9649	0.3901	0.4876	0.9750
Image 2	0.7425	0.9064	0.9550	0.6327	0.7248	0.9219	0.4716	0.5657	0.9424
Image 3	0.7708	0.8851	0.9309	0.5067	0.6615	0.8793	0.2717	0.1815	0.9060
Image 4	0.9303	0.9852	0.9887	0.7525	0.9454	0.9769	0.3915	0.5872	0.9772
Image 5	0.8207	0.8649	0.9306	0.4161	0.5926	0.8818	0.0910	0.2729	0.9090
Image 6	0.7317	0.8583	0.8885	0.3946	0.6271	0.8089	0.1662	0.1662	0.8316
Image 7	0.8933	0.9414	0.9729	0.6328	0.8051	0.9508	0.1927	0.2891	0.9628
Image 8	0.9232	0.8967	0.9773	0.7225	0.6457	0.9583	0.0968	0.2903	0.9672
Image 9	0.8367	0.8375	0.9616	0.7061	0.7137	0.9297	0.2838	0.3784	0.9440
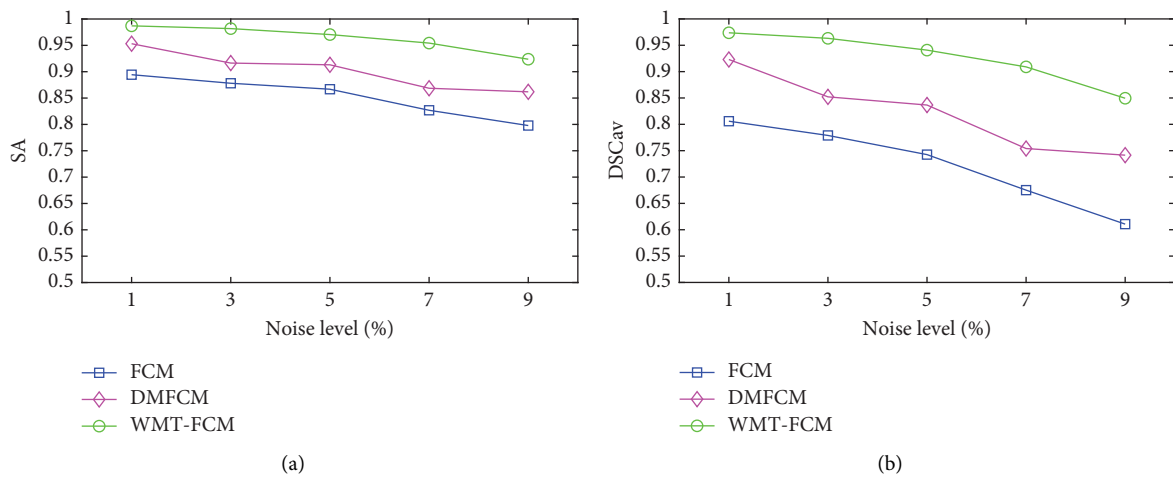
FIGURE 4: The variations of SA and average DSC on images with 20% INU and increasing noise level by FCM, DMFCM, and WMT-FCM: (a) SA and (b) DSC$_{av}$.
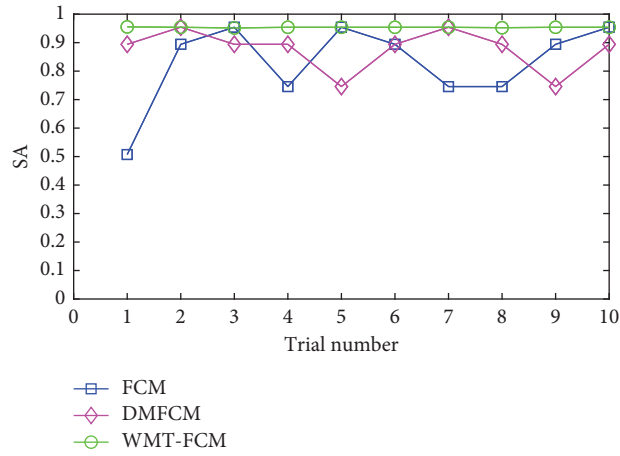
Figure 5: SAvariations of FCM, DMFCM, and WMT-FCM on image 3 in repeated trials.
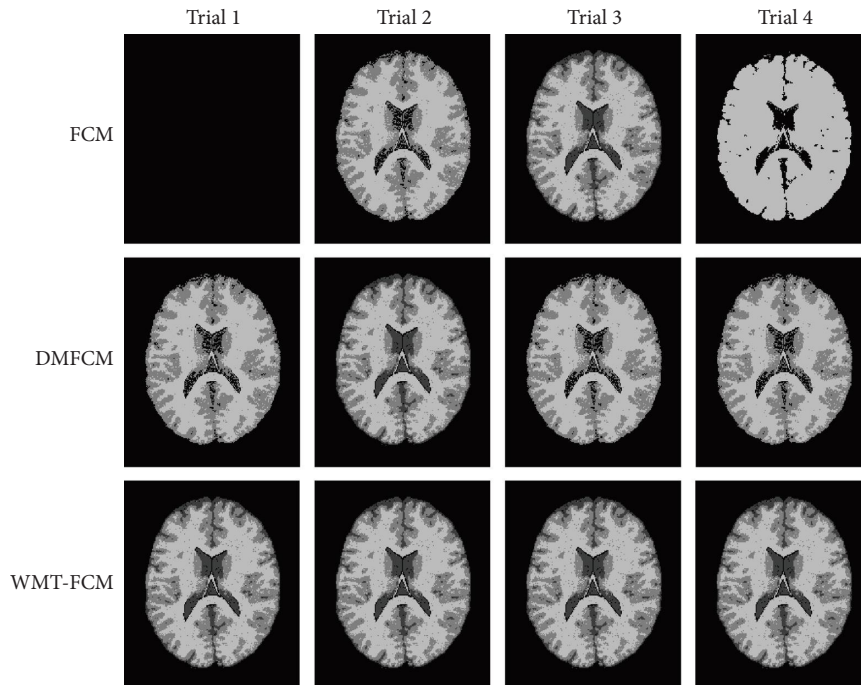
Figure 6: Segmentation results on image 3 in repeated trials (trials 1, 2, 3, and 4). The black image indicates all tissues are segmented as one cluster (background).
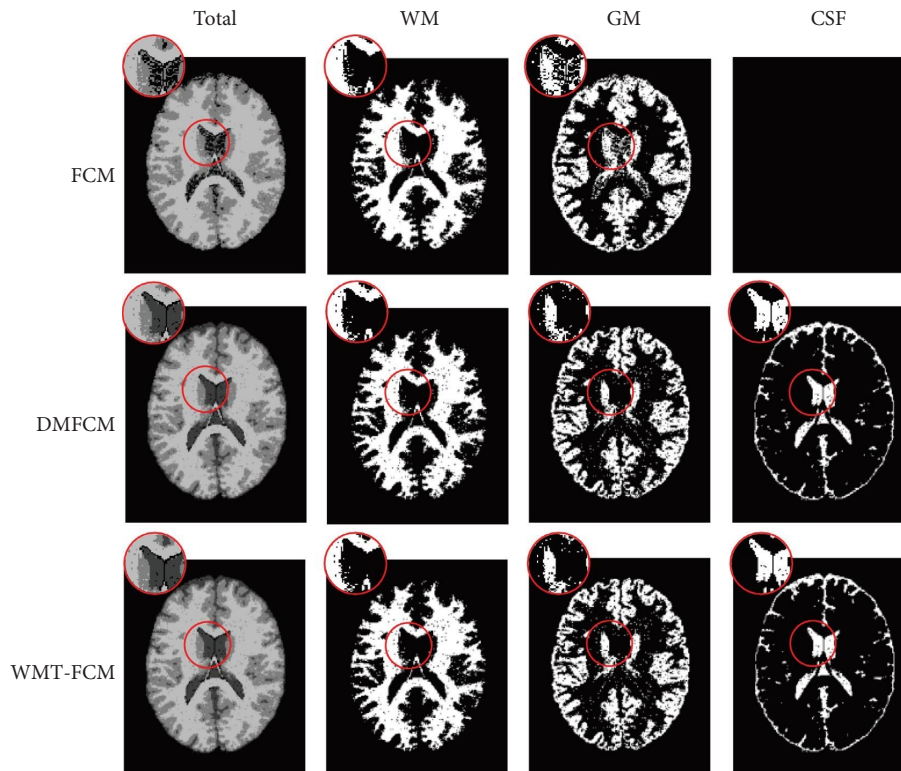
FIGURE 7: Comparison of segmentation results on image 3 in trial 2 between FCM, DMFCM, and WMT-FCM. The black image indicates FCM fails to detect the CSF.

(a)

(b)
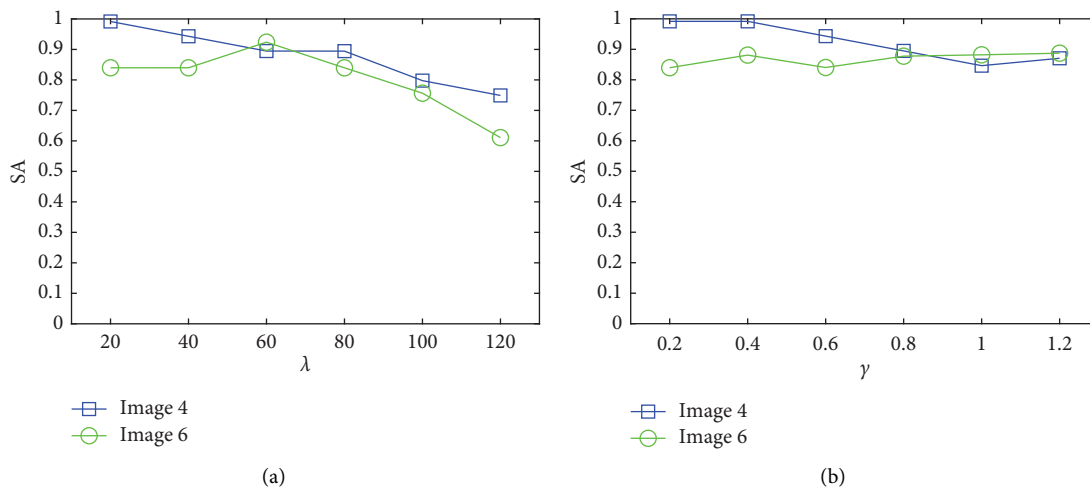
FIGURE 8: Continued.
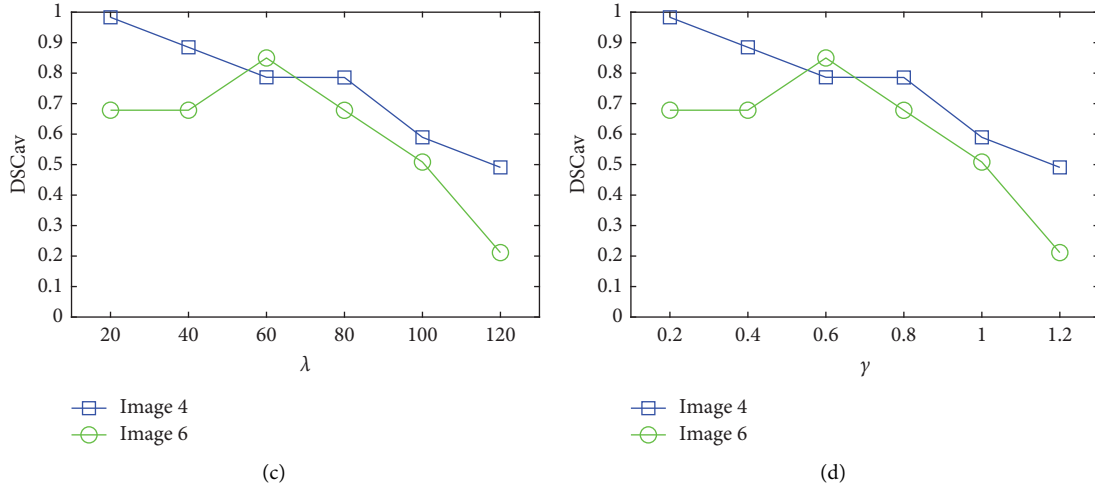
FIGURE 8: Average SA and DSC$_{av}$ of WMT-FCM on image 4 and image 6 with trade-off parameter λ and corresponding regularization parameter γ: (a) SA vs. λ; (b) SA vs. γ; (c) DSC$_{av}$ vs. λ; (d) DSC$_{av}$ vs. γ.

image 3 by FCM, DMFCM, and WMT-FCM. FCM fails to partition the brain tissues in almost all trials, especially CSF, except the third trial. In the first trial, all tissues are segmented as an individual cluster, background. In the second trial, FCM drops the CSF region and oversegmented GM. FCM shows a relatively good result in the third trial. In the fourth trial, FCM fails to detect CSF as well as GM and oversegmented the WM. DMFCM always tends to lose CSF. However, in the four trials, WMT-FCM offers an excellent overlap with ground truth consistently. A detailed comparison is shown in Figure 7, which indicates the proposed algorithm has superior segmentation performance than FCM, especially on GM and CSF. It can be concluded that the WMT-FCM algorithm provides better performance consistently and is less sensitive to the random initialization.

5.3. Sensitivity to Parameters. The experiments explore the sensitivity of the WMT-FCM parameters are conducted. The crucial parameters, i.e., the balance parameter λ and regularization coefficients γ are involved. Figure 8 shows the sensitivity of parameters with respect to the two different MRI images (image 4 and image 6). WMT-FCM provides relatively excellent segmentation results when the core parameters are located within the proper interval. Overall, the algorithm performance is slightly sensitive to the parameters, especially on DSC$_{av}$. The algorithm is more sensitive to trade-off parameter λ than the corresponding regularization parameter γ. Therefore, λ plays a major role in obtaining optimal clustering results. With the λ increasing, the segmentation performance of image 4 (with 1% noise and no INU) shows a decreasing trend. Image 6 (with 9% noise and 20% INU) shows a tendency to rise first and fall after. Excessive trade-off parameter enhances the influence of public information on clustering results and leads to undesirable effects. The performance may decrease, especially on images with a low level of noise and INU. In summary, although the proposed algorithm is slightly sensitive to

trade-off parameter λ, it obtains relatively good performance within an appropriate range.

6. Conclusions

In this paper, we propose a new fuzzy clustering algorithm called WMT-FCM. Multitask learning mechanism is introduced into the FCM algorithm for brain MRI image segmentation. WMT-FCM makes use of both private information in a single task and public information among related tasks. To draw more effective public information from different tasks, we design an adaptive task weighting mechanism. We take experiments to validate the proposed algorithm on synthetic MRI images. The results demonstrate that the proposed algorithm provides more accurate segmentation results than the FCM and DMFCM algorithms. WMT-FCM has the following advantages: (1) WMT-FCM is less sensitive to the initialization of cluster centers; (2) the robustness to noise is improved; (3) WMT-FCM is adaptive to the private clustering effect. There are two main limitations in the WMT-FCM. The algorithm requires more computational time for public information learning and adaptive weights updating. Although the proposed algorithm obtains a relatively good effect when the trade-off parameter λ is in the appropriate range, the performance is slightly sensitive to λ. In later research, we will focus on how to tackle these problems. In conclusion, the algorithm based on FCM and multitask learning significantly improves the segmentation performance of brain MRI images. The main limitations of the FCM algorithm, that is, the sensitivity to initialization and noise have been partially improved.

Data Availability

The public datasets used to validate the study can be obtained from BrainWeb (https://brainweb.bic.mni.mcgill.ca/brainweb/).

Conflicts of Interest

The authors declare that they have no conflicts of interest.

Acknowledgments

References

[1] T. M. Nguyen and Q. M. J. Wu, "A fuzzy logic model based Markov random field for medical image segmentationfield for medical image segmentation," *Evolving Systems*, vol. 4, no. 3, pp. 171–181, 2013.

[2] T. Ren, H. Wang, H. Feng, C. Xu, G. Liu, and P. Ding, "Study on the improved fuzzy clustering algorithm and its application in brain image segmentation," *Applied Soft Computing*, vol. 81, Article ID 105503, 2019.

[3] L. Hua, Y. Gu, X. Q. Gu, J. Xue, and T. G. Ni, "A novel brain MRI image segmentation method using an improved multiview fuzzy c-means clustering algorithm," *Frontiers in Neuroscience*, vol. 15, Article ID 662674, 2021.

[4] J. S. Duncan and N. Ayache, "Medical image analysis: progress over two decades and the challenges ahead," *IEEE Transactions on Pattern Analysis and Machine Intelligence*, vol. 22, no. 1, pp. 85–106, 2000.

[5] S. N. Kumar, A. L. Fred, and P. S. Varghese, "An overview of segmentation algorithms for the analysis of anomalies on medical images," *Journal of Intelligent Systems*, vol. 29, no. 1, pp. 612–625, 2018.

[6] J. C. Bezdek, R. Ehrlich, and W. Full, "FCM: the fuzzy c-means clustering algorithm," *Computers and Geosciences*, vol. 10, no. 2-3, pp. 191–203, 1984.

[7] T. X. Pham, P. Siarry, and H. Oulhadj, "Integrating fuzzy entropy clustering with an improved PSO for MRI brain image segmentation," *Applied Soft Computing*, vol. 65, pp. 230–242, 2018.

[8] J. Q. Miao, X. B. Zhou, and T. Z. Huang, "Local segmentation of images using an improved fuzzy C-means clustering algorithm based on self-adaptive dictionary learning," *Applied Soft Computing*, vol. 91, Article ID 106200, 2020.

[9] Z. Ji, J. Liu, G. Cao, Q. Sun, and Q. Chen, "Robust spatially constrained fuzzy c-means algorithm for brain MR image segmentation," *Pattern Recognition*, vol. 47, no. 7, pp. 2454–2466, 2014.

[10] P. H. Krishnan and P. Ramamoorthy, "Fuzzy clustering based ant colony optimization algorithm for MR brain image segmentation," *Journal of Theoretical and Applied Information Technology*, vol. 65, no. 3, pp. 644–649, 2014.

[11] A. Forestiero, C. Mastroianni, and G. Spezzano, "Building a peer-to-peer information system in grids via self-organizing agents," *Journal of Grid Computing*, vol. 6, no. 2, pp. 125–140, 2008.

[12] A. Forestiero, C. Mastroianni, and G. Spezzano, "Antares: an ant-inspired P2P information system for a self-structured grid," in *Proceedings of the 2007 2nd Bio-Inspired Models of Network Information and Computing Systems*, pp. 151–158, Budapest, Hungary, December 2007.

[13] S. Vinurajkumar and S. Anandhavelu, "An Enhanced Fuzzy Segmentation Framework for extracting white matter from T1-weighted MR images," *Biomedical Signal Processing and Control*, vol. 71, Article ID 103093, 2022.

[14] R. Meena Prakash and R. Shantha Selva Kumari, "'Fuzzy C means integrated with spatial information and contrast enhancement for segmentation of MR brain images," *International Journal of Imaging Systems and Technology*, vol. 26, no. 2, pp. 116–123, 2016.

[15] Y. Xiao, Z. Chang, and B. Liu, "An efficient active learning method for multi-task learning," *Knowledge-Based Systems*, vol. 190, Article ID 105137, 2020.

[16] H. Zhang, J. Liu, D. Zou, and N. Chen, "Knowledge-based transfer fuzzy clustering with non-local spatial information for surface roughness measurement," *Measurement*, vol. 174, Article ID 109076, 2021.

[17] X. Chen, X. Xu, J. Z. Huang, and Y. Ye, "TW-k-means: automated two-level variable weighting clustering algorithm for multiview data," *IEEE Transactions on Knowledge and Data Engineering*, vol. 25, no. 4, pp. 932–944, 2013.

[18] Y. Jiang, K. Zhao, K. Xia et al., "A novel distributed multitask fuzzy clustering algorithm for automatic MR brain image segmentation," *Journal of Medical Systems*, vol. 43, no. 5, p. 118, 2019.

[19] P. Qian, J. Zhou, Y. Jiang et al., "Multi-view maximum entropy clustering by jointly leveraging inter-view collaborations and intraview-weighted attributes," *IEEE Access*, vol. 6, pp. 28594–28610, 2018.

[20] W. Pedrycz, "Collaborative fuzzy clustering," *Pattern Recognition Letters*, vol. 23, no. 14, pp. 1675–1686, 2002.

[21] Z. Liu, B. Huang, Y. Cui et al., "Multi-task deep learning with dynamic programming for embryo early development stage classification from time-lapse videos," *IEEE Access*, vol. 7, pp. 122153–122163, 2019.

[22] L. A. Zadeh, "Fuzzy sets," *Information and Control*, vol. 8, no. 3, pp. 338–353, 1965.

[23] I. Despotovi´c, B. Goossens, and W. Philips, "MRI segmentation of the human brain: challenges, methods, and applications," *Computational and Mathematical Methods in Medicine*, vol. 201523 pages, Article ID 450341, 2015.

[24] E. Ahmed, C. M. Wang, F. C. Jia, J. Wu, and G. Li, "Segmentation of brain tissues from magnetic resonance images using adaptively regularized kernel-based fuzzy -means clustering," *Computational and Mathematical Methods in Medicine*, vol. 201512 pages, Article ID 485495, 2015.

[25] M. Alruwaili, M. H. Siddiqi, and M. A. Javed, "A robust clustering algorithm using spatial fuzzy C-means for brain MR images," *Egyptian Informatics Journal*, vol. 21, no. 1, pp. 51–66, 2020.

[26] L. Chen, C. L. P. Chen, and L. Mingzhu, "A multiple-kernel fuzzy c-means algorithm for image segmentation," *IEEE Transactions on Systems, Man, and Cybernetics, Part B (Cybernetics)*, vol. 41, no. 5, pp. 1263–1274, 2011.

[27] C. Militello, L. Rundo, M. Dimarco et al., "Semi-automated and interactive segmentation of contrast-enhancing masses on breast DCE-MRI using spatial fuzzy clustering," *Biomedical Signal Processing and Control*, vol. 71, Article ID 103113, 2022.

[28] Y. Al-Saeed, H. Soliman, and M. Elmogy, "Liver segmentation using fast-generalized fuzzy C-means (FG-FCM) from CT scans," in *Proceedings of the 2020 International Conference on Data Analytics for Business and Industry: Way towards a Sustainable Economy (ICDABI)*, pp. 1–6, Sakheer, Bahrain, October 2020.

[29] Z. J. Zhao, J. J. Zhao, and K. Song, "Joint DBN and Fuzzy C-Means unsupervised deep clustering for lung cancer patient

stratification," *Engineering Applications of Artificial Intelligence*, vol. 91, Article ID 103571, 2020.

[30] C. Militello, L. Rundo, L. Minafra et al., "MF2C3: multi-feature fuzzy clustering to enhance cell colony detection in automated clonogenic assay evaluation," *Symmetry*, vol. 12, no. 5, p. 773, 2020.

[31] S. Navaei Lavasani, A. Mostaar, and M. Ashtiyani, "Automatic prostate cancer segmentation using kinetic analysis in dynamic contrast-enhanced MRI," *Journal of biomedical physics and engineering*, vol. 8, no. 1, pp. 107–116, 2018.

[32] L. Rundo, C. Militello, G. Russo et al., "Automated prostate gland segmentation based on an unsupervised fuzzy C-means clustering technique using multispectral T1w and T2w MR imaging," *Information*, vol. 8, no. 2, p. 49, 2017.

[33] X. Zhang, X. Zhang, H. Liu, and J. Luo, "Multi-task clustering with model relation learning," in *Proceedings of the 27th International Joint Conference on Artificial Intelligence (IJCAI-18)*, pp. 3132–3140, Stockholm, Sweden, July 2018.

[34] J. Liu, S. Ji, and J. Ye, "Multi-task feature learning via efficient l2, 1-norm minimization," 2009, https://arxiv.org/ftp/arxiv/papers/1205/1205.2631.pdf.

[35] Y. Ren, X. Que, D. Yao, and Z. Xu, "Self-paced multi-task clustering," *Neurocomputing*, vol. 350, pp. 212–220, 2019.

[36] R. S. Kwan, A. C. Evans, and G. B. Pike, "MRI simulation-based evaluation of image-processing and classification methods," *IEEE Transactions on Medical Imaging*, vol. 18, no. 11, pp. 1085–1097, 1999.

[37] M. Hassan, I. Murtza, A. Hira, S. Ali, and K. Kifayat, "Robust spatial fuzzy GMM based MRI segmentation and carotid artery plaque detection in ultrasound images," *Computer Methods and Programs in Biomedicine*, vol. 175, pp. 179–192, 2019.

[38] D. Kumar, R. K. Agrawal, and H. Verma, "Kernel intuitionistic fuzzy entropy clustering for MRI image segmentation," *Soft Computing*, vol. 24, no. 6, pp. 4003–4026, 2020.

[39] H. Verma, A. Gupta, and D. Kumar, "A modified intuitionistic fuzzy c-means algorithm incorporating hesitation degree," *Pattern Recognition Letters*, vol. 122, pp. 45–52, 2019.

Hindawi

Research Article

Pyroptosis-Related Genes as Markers for Identifying Prognosis and Microenvironment in Low-Grade Glioma

Jinkun Han ⓘ **, Yajun Jing** ⓘ **, and Peng Sun** ⓘ

Department of Neurosurgery, The Affiliated Hospital of Qingdao University, Qingdao 266005, China

Correspondence should be addressed to Peng Sun; sunpeng@qdu.edu.cn

Low-grade glioma (LGG) is one of the most common brain tumors and often develops into the worst glioblastoma (GBM). Pyroptosis is related to inflammation and immunization. It has been demonstrated to influence the progression of a variety of cancers. However, the value of pyrosis-related genes (PRGs) in LGG remains unclear. Public TCGA-LGG data are used to analyze the differential expression and genetic variation of PRGs in LGG. Subsequently, this paper identifies pyroptosis-related subtypes and constructs prognostic models. This paper analyzes the expression and function of selected CASP5 in LGG and constructs a ceRNA regulatory network. Final CASP5-related immune infiltration analysis and methylation analysis are performed. Most PRGs are differentially expressed and altered in LGG. Subtypes and prognostic models based on PRGs not only have good functions but also have a great connection with immune infiltration. Enrichment analysis of PRGs with prognostic value of LGG also shows functions correlated mainly with immunity and inflammation. CASP5 is significantly differentially expressed in different grades of gliomas and different prognoses. Despite fewer mutations, CASP5 has a clear correlation for both immune cells and immune checkpoint molecules in the LGG microenvironment. Its methylation may also have a role in the prognosis of LGG. This paper shows the association of pyrosis-related subtypes, prognostic models, and genes, with immune infiltration.

1. Introduction

Diffuse low- and intermediate-grade gliomas constitute low-grade glioma (LGG, World Health Organization (WHO) grades II and III), including astrocytomas, oligodendrogliomas, and oligoastrocytomas [1, 2]. Compared with benign WHO I glioma, WHO II and III gliomas are incurable by surgical resection and often eventually develop into glioblastoma [3, 4]. Surgery and adjuvant therapy (including radiotherapy and chemotherapy) are the basic strategies for the treatment of LGG, which has also been demonstrated in many studies to prolong the survival time of patients with LGG [5–7]. Due to the variability of tumors, pathological diagnosis cannot accurately predict prognosis [8]. Clinical decision-making for LGG now relies more on genetic typing, which is also recommended in glioma classification.

Pyroptosis is a programmed cell death (PCD) characterized by the release of proinflammatory mediators and the induction of an inflammatory response [9]. Pyroptosis is usually initiated by caspase (CASP) family proteases and is performed by gasdermin (GSDM) proteins [10]. As cell death, pyroptosis naturally plays a role in inhibiting tumor progression. Recent studies have also found that pathways and inflammatory mediators involved in pyroptosis are associated with drug resistance of tumors. In fact, much evidence exists that has demonstrated the important role of pyroptosis in a variety of cancers. However, the role of pyroptosis-related genes (PRGs) in LGG remains to some extent unknown.

Since representing tumor and surrounding stromal cells, the tumor microenvironment (TME) has tumor-specific characteristics, especially immune infiltration. The immune microenvironment infiltrated by different immune cells can promote the therapeutic resistance of tumor invasion through immunosuppression. So, immunotherapy can inhibit tumor progression by enhancing the immune system's response to tumor cells. This requires more biomarkers to

characterize the prognosis and microenvironment of tumors. We start from the analysis of the LGG data from TCGA and explored the significance and function of pyroptosis-related genes in LGG by the bioinformatics analysis.

The remainder of this paper is organized as follows. Section 2 presents the construction of the pyroptosis-related prognostic model. Section 3 provides the experimental result and Section 4 illustrates data analysis and result discussion. Finally, the conclusion of this study and some future recommendations are given in Section 5.

2. Construction of the Pyroptosis-Related Prognostic Model

The paper downloads information about the LGG samples as the tumor group using The Cancer Genome Atlas (TCGA). Because TCGA lacks the corresponding normal samples, the paper obtains brain samples as normal samples at Genotype-Tissue Expression (GTEx, https://gtexportal.org/home/). We use R to make statistical analysis and visualize with R package ggplot2. 32 PRGs are obtained from prior reviews, which have described and analyzed the members of PRGs in their studies. We use the integrated database Gene Set Cancer Analysis (GSCA) to check the other information about TCGA-LGG, including the mutation frequency, waterfall plot, and the correlation between immune cell type and GSVA score of PRGs. We use the R package ConsensusClusterPlus for consistency analysis to the RNA-sequencing (RNA-seq) data from TCGA. Then, we use the R package pheatmap for clustering heatmaps and retained PRGs with standard deviation (SD) >0.1. SIGLEC15, TIGIT, CD274, HAVCR2, PDCD1, CTLA4, LAG3, and PDCD1LG2 are selected to be immune-checkpoint-relevant transcripts. We extract transcripts of immune-checkpoint-relevant 8 genes, SIGLEC15, TIGIT, CD274, HAVCR2, PDCD1, CTLA4, LAG3, and PDCD1LG2, to visualize the differential expressions among the 3 LGG subgroups, using R package ggplot2. With the same visualization methods, we utilize the R package immunedeconv which integrates many kinds of algorithms, including TIMER, to make immune infiltration estimations for 3 LGG subtypes. We use the one-class logistic regression (OCLR) algorithm constructed by Malta to calculate mRNAsi, based on the characteristics of 11774 genes' expression profile obtained from TCGA. According to Spearman correlation, we subtracted the minimum value and divide it by the linear transformation of the maximum value to eventually map the dryness index to [0, 1]. Half-maximal inhibitory concentration (IC50) is an important indicator for evaluating the therapeutic response of samples. We predicted the chemotherapeutic response of temozolomide (TMZ) for LGG patients based on the Genomics of Drug Sensitivity in Cancer (GDSC, https://www.cancerrxgene.org). The prediction process is implemented by R package pRRophetic in which the LGG samples' IC50 is estimated by ridge regression. We utilized all default parameters and summarized duplicate gene expression as a mean value for statistical comparison.

We performed the log-rank tests and univariate Cox proportional hazards regression to the expression data and survival data of LGG from TCGA using R package survival and visualized ones with $p < 0.05$ by Kaplan–Meier (KM) survival curves using ggplot2. We constructed the functional network of PRGs in Metascape and identified its functional subsets and members by MCODE component. The GO and KEGG enrichment analyses are performed and visualized through R package clusterProfiler.

We use the least absolute shrinkage and selection operator (LASSO) regression algorithm to perform feature selection on data of TCGA-LGG with the R package glmnet. During the development of the regression model, we screened the factors and reduced overfitting by forcefully changing some coefficients to zero. The log-rank is used to test survival differences in KM. Subsequently, we extracted the LGG data from CGGA (https://www.cgga.org.cn/index.jsp) to validate the constructed prognostic model. The Spearman's correlation analysis is used to describe the correlation between the risk scores and the different immune cell abundances derived by applying the TIMER algorithm.

In the analysis of tumor mutation burden (TMB) and microsatellite instability (MSI), we perform the Spearman correlation analysis to discover PRGs' correlations with them. We downloaded and merged mRNA expression data and drug sensitivity data from GDSC. By performing the Pearson correlation analysis, we obtained the correlation between the IC50 of the top 30 drugs and the PRG expression to make the bubble plot.

We search for differential expression of CASP5 between tumor and normal samples in the data on different tumors from TCGA at TIMER, a website related to immune infiltration. Afterward, we ranked the RNA expression profiles from TCGA-LGG according to the expression values of CASP5. We selected half of the patients with high CASP5 expression values for GSEA enrichment analysis and synthesized the curves of the top 7 hallmarks. We find the data about the distribution of CASP5 expression and the corresponding types of copy number value (CNV) in LGG in cBioportal and visualized their correlation by R software.

We perform prediction and intersection of target miRNAs bound to CASP5 in ENCORI and miRWalk, respectively. The correlation between 15 miRNAs and LGG is calculated by the processing of TCGA-LGG data through R software and then we screened the rest genes using the correlation with CASP5. Eventually, we obtain five miRNAs, hsa-miR-16-5p, hsa-miR-15b-5p, hsa-miR-424-5p, hsa-miR-503-5p, and hsa-miR-3690. ENCORI and LncBase-Predicted v2 are used to predict lncRNA targets that bind to miRNAs. The results of each miRNA in both websites are intersected, and a total of 63 lncRNAs corresponding to the 5 miRNAs are finally found. We construct the lnRNA-miRNA-mRNA triple regulatory network in Cytoscape and obtained a subnetwork composed of 11 hub genes with the EPC algorithm in CytoHubba, a Cytoscape plug-in. We screen 3 lncRNAs which are of prognostic value and differentially distributed between normal and LGG samples by processing data from TCGA-LGG and GTEx-brain using R software. We acquire lncRNA sequences with LNCipedia

and performed cellular localization in lncLocator. The TCGA-LGG data are processed with R software to explore the correlation of the selected MCM3AP-AS1 with other molecules.

We divide LGG patients into 2 groups using the expression of CASP5 by processing the data from TCGA-LGG. We investigate the expression differences of 3 methyltransferase genes and 5 DNA repair genes between the CASP5_high group and the CASP5_low-group. We assess the methylation level of CASP5 in LGG and normal tissue in DiseaseMeth 2.0, the human disease methylation database. We find relevant methylation sites on the CASP5 sequence in MEXPRESS. MethSurv is used to evaluate the scattering of different CpG islands about CASP5.

3. The Experimental Results

3.1. Landscape of Genetic Variation of PRG in LGG. We first explore the differential expression of PRGs in normal and LGG samples. Except for PJVK, the other 31 genes are all upregulated or downregulated in LGG, as shown in Figure 1(a). Accurately, the expressions of GSDMB, ELANE, NLRP2, and IL6 are decreased in LGG, and the expression of the remaining PRGs is increased. In LGG, the frequency of mutation in NLRP2 is the highest, reaching 17%, and all missense mutations, as shown in Figure 1(b). The top 10 genes are listed, as shown in Figure 1(c).

The types of copy number variation (CNV) of PRGs in LGG are different. For example, there is mainly deletion in NLRP2 and CASP9, but mainly amplification in ELANE and GSDME, as shown in Figure 1(d). We also discover the correlation between gene expression and CNV. The results showed that the expression of CASP3, CASP6, NOD1, GSDME, SCA11, CASP9, GSDMC, CASP8, TIRAP, ELANE, IL6, NLRP2, and PLCG1 confirmed a significant positive correlation with CNV (S1). We also calculate gene set expression (GSVA) score and find that of PRGs are mainly significantly positively correlated with macrophages and negatively correlated with naive CD8+ T cell (S2).

3.2. PRGs-Based LGG Subtype. In order to explore the relationship between the expression of PRGs and LGG subtypes, we use consensus clustering analysis to classify the LGG patients. By increasing the clustering variable (k) from 2 to 10, the most appropriate number of classifications is observed when $k = 3$, as shown in Figure 2(a). The heatmap demonstrates the expression of PRGs in the 3 groups (S.3A). We calculated the prognosis of the three clusters and found that C3 had a significantly worse prognosis compared with C1 and C2, as shown in Figure 2(b). We compare the expression of eight immune checkpoint genes for three clusters. The results show that the expression levels of these genes in G3 are all the highest, as shown in Figure 2(c). The same situation is also observed by immune cell score, except for CD8+ T cell, as shown in Figure 2(d). Myeloid dendritic cells are the highest proportion of the six immune cells. Considering that 3 types may reveal that a worse prognosis in LGG is associated with the acquisition of stem-like

features, we apply OCLR to find the highest score in G1 but the lowest one in G3, as shown in Figure 2(e). Finally, we predict the response of the three classes of LGG to treatment with TMZ and found that the IC50 of G3 is the lowest. Moreover, we explore the differential expression of 32 PRGs among 3 clusters, as shown in Figure 2(f). Except for SCAF11 and GPX4, we find that there are differential expressions of all other PRGs among 3 clusters. Most of the PRGs had the highest expression in G3.

3.3. Functional Enrichment Analysis of Prognostically Relevant PRGs in LGG. By the univariate COX regression, we find 18 genes with prognostic value in PRGs, and the KM survival curves are shown in Figure 3. High expressions of all 18 PRGs except for CASP9 and GSDMC are associated with a worse prognosis of LGG. To understand the action pathway of this part of PRGs on LGG, we perform functional enrichment analysis on the genes with prognostic value. Top biological process (BP) is the regulation of cysteine-type endopeptidase activity, response to lipopolysaccharide, and response to molecule of bacterial origin. Cellular component (CC) is mainly enriched in the cytosolic part, and the major molecular function (MF) is cysteine-type endopeptidase activity and cysteine-type peptidase activity. We perform the KEGG enrichment analysis and found that the most relevant KEGG pathways of PRGs with prognostic value are NOD-like receptor signaling pathway, legionellosis, and pathogenic *Escherichia coli* infection. We synthesize their enrichment analysis in Metascape and constructed functional networks, where the subsets and its members of the network involved the two most significant functions. The associated P value network shows NOD-like receptor signaling pathway as the most significant functional term (S.4A), which participated in immune system. Interestingly, the circle shows that NLRP6, NLRP1, and GSDMD only involve this term in the top 20 KEGG pathways (S.4B). Eventually, we visualized the expression correlation of 18 PRGs with prognostic value. The results showed that there are often associations between every 2 PRGs (S.4C). Figure 3 displays the KM curves of PRGs with the prognostic value in LGG. Figure 4 shows functional enrichment analysis of prognostically relevant PRGs.

3.4. Construction of a Prognostic PRG Model. By forcing the regression coefficients of some members of the 32 PRGs to be reduced to zero and applying cross-validation to avoid overfitting, we construct the stable prognostic model. We finally identify and screen 10 genes by the LASSO Cox regression analysis (S. 5A, 5B). Risk score = (0.079) * PRKACA + (−0.4102) * CASP9 + (0.8144) * PLCG1 + (0.5394) * CASP4 + (0.0591) * CASP3 + (0.1184) * IL8 + (0.1916) * CASP8 + (−0.1366) * GSDMC + (−0.2229) * CASP5 + (0.0314) * CASP1. We divide the LGG patients into two groups according to the risk score and explore their prognostic difference, as shown in Figure 5(a). The results demonstrated that patients with high scores had a shorter survival time, as shown in Figure 5(b). The AUC of ROC curves at 1 year, 3 years, and 5 years are 0.885, 0.875, and 0.761, respectively, as shown in
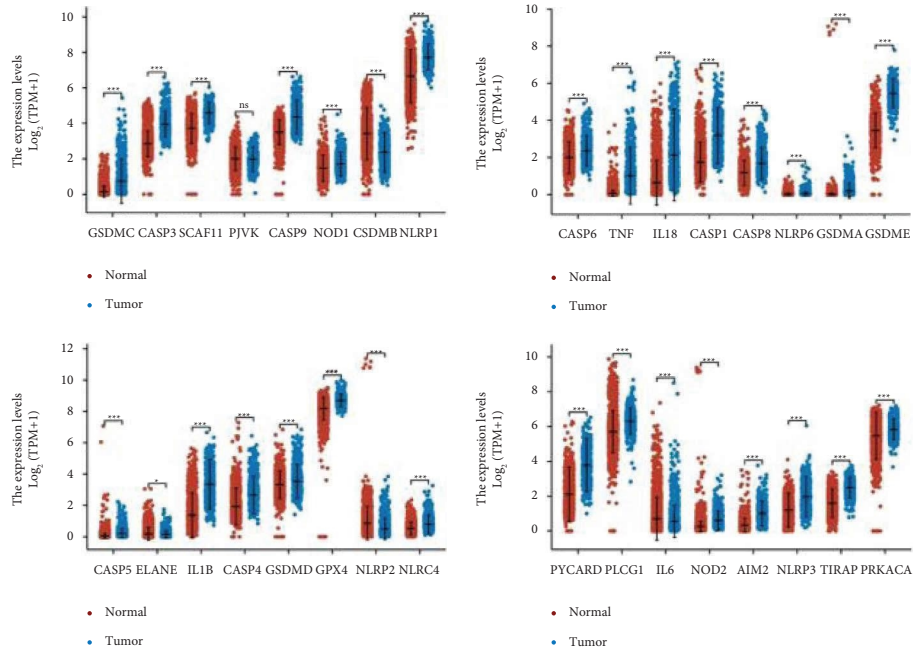
(a)
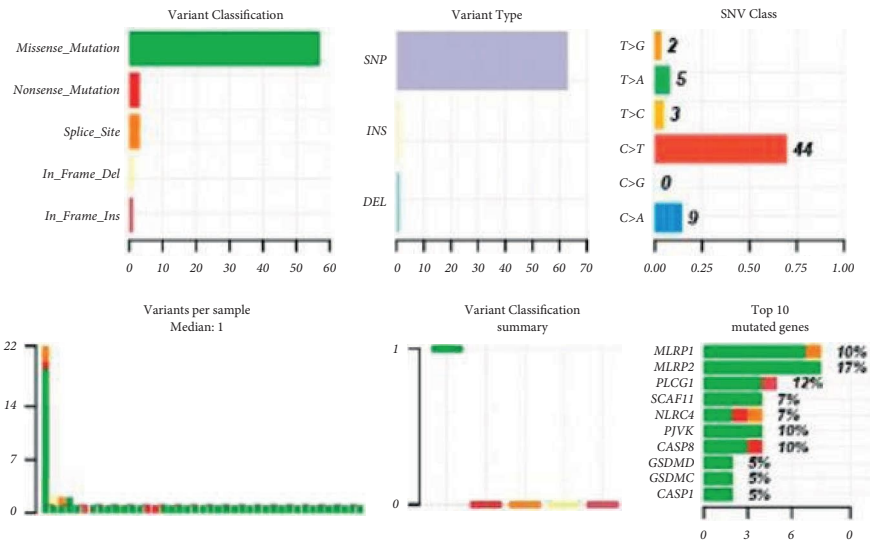
(b)

Figure 1: Continued.

(c)

(d)
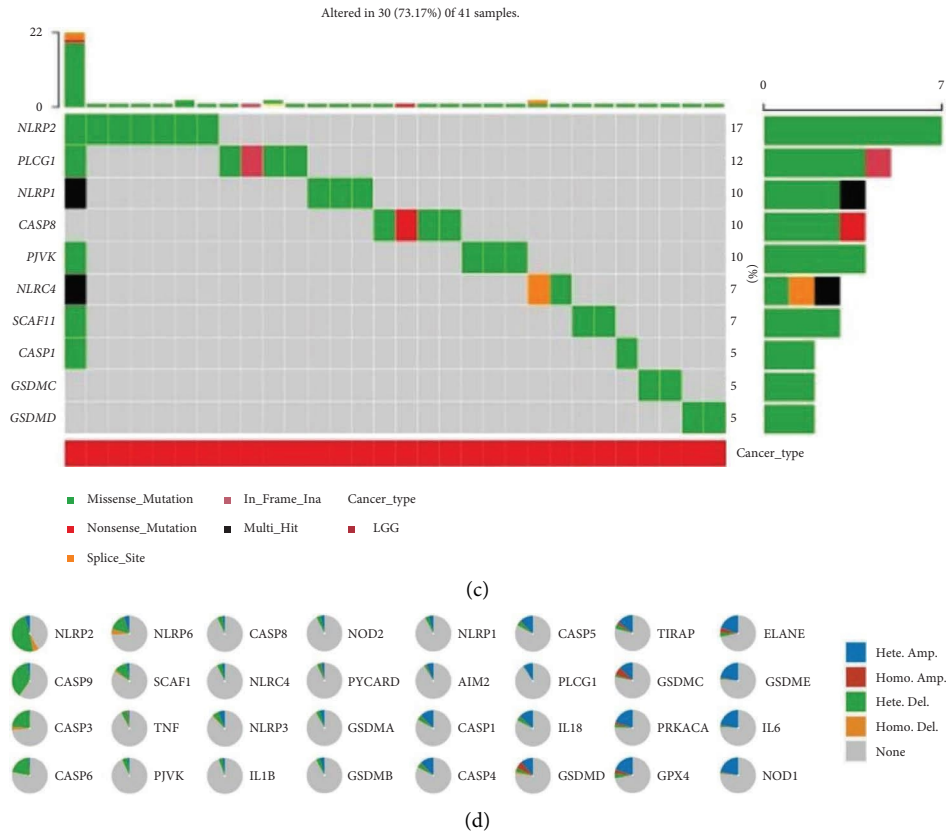
FIGURE 1: Expression and mutation of PRGs in LGG.

(a)

(b)
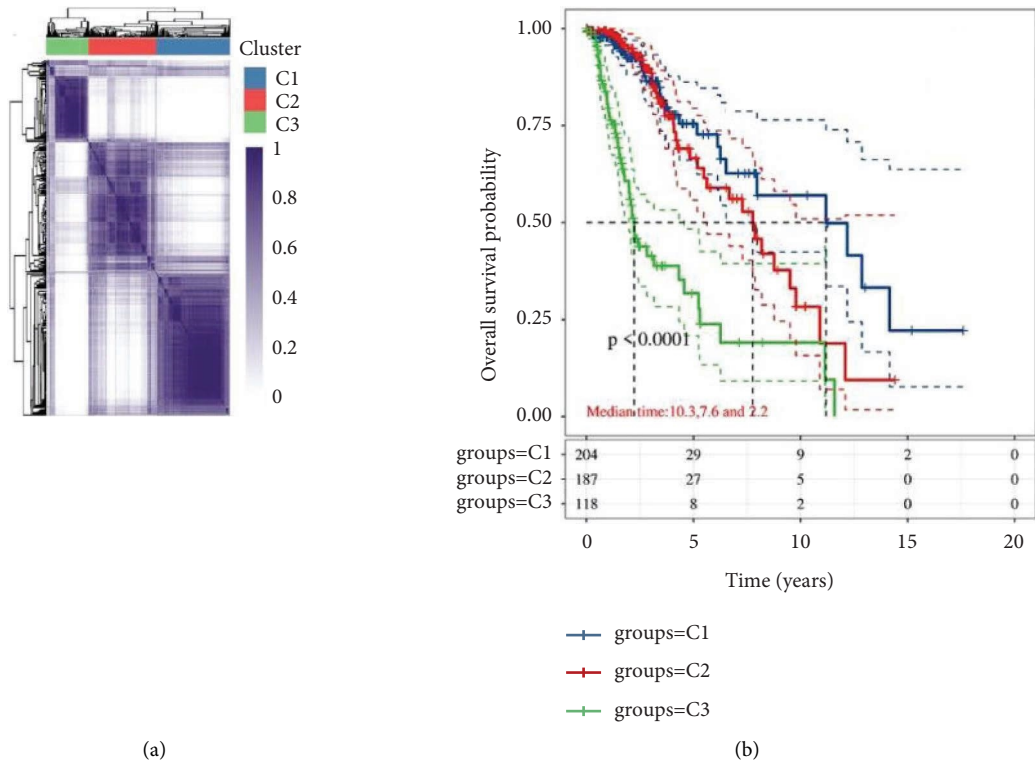
FIGURE 2: Continued.
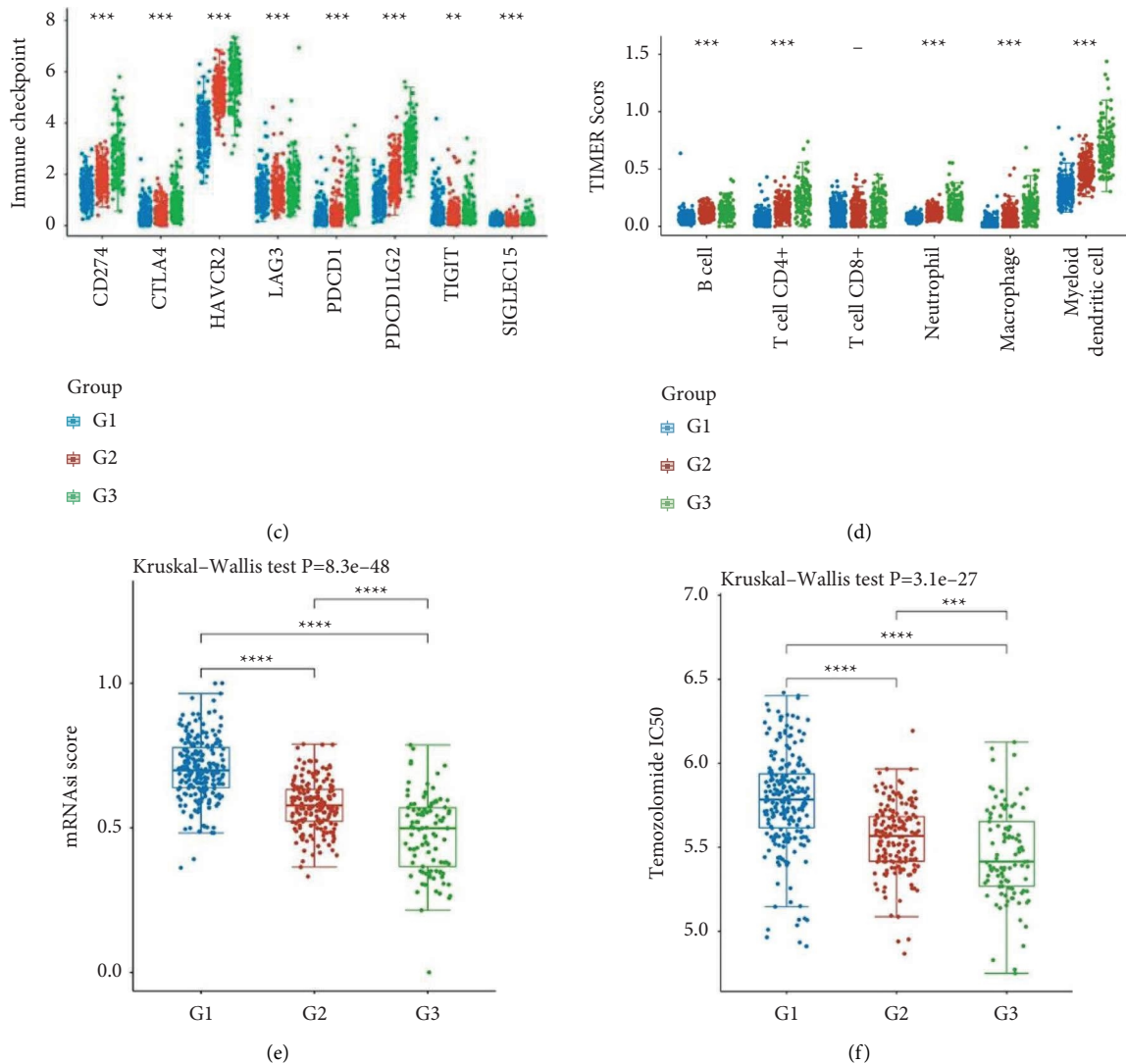
Figure 2: Characteristics of the 3 LGG classifications.

Figure 5(c). In the validated data from CGGA-LGG, there is also a significant survival difference between patients in the high-risk and low-risk groups (S. 5C, 5D). The ROC curves also validated the predictive value of the model for survival in patients with LGG (S. 5E). The combined diagnosis value of these PRGs is also higher than every member alone as shown in Figures 5(d) and 5(e). We perform TIMER immune scoring on the prognostic model and find that the risk score is significantly correlated with B cell, CD4+ T cell, neutrophil, macrophage, and dendritic cell, as shown in Figure 5(f).

3.5. MSI, TMB, and Drug Susceptibility Associated with PRGs.
Tumor mutation burden (TMB) and microsatellite instability (MSI) have received increasing attention as indicators that can predict the efficacy of immunotherapy. We explore the correlation between the expression of PRGs of prognostic models in LGG and TMB and MSI to identify whether they could be used as markers for immunotherapeutic drug

screening. The results demonstrated a negative correlation between the expression of CASP1 and MSI ($p = 0.049$, cor $= -0.09$) and a negative correlation between the expression of PLCG1 and MSI ($p = 0.001$, cor $= 0.15$). GSDMC ($p = 8.49E - 06c$, cor $= -0.2$) is revealed to have a negative relationship with TMB, which is positively correlated with the expression of other members of the prognostic models except for CASP9. To search for possible drugs, we explored the expression of these 10 genes in relation to the sensitivity of existing drugs. Figure 6 shows the correlation of PRGs expression in LGG with TMB, MSI, and sensitivity of existing drugs.

3.6. Building Relevant Nomogram.
Considering the possible response effect of clinical factors on LGG, we construct a nomogram involving clinical factors and PRGs expression to predict overall survival. The univariate and multivariate analyses screened out multiple independent factors, as shown in Figures 7(a) and 7(b). The factors for the best
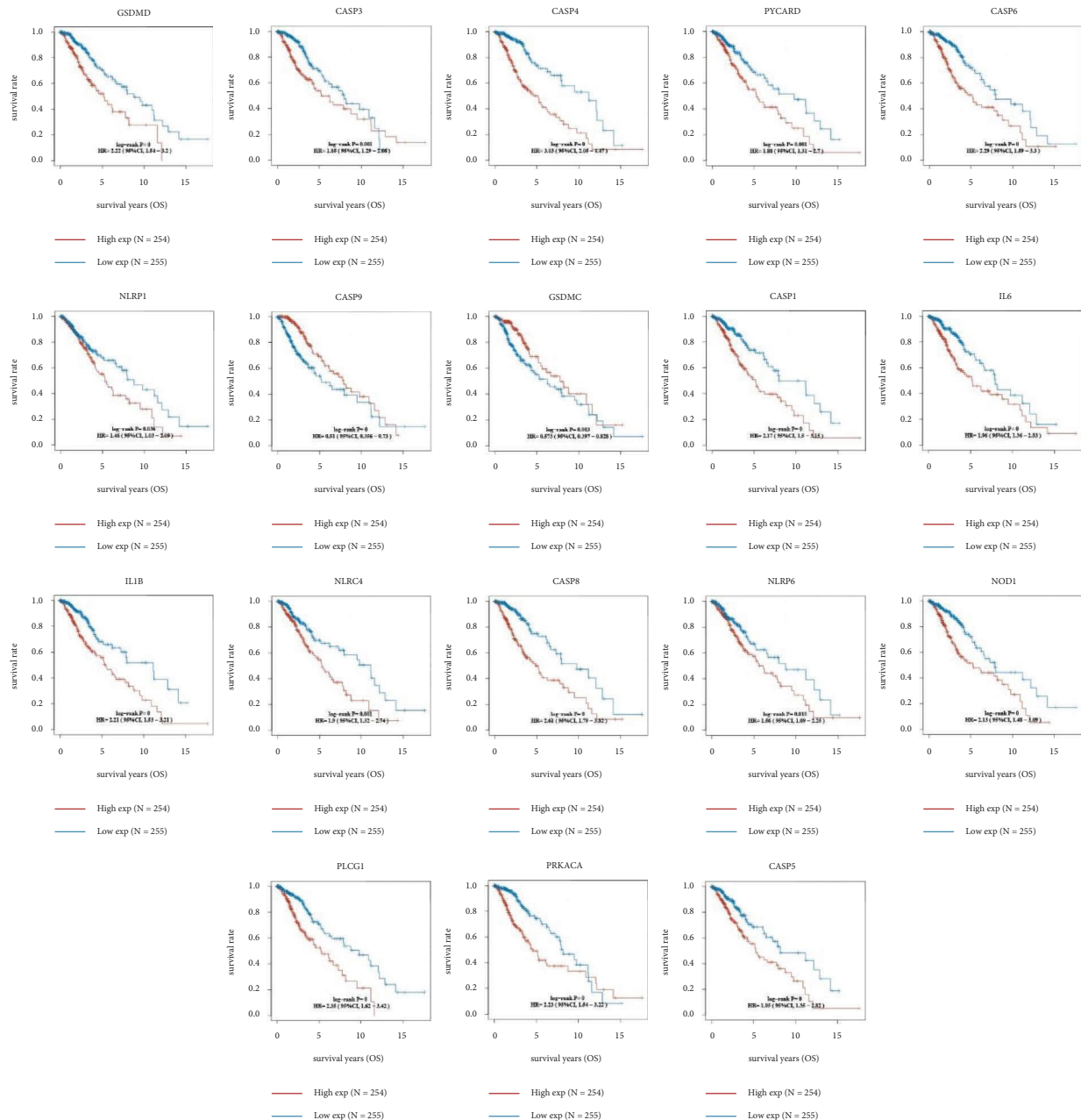
FIGURE 3: KM curves of PRGs with prognostic value in LGG.

nomogram of the final combination include grade and the expression of CASP9, CASP5, and PLCG1, as shown in Figure 7(c). However, this nomogram is shown to well predict the 1-year, 3-year, and 5-year overall survival rate of LGG patients, as shown in Figure 7(d).

3.7. Expression, Variation, and Functional Analysis of CASP5 in LGG. The conversion of LGG to GBM is thought to be one of the reasons for the poor outcome of LGG. We explored the correlation between the expressions of nomogram members in glioma. Only CASP5 is revealed to distinguish 3 grades of gliomas, as shown in Figure 8(a). Therefore, we perform further analysis around CASP5. Similar to LGG,

CASP5 is also significantly highly expressed in esophageal carcinoma (ESCA), head and neck squamous cell carcinoma (HNSC), and uterine corpus endometrial carcinoma (UCEC) (S. 6A). To further search for functions associated with CASP5, we performed GSEA enrichment analysis on patients with high expression of CASP5 in TCGA-LGG. The significant hallmarks are a complement, allograft rejection, as shown in Figure 8(b). The set containing the 200 genes most correlated with the expression of CASP5 is shown to be concentrated in neutrophil activation and neutrophil degranulation in BP, secretory granule membrane and MHC class II protein complex in CC, MHC protein complex binding, and MHC class II protein complex binding in MF by the GO enrichment analysis (S. 6B). The KEGG pathways

(a)

(b)

(c)

(d)

Figure 4: Functional enrichment analysis of prognostically relevant PRGs.

are mainly focused on *Staphylococcus aureus* infection, leishmaniasis, and phagosome (S. 6C). The heatmap shows the expression distribution of the top 15 genes in KEGG-LGG (S. 6D).

We explored the changes of the CASP5 expression among different subgroups of LGG. The expression of CASP5 in astrocytoma is significantly higher than that in oligoastrocytoma and oligodendroglioma, as shown in Figure 8(c). Compared with patients belonging to complete response (CR), partial response (PR), and stable disease (SD), the expression of CASP5 is significantly higher in progressive disease (PD) of LGG, as shown in Figure 8(d). The LGG patients who have wild IDH status or non-codeletion of 1p/19q both have higher CASP5 expression, as shown in Figures 8(e) and 8(f). The expression of CASP5 is associated with the mutation of LGG-related signature genes. We found that CASP5 is highly expressed in patients with mutant EGFR, as shown in Figure 8(g), and the same in

patients with mutant P53, as shown in Figure 8(h). Finally, we also explore the mutation of CASP5 in LGG. The alteration frequency of CASP5 in LGG is low (S. 6E). Although CASP5 expression is higher in patients with shallow deletion (S. 6F), it is not found to have a significant correlation with copy number value (S. 6G).

3.8. Construction of CASP5-Related ceRNA Network. By ENCORI and miRWalk, we predict 5 miRNAs that regulate CASP5, which had not only prognosis value but also correlated expression with CASP5's (S. 7A, 7B). Afterward, we identify a total of 63 lncRNAs associated with these 5 miRNAs by ENCORI and lncBase-Predicted v2. To explore the molecular regulatory mechanism of CASP5, we construct a lncRNA-miRNA-mRNA regulatory network and selected a subnetwork including 11 hub genes by EPC in Cytoscape, as shown in Figures 9(a) and 9(b). We find

(a)

(b)

(c)

(d)

(e)

(f)

FIGURE 5: The construction of the prognostic model.

(a)

(b)

Figure 6: Correlation of PRGs expression in LGG with TMB, MSI, and sensitivity of existing drugs.

(a)

(b)

(c)

(d)

Figure 7: Construction of correlated predictive nomogram.

AGAP2-AS1, LINC00665, and MCM3AP-AS1; all had prognostic value and were differentially expressed between LGG and normal samples among seven hub lncRNA-related genes, as shown in Figures 9(c) and 9(d). Considering that cellular localization determines the underlying mechanism of the molecule, we perform subcellular localization for 3

lncRNAs. The results show that MCM3AP-AS1 is mainly located in the cytoplasm, but AGAP2-AS1 and LINC00665 are mainly distributed in exosome and cytosol, as shown in Figure 9(e). It indicates that MCM3AP-AS1 may act as a ceRNA to regulate the expression of CASP5 through hsa-miR-15b-5p/hsa-miR-424-5p/has-miR-16-5p. We discover

(a)

(b)

(c)

(d)

(e)

(f)

(g)

(h)
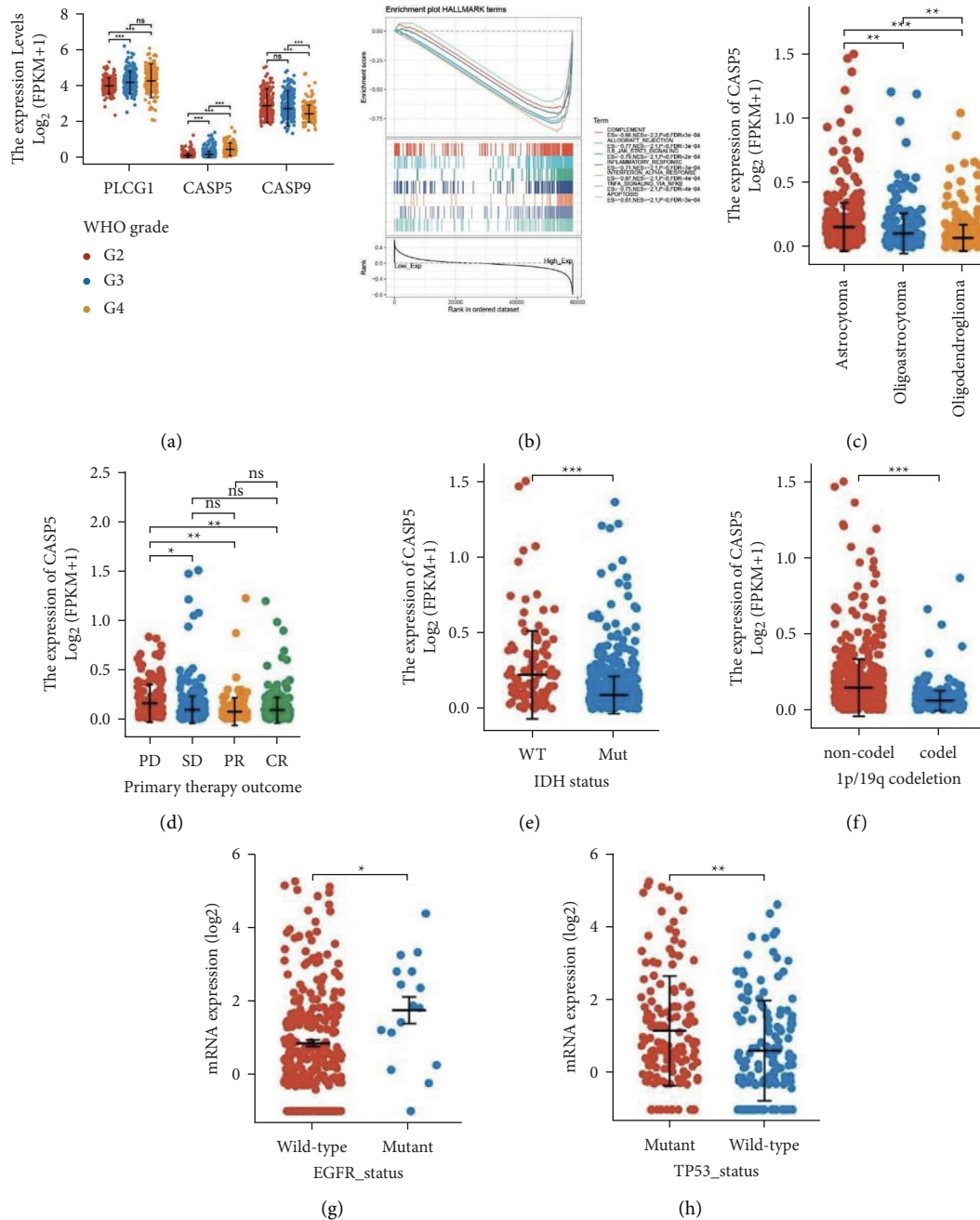
Figure 8: Expression distribution of CASP5 in different subgroups.

correlations between MCM3AP-AS1 and the corresponding miRNAs and constructed ceRNA network, as shown in Figures 9(f) and 9(g).

3.9. Relationship between CASP5 and Immune Infiltration in LGG. Immune infiltration has received increasing attention due to its important role in tumor growth and immunotherapy. We performed immune infiltration analysis on TIMER in relation to the expression of CASP5 in LGG. We first explore the correlation of CASP5 expression with different immune cells. We found that CASP5 expression

showed a significant positive correlation with all 6 immune cells, as shown in Figure 10(a). In 5 types of copy number alteration, arm-level deletion and arm-level gain are confirmed to be associated with B cell, CD4+ T cell, macrophage, neutrophil, and dendritic cell, as shown in Figure 10(b). To further validate the relationship between immune cell infiltration and CASP5 in LGG, we explored the correlation between CASP5 and the immune marker gene set of 16 immune cells. The results demonstrated that each gene set standing immune cell had members that are significantly correlated with CASP5 expression in LGG (S8). We collected
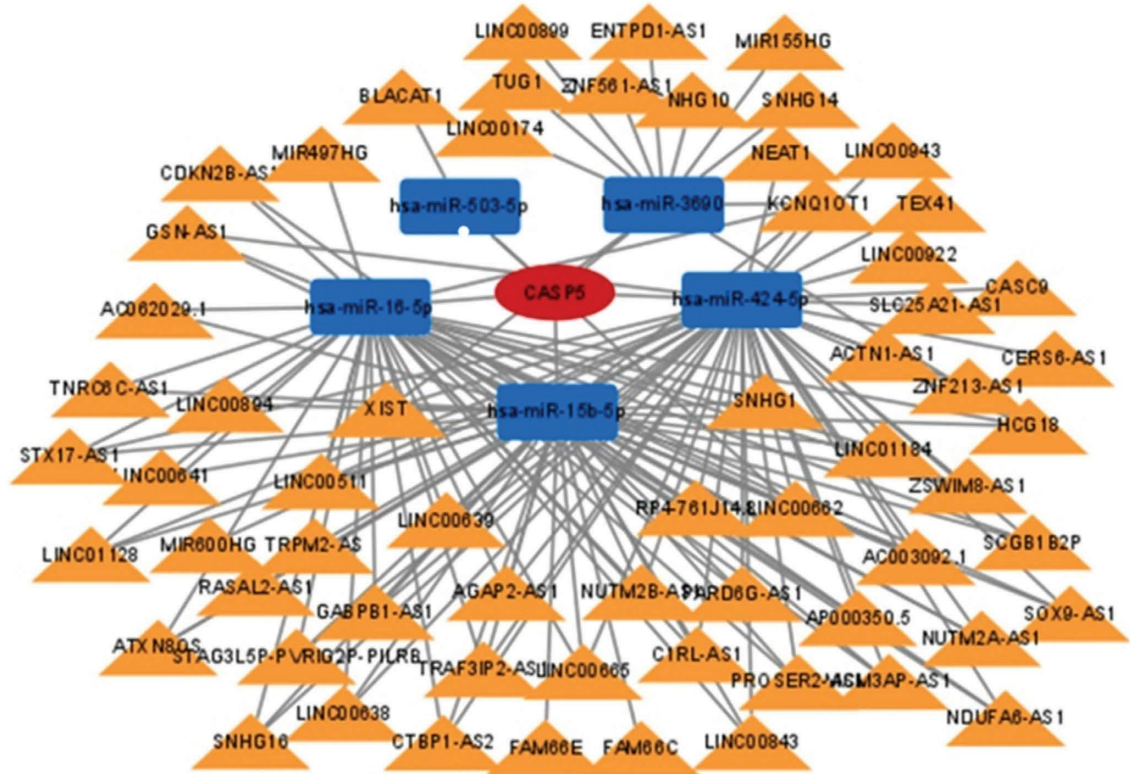
(a)
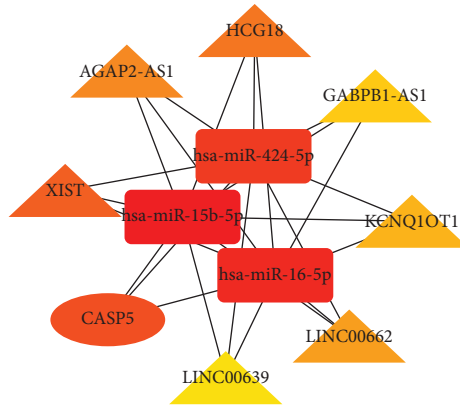
(b)
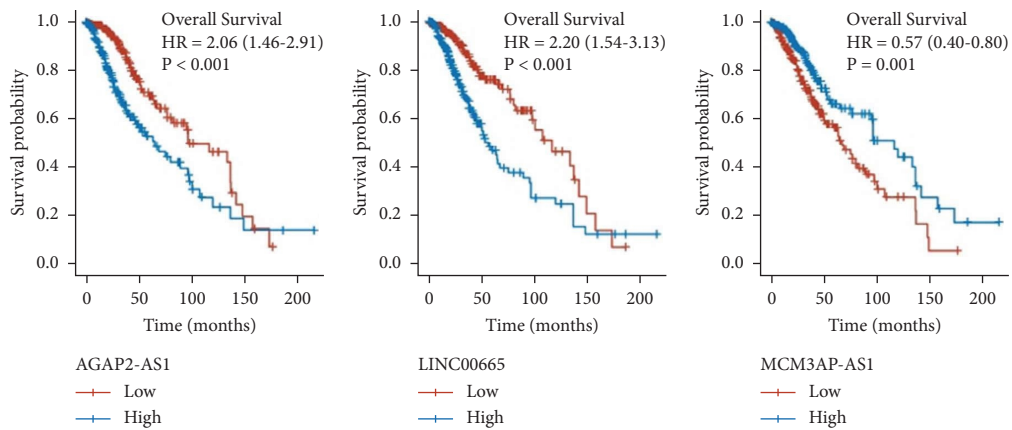
(c)

Figure 9: Continued.
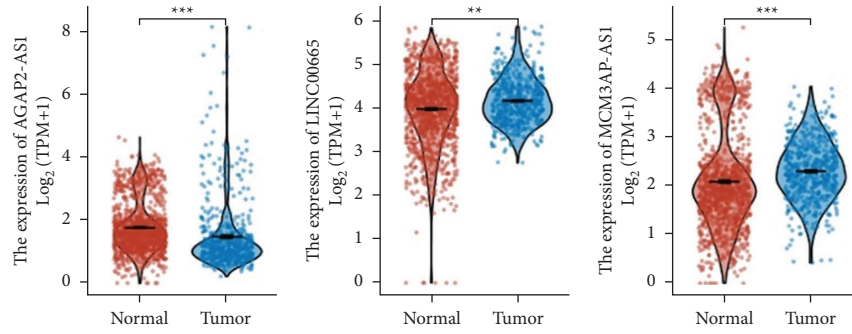
(d)
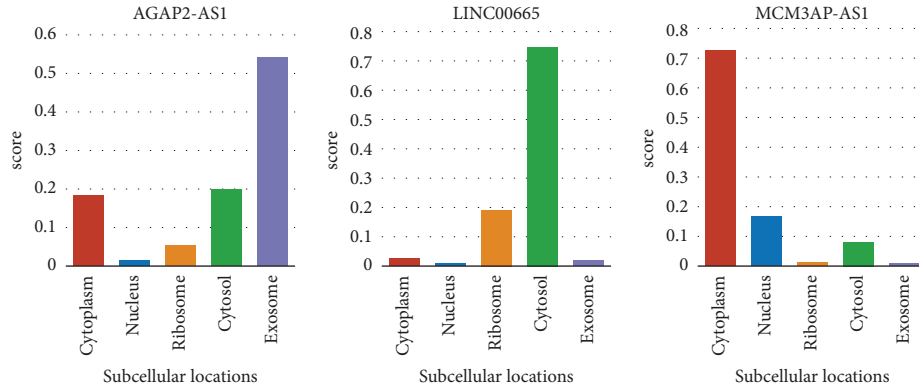
(e)
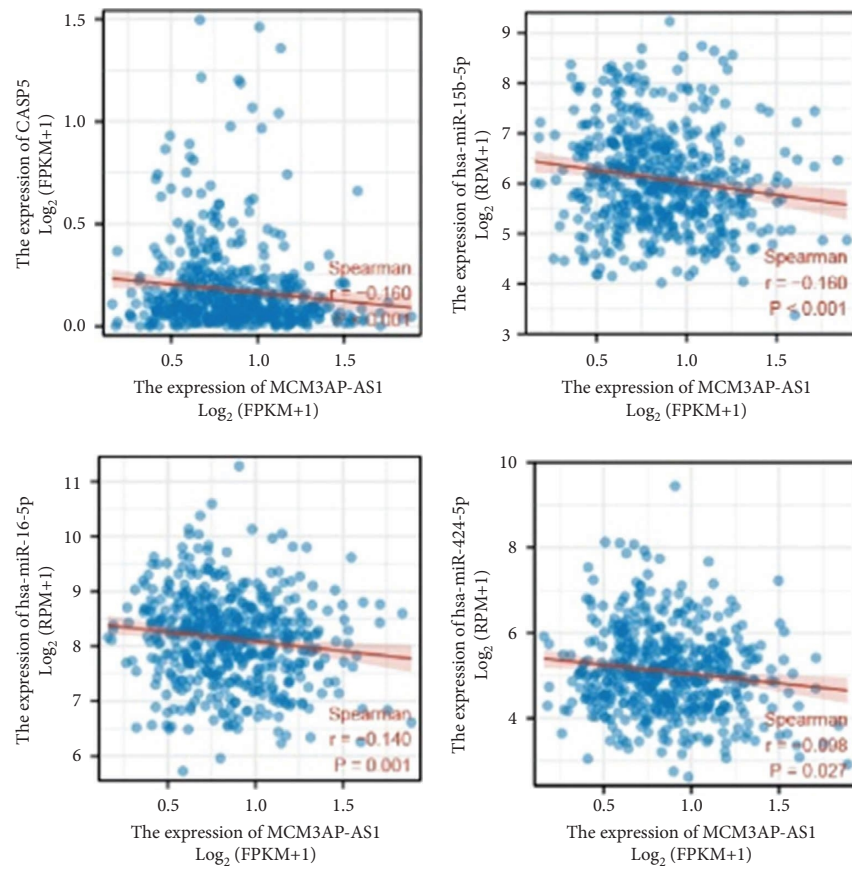
(f)

Figure 9: Continued.

(g)
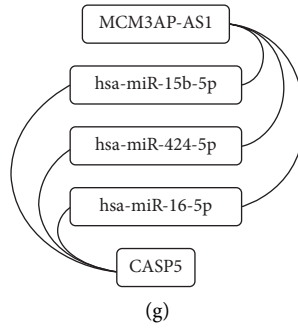
FIGURE 9: Construction of ceRNA network.

(a)

(b)

(c)
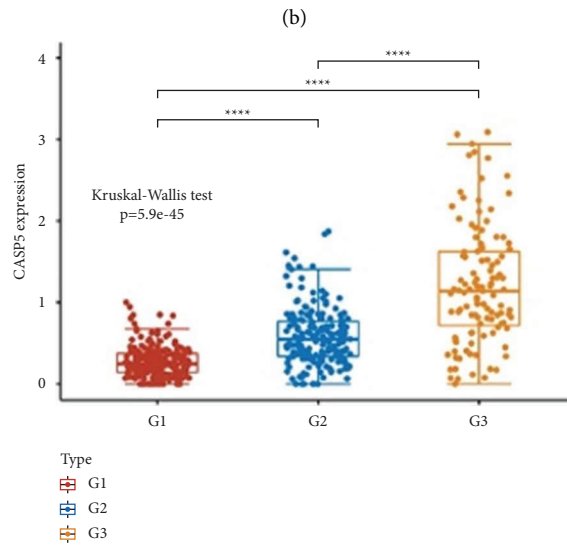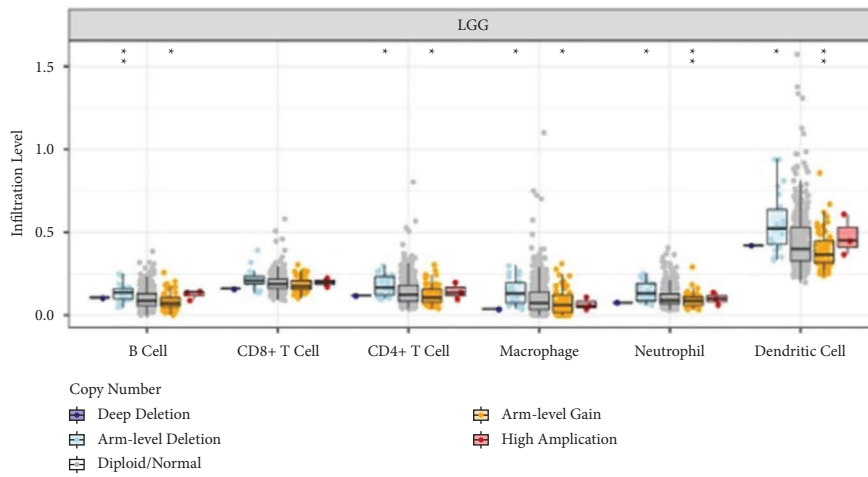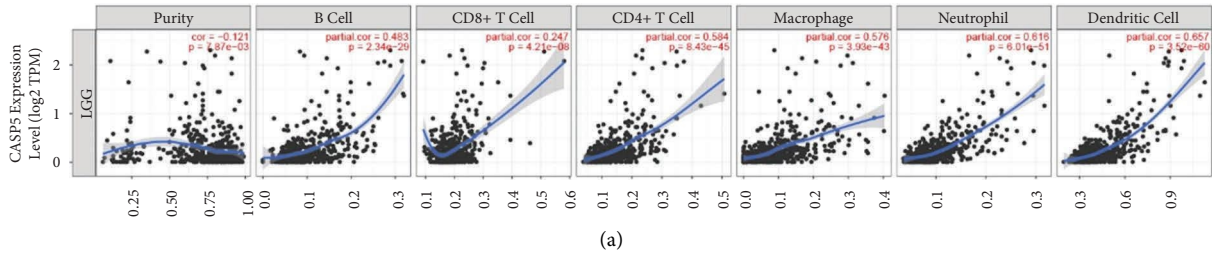
FIGURE 10: Continued.

(d)
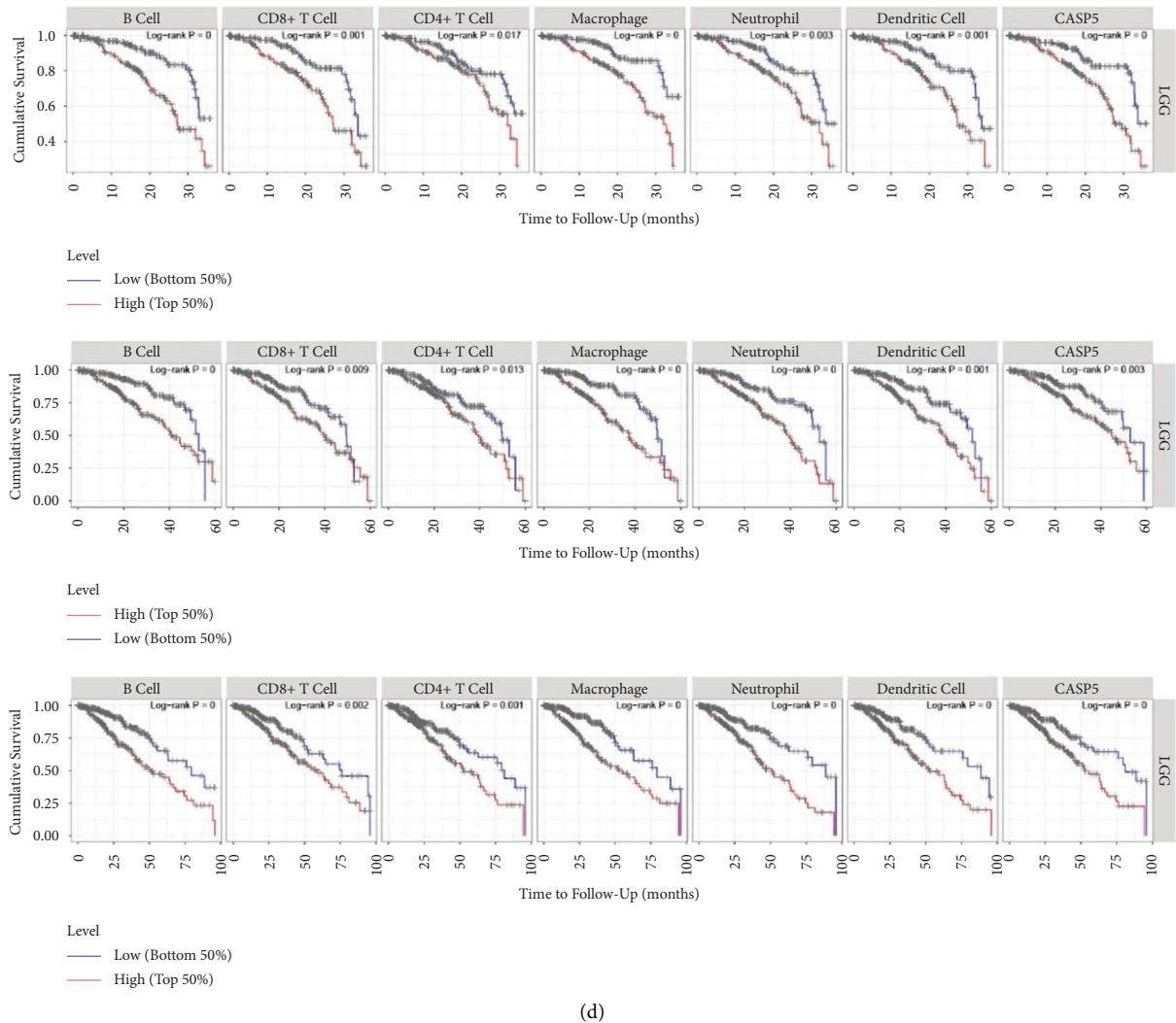
FIGURE 10: Association of CASP5 with immune infiltration: (a) correlation between expression of CASP5 and immune cell infiltration; (b) gene copy number of CASP5 in relation to immune cells in LGG; (c) distribution of CASP5 in LGG classification; (d) KM curves analyzing the relationship between immune cell levels and overall survival in LGG.

44 immune checkpoint genes and explored the association of CASP5 with them. We revealed that CASP5 expression correlates with a variety of immune checkpoint molecules (S9).

Considering that PRGs-based subtypes are also significantly associated with immune cells and immune checkpoint molecules, we explore the expression distribution of CASP5 among the three subtypes and showed that the direction of change of CASP5 among different subtypes is consistent with the direction of the change of immune checkpoint and immune cell abundance with 3 subtypes, as shown in Figure 10(c). It demonstrates that the association of PRGs-based LGG typing with immunity may be related to CASP5. We also find a high level of 6 immune cells which indicated worse 3-year, 5-year, and 8-year overall survival, as shown in Figure 10(d).

3.10. Relationship of CASP5 Expression with Methylation and DNA Repair in LGG. Methylation of DNA controls gene expression by regulating DNA structure, DNA stability, and the interaction between DNA and protein. We explored the effect of CASP5 expression on the expression of 3 methyltransferases and found that DNMT1 and DNMT3A are highly expressed in the CASP5_high group, as shown in Figure 11(a). The information in DiseaseMeth version 2.0 revealed that CASP5 had significantly higher methylation values in normal samples than in disease samples, as shown in Figure 11(b). In addition, we found the presence of methylation sites (cg10825847) in the sequence of CASP5, which negatively correlated with the expression of CASP5, as shown in Figure 11(d). The methylated regions associated with CASP5 are shown as a heatmap (S. 10A). We found an identical methylation site, cg10825847, which is located in the open sea region and TSS1500 region. Survival analysis showed

(a)

(b)

(c)

(d)
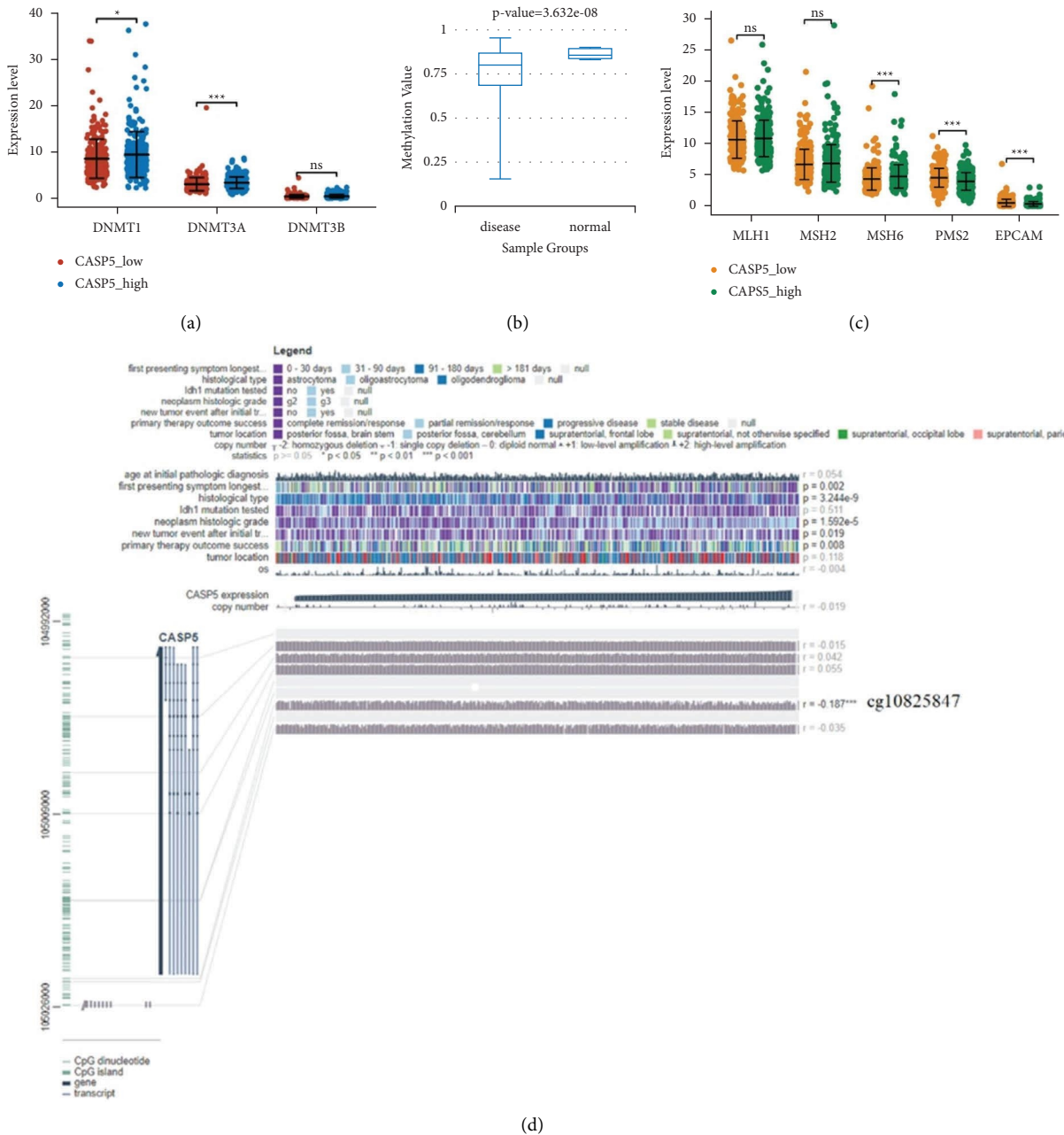
Figure 11: Methylation analysis of CASP5 in LGG: (a) correlation between the expression of three methyltransferases and CASP5; (b) different distribution of methylation values between normal samples and LGG samples; (c) correlation between the expression of DNA repair genes and CASP5 expression; (d) relationship between methylation sites of CASP5 and gene expression are visualized with MEXPRESS.

that it is associated with a better prognosis (S. 10B). Finally, we also explored the relationship between the expression of CASP5 and DNA repair genes, and the results showed that MSH6 is highly expressed in the CASP5_high group, but PMS2 and EPCAM are opposite, as shown in Figure 11(c).

4. The Experimental Result Analysis

Pyroptosis has been suggested to be a form of regulated cell death (RCD) due to its dependence on the activation of inflammatory CASP and plasma membrane pores composed of GSDM protein. RCD plays an important role in removing abnormal cells and even neural development. Pyroptosis can kill infected cells and fix bacteria, which will later be killed and phagocytosed by neutrophils and macrophages. In neuroscience, pyroptosis has been found to be involved in a variety of neurological injuries, including stroke, traumatic brain injury, and brain infection. In addition, pyroptosis is also involved in the disease process of neurological diseases such as Alzheimer's disease, epilepsy, and multiple sclerosis due to the pyroptosis of neurons. The relationship between pyroptosis and cancer

is complex. In addition to the anticancer effect of the pyroptosis process, the microenvironment constituted by pyroptosis molecules promotes tumor progression. In our study, we explored the impact of pyroptosis on the prognosis of LGG and identified TME associated with pyroptosis in LGG, especially the immune microenvironment. Finally, we focused on the analysis of the role of the pyroptosis-related CASP5 in LGG.

We identify 3 subtypes with significant prognostic differences by analysis of the expression profile of PRGs in LGG ($P < 0.0001$). The progression of cancer is associated with the acquisition of stem cell-like features. Glioma stem cell is an important reason why gliomas remain resistant and eventually recur. The discordance between the OCLR score and the prognostic situation of the 3 subtypes demonstrates that the prognostic value of glioma subtypes identified by PRGs involves fewer factors of cancer stem cells. An immune microenvironment is also an important factor affecting tumor progression. Originally, antitumor immune cells are reprogramed into an immunosuppressive phenotype in the TME, which can help gliomas suppress, regulate, or even escape from the immune response. We found that the GSVA scores for the collection of PRGs are associated with a variety of immune cells in LGG. Among the 3 types associated with pyroptosis, the type with a worse prognosis is often identified with higher infiltration of immune cells by the TIMER algorithm. Immune checkpoints have recently been increasingly recognized as an important interfering target for cancer immunotherapy because they are thought to promote the immunosuppressive function of TME. For example, CTLA4 can inhibit T cell activation and promote its exhaustion, while enhancing regulatory T cell-induced immunosuppression by downregulating CD80 and CD86 on antigen-presenting cells. In our study, the expressions of 8 immune checkpoint molecules including CTLA4 are all highest in Group3. Combined with its worst prognosis and lowest temozolomide sensitivity, these reasons suggest that PRGs may alter TME by affecting immune infiltration of LGG, ultimately distinguishing different resistance and survival of the LGG patients.

Functional enrichment analysis of 18 PRGs with prognostic value in LGG showed that they mainly involved infection and inflammation. In addition to the involvement of immune function, inflammation has been suggested to induce tumor progression and angiogenesis, which is also the target of antivascular agents for gliomas. Marinari's study also demonstrated that inflammation is associated with a worse prognosis in gliomas. These results demonstrate that these 32 PRGs may play a role in the progression and prognosis of LGG.

We screen 10 PRGs with prognostic value by the LASSO regression to construct a prognostic model of LGG. The prognostic models have a satisfying predictive effect on the 1-, 3-, and 5-year survival rates of patients with LGG. The difference in median survival time between the high-risk and low-risk groups according to the risk score based on 10 PRGs is approximately 6 years. In addition to this, the great value of the combined diagnosis to LGG based on 10 PRGs

indicates their potential to distinguish glioma from normal. Interestingly, we also found a significant association of 6 immune cells with a risk score based on the PRGs. However, high scores always imply an upregulation of immune cell abundance, which further demonstrates that pyroptosis affects the prognosis of LGG through immune infiltration.

MSI, as a molecular signature in cancers with deficient DNA mismatch repair, is the marker for the diagnosis and effective immune checkpoint blocking therapy in a variety of cancers. TMB has recently been shown to predict immunotherapeutic responses in a variety of tumors, also correlates with immune infiltration and cancer prognosis. High TMB frequently predicts a better prognosis after immunotherapy. Our study found multiple PRGs associated with MSI or TMB in LGG. These genes have the potential to predict the immunotherapeutic response of LGG. Subsequently, we screened PLCG1, CASP5, and CASP9 as independent prognostic factors of LGG by the Cox regression, which constituted a nomogram with glioma grade. Calibration plots show that nomograms can predict survival at 3 years and 5 years relatively well compared to ideal models.

Since CASP5 is found to be the only pyroptosis-related gene among the individual independent prognostic factors of LGG that could distinguish grade II, III, and IV gliomas, we chose CASP5 for subsequent analysis. CASP5 is an inflammatory protease involved in inflammatory and cell death processes, which involves a cascade of enzymatic reactions mediated by multiple members of the CASP family. CASP5 has a role in a variety of diseases such as arthritis, psoriasis, and cancer. We also find that CASP5 had high expression similar to LGG in ESCA, HNSC, and UCEC in our study. However, the mutation frequency of CASP5 is low, which indicates that the role of CASP5 in LGG is less associated with mutations. This is the same conclusion as the previous study. We perform the GSEA enrichment analysis on the highly expressed cohort, while the GO and KEGG enrichment analysis on the related genes. The results show multiple functions regarding immunity and inflammation such as complement, neutrophil activation, MHC class II protein complex, MHC protein complex binding, and *Staphylococcus aureus* infection. These imply the correlation of CASP5-involved pyroptosis with a variety of biological processes. In addition to differential expression in different pathological types, CASP5 is also significantly highly expressed in PD, which also confirms the abovementioned result that the LGG patients with high CASP5expression are accompanied by poor prognosis. The LGG patients with IDH mutation are generally considered to have both ATRX and TP53 mutations. IDH mutation and 1p/9q codeletion both are important factors in the poor prognosis of glioma. The significantly low expression of CASP5 in patients with IDH mutations and 1p/9q codeletion in our study indicates the relationship of CASP5 with multiple factors affecting the prognosis of LGG.

The ceRNA regulatory network is involved in the progression of a variety of cancers. In order to further explore the regulatory process of CASP5, we construct a CASP5-related ceRNA triple network in LGG. We finally find three miRNAs and one lncRNA regulating CASP5, hsa-miR-15b-

5p, hsa-miR-424-5p, hsa-miR-16-5p, and MCM3AP-AS1, by prediction and screening processes including survival analysis, correlation analysis, and subcellular localization. hsa-miR-15b-5p is demonstrated to predict the LGG outcome and participate in the pathogenesis of intracerebral hemorrhage. In addition to the association of hsa-miR-424-5p with thyroid cancer, esophageal cancer, and cholangiocarcinoma, it can also be enriched in extracellular vesicles in patients with Alzheimer's disease and has diagnostic value. As for hsa-miR-16-5p, it involves research on cancer, immune disorders, and even psychosis. MCM3AP-AS1 has been shown to be involved in glioma progression and regulates angiogenesis in glioblastoma through the ceRNA axis. Our analysis revealed that it also has prognostic and regulatory value in LGG.

The immune infiltration of cancer can affect the prognosis of patients. We confirm a significant positive correlation between CASP5 expression in LGG and the abundance of all six immune cells. This is also consistent with the results of the abovementioned enrichment analysis focusing PRGs and functional analysis of CASP5-related genes. We find differential expression of CASP5 in the LGG subtypes identified by us. Combined with the prognostic difference of LGG subtypes and the prognostic impact of CASP5 on LGG, we speculate that CASP5 may be the role of immune infiltration affected by CASP5 on LGG subtypes, which needs further experimental confirmation. We subsequently also revealed the dramatic impact of the infiltration of six immune cells on the prognosis of LGG. In addition, we also demonstrate that CASP5 has different degrees of correlation with 16 immune marker gene sets and many immune checkpoints. These all imply the great potential of CASP5 in the immunotherapy of LGG. Although there is no experimental evidence, immunosuppression against CASP5 is theoretically feasible, which is similar to the current use of different immune checkpoint inhibitors in different cancers.

The DNA mismatch repair system maintains genetic stability and integrity, and we found that the LGG patients with high CASP5 expression had elevated expression of two DNA repair genes, PMS2 and EPCAM. DNA methylation plays an important role in gene regulation. We attempt to analyze the pattern of CASP5 abnormal expression in LGG by exploring DNA methylation and found CASP5 hypomethylation in LGG samples, which is consistent with the upregulation of CASP5 observed by analysis to DNA methyltransferases (DNMT1H and DNMT3A). In addition, we found that some methylation sites had significant associations with the prognosis of the HCC patients, especially cg10825847, which is validated in both databases. Its methylation is associated with a better prognosis in patients with LGG. Interestingly, all the hypermethylated sites of CASP5 fall into the open sea region. These suggest that abnormalities in methylation may be associated with the prognosis of LGG.

5. Conclusion

Although our study demonstrates the great potential application value of prognosis in LGG, there are still some limitations, especially the lack of experimental validation. In the future, we can experimentally analyze the mechanism of PRGs' impact to immune microenvironment in LGG. It is also necessary to explore the possibility of alleviating or even reversing the deterioration of the immune microenvironment in LGG by targeting PRGs, ultimately inhibiting the progression of LGG. Our study can serve as the first step in this encouraging process.

In summary, using public TCGA-LGG data, we construct pyroptosis-related subtypes, which may affect prognosis through differences in immune infiltration. We also construct a prognostic model for PRGs, which also showed a huge relationship with immunity. Subsequently, we focus on analyzing the function of pyroptosis-related CASP5 in LGG. We construct a potential ceRNA network of CASP5 and revealed the great impact of CASP5 on the immune microenvironment of LGG. All these imply an important role of pyroptosis in LGG, which deserves further experimental investigation.

Data Availability

Publicly available datasets are analyzed in this study. The datasets analyzed during the current study are available in the following web links: GTEx, https://gtexportal.org/home/; GDSC, https://www.cancerrxgene.org; CGGA, http://www.cgga.org.cn/index.jsp; TIMER, https://cistrome.shinyapps.io/timer/; cBioportal, https://www.cbioportal.org/; ENCORI, https://starbase.sysu.edu.cn/; miRWalk, http://mirwalk.umm.uni-heidelberg.de/; LncBase Predicted v2, https://carolina.imis.athena-innovation.gr/diana_tools/web/index.php?r=lncbasev2/index-predicted; DiseaseMeth 2.0, http://bio-bigdata.hrbmu.edu.cn/diseasemeth/; MEXPRESS, https://mexpress.be/; MethSurv, https://biit.cs.ut.ee/methsurv/.

Ethical Approval

Not applicable.

Disclosure

The institutions that provided funding did not participate in the data analysis, article writing, and submission decision of this paper.

Conflicts of Interest

The authors declare that they have no conflicts of interest.

Authors' Contributions

JH designed the study plan and is the main writer of the manuscript. YJ participated in the design of the study and is the main modifier of the manuscript. PS provided financial support and critically revised the manuscript.

Acknowledgments

References

[1] J. S. Young, A. J. Gogos, R. A. Morshed, S. L. Hervey-Jumper, and M. S. Berger, "Molecular characteristics of diffuse lower grade gliomas: what neurosurgeons need to know," *Acta Neurochirurgica*, vol. 162, no. 8, pp. 1929–1939, 2020.

[2] D. N. Louis, A. Perry, G. Reifenberger et al., "The 2016 World Health Organization classification of tumors of the central nervous system: a summary," *Acta Neuropathologica*, vol. 131, no. 6, pp. 803–820, 2016.

[3] P. H. Wessels, W. E. Weber, G. Raven, F. C. Ramaekers, A. H. Hopman, and A. Twijnstra, "Supratentorial grade II astrocytoma: biological features and clinical course," *The Lancet Neurology*, vol. 2, no. 7, pp. 395–403, 2003.

[4] H. Duffau and L. Taillandier, "New concepts in the management of diffuse low-grade glioma: proposal of a multistage and individualized therapeutic approach," *Neuro-Oncology*, vol. 17, no. 3, pp. 332–342, 2015.

[5] M. J. McGirt, K. L. Chaichana, F. J. Attenello et al., "Extent of surgical resection is independently associated with survival in patients with hemispheric infiltrating low-grade gliomas," *Neurosurgery*, vol. 63, no. 4, pp. 700–708, 2008.

[6] J. C. Reijneveld, M. J. B. Taphoorn, C. Coens et al., "Health-related quality of life in patients with high-risk low-grade glioma (EORTC 22033-26033): a randomised, open-label, phase 3 intergroup study," *The Lancet Oncology*, vol. 17, no. 11, pp. 1533–1542, 2016.

[7] N. Sanai, S. Chang, and M. S. Berger, "Low-grade gliomas in adults: a review," *Journal of Neurosurgery*, vol. 115, no. 5, pp. 948–965, 2011.

[8] M. J. Van den Bent, "Interobserver variation of the histopathological diagnosis in clinical trials on glioma: a clinician's perspective," *Acta Neuropathologica*, vol. 120, no. 3, pp. 297–304, 2010.

[9] S. L. Fink and B. T. Cookson, "Caspase-1-dependent pore formation during pyroptosis leads to osmotic lysis of infected host macrophages," *Cellular Microbiology*, vol. 8, no. 11, pp. 1812–1825, 2006.

[10] J. Shi, W. Gao, and F. Shao, "Pyroptosis: gasdermin-mediated programmed necrotic cell death," *Trends in Biochemical Sciences*, vol. 42, no. 4, pp. 245–254, 2017.

Retraction

Retracted: Knowledge Discovery-Based Analysis of Health Factors of Urinary Infections in Elderly Cardiology Inpatients

Journal of Healthcare Engineering

This article has been retracted by Hindawi following an investigation undertaken by the publisher [1]. This investigation has uncovered evidence of one or more of the following indicators of systematic manipulation of the publication process:

(1) Discrepancies in scope

(2) Discrepancies in the description of the research reported

(3) Discrepancies between the availability of data and the research described

(4) Inappropriate citations

(5) Incoherent, meaningless and/or irrelevant content included in the article

(6) Peer-review manipulation

The presence of these indicators undermines our confidence in the integrity of the article's content and we cannot, therefore, vouch for its reliability. Please note that this notice is intended solely to alert readers that the content of this article is unreliable. We have not investigated whether authors were aware of or involved in the systematic manipulation of the publication process.

In addition, our investigation has also shown that one or more of the following human-subject reporting requirements has not been met in this article: ethical approval by an Institutional Review Board (IRB) committee or equivalent, patient/participant consent to participate, and/or agreement to publish patient/participant details (where relevant).

Wiley and Hindawi regrets that the usual quality checks did not identify these issues before publication and have since put additional measures in place to safeguard research integrity.

We wish to credit our own Research Integrity and Research Publishing teams and anonymous and named external researchers and research integrity experts for contributing to this investigation.

The corresponding author, as the representative of all authors, has been given the opportunity to register their agreement or disagreement to this retraction. We have kept a record of any response received.

References

[1] M. Zhao, Y. Pi, and L. Zhang, "Knowledge Discovery-Based Analysis of Health Factors of Urinary Infections in Elderly Cardiology Inpatients," *Journal of Healthcare Engineering*, vol. 2022, Article ID 7037037, 8 pages, 2022.

Research Article

Knowledge Discovery-Based Analysis of Health Factors of Urinary Infections in Elderly Cardiology Inpatients

Min Zhao,[1] **Yan Pi,**[2] **and Longbo Zhang** ®[3]

[1]*Department of Cardiovascular Medicine, Chongqing Seventh People's Hospital, Chongqing 401320, China*
[2]*Department of Endocrinology and Nephrology, Chongqing Seventh People's Hospital, Chongqing 401320, China*
[3]*Urology Surgery, People's Hospital Affiliated to Chongqing Three Gorges Medical College, Wanzhou, Chongqing 404000, China*

Correspondence should be addressed to Longbo Zhang; 201904020233@stu.zjsru.edu.cn

A set of semantic similarity calculation methods combining full-text text and domain knowledge topics is proposed for the current study of entity association relations such as disease–gene in medical texts combined with topics in knowledge discovery, which is insufficient to reveal the deep semantic association relations of medical domain knowledge at topic level. Taking urinary infections in elderly inpatients as the research subject, word embedding representation of word vectors and topic vectors is performed by the TWE model, and similarity calculation is performed by combining text and domain knowledge topics based on Siamese Network framework. The urinary microbiological culture results of both groups were dominated by *Escherichia coli*, accounting for 34.65% and 47.92%, respectively; the use of antimicrobial drugs in the symptomatic urinary infection group was 94.19% higher than that in the asymptomatic bacteriuria group, 77.27% (x^2 = 8.158, P = 0.004).

1. Introduction

Urinary tract infection (UTI) is an inflammatory response produced by the urinary epithelium after pathogens have invaded the urinary system, usually accompanied by bacteriuria and pyuria. The infection is classified according to the site of infection, and there are different sites of infection such as the kidney, the ureter, the bladder, and the urethra [1].

Depending on the presence or absence of clinical symptoms of infection, there are symptomatic urinary infections and asymptomatic urinary infections (also known as asymptomatic bacteriuria). Urinary infections are common infectious diseases, accounting for the second most common infections in the community and one of the most important hospital infections [2], and urinary tract infections account for about 20.8% to 31.7% of nosocomial infections in China [3]; urinary tract infections in the elderly account for the fourth most common hospital infections in the elderly [4]. Urinary tract infections leading to shock or even death are the 3rd most common among all patients who die from

infections [5]. The incidence of urinary infections in elderly patients is high, and studies have shown that urinary infections account for 25% of all elderly patients with infections [6], followed by atypical symptoms, diagnosis, and treatment in the clinic being difficult; acute urinary infections, if not treated in a timely manner, can easily delay the disease and transform into chronic urinary infections, and even cause substantial renal injury and renal failure. Positive urine microbiological culture is the main indicator for the diagnosis of urinary infections, but not all positive cultures require anti-infective treatment, and most patients with asymptomatic bacteriuria do not require anti-infective treatment. The correct distinction between symptomatic urinary infections and asymptomatic bacteriuria is the basis for the rational use of antibacterial drugs. Most past studies on urinary infections in elderly patients in China [7] focused on the factors related to the development of symptomatic urinary infections and the distribution of pathogenic bacteria, while the distribution of pathogenic bacteria between asymptomatic bacteriuria and symptomatic urinary infections was not categorized and analyzed, with the use of

antimicrobial drugs and the differential treatments between them being rare [8].

Cardiology inpatients are generally associated with cardiac insufficiency, reduced cardiac ejection, decreased organ function, and inadequate blood supply to tissues and organs, which, combined with long duration of illness, poor body immunity, and combined underlying diseases, make them highly susceptible to nosocomial infections [9]. At the same time, the immune function and defense mechanisms of elderly cardiology inpatients are decreasing with age, making them a high-risk group for nosocomial infections [10]. In the study, 102 (8.36%) of 1,220 elderly cardiology inpatients developed nosocomial infections, including 70.59% respiratory infections and 29.41% urinary tract infections, which is similar to some reported results [11]. Once infections occur in elderly cardiology patients, it not only increases their physical and mental suffering, but also causes unnecessary waste of medical resources [12]. Therefore, it is imperative to analyze the high-risk factors of nosocomial infections in elderly cardiology inpatients and explore effective intervention programs.

The article found that university and multivariate logistic regression analysis showed that cardiac function grade III-IV, use of ≥2 antimicrobial drugs, use of antimicrobial drugs for ≥2 weeks, length of stay for ≥2 weeks, invasive operations, and other cucurbit diseases were independent risk factors for nosocomial infections in elderly cardiology inpatients, with statistically significant differences ($P < 0.05$) [13]. The higher the cardiac function grade, the more severe the patient's condition; the presence of poor mobility, inadequate tissue blood supply, long hospital stay, and complex treatment protocols can trigger nosocomial infections. The use of many types of antimicrobial drugs for a long time can increase the resistance of drug-resistant strains and add drug-resistant strains, interfering with the balance of the normal flora and causing various pathogenic infections, resulting in nosocomial infections [14, 15].

The study of medical text similarity computation focuses on obtaining the similarity between sentences by computing word-level similarity, which is then used for knowledge discovery in the medical domain. Currently, there are three main types of medical text similarity computation methods, such as similarity computation based on Gene Ontology GO (Gene Ontology) [9], similarity computation based on topic level [16], and similarity computation based on MeSH word list [17], and other main methods. Among them, [18] demonstrated that a distributed representation based on unsupervised learning of sentences from a large biomedical corpus is not necessarily optimal for domain-specific semantic sentence-level similarity computation, and proposed a method for sentence semantic similarity computation incorporating biomedical ontology. To reduce the burden on clinical researchers and provide decision support, [19] developed an automated text mining method and tool (CHAT), which classifies sentences in the literature based on cancer markers and by calculating the similarity between them it can finally organize and classify cancer-related literature. [20] manually annotated PubMed literature abstracts using MeSH terms and calculated potential

associations between terms through co-occurrence relationships between terms and potential associations between MeSH. The method based on word lists and gene ontology in the above study poses some difficulties for the implementation of this method because of the need for pre-tagged corpus and lexical entries. In contrast, there are various methods to obtain literature topics with good extensibility and generalizability.

Therefore, in this study, a deep learning representation was used to explore the similarity computation at the topic level for cardiology inpatients. In order to better learn the information such as words and topics, the semantic information of medical literature at the topic level is learned by the Topic Word Embedding representation model [2] (Topic Word Embedding, TWE), and then the twin neural network model (Siamese Network) [3] in deep learning is used for similarity calculation; the similarity calculation results are used for knowledge discovery analysis based on clustering results.

2. Related Work

Deep learning word embedding representation method represents words as vectors with specific semantic information, and deeper semantic association information can be obtained by similarity calculation. Based on the deep learning medical literature similarity calculation, [13] proposed a new ontology vector representation method OPA2Vec, which combines the ontology and ontology annotation data in PubMed abstracts and obtains the vector representation of ontology by Word2Vec model training, which is finally used for the prediction of protein interaction relationships. [14] Based on the representation of the medical literature abstracts into semantic triads, adversarial networks were used to generate threshold criteria for distinguishing similar texts from more divergent texts, and the effectiveness of the method in information retrieval applications of literature in the clinical domain was demonstrated experimentally. [15] proposed a method for word similarity computation based on deep learning semantic representation using subwords and MeSH word lists, and achieved better results in both sentence similarity computation and biomedical relationship extraction tasks. The above deep learning semantic representation for similarity exploration in the medical domain basically uses only abstract-related information from the literature; however, the study of [1] showed that incomplete gene and disease association relationships included in the abstract may affect the accuracy of the results. Meanwhile, the study of [17] demonstrated that the extraction and automatic classification performance of side effect information of anticancer drugs in medical literature can be effectively improved using the results of drug side effect markers in full-text medical texts. In addition, few investigations have applied the deep learning models that can combine text and topics proposed by [19] and others to the medical field. [20] showed in their study that word embedding models trained in medical collections do not capture well the connections between some specific words, such as heart and related words mentioned in prescriptions,
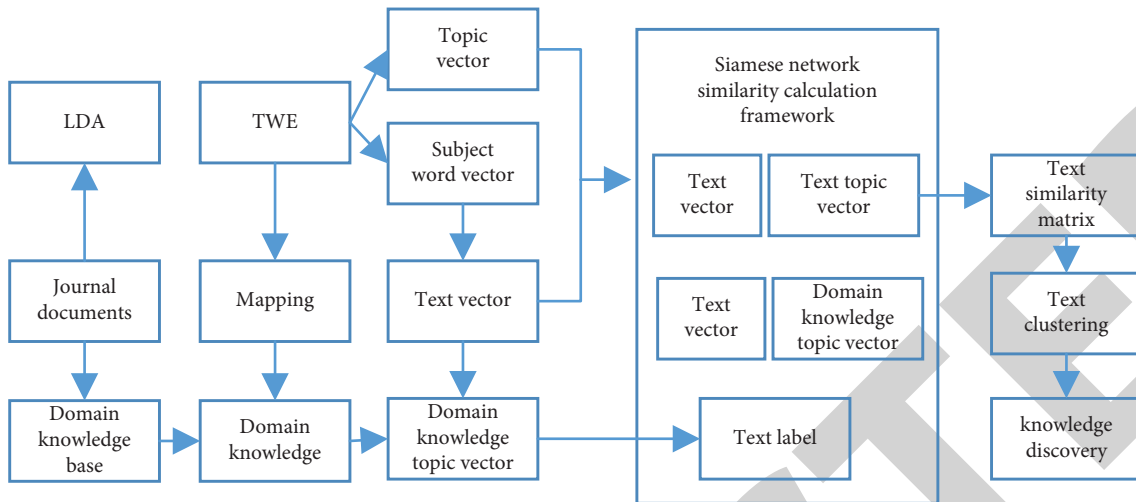
FIGURE 1: Research framework.

while adding knowledge information to word embeddings can be better applied to medical text representation computational tasks.

3. Model Construction

3.1. Siamese Network Model-Based Medical Full-Text Similarity Calculation. The Siamese Network model-based medical full-text similarity calculation is divided into the following three parts: (i) text annotation and extraction based on domain knowledge; (ii) similarity calculation based on the Bi LSTM Siamese Network; (iii) text clustering and target gene knowledge discovery. The specific research framework is shown in Figure 1.

3.2. Research Methodology and Steps

3.2.1. Domain Knowledge-Based Text Annotation and Extraction. In this study, the full text of the oncology literature was used for annotation, and the study of [4] showed that the annotation of domain knowledge such as genes and drugs in medical literature abstracts can effectively improve the prediction results of drug indications and side effects. We refer to the annotation system for medical literature in the work of [4], and combined with the actual situation of markup accessibility of the medical full text selected for analysis, a total of disease, gene, causative factor, and drug information was selected for markup. The need for tagging of words appearing in academic full-text texts was mainly based on the word lists in medical databases [7] or on the normative descriptions obtained in the relevant literature. Subsequently, information on diseases, genes, causative factors, and drugs in urinary infections in elderly hospitalized patients was manually labeled according to the labeling rules in the literature [8]. The annotation staff consisted of experts and graduate students in intelligence and medicine. To ensure the quality of the annotation results, manual verification was performed on a case-by-case basis for annotation inconsistencies on the basis of double

annotation. Thus, "Ki67," "expression," and "breast cancer" were annotated. The number of each medical entity labeled and the statistics of the number of genes labeled in the article are shown in Figures 2 and 3, respectively.

3.2.2. Similarity Calculation Based on the Bi LSTM Siamese Network

(1) TWE subject word embedding representation. First, the extraction of relevant topics in full-text journal texts is performed based on the LDA model, and the optimal number of topics is obtained by calculating the perplexity. The LDA model has been shown to be effective for extracting and analyzing topics in the medical field. Subsequently, we perform the word embedding representation of the word–topic pairs generated by the LDA model using the topic word embedding representation, TWE, model, which learns different word embedding representation results for each word under different topics. The specific framework is shown in Figure 4

The TWE model learns topic vector T_i and word vector W_i, respectively, using word–topic pairs $\langle W_i, T_i \rangle$ trained in LDA as input, treating each topic as a pseudoWord, and incorporating the topic into the basic word embedding representation by considering that the resulting topic word embeddings acquire different meanings of a word in different contexts. The optimization function of the learning objective of TWE is shown in equation (1):

$$L(D) = \frac{1}{M} \sum_{i=0}^{M} \sum_{-k,c,k,c \neq 0} \log \Pr(W_{i+c}|W_i) + \log \Pr(W_{i+c}|T_i).$$

(1)

In this study, we take the text results of the word–topic distribution generated from urinary infections in elderly inpatients as input and generate word embedding vectors and topic vectors under each tumor topic by training with the TWE model.
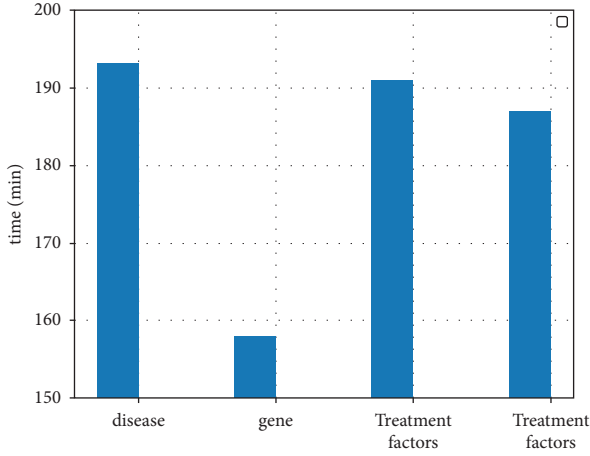
Figure 2: Number of medical entity markers.
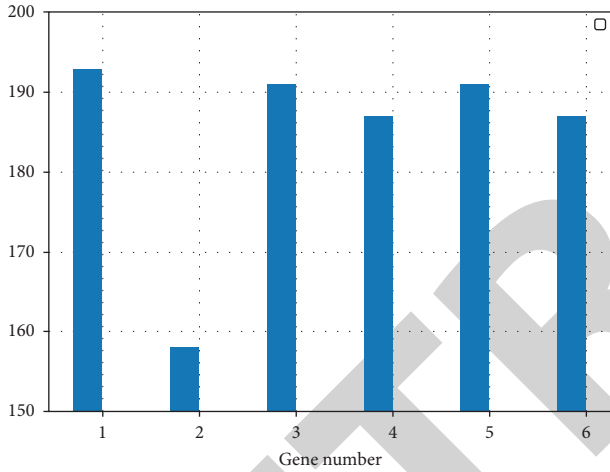
Figure 3: Statistical distribution of the number of genetic markers.

(2) Introduction of the Bi LSTM Siamese Network Model. The Siamese Network framework is a neural network framework for evaluating the similarity of two input samples, and the framework of the Siamese Network in this study is shown in Figure 5.

The Siamese Network has two sub-networks with the same structure and shared weights W, which receive two input texts D1 and D2 and the label y between D1 and D2 in this paper, respectively. This network can better achieve effective mining of syntactic or semantic association knowledge of two words. The LSTM is composed of four important elements: memory unit c_t, input gate i_t, output gate o_t, and forgetting gate f_t. The memory unit c_t determines the memory state based on the current input, the output gate o_t determines how much c_t should be exposed to the next node, and the input gate i_t controls the current input information w_t. The forgetting gate f_t determines whether the state information of the previous memory unit should be forgotten. The specific calculation is shown by equations (2) to (7).
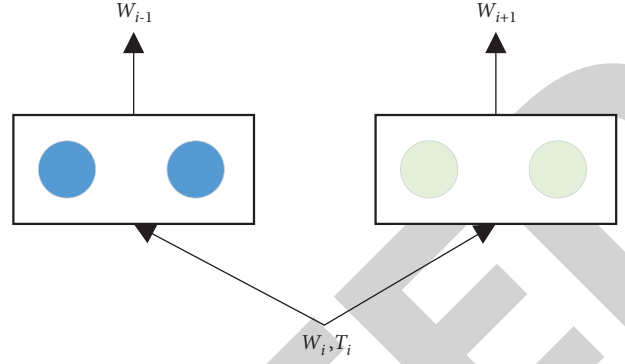
Figure 4: TWE model framework.

$$f_t = \sigma\left(U_f\left[h_{t-1}, w_t\right] + b_f\right), \tag{2}$$

$$i_t = \sigma\left(U_i\left[h_{t-1}, w_t\right] + b_i\right), \tag{3}$$

$$\bar{c}_t = \sigma\left(U_c\left[h_{t-1}, w_t\right] + b_c\right), \tag{4}$$

$$c_t = f_t * c_{t-1} + i_t * \bar{c}_t, \tag{5}$$

$$o_t = \sigma\left(U_o\left[h_{t-1}, w_t\right] + b_o\right), \tag{6}$$

$$h_t = o_t * \tanh\left(c_t\right), \tag{7}$$

where σ is the logistic regression function; U denotes the matrix multiplication operation; b is the function bias term; tanh is the activation function; and h_t denotes the state of the memory cell.

Firstly, the sentence vector is generated by Bi LSTM; then the text vector W is generated by one layer of Bi LSTM, and then the text vector W and the domain knowledge topic vector T or the text topic vector V are sequentially stitched together. A text may contain more than one domain knowledge, corresponding to more than one domain knowledge topic vector T_i, and the method of generating the domain knowledge topic vector T is shown in equation (8). The vector order stitching method is shown in equation (9). This study expects that a more accurate representation of medical text vectors can be obtained than using text vectors alone, and it can be used to improve the text semantic similarity calculation.

$$T = \frac{1}{m}\sum_1^m T_i, \tag{8}$$

$$G_w(D) = \{W, T\}, G_w(D) = \{W, V\}. \tag{9}$$

The Siamese Network framework input information is E_w and the labels y between the texts. This study calculates the distance between vectors $G_w(D_1)$ and $G_w(D_2)$ by the cosine similarity method E_w. The text labels y are calculated using the BMA [13] (Best Match Average) method. This method mainly uses the domain knowledge information obtained from the full text and the domain knowledge topic
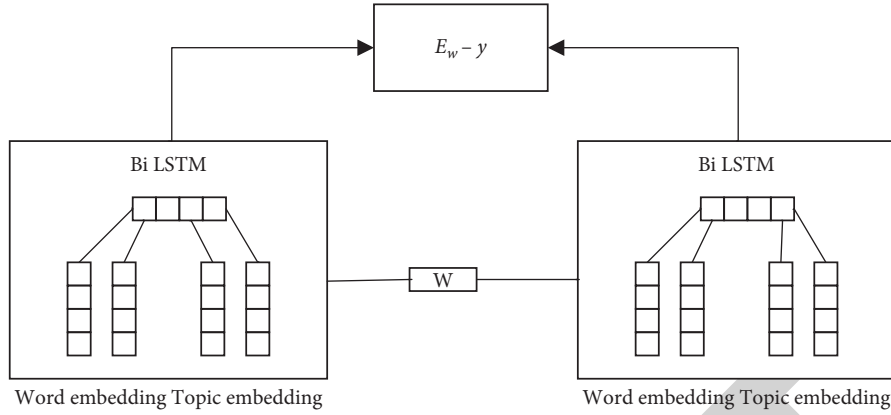
Figure 5: BiLSTM Siamese network framework.

vector obtained from the TWE model. The text labels are calculated as shown in Figure 6.

As shown in Figure 6, assuming that there are two texts, D_1 and D_2, the domain knowledge extracted by the mark in D_1 is $(A_1, A_2, A_3, \ldots, A_m)$ and the domain knowledge extracted by the mark in D_2 is $(B_1, B_2, B_3, \ldots, B_n)$.

$$y(D_1, D_2) = \frac{1}{2}\left(\frac{1}{m}\sum_{A_m \in D_1}\max_{B_n \in D_2}\cos\left(T_{A_m}, T_{B_n}\right) + \frac{1}{n}\sum_{B_n \in D_2}\max_{A_m \in D_1}\cos\left(T_{B_n}, T_{A_m}\right)\right). \tag{10}$$

To further improve the prediction performance of this study, the above annotation method is compared with the text topic-based annotation method, assuming that the text topics of the two articles are v_1 and v_2, and the text topic-based label y is calculated by $\cos(v_1, v_2)$. After selecting the best annotation method, the Siamese Network is used to learn the similarity measure between the two text vectors, which is validated by test set data and the similarity matrix between the texts is obtained for clustering analysis.

The loss function of the Siamese Network model is shown in equation (11):

$$L_w = \frac{1}{4}\left(1 - E_w^2\right)y + (1 - y)E_w^2. \tag{11}$$

4. Case Study

4.1. Source.
Patients with urinary infections who had no indwelling catheters were included. According to the "Diagnosis and Treatment of Urinary Infections Chinese Experts' Common Knowledge" (2015 Edition) [6], the diagnostic criteria for asymptomatic bacteriuria, also known as asymptomatic urinary infection, in which a certain amount of bacteria is isolated from the urine specimen without any signs or symptoms of urinary infection in the patient, are a urine culture bacterial colony count ≥105 CFU/ml for asymptomatic female patients; 1 strain of bacteria colony count ≥103 CFU/ml for clean urine specimens cultured from male patients. Patients with urinary infections

who did not meet the criteria for asymptomatic bacteriuria were included in the symptomatic urinary infection group.

4.2. Results.
There was no statistically significant difference between the two groups in terms of age and gender. See Table 1.

The two groups of patients were mainly distributed in geriatric-related departments, with 21 cases in geriatric neurology accounting for 24.42% and 8 cases accounting for 18.18%, and 13 cases in geriatric cardiovascular department accounting for 15.12% and 10 cases accounting for 22.73%, respectively. See Table 2.

The antibacterial drug use rate was 94.19% (81/86) in the symptomatic urinary infection group than 77.27% (34/44) in the asymptomatic bacteriuria group, with a statistically significant difference ($\chi 2 = 8.158$, $P = 0.004$); the duration of antibacterial drug use was 10.5 (6, 17.25) d more in the symptomatic urinary infection group than in the asymptomatic bacteriuria group (5 (1, 10) d), with a statistically significant difference ($Z = -3.889$, $P < 0.001$).

To further evaluate the diagnostic value of urinary leukocyte count in differentiating symptomatic urinary infection from asymptomatic bacteriuria, the ROC curves of urinary leukocytes in the two groups were plotted, and the area under the curve was 0.767 (95% CI: 0.666–0.869), and the cut-off value of urinary leukocytes was 231.90, with a sensitivity of 80.00% and specificity of 67.60%. The area under the curve of serum PCT in both groups was 0.739
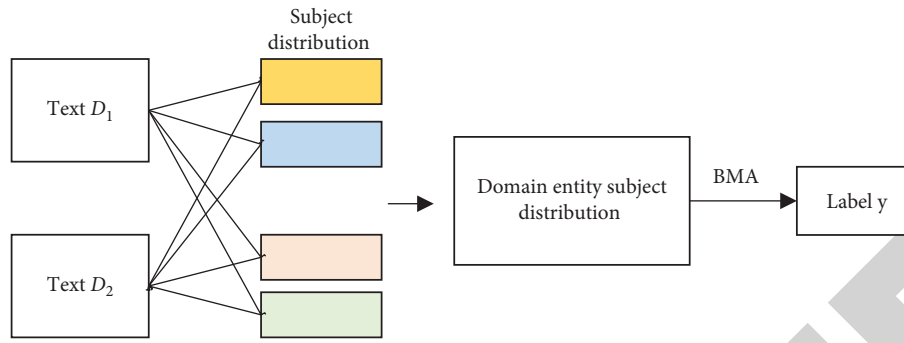
Figure 6: Text label calculation method.

Table 1: Clinical data of the two groups of patients.

Clinical data		Symptomatic urinary tract infection group ($n = 86$)	Asymptomatic bacteriuria group ($n = 44$)	Statistic	P value
0.136Gender (cases)	Male		49	19	2.22
	Female		37	25	
Age (years)		81.38 ± 10.75	80.16 ± 10.39	0.391	0.697

Table 2: Composition ratio of the distribution of infected departments in the two groups of patients.

Department	Symptomatic urinary tract infection group ($n = 6$)		Asymptomatic bacteriuria group ($n = 44$)	
	Number of cases	Composition ratio (%)	Number of cases	Composition ratio (%)
Geriatric neurology	21	24.42	8	18.18
Geriatric cardiovascular department	13	15.12	10	22.73
Geriatric nephrology	8	9.3	0	0
Geriatric respiratory department	7	8.14	3	6.82
Geriatric endocrinology department	5	5.81	0	0
Geriatric gastroenterology	0	0	4	9.09
Urology surgery	0	0	3	6.82
Other	32	37.21	16	36.36
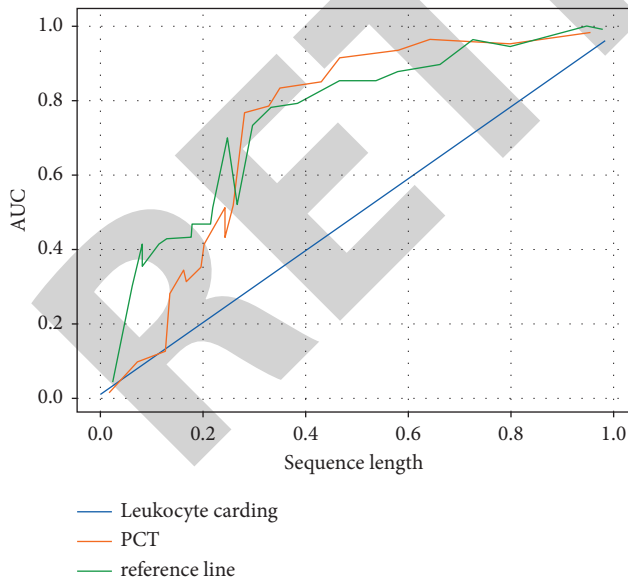
Figure 7: Urinary leukocytes and serum calcitoninogen ROC curves.

Figure 8: Analysis of different urinary tracts.

(95% CI: 0.548–0.930), and the cut-off value of serum PCT was 0.0405, with a sensitivity of 100.00% and specificity of 57.10%. The urinary leukocyte and serum calcitoninogen ROC curves are shown in Figure 7.

With age, the systemic and local immune function of the elderly gradually declines, and the mucosa of the urinary tract and the bladder and other organs become atrophied and thin, resulting in reduced defense functions and susceptibility to infection; especially, elderly inpatients often have one or more chronic underlying diseases such as hypertension, diabetes, tumors, etc., and are at high risk for
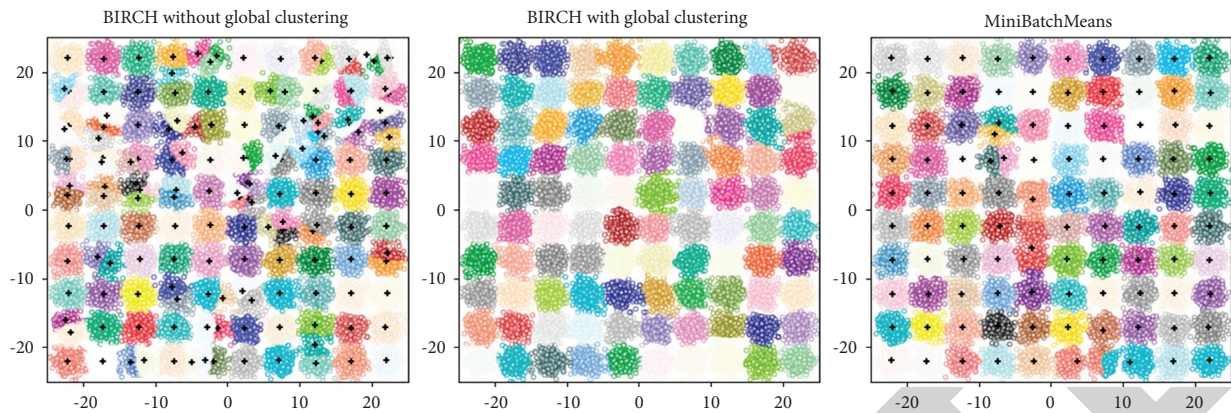
FIGURE 9: Different clustering effects.

urinary tract infections. Urinary tract infections are usually differentiated into symptomatic urinary infections and asymptomatic bacteriuria according to the presence or absence of urinary irritation symptoms such as urinary frequency, urinary urgency, and urinary pain; there are essential differences in their anti-infective treatment modalities, except for the differences in clinical manifestations. Studies have confirmed [8] that the probability of asymptomatic bacteriuria in elderly women hospitalized in long-term care facilities is as high as 25% to 50%, and the probability of asymptomatic bacteriuria in elderly men is as high as 15% to 40%, as shown in Figure 8 for the analysis of different urinary tracts.

Geriatric urinary infection patient units are mainly distributed in geriatric-related clinical departments, and patients are mostly hospitalized for a long time. The risk of urinary infection is much higher than that of geriatric patients in other non-geriatric departments, and clinical work should pay special attention to the risk of urinary infection in geriatric patients who are hospitalized for a long time. It is worth noting that elderly urological patients have a certain probability in asymptomatic bacteriuria, suggesting that surgical operations for urological diseases may increase the incidence of bacteriuria. The results of this study showed that the pathogenic bacteria were predominantly Gram-negative, with *Escherichia coli* predominating, which is consistent with the report [9] and similar to the distribution of pathogens in the whole population [10, 11]. In this study, after removing patients with the above indications for antimicrobial drug use, it was found that the rate of antimicrobial drug use in the asymptomatic bacteriuria group was as high as 77.27%, indicating that 77.27% of the use was unreasonable. The abuse of antimicrobial drugs not only cannot improve the chronic genitourinary symptoms of patients, but also increases the probability of double infection and increase adverse drug reactions, as shown in Figure 9 for different clustering effects.

5. Conclusions

In recent years, the incidence of cardiovascular diseases has increased as the number of elderly people in China has increased. The cardiology department is the main place to admit patients with cardiovascular diseases, which are characterized by long durations of illness, high age, low immune status, and many complications, and some patients need to perform invasive operations, which are very likely to induce nosocomial infections. The TWE model was used to represent word vectors and topic vectors in the study of urinary infections in elderly inpatients, and the similarity was calculated based on the Siamese Network framework combining text and domain knowledge topics.

Data Availability

The data underlying the results presented in the study are available within the manuscript.

Conflicts of Interest

There are no potential conflicts of interest.

Authors' Contributions

Min Zhao and Yan Pi made equal contributions to the manuscript. They worked together.

References

[1] W. H. W. Tang, F. Bäckhed, U. Landmesser, and S. L. Hazen, "Intestinal microbiota in cardiovascular health and disease," *Journal of the American College of Cardiology*, vol. 73, no. 16, pp. 2089–2105, 2019.

[2] E. Rinninella, M. Cintoni, P. Raoul et al., "Food components and dietary habits: keys for a healthy gut microbiota composition," *Nutrients*, vol. 11, no. 10, p. 2393, 2019.

[3] S. Zhu, Y. Jiang, K. Xu et al., "The progress of gut microbiome research related to brain disorders," *Journal of Neuroinflammation*, vol. 17, no. 1, pp. 25–20, 2020.

[4] H.-J. Sun, Z.-Y. Wu, X.-W. Nie, and J.-S. Bian, "Role of endothelial dysfunction in cardiovascular diseases: the link between inflammation and hydrogen sulfide," *Frontiers in Pharmacology*, vol. 10, p. 1568, 2020.

[5] P. Kasper, A. Martin, S. Lang et al., "NAFLD and cardiovascular diseases: a clinical review," *Clinical Research in Cardiology*, vol. 110, no. 7, pp. 921–937, 2021.

Research Article

Dendritic Cell Vaccine Loaded with MG-7 Antigen Induces Cytotoxic T Lymphocyte Responses against Gastric Cancer

Bohui Zhu [iD],[1] **Yiyuan Sun** [iD],[1] **Xiaoqing Wei** [iD],[1] **Huibin Zhou** [iD],[2] **Jingchen Cao** [iD],[2] **Chenwei Li** [iD],[2] **and Ning Wu** [iD][1]

[1]*Department of Oncology, Shanghai Pudong New Area Gongli Hospital, Shanghai 200127, China*
[2]*Shanghai Sunstem Biotechnology Co., Ltd., Pudong, Shanghai 200127, China*

Correspondence should be addressed to Chenwei Li; sunstem1@163.com and Ning Wu; wuningsd@163.com

Dendritic cells (DCs) are antigen-presenting cells that can activate T cells and initiate a primary immune response. Personalized DC vaccines have demonstrated a modest antitumor potential in some clinical pilot studies. However, those vaccines are difficult to manufacture and have a limited antitumor response. In this study, a lentiviral vector-programmed DC vaccine with high antitumor responses is developed. By transfecting with a lentiviral vector, the DC vaccine is loaded with MG-7 antigen (MG-7Ag). Three representative gastric cancer cell lines, such as KATO-3, MKN45, and SNU16, are used to estimate the in vitro cytotoxic effect of the MG-7Ag DC vaccine. Furthermore, we examine the in vivo antitumor efficacy of specific cytotoxic T lymphocytes (CTLs) induced by the MG-7Ag DC vaccine in patient-derived xenograft (PDX) mice models. The current data demonstrate that the MG-7Ag DC vaccine induced a potent CTL activity. Those CTLs have a significant cytotoxic effect on both KATO-3 and MKN45 with high level of MG-7 expression. In addition, MG-7Ag DC vaccine-mediated CTLs significantly inhibit the growth of tumor xenografts in nude mice. The MG-7Ag DC vaccine activate the cytotoxic effect of lymphocytes and can be employed as a vaccine in gastric cancer immunotherapy.

1. Introduction

As the fifth frequently diagnosed cancer, gastric cancer causes approximately 783000 deaths and more than 1000000 new cases in 2018, which is regarded as the third most common cause of cancer-related deaths throughout the world [1]. The incidence rate of gastric cancer is higher in Eastern Asia (Japan, China, and the Republic of Korea) than in other regions [2]. In China, about 679100 newly diagnosed cases and 498000 deaths from gastric cancer were estimated in 2015 [3], and this type of cancer is the second leading cause of cancer-related deaths in China [4]. Traditional treatment, including surgical resection, radiation therapy, and chemotherapy, has not increased the 5-year overall survival rate for gastric cancer patients [5]. Thus, it is imperative to develop new therapeutic alternatives. Immunotherapy is regarded as a promising strategy that complements the current cancer therapies. Some malignant tumors, such as nonsmall cell lung cancer and melanoma, appear to benefit from immunotherapy [6], and a cancer vaccine is a critical part of this therapy. Dendritic cells (DCs) activate T cells to become cytotoxic T lymphocytes (CTLs) and initiate a primary immune response [7]. The current DC vaccines constitute a tumor therapy strategy that activates the immune system, and promising results have been obtained [8–10], which are safe and effective [11].

The current substances for antigen loading in the DC vaccine comprise DNA, synthetic peptides, whole tumor RNA, and tumor cell lysates [12]. Among these, the antigen-loading strategy using whole tumor cells is commonly used; however, DCs loaded with such lysates have stimulated only limited responses in a wide range of clinical trials, and these DC vaccines are difficult to manufacture and industrialize. Some studies have demonstrated lentiviral vector-programmed DCs, and this new method has a high potency and can be automatized [13]. MG-7 antigen (MG-7Ag) is a specific

antigen of gastric cancer screened by the corresponding antibody, which is highly expressed in gastric cancer tissues but not in normal tissues [14]. MG-7Ag is a monoclonal antibody against gastric cancer prepared by immunizing mice with gastric cancer cell line MKN-46-9 as immunogen. MG-7Ag recognized by MG-7Ag is a newly discovered gastric cancer-related antigen. MG-7Ag is a neutral glycolipid. The epitope is located on the sugar chain. It is a glycoprotein antigen. It has the characteristics of secretory antigen, that is, it is synthesized in cells and then secreted outside cells. MG-7Ag can be roughly divided into four types in cells: cytoplasmic type, membrane type, extracellular type, and mixed type. The expression of MG-7Ag in gastric cancer has a relative tendency of histological type. The changes of morphology, biochemistry, and antigenicity of gastric mucosal epithelial cells in the process of carcinogenesis are related to gene damage and control imbalance [15]. Due to different genetic changes, the antigen expression order and tissue type of different types of gastric cancer are also different. Importantly, the prognosis for those with MG-7Ag-positive gastric cancer is worse than for those with MG-7Ag-negative gastric cancer.

2. Related Work

Gastric cancer is the fifth most commonly diagnosed cancer and the third most common cause of cancer-related deaths worldwide [16]. The incidence rates of gastric cancer are high in East Asian countries, such as Japan, China, and Korea. With nearly 500000 deaths annually, gastric cancer is the second leading cause of death in China.

Traditional surgery, radiotherapy, and chemotherapy cannot resolve the metastasis and recurrence of these tumors; therefore, new techniques are needed to break through the bottleneck of tumor therapy. Because it is safe and clinically effective, tumor autologous immune cell therapy is the best systemic therapy for tumor patients [17]. After development for more than 50 years, immune cell therapy has become the fourth most used method in tumor treatment after secondary surgery, radiotherapy, and chemotherapy. A cancer vaccine is a major part of immunotherapy. It is used to activate the immune system and induce a specific immune response against tumor cells. The DC vaccine is a cancer vaccine and a robust antigen-presenting cell because it can stimulate the proliferation of T cells. It is the initiator of the body's immune response and a natural "immune adjuvant" [18]. DC-based cancer vaccines aim to stimulate anticancer immunity by harnessing the capacity of DCs to activate specific T cells to become CTLs. In 2010, sipuleucel-T (Provenge) was approved by the United States Federal Drug Administration (FDA) to treat advanced prostate cancer. This was the first and only FDA-approved DC cancer vaccine [19, 20]. In recent years, some achievements have been made in the study of a gastric cancer DC vaccine [21–23].

MG-7Ag is a sensitive and specific antigen for gastric cancer screened by the corresponding antibody. The detection of gastric mucosal tissue by immunohistochemistry shows that MG-7Ag is highly expressed in superficial gastritis, atrophic gastritis, intestinal metaplasia, atypical hyperplasia, and gastric cancer [15], and the positive rate in

gastric cancer is 82.8% [24]. Han et al. [25] used phage display library technology to successfully screen the mimotope peptide of gastric cancer MG-7Ag. In vitro studies have confirmed that the mimotope peptide mimics the original antigen and induces immunity against gastric cancer; the oral DNA vaccine for gastric cancer MG-7Ag-mimic epitope was developed using attenuated *Salmonella typhimurium*, and the immune efficacy of the vaccine was observed after immunizing mice [26]. Tumor antigens are critical in the preparation of vaccines, but the presentation of antigens is also essential [27]. We used lentivirus as a delivery vehicle because this vector has many advantages. For example, the lentiviral vector can transfect cells that divide slowly and at the end of the division, such as DCs. In addition, it can transfer gene fragments for target gene expression, making it difficult to induce an immune response.

In this study, we developed a DC vaccine loaded with MG-7Ag by transfecting with lentiviral vector. At the cellular level, the DC vaccine was used to stimulate T cells to form CTLs, and the cytotoxic effects of CTLs were evaluated on three gastric cancer cell lines. The results showed that the MG-7Ag DC vaccine-mediated CTL had a satisfactory cytotoxic effect on both KATO-3 and MKN45 cells, in which MG-7 was highly expressed. The cell killing indicated that specific monoclonal antigen DC vaccine-mediated CTL had a better killing effect on high-expression cells. Similarly, the DC vaccine loaded with MG-7Ag at the animal level also exhibited a tumor-inhibiting effect. Compared to that in the control and NC groups, the cytotoxic effect of the MG-7Ag DC vaccine-mediated CTL was the best. The MG-7Ag DC vaccine-mediated CTLs significantly inhibited tumor growth. We determined the cytotoxic effect of the MG-7Ag DC vaccine on gastric cancer. Thus, the DC cell vaccine was injected intravenously into the subjects, and the clinical effect was determined by observing and detecting the size of solid tumors and the specific sensitive antigen content of gastric cancer in blood. Finally, we obtained an effective DC cell vaccine for gastric cancer treatment.

3. Proposed Methods

3.1. Cell Lines and Animals. KATO-3, MKN45, and SNU16 cell lines were purchased from Shanghai Enzyme Research Biotechnology Co., Ltd., China. KATO-3 cells were cultured in Dulbecco's modified Eagle's medium (DMEM, Life Technologies, San Diego, CA, USA) containing 20% fetal bovine serum (FBS, Life Technologies) and 1% penicillin-streptomycin (Sigma-Aldrich, St. Louis, MO, USA). MKN45 and SNU16 cells were cultured in RPMI 1640 medium (Life Technologies) containing 10% FBS and 1% penicillin-streptomycin. Male NOD/SCID mice, 8 weeks old, were purchased from Shanghai SLAC Laboratory Animal Co., Ltd. All animal studies were conducted at the Shanghai Laboratory Animal Center, Shanghai, China.

3.2. Real-Time Quantitative Polymerase Chain Reaction. The RNA extraction kit (TaKaRa, Beijing, China) was used to extract total cell RNA, and a reverse transcription kit

(TaKaRa) was used to reverse transcribe the total RNA into cDNA. The cDNA concentration was measured on a microplate reader. The forward and reverse primer sequences were as follows: 5′-CATACAAAAGGAGGAG GAAGTAAG-3′, 5′-CAGGTGGCTGTGGGGTTTA-3′. Glyceraldehyde 3-phosphate dehydrogenase served as an internal control.

3.3. Patient-Derived Xenograft Models.
NOD/SCID mice were anesthetized intraperitoneally with 50 mg/kg pentobarbital and placed in a stereotactic frame. Gastric cancer tumor tissue was removed from liquid nitrogen to thaw and sliced into 4 mm^3 pieces to subcutaneously inoculate into the mice. The mice were observed and weighed every 2 d.

3.4. Construction of MG-7Ag Lentiviral Vector.
A synthetic fragment of MG-7Ag and carrier shRNA were digested with AscI and XbaI (TaKaRa) and analyzed by agarose gel electrophoresis. The target gene fragments and shRNA (+) fragments were excised from the gel. The MG-7Ag fragment was ligated to the vector overnight using T4 DNA ligase at 16°C. The ligation product was transformed into *Escherichia coli* DH5, and positive clones were screened on ampicillin-resistance plates and validated by polymerase chain reaction (PCR) (5′-CGCAAATGGGCGGTAGGCGTG-3′, 5′-CAT-AGCGTAAAAGG AGCAACA-3′) and sequencing.

3.5. Lentiviral Packaging.
HEK-293FT cells were cultured in a Petri dish 10 cm in diameter. The serum-free medium was replaced 2 h before transfection. The DNA (containing expression plasmids pLVX-MG-7 and packaging plasmid pLP1, pLP2, and pLP/VSVG) was transfected into the cells using calcium phosphate [16]. The mixture was incubated under 5% CO_2 at 37°C for 6 h, after which the medium was replaced and incubation continued for 2-3 d. The supernatant was collected by cell centrifugation at 4000 ×g at 4°C for 10 min, filtered through a 0.45 m filter, and centrifuged again using a Beckman ultracentrifuge (Beckman Coulter, Brea, CA, USA) at 4°C and 25000 rpm for 2 h. The supernatant was discarded, and the pellet was resuspended in the virus preservation solution and centrifuged at 10000 rpm for 5 min, after which the physical status and sterility were assessed, and the viral titer of the lentivirus was calculated using the following formula: virus titer = number of fluorescent cells/amount of virus stock [17].

3.6. Preparation of DC Vaccines.
Peripheral blood mononuclear cells (PBMCs) were isolated from patients' peripheral blood using Ficoll-Hypaque (Solarbio, Beijing, China) and cultured in RPMI 1640 containing 5% autologous plasma, 10 ng/mL hGM-CSF (Miltenyi Biotec, Bergisch Gladbach, Germany), and 10 ng/mL hIL-4 (Miltenyi Biotec). The immature DCs were infected with lentivirus on day 5, and polybrene (transfection enhancer) was added. Fresh medium was replaced after 24 h of transfection, and poly I : C was added on day 6 to promote the expression of endogenous genes. The mature DCs were then collected on day 7.
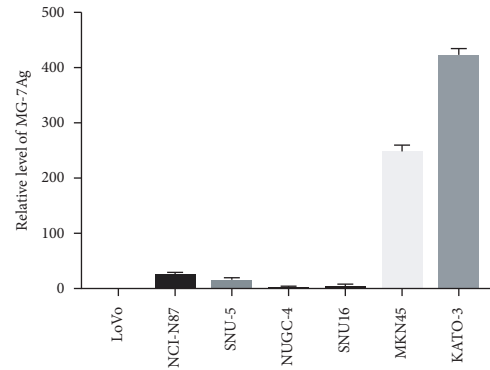
FIGURE 1: Relative level of MG-7Ag.

The maturation status of DCs was observed through a microscope (Leica Microsystems Inc., Wetzlar, Germany). The expression of CD80, CD83, CD86, and human leukocyte antigen (locus) DR (HLA-DR) in DCs were measured by flow cytometry (Beckman Coulter). To assess DC maturation, flow cytometry and enzyme-linked immunosorbent assay (ELISA) were used to detect secreted cytokines. MG-7Ag expression in DCs was detected by quantitative PCR (qPCR) and gel electrophoresis.

3.7. Study Design.
T cells were cocultured with DCs (at a responder-to-stimulator ratio of 10 : 1) in the presence of 0.2 ng/mL hIL-2 (Miltenyi Biotec) at 37°C for 48 h. Then, CTLs were harvested and used as effector cells to detect CTL cytotoxicity; gastric cancer cells KATO-3 and MKN45 were selected as target cells, and CCK-8 (Shanghai Yeasen Biological Technology Co., Ltd, Shanghai, China) assay was used to determine the inhibition of CTLs on two gastric cancer cell lines in vitro.

To further verify the cytotoxic effect of DC vaccine-mediated CTL, a PDX mouse model was established and divided into the following three groups: control, negative control (NC), and MG-7Ag ($n = 6$ mice/group). The mice in MG-7Ag and NC groups were infused with normal saline solution, and those in the control group were infused with simple normal saline with CTL through a tail vein once a day for 3 consecutive days. The diameters of the tumor were measured using Vernier calipers, the weight of mice was measured, and the changes in tumor growth and mouse weight were plotted. Besides, the changes in the tumor were observed for 22 d.

3.8. Statistical Analyses.
SPSS 16.0 (SPSS Inc., Chicago, USA) was used for biostatistical analyses, and the baseline description analysis was conducted. The Kaplan–Meier method was used to analyze survival, and the differences among the groups were compared using the log-rank test. $P < 0.05$ indicated statistical significance.

4. Results Analysis

4.1. Screened Cell Lines That Express MG-7Ag Target Antigen.
To reflect how the MG-7Ag DC vaccine inhibited cancer growth, we measured the content of MG-7Ag in the gastric
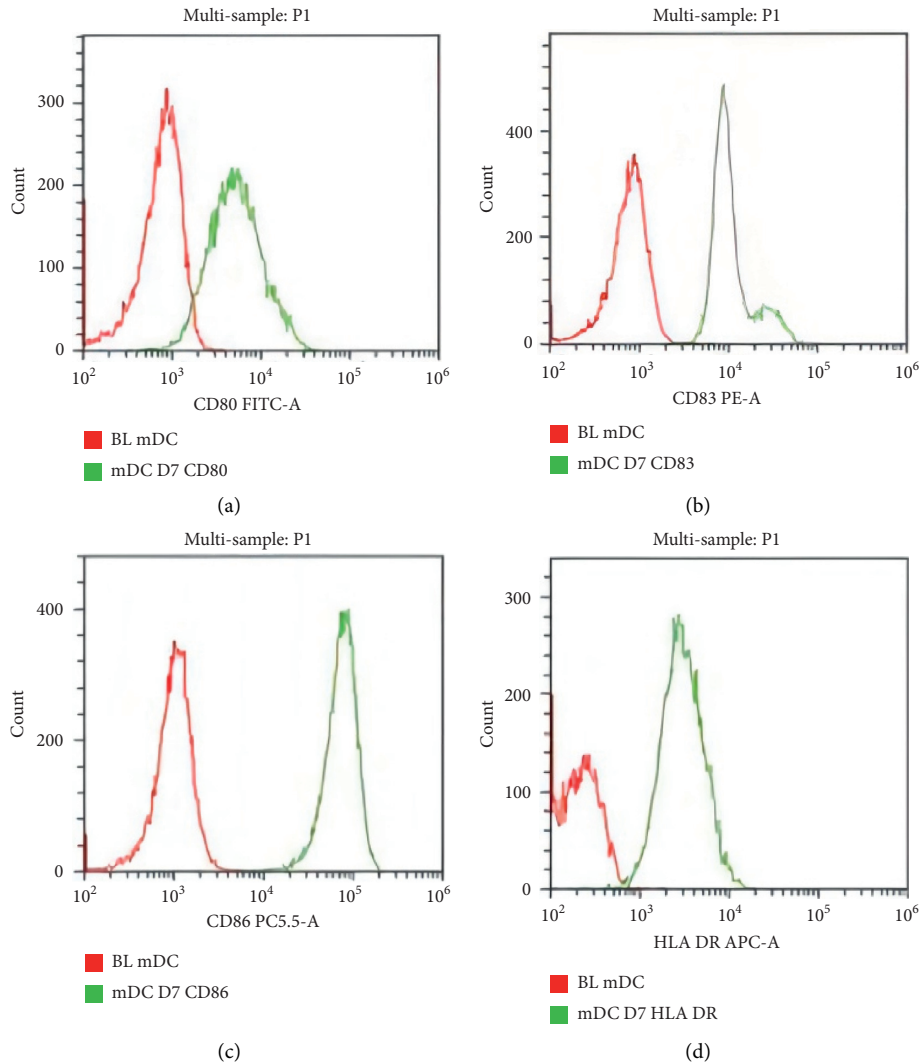
Figure 2: DCs express high levels of surface markers: (a) CD80 FITC-A; (b) CD83 PE-A; (c) CD86 PC5.5-A; (d) HLA-DR APC-A.

cancer cell lines and found that MKN45 and KATO-3 had high expressions of MG-7Ag, while cell lines NUGC-4, NCI-N87, SNU16, and SNU-5 had low expressions, as shown in Figure 1. Total RNA is isolated from LoVo, NUGC-4, NCI-N87, SNU16, SNU-5, MKN45, and KATO-3 cell lines, reverse transcribed to cDNA, and amplified by qPCR to evaluate MG-7Ag expression. The LoVo (intestinal cancer) cell line is used as a control.

4.2. DCs Express High Levels of Surface Markers. To cultivate high-quality DCs, we optimized the DC culture conditions. Mature DCs were characterized by high expression of MHC I, MHC II, CD80, CD83, CD86, and other costimulatory molecules, which process and present antigens for T cell recognition. Naive T cells could be activated only by mature DCs to convert them into CTLs that exert an antiinfective effect. Next, we estimate the surface markers CD80, CD83, CD86, and HLA-DR of DCs and found that after adopting our DC culture program, the expression levels of the DC

surface markers markedly improved, as shown in Figure 2. These results further indicated that the DCs cultivated in the present study could induce CTL responses and regulate immune responses. The mature DCs were collected, washed, and resuspended in PBS. The experimental group containing 10 L of HLA-DR, CD80, CD83, and CD86 flow cytometry antibodies and the blank control group were incubated in the dark at 4°C for 30 min for testing.

4.3. DC Vaccine Can Express MG-7Ag Target at High Levels. A lentiviral overexpression vector expressing MG-7Ag was constructed, as shown in Figure 3(a), and the virus was packaged. After the virus titer was measured, it was transfected into cultured DCs. At 48 h after transfection, total RNA was isolated from DCs, and MG-7Ag expression was evaluated by qPCR. Figure 3(b) shows that total RNA was isolated from the dendritic cell (DC) vaccine, reverse transcribed to cDNA, and amplified by quantitative polymerase chain reaction to evaluate MG-7Ag expression. The

(a) (b)
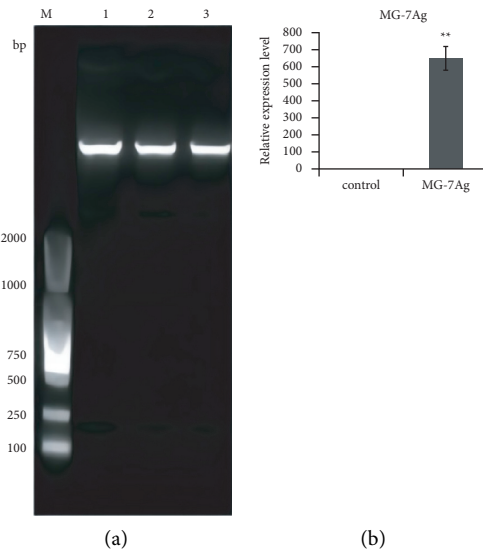
FIGURE 3: MG-7Ag DCs express high levels of MG-7Ag target: (a) restriction digestion and electrophoresis results of MG-7 antigen (MG-7Ag) overexpressing lentiviral expression vector; (b) MG-7Ag expression.
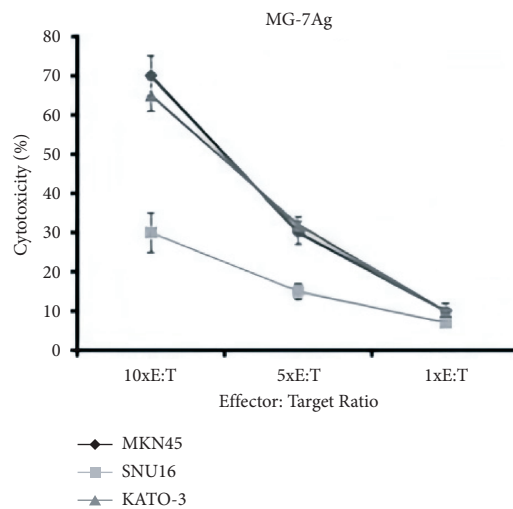
FIGURE 4: The inhibitory effect of the dendritic cell (DC) vaccine loaded with MG-7 on gastric cancer cells, KATO-3, MKN45, and SNU16.

results showed that the expression of MG-7Ag was significantly high in DCs but not in the control group, which indicated that our antigen was successfully expressed in DCs.

4.4. Effect of DC Vaccine In Vitro. DCs were pulsed with MG-7Ag and CD3+ T cells were coincubated with MG-7Ag-loaded DCs or unloaded DCs to induce CTL cells. The CTL cells and the target cells KATO-3 and MKN45 were then mixed at a ratio of $10:1$, $5:1$, and $1:1$, respectively, after 16 h, and total CTL cytotoxicity was detected by CCK-8 assay. The results showed that CTLs sensitized by the MG-7Ag DC vaccine had extraordinary cytotoxic effects on both KATO-3 and MKN45 cells. The experimental results at the cellular level showed that the DC vaccine expressing MG-7 had a marked inhibitory effect on the cell line expressing MG-7, as shown in Figure 4.

In lactate dehydrogenase-based cytotoxicity assays, CD3+ T cells stimulated with MG-7 antigen (MG-7Ag)-loaded DCs or unloaded DCs (NC group) were tested against KATO-3, MKN45, and SNU16 cells at various effector-target ratios. Data are expressed as the percentage of specific lysis ±standard deviation (SD) ($n = 3$).

4.5. Effect of DC Vaccine In Vivo. To further verify the cytotoxic effect of CTLs sensitized by the DC vaccine, we conducted animal experiments. The MG-7Ag-pulsed DC vaccine or unpulsed DC vaccine was cocultured to induce CTLs. After the mouse PDX model was constructed, the mice in each group were administered CTL saline solution (MG-7Ag-loaded DC vaccine and NC groups) and saline solution (control group) once a day through the tail vein for 3 consecutive days. The mouse tumor volume and mouse
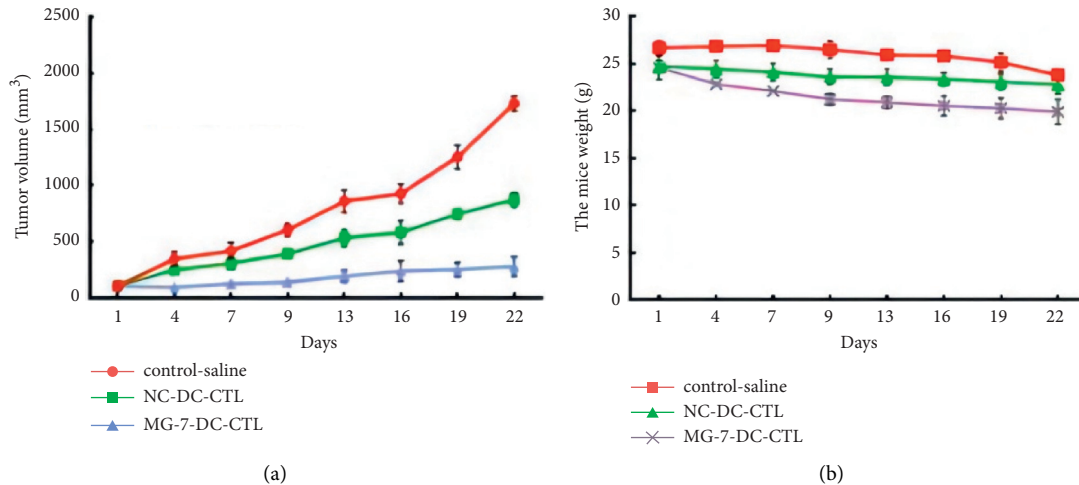
Figure 5: Changes in the PDX model of gastric cancer on day 22: (a) tumor volume; (b) mouse bodyweight.

bodyweight were then measured every 2 d for 22 d. On day 22, the mouse weight and tumor volume were measured to observe the antitumor effect of CTLs. Compared to the control and NC groups, the DC vaccine loaded with MG-7Ag significantly inhibited the growth of tumors, albeit the weight of the mice was not markedly altered, as shown in Figure 5.

5. Conclusions

In this study, we develop a lentiviral vector-programmed DC vaccine with high antitumor responses. By transfecting with a lentiviral vector, the DC vaccine is loaded with MG-7 antigen (MG-7Ag). Three representative gastric cancer cell lines, such as KATO-3, MKN45, and SNU16, are used to estimate the in vitro cytotoxic effect of the MG-7Ag DC vaccine. Furthermore, we examine the in vivo antitumor efficacy of specific cytotoxic T lymphocytes (CTLs) induced by the MG-7Ag DC vaccine in patient-derived xenograft (PDX) mice models. The current data demonstrate that the MG-7Ag DC vaccine induced a potent CTL activity. From the experimental results, it can be observed that those CTLs have a significant cytotoxic effect on both KATO-3 and MKN45 with high level of the MG-7 expression. Also, the MG-7Ag DC vaccine-mediated CTLs significantly inhibit the growth of tumor xenografts in nude mice. We suggest that the MG-7Ag DC vaccine can activate the cytotoxic effect of lymphocytes and can be employed as a vaccine in gastric cancer immunotherapy.

Data Availability

The data used to support the findings of this study are available from the corresponding author upon request.

Disclosure

Funding agencies have no role in research design or manuscript writing.

Conflicts of Interest

The authors declare that there are no conflicts of interest.

Authors' Contributions

Bohui Zhu, Yiyuan Sun, and Xiaoqing Wei designed the experiments and research project. Huibin zhou and Jingchen Cao performed the experiments and analyzed the data. Ning Wu and Chenwei Li participated in the discussion.

Acknowledgments

References

[1] F. Bray, J. Ferlay, I. Soerjomataram, R. L. Siegel, L. A. Torre, and A. Jemal, "Global cancer statistics 2018: GLOBOCAN estimates of incidence and mortality worldwide for 36 cancers in 185 countries," *CA: A Cancer Journal for Clinicians*, vol. 68, no. 6, pp. 394–424, 2018.

[2] E. C. Smyth, M. Nilsson, H. I. Grabsch, N. C. van Grieken, and F. Lordick, "Gastric cancer," *The Lancet*, vol. 396, no. 10251, pp. 635–648, 2020.

[3] M. Venerito, A. Link, T. Rokkas, and P. Malfertheiner, "Review: gastric cancer-Clinical aspects," *Helicobacter*, vol. 24, no. 1, pp. 12643–12655, 2019.

[4] W. Chen, R. Zheng, P. D. Baade et al., "Cancer statistics in China, 2015," *CA: A Cancer Journal for Clinicians*, vol. 66, no. 2, pp. 115–132, 2016.

[5] L. Zong, M. Abe, Y. Seto, and J. Ji, "The challenge of screening for early gastric cancer in China," *The Lancet*, vol. 388, no. 10060, pp. 2606–2610, 2016.

[6] Q. Zhao, L. Cao, L. Guan et al., "Immunotherapy for gastric cancer: dilemmas and prospect," *Briefings in Functional Genomics*, vol. 18, no. 2, pp. 107–112, 2019.

[7] M. Collin and V. Bigley, "Human dendritic cell subsets: an update," *Immunology*, vol. 154, no. 1, pp. 3–20, 2018.

[8] G. A. Pizzurro and M. M. Barrio, "Dendritic cell-based vaccine efficacy: aiming for hot spots," *Frontiers in Immunology*, vol. 6, pp. 91–100, 2019.

[9] W. Kastenmüller, K. Kastenmüller, C. Kurts, and R. A. Seder, "Dendritic cell-targeted vaccines - hope or hype?" *Nature Reviews Immunology*, vol. 14, no. 10, pp. 705–711, 2014.

[10] T. Katz, I Avivi, N Benyamini, J. Rosenblatt, and D. Avigan, "Dendritic cell cancer vaccines: from the bench to the bedside," *Rambam Maimonides medical journal*, vol. 5, no. 4, pp. e0024–31, 2014.

[11] S. Anguille, E. L Smits, E Lion, V. F van Tendeloo, and Z. N. Berneman, "Clinical use of dendritic cells for cancer therapy," *The Lancet Oncology*, vol. 15, no. 7, pp. e257–67, 2014.

[12] F. Q. Wei, W. Sun, T. S. Wong et al., "Eliciting cytotoxic T lymphocytes against human laryngeal cancer-derived antigens: evaluation of dendritic cells pulsed with a heat-treated tumor lysate and other antigen-loading strategies for dendritic-cell-based vaccination," *Journal of Experimental & Clinical Cancer Research: Climate Research*, vol. 35, no. 3, pp. 18–25, 2016.

[13] B. S. Sundarasetty, L. Chan, D. Darling et al., "Lentivirus-induced 'Smart' dendritic cells: pharmacodynamics and GMP-compliant production for immunotherapy against TRP2-positive melanoma," *Gene Therapy*, vol. 22, no. 9, pp. 707–720, 2015.

[14] X. Zhang, L. Hong, W. Y. Chan et al., "Expression of MG7-Ag in patients with gastric cancer correlates with weaker T cell immune response and more proinflammatory cytokine secretion," *Biochemistry and Cell Biology*, vol. 84, no. 2, pp. 135–141, 2006.

[15] Z. Chen, L. Hong, L. Liu et al., "Monoclonal antibody MG7 as a screening tool for gastric cancer," *Hybridoma*, vol. 29, no. 1, pp. 27–30, 2010.

[16] M. Kwon and B. L. Firestein, "DNA transfection: calcium phosphate method," *Methods in Molecular Biology*, vol. 1018, pp. 107–110, 2013.

[17] G. Tiscornia, O. Singer, and I. M. Verma, "Production and purification of lentiviral vectors," *Nature Protocols*, vol. 1, no. 1, pp. 241–245, 2006.

[18] R. M. Steinman and J. Banchereau, "Taking dendritic cells into medicine," *Nature*, vol. 449, no. 7161, pp. 419–426, 2007.

[19] P. W. Kantoff, C. S. Higano, N. D. Shore et al., "Sipuleucel-T immunotherapy for castration-resistant prostate cancer," *New England Journal of Medicine*, vol. 363, no. 5, pp. 411–422, 2000.

[20] A. Matsiko, "Cancer immunotherapy making headway," *Nature Materials*, vol. 17, no. 6, 472 pages, 2018.

[21] C. Kohnepoushi, V. Nejati, N. Delirezh, and P. Biparva, "Poly lactic-co-glycolic acid nanoparticles containing human gastric tumor lysates as antigen delivery vehicles for dendritic cell-based antitumor immunotherapy," *Immunological Investigations*, vol. 48, no. 8, pp. 794–808, 2019.

[22] W. Zhang, X. Lu, P. Cui et al., "Phase I/II clinical trial of a Wilms' tumor 1-targeted dendritic cell vaccination-based immunotherapy in patients with advanced cancer," *Cancer Immunology, Immunotherapy*, vol. 68, no. 1, pp. 121–130, 2019.

[23] M. Kobayashi, T. Sakabe, A. Chiba et al., "Therapeutic effect of intratumoral injections of dendritic cells for locally recurrent gastric cancer: a case report," *World Journal of Surgical Oncology*, vol. 12, no. 1, pp. 390–396, 2014.

[24] J. Ren, Z. Chen, S. J. Zhou, X. Y. Zhang, B. R. Pan, and D. M. Fan, "Detection of circulating gastric carcinoma-associated antigen MG7-Ag in human sera using an established single determinant immuno-polymerase chain reaction technique," *Cancer*, vol. 88, no. 2, pp. 280–285, 2000.

[25] H. Y. Liu, L. P. Peng, Y. Ran, and L. Z. Zhang, "Screening and identification of human lung cancer-related antigens," *Acta Biochimica et Biophysica Sinica*, vol. 34, no. 2, pp. 171–175, 2002.

[26] F. P. Naliu, C. C. Jieding, and C. Y. Zhao, "Development of an oral DNA vaccine against MG7-Ag of gastric cancer using attenuated salmonella typhimurium as carrier," *World Journal of Gastroenterology*, vol. 9, no. 6, pp. 1191–1195, 2003.

[27] M. Gunzer and S. Grabbe, "Dendritic cells in cancer immunotherapy," *Critical Reviews in Immunology*, vol. 21, no. 1-3, pp. 133–45, 2001.

Retraction

Retracted: Study of Subfascial Endoscopic Perforator Surgery Combined with Endovenous Laser Treatment in the Treatment of Great Saphenous Varicose Veins

Journal of Healthcare Engineering

This article has been retracted by Hindawi following an investigation undertaken by the publisher [1]. This investigation has uncovered evidence of one or more of the following indicators of systematic manipulation of the publication process:

(1) Discrepancies in scope

(2) Discrepancies in the description of the research reported

(3) Discrepancies between the availability of data and the research described

(4) Inappropriate citations

(5) Incoherent, meaningless and/or irrelevant content included in the article

(6) Peer-review manipulation

The presence of these indicators undermines our confidence in the integrity of the article's content and we cannot, therefore, vouch for its reliability. Please note that this notice is intended solely to alert readers that the content of this article is unreliable. We have not investigated whether authors were aware of or involved in the systematic manipulation of the publication process.

In addition, our investigation has also shown that one or more of the following human-subject reporting requirements has not been met in this article: ethical approval by an Institutional Review Board (IRB) committee or equivalent, patient/participant consent to participate, and/or agreement to publish patient/participant details (where relevant).

Wiley and Hindawi regrets that the usual quality checks did not identify these issues before publication and have since put additional measures in place to safeguard research integrity.

We wish to credit our own Research Integrity and Research Publishing teams and anonymous and named external researchers and research integrity experts for contributing to this investigation.

The corresponding author, as the representative of all authors, has been given the opportunity to register their agreement or disagreement to this retraction. We have kept a record of any response received.

References

[1] L. Wang, J. Du, and H. Zhang, "Study of Subfascial Endoscopic Perforator Surgery Combined with Endovenous Laser Treatment in the Treatment of Great Saphenous Varicose Veins," *Journal of Healthcare Engineering*, vol. 2022, Article ID 1801099, 7 pages, 2022.

Research Article

Study of Subfascial Endoscopic Perforator Surgery Combined with Endovenous Laser Treatment in the Treatment of Great Saphenous Varicose Veins

Li Wang, Jianqing Du, and Hong Zhang [iD]

Vascular and General Surgery, Affilited Hospital of Chengde Medical University, Chengde 067000, China

Correspondence should be addressed to Hong Zhang; cdzh1977@163.com

Great saphenous varicose vein (GSVV) is a venous reflux disease of the lower extremity. In order to explore the clinical effect of subfascial endoscopic perforator surgery (SEPS) with endovenous laser treatment (EVLT) in the treatment of GSVV, 80 patients who underwent unilateral saphenous varicose surgery are analyzed. The operation results show that the patients who used SEPS + EVLT have less operation time and mean blood loss, shorter postoperative active time and hospitalization stay, better curative effect, and higher notch aesthetics ($P < 0.05$). SEPS combined with EVLT has a remarkable curative effect in the treatment of saphenous varicose veins of lower extremity, which can significantly shorten the hospitalization time of patients and improve the coagulation index and stress index.

1. Introduction

GSVV is a venous reflux disease of the lower extremity that is caused by the inability of the deep venous valve to close tightly. GSVV can manifest as superficial varicose veins, segmental cystic, or columnar dilatation of the main or branch of the veins, as well as lower extremity swelling, pain, hyperpigmentation, pruritus, and even ulceration [1, 2]. Factors that can cause increased intraabdominal pressure such as smoking, long-term standing, or sedentary are all risk factors for saphenous varicose veins [3]. Relevant literature reports that the prevalence of GSVV in women is higher than that in men, with prevalence rates ranging from 10% to 15% and 20% to 25%, respectively [4, 5]. If GSVV is not treated in time, complications such as superficial thrombophlebitis, venous heart ulcer, and variceal bleeding can occur, which seriously affect the work and life of patients [6].

Surgery is the main method for the treatment of GSVV. Through surgery, it can help patients restore the venous valve closure function as much as possible and inhibit venous blood backflow, thereby, improving venous hypertension and blood stasis, quickly relieving patients' symptoms and signs, and helping patients restore the function of the affected limb. High saphenous vein ligation is an effective method for the treatment of GSVV, which can completely strip the diseased saphenous vein, but it will cause great trauma to the surrounding tissue during the stripping process, and it is easy to damage the saphenous nerve and cause postoperative paresthesia [7, 8]. In addition, the residual vascular bed after high ligation is prone to accumulation of blood and fluid, and the incision often affects the appearance. With the improvement of medical technology, the treatment of GSVV has gradually entered the era of minimally invasive beauty. Subfascial endoscopic perforator surgery (SEPS) is to cut the skin to the deep fascia and ligate the communicating vein under the guidance of direct vision. SEPS has the advantages of simple operation, small trauma, clear visual field, low recurrence rate, and good curative effect. Endovenous laser treatment (EVLT) is also one of the minimally invasive methods of endovenous treatment.

The principle of treatment is to use the thermal effect released by the laser to damage the venous endothelium, damage the vein wall, and deposit thrombosis to occlude the varicose vein, which in turn obliterates the vena cava [9, 10]. At present, most patients in clinical practice generally require combined treatment due to etiology, symptoms, severity, and other reasons.

The rest of this study is organized as follows: Section 2 discusses related work and analysis, followed by the clinical treatment methods and evaluation indicators in Section 3. Comparative analysis and data statistics are given in Section 4. Section 5 concludes the study with summary and future research directions.

2. Related Work

Under the guidance of previous studies related to minimally invasive surgery, this study used SEPS combined with EVLT to treat patients with unilateral GSVV. Comparing the changes in perioperative indicators with traditional surgery, more comprehensive data for the treatment of GSVV can be supported.

With the progression of the GSVV, it can also lead to skin pigmentation, eczema, and ulcers, and effective treatment should be implemented in time to relieve the pain of the patients [11, 12]. Surgical therapy can change the local hemodynamic state from the anatomical level and prevent the pathological process. It is the main way of clinical treatment of severe saphenous varicose veins. With the further development of minimally invasive technology and equipment, a series of minimally invasive procedures have been gradually applied in clinical practice.

The traditional communicating branch vein ligation is a destructive treatment method, which requires high segmental dissection of the trunk of the great saphenous vein. In addition, multiple surgical incisions are required to ligate the communicating branch veins, and the intraoperative trauma is large, which may easily cause damage to the skin, veins, soft tissues, and nerves. These injuries increase patient distress and prolong postoperative active and hospitalization time. These injuries increase patient distress and prolong postoperative active and hospitalization. SEPS is performed by endoscopic ligation of the deep subfascial communicating branch vein, and its precise positioning can reduce unnecessary trauma, thereby shortening the time for patients to get out of postoperative active and hospitalization stay after surgery [13, 14]. It is found that SEPS can reduce the occlusion rate of the incidence of ulcers in patients after surgery. EVLT uses percutaneous puncture to occlude the superficial varicose vein under the action of cautery, which can preserve the normal saphenous vein and reduce the damage caused by ligation [15, 16]. Cavallini and other scholars believed that EVLT can reduce the risk of saphenofemoral valve regurgitation after ligation and stripping of the great saphenous vein [17]. The results of this study also show that compared with the patients who used traditional communicating branch ligation + EVLT, the patients who used SEPS + EVLT have more significant curative effects and higher notch aesthetics.

It is worth noting that surgical trauma can cause traumatic stress in the body and make blood in a hypercoagulable state, which is not conducive to the postoperative recovery of patients [18]. In this study, when comparing the coagulation indexes of patients during the perioperative period, it is found that the levels of PT and TT in the two groups postoperative are lower than preoperative, but the levels in the patients who used SEPS + EVLT are higher than those who used traditional communicating branch ligation + EVLT. When comparing the stress indicators of the two groups, it is found that contrast by preoperative, the levels of IL-6 and hs-CRP in the two groups are increased in postoperative, and the levels in the patients who used SEPS + EVLT are lower than those who used traditional communicating branch ligation + EVLT. Main serological manifestations of surgical trauma stress response in GSVV patients with elevated levels of IL-6 and hs-CRP after surgery. Elevated levels of IL-6 and hs-CRP can damage the vascular endothelial function of patients, promote platelet aggregation, affect the coagulation system of patients, and are not conducive to the recovery of postoperative limb skills [19, 20]. In addition, due to the hypercoagulability of blood in patients with GSVV, the body damage caused by surgery may aggravate the disorder of the coagulation system, resulting in abnormal changes in the levels of PT and TT.

3. Clinical Treatment Methods and Evaluation Indicators

3.1. Research Object. The data of 80 patients who underwent unilateral GSVV surgery from January 2019 to January 2021 are retrospectively analyzed. Patients are selected with the following rules: first, meet the relevant diagnostic criteria of GSVV and have been confirmed by imaging. Second, it is unilateral lesions. Third, clinical, etiological, anatomical, pathophysiological classification (CEAP) grade C5-C6. Finally, the data of preoperative examination, operation-related parameters, and postoperative reexamination are complete. Exclusion criteria is as follows: first, combined with other vascular diseases. Second, insufficiency of important organs. Third, venous vascular disease due to congenital factors. Fourth, combined with malignant tumors. Finally, the history of lower extremity venous surgery.

The number of patients in the study is 80. In the light of the surgical methods, the patients are divided into the control (traditional communicating branch ligation + EVLT) and the combine group (SEPS + EVLT).

3.2. Therapeutic Methods. The combined group is treated with SEPS + EVLT. The patient is placed in a supine position with the head loared and the feet high, the affected limb flexed and the knee is abducted by 130°, the hip joint is slightly externally rotated, and the knee is properly elevated. Routine sterile drape and anesthesia are performed. A transverse skin incision of about 1 cm in length is made 6 cm below the tibial tuberosity and 4 cm medial to the tibia, and the subcutaneous tissue is incised successively until the deep

fascia. The subfascial space is bluntly separated with the fingers, and the separation range is up to 5 cm medial to form an operating space.

Between the deep fascia and the muscularis layer along the incision, a laparoscopic system is placed, and CO_2 is filled under the fascia to maintain a pressure of 12 mmHg. Under the direct vision of the endoscope, a second incision with a length of about 0.5 cm is made at about 5 cm inside and about 3 cm below the original incision, and a Trocar and an ultrasonic scalpel are placed. Blunt dissection of the loose connective tissue is under the deep fascia, exposure of the communicating veins, and separation of communicating veins of varying thickness. The communicating veins are separated one by one using the ultrasonic scalpel, and the separation range is from the anterior border of the tibia to the midline, down to the Achilles tendon and medial malleolus, to avoid missing the communicating veins. The endoscopy system is withdrawn, the residual gas in the cavity is discharged, and the two surgical incisions are sutured intermittently.

An incision is made 2 cm anterior to the medial malleolus and a laser fiber is placed. An 18G trocar is used to puncture the great saphenous vein at the medial malleolus, and a 5F catheter dilator is introduced. The laser fiber is inserted into the 5F straight catheter and sent to the saphenofemoral vein, the catheter is retracted, and the fiber is pushed forward until the catheter is exposed 3 cm. Connect the semiconductor laser therapy instrument and adjust the laser wavelength to 810 nm and the laser emission power to 12–15 W. Using a continuous pulse method, the fiber is withdrawn and the laser is cauterized until the medial malleolus. The catheter and fiber are withdrawn slowly at the same time to close the vein wall. After the operation, the surgical area of the affected limb is compressed with an elastic bandage.

The control group is treated with traditional communicating branch vein ligation + EVLT: the patient position, EVLT treatment method, and postoperative treatment are the same as those in the combined group. Traditional communicating branch vein ligation: according to the preoperative color Doppler ultrasound to locate the surface markings of the communicating branch vein, the communicating branch vein is separated with a small incision and ligated in the superficial fascia layer.

3.3. Observation Indexes. Time of operation, mean bleeding volume, postoperative activity time, hospitalization time, and other related indicators are recorded. The operation time is from the start of anesthesia to the end of compression bandage with elastic bandage.

The clinical efficacy is evaluated according to the patients' lower extremity symptoms and vascular color Doppler ultrasonography 1 month after operation. The clinical symptoms basically disappeared, there is no obvious varicose veins, and the color ultrasound shows that there is no regurgitation in the great saphenous vein, and it is evaluated as curative. The clinical symptoms are significantly improved, slight varicose veins are seen, and the color ultrasound shows that the partial regurgitation of the great

saphenous vein is evaluated as effective. Patients with no improvement in clinical symptoms, obvious varicose veins, and regurgitation of the great saphenous vein still visible on vascular color ultrasound are evaluated as invalid.

The self-made incision satisfaction questionnaire is used to evaluate the patients' satisfaction with the notch aesthetics. The incision aesthetics score ranged 0–10, and the scores are proportional to satisfaction.

Some things are measured 1 day before surgery and 1 day and 3 days after surgery: prothrombin time (PT), thrombin time (TT), interleukin-6 (IL-6), and high-sensitive C-reactive protein (hs-CRP) levels.

3.4. Statistical Methods. SPSS 25.0 and GraphPad Prism 8.3 statistical software are used to analyze the research data. Qualitative data are expressed by frequency and percentage, and the chi-square test and rank sum test are performed. Quantitative data conforming to a normal distribution are expressed in the form of mean ± standard deviation, and the t-test is used. $P < 0.05$ indicated that the difference is significant.

4. Comparative Analysis and Data Statistics

4.1. Baseline Data. The baseline data of patients with different treatment methods are compared before surgery, and it is found that there is no great difference in the baseline data of the two groups of patients ($P > 0.05$). Table 1 provides the specific data.

4.2. Patient Surgery-Related Indicators. Comparing the operation-related indicators between the two groups, it is found that the time of operation, mean bleeding volume, postoperative active time, and hospitalization time of the patients who used SEPS + EVLT are lower than those who used traditional communicating branch ligation + EVLT ($P < 0.05$), as given in Table 2.

4.3. Curative Effect and Incision Aesthetics. It can be seen from Table 3 that the results of the rank sum test indicated that the curative effect of the two groups of patients is significantly different. Table 3 provides the curative effect and incision.

The evaluation of the aesthetics of the incision in the two groups of patients and the patients who used SEPS + EVLT are significantly more satisfied with the aesthetics of the incision than the patients who used traditional communicating branch ligation + EVLT ($P < 0.05$). Figure 1 shows the comparison of notch aesthetics. In Figure 1, $^*P < 0.05$.

4.4. Changes of Related Indexes of the Coagulation System during the Perioperative Period. Comparing the changes of blood coagulation system-related indexes between the two groups, it is found that at 1 and 3 days postoperative, the levels of PT and TT in the two groups are lower than those preoperative, as given in Table 4.

The levels in the patients who used SEPS + EVLT are higher than those who used traditional communicating

TABLE 1: Baseline data of patients.

Baseline information	Control ($n = 40$)	Combine ($n = 40$)	t/χ^2	P
Gender				
Male	14 (35.00)	17 (42.50)		
Female	26 (65.00)	23 (57.50)	0.474	0.491
Age	55.26 ± 5.93	56.31 ± 6.21	0.773	0.442
Disease duration (years)	6.09 ± 1.34	6.31 ± 1.28	0.751	0.455
BMI (kg/m^2)	23.05 ± 0.97	22.98 ± 1.01	0.316	0.752
Affected limb				
Left	18 (45.00)	21 (52.50)		
Right	22 (55.00)	19 (47.50)	0.45	0.502
CEPA grade				
C5	31 (77.50)	29 (72.50)		
C6	9 (22.50)	11 (27.50)	0.267	0.606

TABLE 2: Surgery-related indicators of patients.

Group	Time of operation (min)	Mean bleeding volume (mL)	Postoperative activity time (d)	Hospitalization time (d)
Control ($n = 40$)	92.13 ± 9.15	41.26 ± 7.59	5.84 ± 1.13	9.25 ± 1.31
Combine ($n = 40$)	67.58 ± 8.06	19.26 ± 6.28	3.59 ± 0.95	6.74 ± 0.95
t	12.731	14.122	9.639	9.81
P	< 0.001	< 0.001	< 0.001	< 0.001

TABLE 3: Curative effect and incision aesthetics.

Group	Curative	Effective	Invalid	Notch aesthetics
Control ($n = 40$)	15 (37.50)	18 (45.00)	7 (17.50)	7.31 ± 1.25
Combine ($n = 40$)	22 (55.00)	17 (42.50)	1 (2.50)	8.14 ± 0.97
Z/t		−2.029		3.318
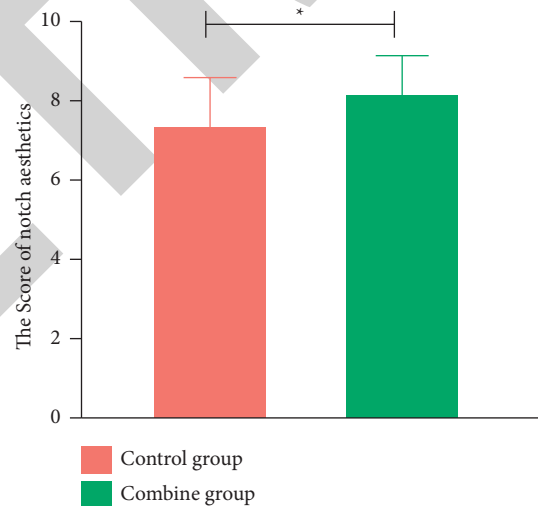
FIGURE 1: Comparison of notch aesthetics.

branch ligation + EVLT ($P < 0.05$). Those results are plotted as a bar chart, as shown in Figure 2. In Figure 2, $^*P < 0.05$.

4.5. Changes in the Level of Stress Indicators. Comparing the changes of stress indexes in the two groups, it is found that at 1 and 3 days postoperative, the levels of IL-6 and hs-CRP in the two groups are increased compared with those preoperative. Table 5 provides the changes in the level of stress indicators.

The levels in the patients who used SEPS + EVLT are lower than those who used traditional communicating branch ligation + EVLT ($P < 0.05$). Those results are plotted as a bar chart, as shown in Figure 3. In Figure 3, $^*P < 0.05$.

TABLE 4: Changes of related indexes of the coagulation system during the perioperative period.

Index	Group	Preoperative 1 day	Postoperative 1 day	Postoperative 3 day
PT (s)	Control ($n = 40$)	11.79 ± 1.29	8.16 ± 0.94	9.51 ± 0.98
	Combine ($n = 40$)	12.03 ± 1.31	9.75 ± 1.02	10.82 ± 1.14
	t	0.826	7.250	5.511
	P	0.442	**< 0.001**	**< 0.001**
TT (s)	Control ($n = 40$)	15.22 ± 1.97	12.17 ± 1.06	14.22 ± 1.21
	Combine ($n = 40$)	15.83 ± 1.92	13.84 ± 1.11	15.68 ± 1.27
	t	1.402	6.882	5.264
	P	0.165	**< 0.001**	**< 0.001**
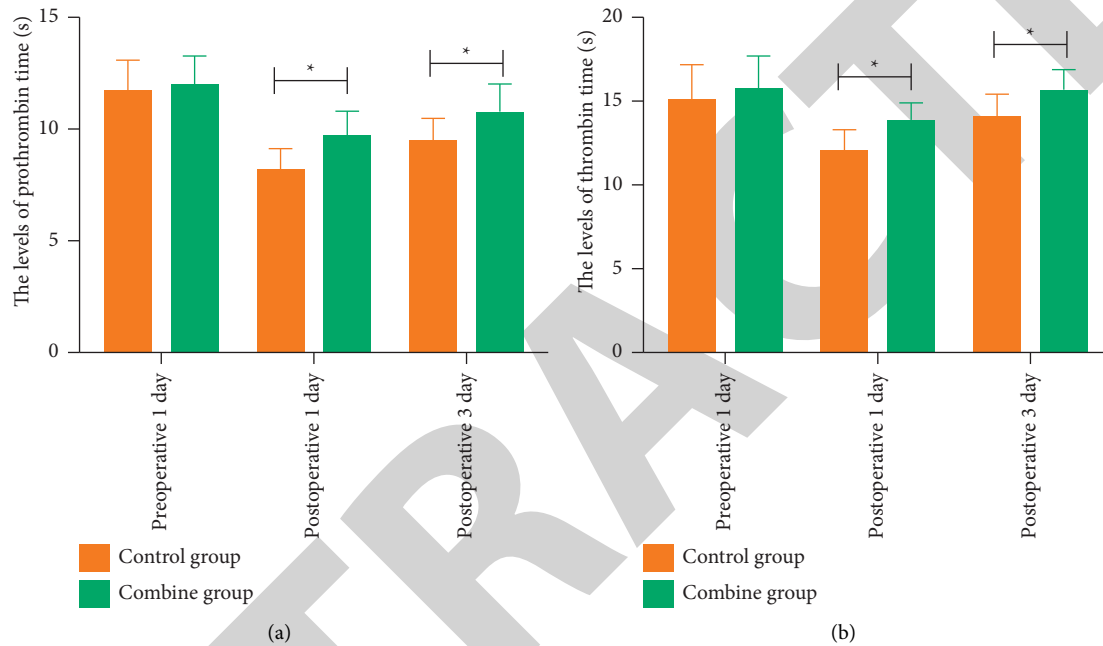
FIGURE 2: Changes of related indexes of the coagulation system in patients during the perioperative period: (a) changes of related indexes of the coagulation system in patients from 0 to 15; (b) changes of related indexes of the coagulation system in patients from 0 to 20.

TABLE 5: Changes in the level of stress indicators.

Index	Group	Preoperative 1 day	Postoperative 1 day	Postoperative 3 day
IL-6 (ng/L)	Control ($n = 40$)	13.02 ± 1.26	30.25 ± 2.59	26.77 ± 2.05
	Combine ($n = 40$)	12.85 ± 1.31	24.33 ± 2.47	19.32 ± 5.16
	t	0.592	10.460	8.486
	P	0.556	**< 0.001**	**< 0.001**
hs-CRP (mg/L)	Control ($n = 40$)	18.26 ± 3.52	38.22 ± 4.59	32.02 ± 4.16
	Combine ($n = 40$)	18.97 ± 3.84	31.15 ± 4.05	26.55 ± 3.45
	t	0.862	7.305	6.401
	P	0.391	**< 0.001**	**< 0.001**
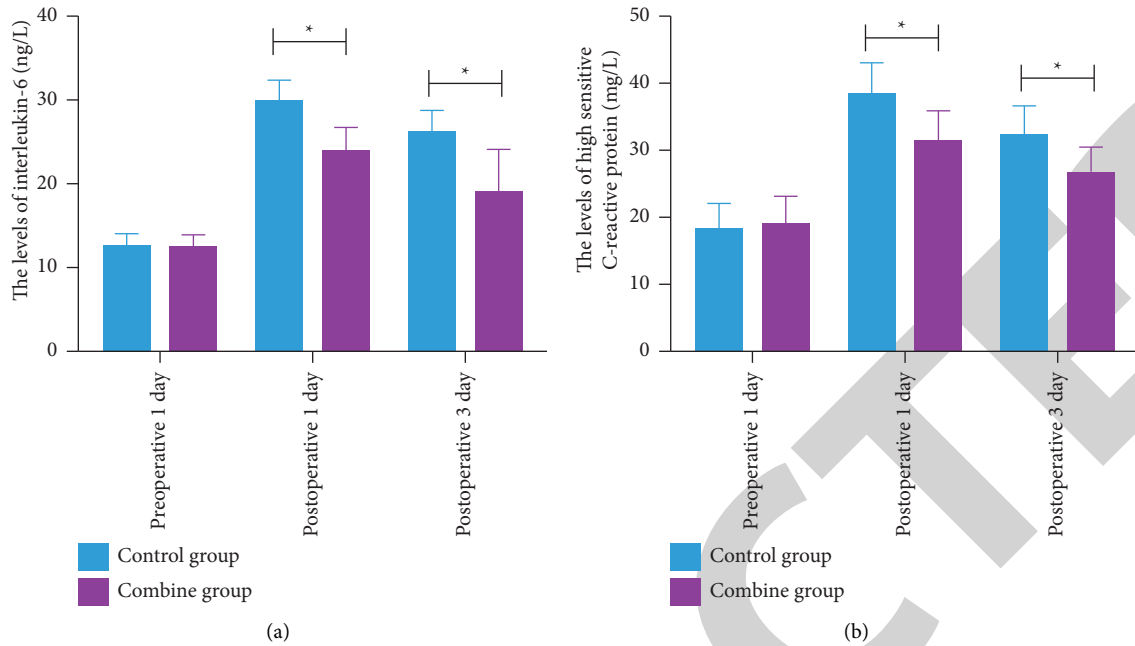
FIGURE 3: Changes in the level of stress indicators: (a) changes of related indexes of the coagulation system in patients from 0 to 40; (b) changes of related indexes of the coagulation system in patients from 0 to 50.

5. Conclusions

The therapeutic effect of SEPS + EVLT and traditional communicating branch vein ligation + EVLT on GSVV patients are compared in this study. The results show that SEPS + EVLT could significantly reduce the operation time and mean bleeding volume of patients and shorten the postoperative active time and hospitalization time. In addition, due to the hypercoagulability of blood in GSVV patients, the body injury caused by surgery can aggravate the disorder of the coagulation system, which will lead to abnormal changes in the levels of PT and TT. The traditional communicating branch vein ligation can cause great damage to the vein wall, strong stress in the body, and the function of vascular endothelial cells. At the same time, the traditional communicating branch vein ligation has many incisions, and a large number of bandages are used to wrap the wound after surgery, which limits the movement of the body and may aggravate blood coagulation. The surgical operation of SEPS combined with EVLT is more precise, which can effectively avoid damage to the surrounding normal veins and soft tissues, maintain the stability of the vascular endothelium, and reduce the stress response. The treatment mode of SEPS combined with EVLT therapy can reduce the postoperative stress response of patients and is not easy to have serious adverse effects on the coagulation system, so that a higher clinical effect can be obtained.

To sum up, SEPS combined with EVLT has a significant curative effect in the treatment of saphenous varicose veins of lower extremity. It can significantly shorten the hospitalization time of patients, improve the treatment effect and notch aesthetics, and improve the coagulation index and stress index.

Data Availability

The simulation experiment data used to support the findings of this study are available from the corresponding author upon request.

Conflicts of Interest

The authors declare that there are no conflicts of interest.

Acknowledgments

References

[1] A. Kundal, N. Kumar, D. Rajput, and U. Chauhan, "Great saphenous vein sparing versus stripping in Trendelenburg operation for primary varicose veins: a prospective study," *Polish Journal of Surgery*, vol. 93, no. 1, pp. 34–39, 2020.

[2] S. Yoshida, I. Koshima Haddad, H. Imai et al., "Combined lymphovenous anastomosis and great saphenous vein stripping for comorbid lymphedema and varicose veins," *Lymphatic Research and Biology*, vol. 3, p. 31, 2020.

[3] Y. Tseng, C. Chen, M. Wong et al., "Blood flow analysis of the great saphenous vein in the su-pine position in clinical manifestations of varicose veins of different severities: application of phase-contrast magnetic resonance imaging data," *Diagnostics*, vol. 102, no. 7, p. 118, 2020.

[4] P. Sandhya, R. Mohil, and R. Sricharan, "Randomised controlled study to compare radiofrequency ablation with minimally invasive ultrasound-guided non-flush ligation and stripping of great saphenous vein in the treatment of varicose veins," *Annals of the Royal College of Surgeons of England*, vol. 39, no. 2, pp. 105–111, 2020.

Retraction

Retracted: U-Net-Based Medical Image Segmentation

Journal of Healthcare Engineering

This article has been retracted by Hindawi following an investigation undertaken by the publisher [1]. This investigation has uncovered evidence of one or more of the following indicators of systematic manipulation of the publication process:

(1) Discrepancies in scope

(2) Discrepancies in the description of the research reported

(3) Discrepancies between the availability of data and the research described

(4) Inappropriate citations

(5) Incoherent, meaningless and/or irrelevant content included in the article

(6) Peer-review manipulation

The presence of these indicators undermines our confidence in the integrity of the article's content and we cannot, therefore, vouch for its reliability. Please note that this notice is intended solely to alert readers that the content of this article is unreliable. We have not investigated whether authors were aware of or involved in the systematic manipulation of the publication process.

Wiley and Hindawi regrets that the usual quality checks did not identify these issues before publication and have since put additional measures in place to safeguard research integrity.

We wish to credit our own Research Integrity and Research Publishing teams and anonymous and named external researchers and research integrity experts for contributing to this investigation.

The corresponding author, as the representative of all authors, has been given the opportunity to register their agreement or disagreement to this retraction. We have kept a record of any response received.

References

[1] X. Yin, L. Sun, Y. Fu, R. Lu, and Y. Zhang, "U-Net-Based Medical Image Segmentation," *Journal of Healthcare Engineering*, vol. 2022, Article ID 4189781, 16 pages, 2022.

Review Article

U-Net-Based Medical Image Segmentation

Xiao-Xia Yin [ID],[1,2] **Le Sun,**[3] **Yuhan Fu,**[1] **Ruiliang Lu,**[4] **and Yanchun Zhang** [ID][1]

[1]*Cyberspace Institute of Advanced Technology, Guangzhou University, Guangzhou 510006, China*
[2]*College of Engineering and Science, Victoria University, Melbourne, VIC 8001, Australia*
[3]*Engineering Research Center of Digital Forensics, Ministry of Education,*
 Nanjing University of Information Science and Technology, Nanjing, China
[4]*Department of Radiology, The First People's Hospital of Foshan, Foshan 528000, China*

Correspondence should be addressed to Xiao-Xia Yin; xiaoxia.yin@gzhu.edu.cn

Deep learning has been extensively applied to segmentation in medical imaging. U-Net proposed in 2015 shows the advantages of accurate segmentation of small targets and its scalable network architecture. With the increasing requirements for the performance of segmentation in medical imaging in recent years, U-Net has been cited academically more than 2500 times. Many scholars have been constantly developing the U-Net architecture. This paper summarizes the medical image segmentation technologies based on the U-Net structure variants concerning their structure, innovation, efficiency, etc.; reviews and categorizes the related methodology; and introduces the loss functions, evaluation parameters, and modules commonly applied to segmentation in medical imaging, which will provide a good reference for the future research.

1. Introduction

Interpretation of medical images such as CT and MRI requires extensive training and skills because the segmentation of organs and lesions needs to be performed layer by layer. Manual segmentation means a heavy workload to the doctors, which can introduce bias if it involves the subjective opinions of doctors. To analyze complicated images, it usually requires doctors to make a joint diagnosis, which is time consuming. Furthermore, automatic segmentation is a challenging task, and it is still an unsolved problem for most medical applications due to the wide variety connected with image modalities, encoding parameters, and organic variability.

According to [1], medical imaging increased rapidly from 2000 to 2016. As illustrated in Figure 1(a), retrospective cohort study of patterns of medical imaging between 2000 and 2016 was conducted among 16 million to 21 million patients. These patients were enrolled annually in 7 US integrated and mixed-model insurance health care systems and for individuals receiving care in Ontario, Canada. Relative imaging rates by different imaging modality, such as computed tomography (CT), magnetic resonance imaging (MRI), and ultrasound that are used by adults [18–64 years] annually in US and Ontario are also illustrated in Figures 1(b)–1(d), respectively. The imaging rates (per 1000 people) of CT, MRI, and ultrasound use continued to increase among adults, but at lower pace in more recent years. Whether the observed imaging utilization was appropriate or was associated with improved patient outcomes is unknown.

Nowadays, the application of deep learning technology in medical imaging has attracted extensive attention. How to automatically recognize and segment the lesions in medical images has become one of the issues that concern lots of researchers. Ronneberger et al. [2] proposed U-Net at the MICCAI conference in 2015 to tackle this problem, which was a breakthrough of deep learning in segmentation of medical imaging. U-Net is a Fully Convolutional Network (FCN) applied to biomedical image segmentation, which is composed of the encoder, the bottleneck module, and the decoder. The widely used U-Net meets the requirements of medical image segmentation for its U-shaped structure combined with context information, fast training speed, and
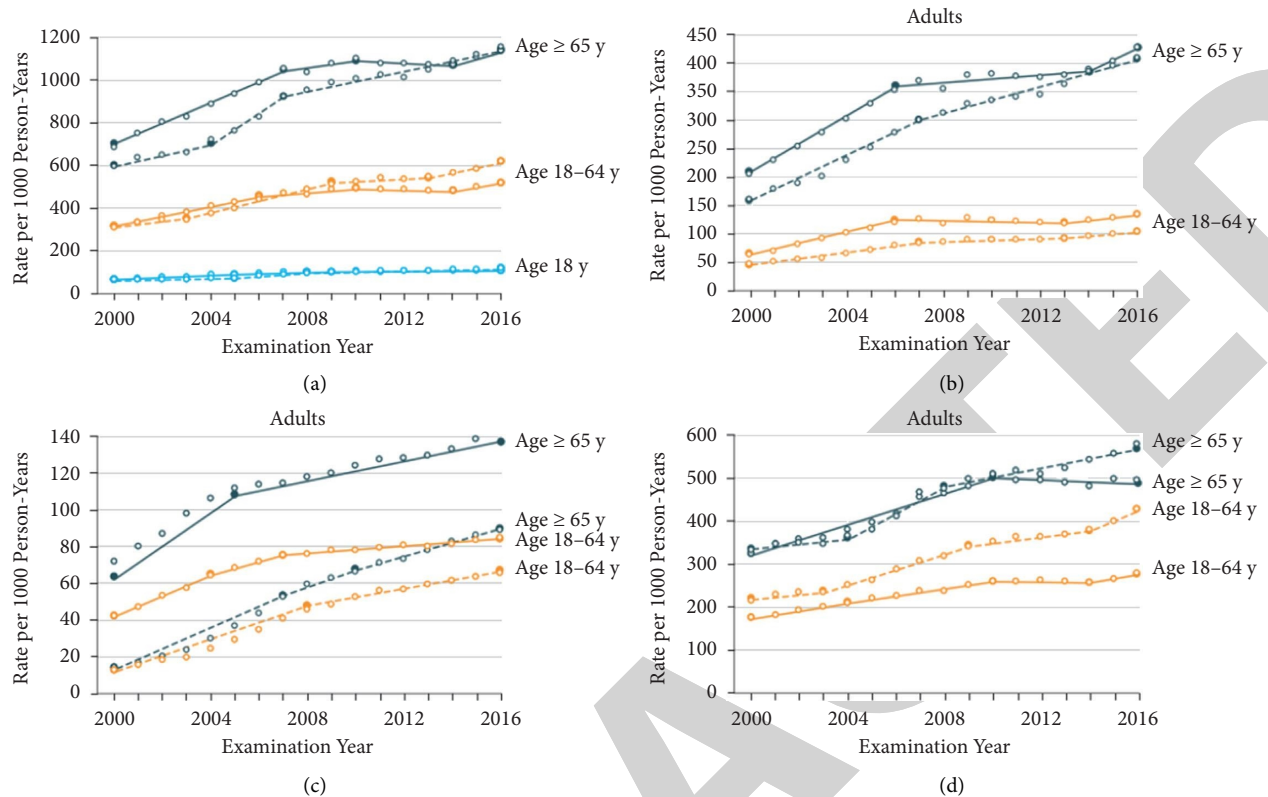
Figure 1: Illustration of relative rates of imaging for United States compared with Ontario from year 2000 to year 2016. CT indicates computed tomography; MRI indicates magnetic resonance imaging. All US data are shown as solid curves; Ontario data are shown as dashed curves [1]. (a) All examinations. (b) CT. (c) MRI. (d) Ultrasound.

a small amount of data used. The structure of U-Net is shown in Figure 2.

Containing many slices, biomedical images are often blocky in a volume space. An image processing algorithm of 2D is often used to analyze a 3D image [3–7]. But when the information is sorted and trained one by one, it would result in increased computational expenses and low efficiency. Therefore, it is difficult to deal with volume images in many cases. A 3D U-Net model derived from the 2D U-Net is designed to address these problems. To further target on architectures of different forms and dimensions, Oktay et al. [8] proposed a new attention gate (AG) model for medical imaging analysis. The model trained with AG indirectly learns to restrain irrelevant regions in an input image and highlight striking features suitable for specific tasks. This is conducive to eradicating the inevitability of applying overt exterior tissue/organ localization units of cascading convolutional neural networks (CNNs) [8, 11]. AG could be combined with standard CNN structure like U-Net, which increases the sensitivity and the precision of the model. To get more advanced data and retain spatial data aimed at 2D segmentation, Gu et al. in 2019 [12] proposed the context encoder network (CE-Net), using pretrained Res-Net blocks as fixed feature extractors. It is mainly composed of three parts—feature encoder, context extractor, and feature decoder. The context extractor is composed of a newly introduced dense atrous convolution (DAC) block and a

residual multikernel pooling block (RMP). The introduced CE-Net is widely applied to segmentation in 2D medical imaging [11] and outperforms the original U-Net method.

To further advance the segmentation, UNet++, a novel and greater neural network structure for image segmentation was proposed by Zhou et al. [13]. Moreover, it is a deeply supervised encoder-decoder network connected by a series of nested and dense hopping paths to narrow the semantic gap between the encoding and decoding subnetwork feature maps. Later, to improve more accuracy, especially for organs of different sizes, a new version UNET 3+ was designed by Huang et al. [14]. It utilizes full-scale skip links and deep supervisions, which combines low-level details and high-level semantics mapped at different scales of features and learns hierarchical representation from full-scale aggregated feature maps. The suggested UNet 3+ could increase computational productivity by decreasing network parameters.

Framework regarding nnU-Net ("no-new-Net") is developed by Isensee et al. [15] as a robust self-adaptive framework from U-Net. It was designed by making slight alterations to the 2D and 3D U-Net, where 2D, 3D, 2D, and 3D links were proposed to work together and form a network pool. The nnU-Net could not only automatically adapt its architecture to the given image geometry, but thoroughly define all the other steps including image preprocessing, data training, testing, and potential postprocessing.
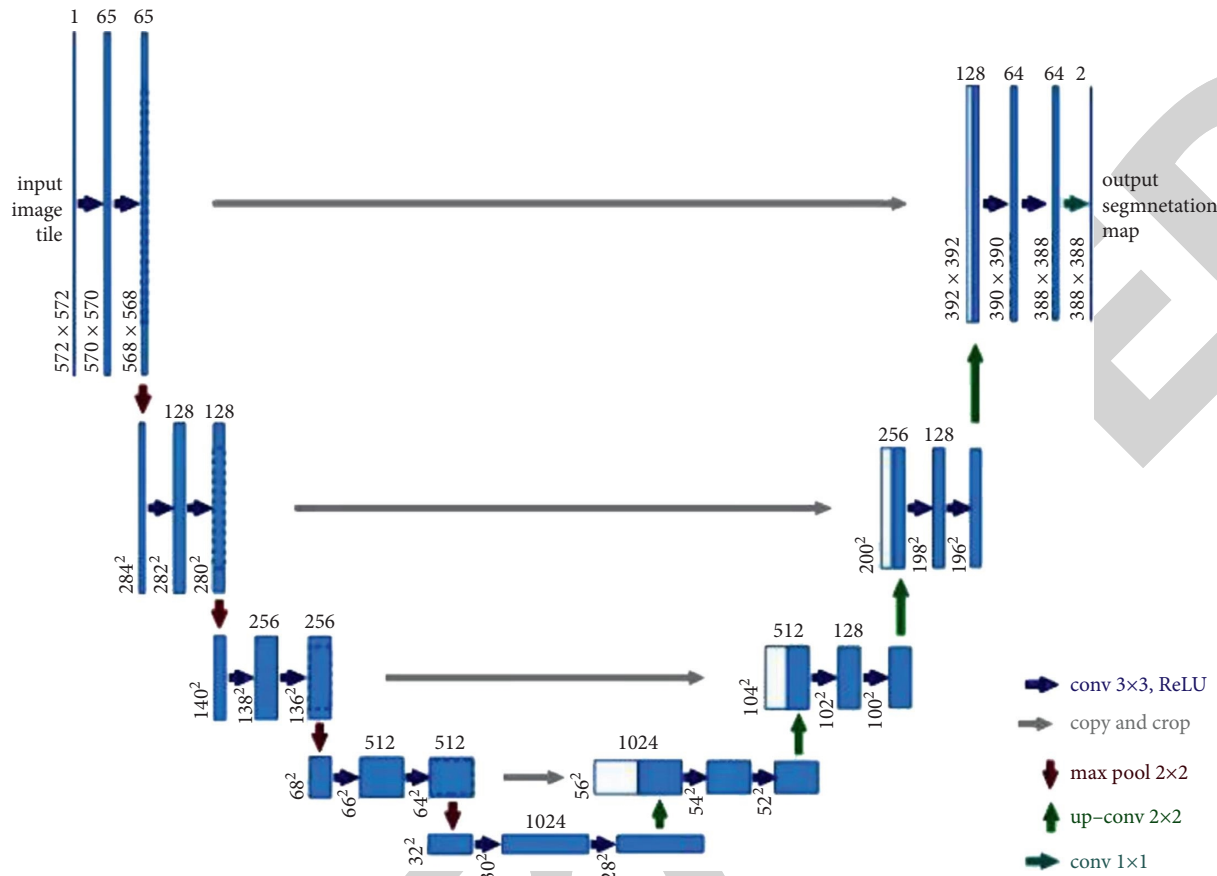
FIGURE 2: Illustration of U-Net convolution network structure. The left side of the U-shape is the encoding stage, also called contraction path with each layer consisting of two 3 ∗ 3 convolutions with ReLu activation and a 2 ∗ 2 maximum pooling layer. The right side of the U-shape, also called expansion part, consists of the decoding stage and the upsampling process that is realized via 2 ∗ 2 deconvolution to reduce the quantity of input channels by half [2].

U2-Net as a simple and powerful deep network architecture developed by Qin et al. [16] consists of a two-level nested U-shaped structure applied to salient target detection (SOD). It has the following advantages: (1) due to the mixed receptive fields of various sizes in the proposed residual U-shaped block (RSU), it could capture a larger amount of contextual data at various scales. (2) The pooling operation used in the RSU block increases the depth of the entire structure without substantially pushing up the computational cost.

TransUNet designed by Chen et al. [17] encodes tokenized image patches and extracts global contexts from the input sequence of CNN feature map; the decoder upsamples the encoded features and combines with the high-resolution CNN feature maps for precise localization. It uses transformers as a powerful encoding structure for segmentation. Due to the inherent locality of convolution operations, U-Net usually shows limitations in clearly modeling dependencies. The transformer designed for sequence-to-sequence prediction has become an alternative architecture with an innate global self-attention mechanism while localization capabilities of the transformer frame may be limited due to insufficient low-level details.

Since U-Net was proposed, its encoder-decoder-hop network structure has inspired a large amount of segmentation means in medical imaging. Such deeplearning technologies as attention mechanism, dense module, feature enhancement, evaluation function improvement, and other basic U-Net structures have been introduced into medical image segmentation and become widely adopted. These variations of U-Net-related deep learning networks are designed to optimize results by improving the accuracy and computing efficiency of medical image segmentation through changing network structures, adding new modules, etc. However, most of the existing literature related to U-Net focused on introducing isolated new ideas and rarely gave a comprehensive review that summarizes the variations of the U-Net structure for deep learning of segmentation in medical imaging. This paper discussed some of these ideas in more depth.

To sum up, the basic motivation behind this work is not to elaborate into new ideas in U-Net-related deep learning networks but to use effectively U-Net-related deep learning networks techniques into the segmentation of multidimensional data for biomedical applications. The presented method can be generalized to any dimension and can be

used effectively to other types of multidimensional data as well.

This paper is organized as follows. Section 2 addresses the current challenges faced by medical image segmentation. Section 3 reviews these variations of U-Net-related deep learning networks. Section 4 collects various experiment results in literature in relation to different U-Net networks, along with the validation parameters for optimized network structure through the associated deep learning models. The future development in the U-Net-based variant networks is analyzed and discussed. Finally, Section 5 concludes this paper.

2. Existing Challenges

This section presents the current challenges faced by medical image segmentation which make it inevitable to improve and innovate U-Net-based deep learning approaches.

First, medical image processing requires extremely high accuracy for disease diagnosis [18–23]. Segmentation in medical imaging refers to pixel-level or voxel-level segmentation. Generally, the boundary between multiple cells and organs is difficult to be distinguished on the image [3]. Moreover, the data obtained from the image are usually preprocessed, the relevant network is built, which continues to be run by adjusting the parameters even though a certain level of accuracy is reached by using the relevant deep learning model [24].

Second, medical images are acquired from various medical equipment and the standards for them and annotations or performance of CT/MRI machines are not uniform. Hence deep-learning-related trained models are only suitable for specific scenarios. Meanwhile, the deep network with weak generalization may easily capture wrong features from the analyzed medical images. Furthermore, significant inequality always exists between the size of negative and positive samples, which may have a greater impact on the segmentation. However, U-Net could afford an approach achieving better performance in reducing overfitting [25].

Third, interpretable deep learning models applied to analyze medical images are highly required, but there is a lack of confidence in its predicted results [26, 27]. U-Net is a CNN showing poor interpretability. Segmentation in medical imaging could reflect the patient's physiological condition and accurate disease diagnosis. It is not easy for the segmentation lacking interpretability and confidence to be trusted and recognized by professional doctors for clinic application. Although disease diagnosis mainly relies on images, combined with other supplements, which has also increased the complexity. It is a challenge to realize the interpretability and confidence of medical image segmentation via perceiving and adjusting these trade-offs.

3. Methodology

Various medical image segmentation methods have been developed very quickly based on U-Net for performance optimization. U-Net is improved in the areas of application range, feature enhancement, training speed optimization, training accuracy, feature fusion, small sample training set, and generalization improvement. Various strategies are applied in the designing of different network structures to address different segmentation problems.

This section is focused on variations of U-Net-based networks, with the description of U-Net framework, followed by the comprehensive analysis of the U-Net variants by performing (1) intermodality and (2) intramodality categorization to establish better insights into the associated challenges and solutions. The main related work is summarized from the aspects of the improved performance indicators and the main structural characteristics.

3.1. Traditional U-Net. The traditional U-Net is two-dimensional network architecture whose structure is shown in Figure 2. U-Net modifies and extends the Fully Convolutional Network (FCN), making it work with very few training images and produce more accurate segmentation. The major idea is to replace the general shrinkage network with sequential layers and the pooling operation is related to downsampling operator, which is supplemented by upsampling operator. Hence the output's resolution is raised by these layers. The high-resolution of the contracted path is combined with the upsampled output for localization. Hence sequential convolutional layers could study fine features and result in a more accurate segmentation.

An important modification in the U-Net architecture lies in the upsampling section, where there are huge amounts of feature channels allowing the network to spread contextual data to higher-resolution layers. Therefore, the expansion path is roughly symmetrical to the contraction path, forming a U-shaped structure. The network applies the effective part of every convolution—the map of segmentation contains mere pixels, and the complete context of the pixels could be obtained in the input image. This method allows seamless segmentation in arbitrarily large imaging using crucial overlapping tiling strategies, without which the resolution will be limited by GPU memory [1].

The traditional CNN is usually connected to several fully connected layers after convolution and the feature map produced by the convolutional layer is mapped into a feature vector with a fixed length for image-level classification. An improved FCN structure, however, identifies the image at the pixel level, thereby facilitating the task of segmentation in imaging at the semantic level [28].

U-Net could be applied to the segmentation due to its large measurement size of medical images. It is impossible to input the large medical images into the network when they are segmented and required to be cut into small pieces. Overlapping-tilling strategies are suitable for small pieces cutting using U-Net due to its network structure. Thus, it could accept images of any size as inputs [29].

3.2. 3D U-Net. Biomedical imaging is a set of three-dimensional images composed of slices at different locations. Biomedical image analysis involves dealing with a large amount of volume data. Annotating these data labeled by segmentation could cause difficulties because only two-

dimensional slices can be displayed on computers. Therefore, low efficiency and loss of contexts are common during 3D-image processing by traditional 2D image models. To solve this, Ozgun Cicek et al. [30] put forward a 3D U-Net with a shrinking encoder part for analyzing the entire image and a continuous expansion decoder part for generating full-resolution segmentation on the basis of the previous U-Net structure. The structure of 3D U-Net is similar to 2D U-Net in many aspects, except that all operations in the 3D network are replaced with corresponding 3D convolution, 3D pooling, and 3D upsampling. Batch normalization (BN) [31] is used to prevent the network bottlenecks.

Just like the standard U-Net, there is an encoding path and a decoding path with 4 parsing steps in every layer in the encoding path. It contains two $3 \times 3 \times 3$ convolutions followed by a corrected linear unit (ReLu) and then a $2 \times 2 \times 2$ maximum pooling layer with 2-step size of each. Every layer in the synthesis path is composed of $2 \times 2 \times 2$ upper convolutions with two steps in each dimension and two subsequent $3 \times 3 \times 3$ convolutions with a ReLu active layer behind each. The skip connections from the equal-resolution feature map in the encoding path provide the necessary high-resolution features for the decoding path. In the last layer, $1 \times 1 \times 1$ convolution decreases the quantity of output channels to that of labels standing at 3. The structure has 19069955 parameters in total.

In addition to the rotation, scaling, and gray value increase, smooth dense deformation fields are applied to the data and ground truth labelers before training Therefore, random vectors are sampled from a general distribution whose standard deviation is 4 in a grid spaced 32 voxels in each direction, followed by the application of B-spline interpolation. The softmax with weighted cross-entropy loss is used to compare the network output and the ground truth label, to reduce the weight of the common background, increase the weight of internal tubules, and realize the balance effect of small blood vessels and background voxels on the loss.

This end-to-end learning strategy could use semiautomatic and completely automatic methods to segment 3D targets from sparse annotations. The structure and data enhancement of this network allow it to learn from a small number of labeled data and to obtain good generalization capabilities. Appropriate rigid transformation and minor elastic deformation applications could generate reasonable images, rationalize its preprocessing method, and enable the network structure to be extended to any size of the 3D data set.

3.3. Attention U-Net.
Attention could be considered as a method of organizing computational resources to interpret the signal informatively. Since its introduction, the attention mechanism has become more and more popular in the deep learning industry. This paper summarizes a method in the application of the attention mechanism onto the U-Net network. Given the small lesions and large shape changes, the attention module is generally added in image segmentation before the encoder- and decoder-related features are stitched or at the bottleneck of U-Net to reduce false-positive predictions.

The Attention U-Net put forward by Oktay et al. [8] in 2018 adds an integrated attention gate (AG) before U-Net splices the corresponding features in the encoder and decoder and readjusted the output features of the encoder. This module facilitates generation of gating signal to eliminate the response of irrelevant and noisy ambiguity in the skip connection, emphasizing the salient features transmitted via the skip connection. Figure 2 displays the inside structure of the attention module.

The salient features useful for specific tasks are stressed in the model trained by AG, which indirectly learns and suppresses unconcerned areas of the input image. Thus, obvious exterior tissue/organ positioning modules are not necessarily used in the Cascaded CNN. Without extra computational cost, the forecast precision and sensitivity of the model could be improved by AG due to its compatibility in standard CNN architectures like U-Net. To estimate the attention U-Net structure, two big CT abdominal data sets were used for multiclass segmentation in imaging. The results show a significant enhancement of U-Net's prediction performance by AG under different data sets and training scales, and the computational efficiency is maintained as well.

The structure of attention U-Net, as shown in Figure 3, is a U-Net-based structure with two stages: encoding and decoding. The coarse-grained map of the left structure captures information in the context and highlights the type and position of foreground objects. Subsequently, feature maps extracted from numerous scales are fused via jump links to merge coarse-grained and fine-grained dense predictions. As for the method put forward in the paper, the attention gate mechanism is to add an AG to each skip connection layer to spread the attention coefficient. AG has two inputs, x from the feature map of the shallow network on the left and g from that of the lower network, which will be output from AG. Then the feature fusion is performed on the feature map after sampling on the right.

This method makes it unnecessary to utilize external object positioning models. It is a convenient tool not only used in natural image analysis and machine translation but also in image classification and regression. Studies showed that the algorithm is very useful for the identification and positioning of tissues/organs, and a certain degree of accuracy could be achieved in the use of smaller computing resources, especially for small-sized organs such as the pancreas [32].

3.4. CE-Net.
A fusion of features with different scales serves as a crucial approach to optimizing segmentation performance. Due to fewer convolutions, the low-level features experience lower semantics and more noise despite of their higher resolution and more position. In addition, the resolution is considerably low and the detail perception is poor despite that high-level features contain more intensive semantic information. It is of huge significance to efficiently combine the advantages of these two to improve the
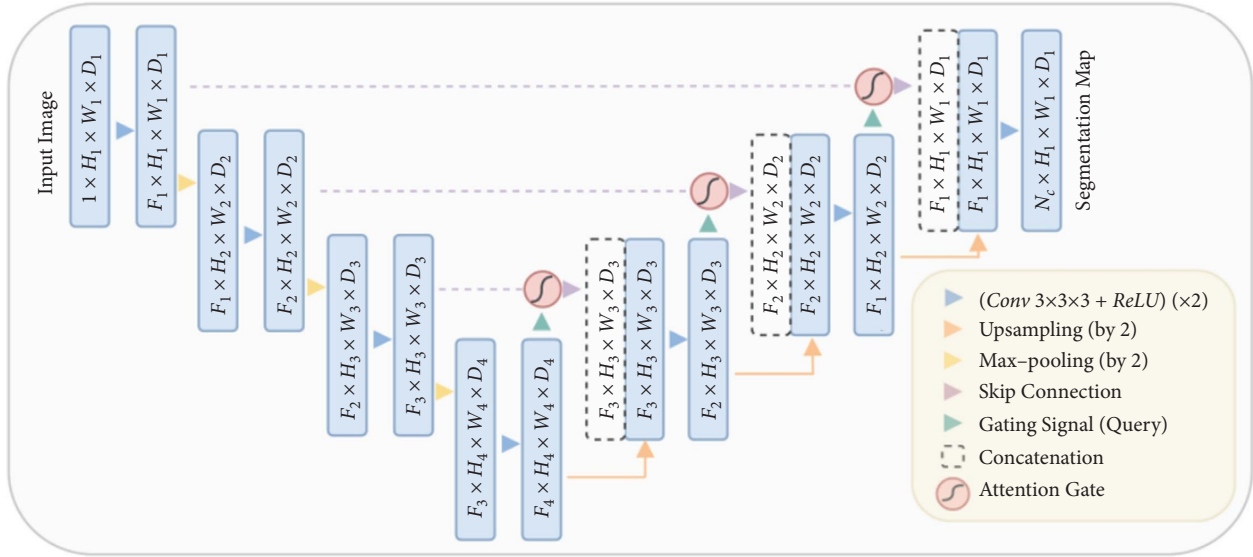
FIGURE 3: The U-Net model structure of the proposed AG is added. The input image is gradually filtered and downsampled at each scale in the network's encoding part (for example, H4 = H1/8), indicating the quantity of classes. The gates (AGs) filter the characteristics of propagation by skipping connections. The feature AGs is selected by extracting context information (gating) from a coarser scale [8].

segmentation model. Feature fusion includes the contextual features' fusion of the network and the fusion of different modal features in a larger sense. Gu et al. [10] designed a new network called CE-Net, which adopts new modules of dense atrous convolution block (DAC) and residual multikernel pooling block (RMP) to offer fused information like the fusion of contextual features from the encoder, to get higher-level information with a decrease in the feature loss [33], for example, to retain spatial information for 2D segmentation in medical imaging and classification [34].

The overall framework of CE-Net is shown in Figure 4. The DAC block could identify broader and more in-depth semantic features via injecting four cascaded branches with multiscale dense hole convolution. The remaining connections are used to prevent the gradient from disappearing. In addition, the RMP block is a residual multicore pool based on the spatial pyramid pool, which encodes the multiscale context features of the object extracted from the DAC module without extra learning weights using various size pool operations. In summary, the DAC block extracts rich feature representations through multiscale dense hole convolution and then uses the RMP block to extract more context information through multiscale pooling operations. The joint use of newly proposed DAC block and RMP block with the backbone codec structure is unprecedented in CE-Net's context encoder network. This allows the enhancement of the segmentation by further collecting abstract features and maintaining more spatial information.

3.4.1. Feature Encoder Module. In the U-Net structure, each encoder block includes two convolutional layers and a maximum pooling layer. As for the CE-Net network structure, a pretrained ResNet-34 is used in the feature encoding module and the first four feature extraction blocks are retained without mean pooling and full

connection. Res-Net adds a shortcut mechanism to avoid gradient disappearance and improve the network convergence efficiency, as shown in Figure 4(b). It is a basic method to improve U-Net segmentation performance using pretrained Res-Net.

3.4.2. Context Extraction Module. The context extraction module, composed of DAC and RMP, extracts contextual semantic information and produces more advanced feature maps.

(1) Hollow Convolution. As for semantic segmentation and object detection, deep convolutional layers have displayed superiority in image feature representation extraction. But the pooling layer might cause loss of image semantic information, which is solved by applying dense hole convolution [35] to dense image segmentation. The hole convolution has an expansion rate parameter which implies that the size of the expansion and the convolution kernel is the same with the ordinary convolution. It means parameters remain unchanged in the neural network, but the hole convolution has a larger receptive field, which refers to the size involved by the convolution kernel on the image. The size of the receptive field is related to stride, the number of convolutional layers, and padding parameters.

(2) DAC. Inspired by Inception [36, 37], Res-Net [38], and hole convolution, dense hole convolution blocks (DAC) [11] are used for encoding high-level semantic feature maps. The DAC has four branches cascading down, with the acceptance field of each branch being 3, 7, 9, and 19, respectively and a gradual increase in the number of atrous convolutions. DAC uses different receptive fields like the inception structure. In each hole convolution branch, a 1×1 convolution is applied to ReLu. The shortcut links in Res-Net are used directly to add the original features. Generally, the convolution of the
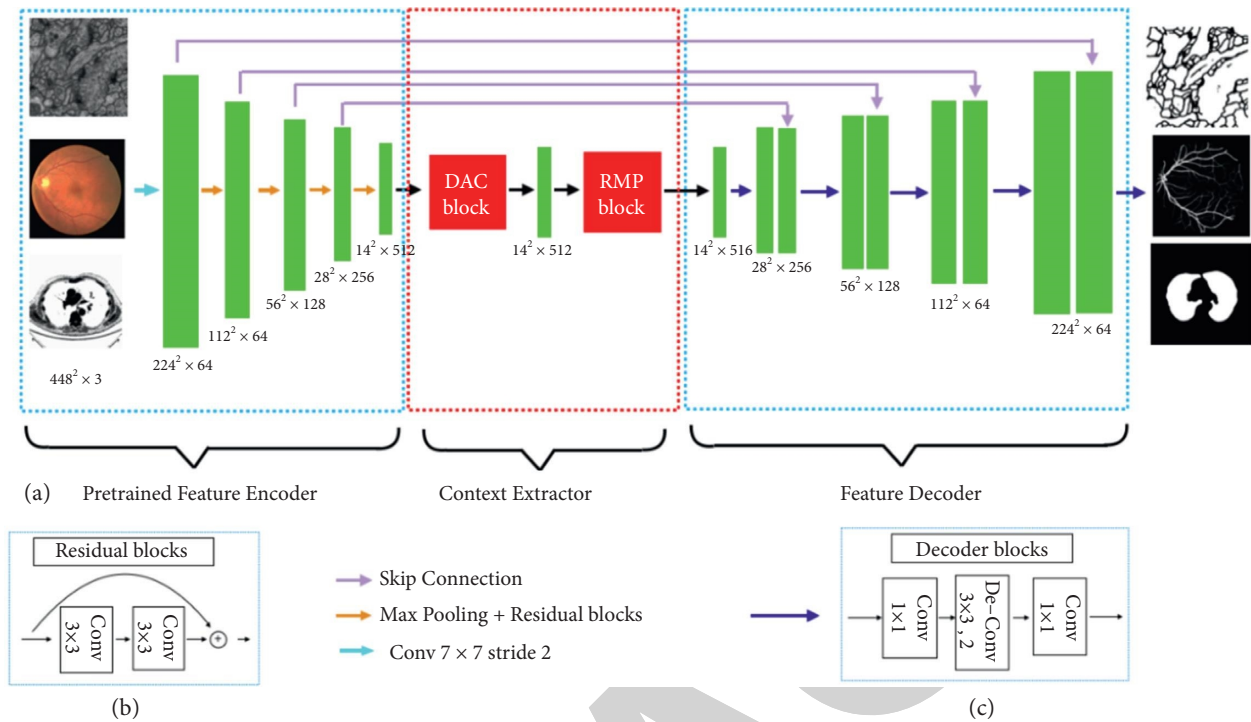
FIGURE 4: CE-net network structure diagram. (a) The original U-Net encoder block is first supplemented by the ResNet-34 block, shown as (b), to be pretrained by ImageNet. A dense convolution (DAC) block and a RMP block were contained in the bottleneck module. Eventually, the features are withdrawn and gathered in the decoder module. The feature size is enlarged by a decoder block (c), including 1×1 convolution and 3×3 deconvolution operations, to supplement the original upsampling operation [11].

large receptive field could extract and produce a larger number of abstract features for the large target and vice versa. The DAC block can extract features from the targets of various sizes through the combination of hole convolutions and different expansion rates.

(3) RMP. One of the challenges in medical image segmentation lies in the significant change in target size [39, 40]. For instance, an advanced tumor is usually much bigger than the early one [41]. An RMP [11] is proposed to solve this problem, by which targets with various sizes could be detected by applying numerous effective fields of view. The proposed RMP utilizes four receptive fields with different size to encode global context information. To reduce the dimensionality of the weights and the computational cost, a 1×1 convolution is used after each pooling branch. Afterwards, the upsampling of the low-dimensional feature map is performed to obtain the same size of features as an original feature map through bilinear interpolation, allowing extraction of features of various scales.

3.4.3. Feature Decoder Module. The feature decoder module allows the recovery of the high-level semantic features extracted from the context extractor module and the feature encoder module. Continuous pooling and convolution operations often lead to the loss of information, which, however, can be remedied by conducting a quick connection from the encoder to the decoder. In U-shaped networks, the two basic operations of decoder are simple upsampling and

deconvolution. The image can be enlarged by conducting upsampling through linear interpolation. Deconvolution (also known as transposed convolution) uses convolution to expand the image. Adaptive mapping is used in transposed convolution to recover more comprehensive information. Therefore, transposed convolution is implemented to achieve a higher resolution in the decoder. Based on the shortcut connection and the decoder block, the feature decoder module produces a mask of the same size as the original input.

Unlike U-Net, CE-Net applies a pretrained Res-Net block in the feature encoder. The integration of DAC module, RMP module and Res-Net into the U-Net architecture allows it to retain more spatial information. It was suggested that this approach could optimize segmentation in medical imaging for various tasks of optic disc segmentation [42], retinal blood vessel detection [11], lung segmentation [11], cell contour segmentation [35], and retinal OCT layer segmentation [43]. This approach could be extensively utilized in other 2D medical image segmentation tasks.

3.5. UNET++. Variants of encoder and decoder architectures such as U-Net and FCN are found to be the most advanced image segmentation models [44]. These segmentation networks share a common feature—skip connections that link the depth, semantics, and coarse-grained feature maps from the decoder subnetwork together with the shallow, low-level, and fine-grained feature mapping from the encoder subnetwork. More pinpoint precision is needed

in segmentation of lesions or abnormalities in medical images needs than regular images. Edge segmentation faults in medical imaging may cause some serious consequences in clinic. Therefore, a variety of methods to improve feature fusion have been proposed to address that. In addition, Zhou et al. [13, 45] improved the skip connection and proposed UNet++ with deep monitoring nested dense jump connection path.

As for U-Net, the feature map of the encoder is received by the decoder. But UNet++ uses a dense convolutional block and the quantity of convolutional layers relies on that of the U-shaped structure. In essence, the dense convolution block connects the semantic gap between the encoder and decoder feature maps. It is assumed that when the received encoder feature map and the related decoder feature map are similar at the semantic level, the optimizer can easily tackle the problems it encounters. The effective integration of U-Nets of different depths is used to alleviate unknown network depths. These U-Nets could share an encoder in part and simultaneously learn together through deep supervision, which will allow the model to be pruned and improved. This redesigned skip connection could aggregate semantic features of different scales on the decoder subnet, thereby automatically generating a highly flexible feature fusion scheme.

3.6. UNET 3+. UNet++, an improvement based on U-Net, was designed by developing a structure with nested and dense skip connections. But it does not express enough information from multiple scales and the network parameters are numerous and complex. UNet 3+ (UNet+++) is an innovative network structure proposed by Huang et al. [46], which uses full-scale skip connections and deep supervisions. Full-scale jump connection combines high-level semantics with low-level semantics from feature maps of various scales. Deep supervision learns hierarchical representations from feature maps aggregated at multiple scales. This method uses the newly proposed hybrid loss function to refine the results, particularly suitable for resolving organs of different sizes. It not only improves accuracy and computational efficiency, but also reduces network parameters after fewer channels compared to U-Net and UNet++. The network structure of UNet 3+ is shown in Figure 5.

To learn hierarchical representation from full-scale aggregated feature maps, UNet 3+ further adopts full-scale deep supervision. Different from UNet++, each decoder stage in UNet 3+ has a side output, which uses standard ground truth for supervision. To achieve in-depth supervision, the last layer at each decoder stage is sent to an ordinary 3×3 convolutional layer, followed by a bilinear upsampling and a sigmoid function to enlarge it to full resolution.

To further strengthen the organ's boundary, a multiscale structural similarity index loss function is proposed to give more weight to the fuzzy boundary. Facilitated by this, UNet 3+ will focus on fuzzy boundaries. The more significant the difference in regional distribution is, the greater the MS-SSIM value becomes [47].

In segmentation of most nonorgan images, false positives are inevitable. The background noise information most likely stays at a shallower level, causing oversegmentation. UNet3++ solves this problem by adding classification-guidance module (CGM) designed to foresee whether the input image has organs to realize more accurate segmentation. With the largest number of semantic information, the classification results could further direct each segmentation side to be output in two steps. With the help of the argmax function, the two-dimensional tensor is converted into a single output of {0, 1}, which represents the presence/absence of organs. Subsequently, the single classification output is multiplied with the side segmentation output. Given the simplicity of the binary classification task, this module could easily obtain accurate classification by optimizing the binary cross-entropy loss function [48] and realize the direction of oversegmentation of nonorgan images.

In summary, UNet 3+ maximizes the application of full-scale feature maps and achieves precise segmentation and efficient network structure with fewer parameters and deep supervision. It has been extensively validated, for example, on representative but demanding volumetric segmentation in medical imaging: (i) liver segmentation from 3D CT scans and (ii) whole heart and big vessels segmentation from 3D MR images [49]. The CGM and the hybrid loss function are further applied to obtain a higher level of accuracy in location-aware and boundary-aware segmented images.

3.7. nnU-Net. It has been designed for different tasks since U-Net was first proposed, with its different network structure, preprocessing, training, and inference. These options are dependent on each other and significant to the final result. Fabian et al. [15, 50] proposed nnU-Net, namely no new-Net. The network is based on 2D and 3D U-Net with a robust self-adaptive framework. It involves a set of three relatively simple U-Net models. Only slight modifications are made to the original U-Net, and no various extension plug-ins were used, including residual connection, dense connection, and various attention mechanisms. The nnU-Net gives unexpectedly accurate results in applications like accurate brain tumor segmentation [51]. Since medical images are often three-dimensional, the design of nnU-Net considers a basic U-Net architecture pool composed of 2D U-Net, 3D U-Net, and U-Net cascade. 2D and 3D U-Net could generate full-resolution results. The first stage of the cascaded network produces a low-resolution result and the second stage optimizes it.

Now that 3D U-Net is widely used, why is 2D still useful? This is because the author proves that when the data are anisotropic, the traditional 3D segmentation method becomes very poor in resolution. The 3D network takes up a lot of GPU memory. Then you could use smaller image slices for training, but for images of larger organs such as livers, this block-based method will hinder training. This is caused by the limited size of the receptive field; the network structure cannot collect enough contextual information to identify the target objects. A cascade model is used here to overcome the shortcomings of 3D U-Net on data sets with large image size.
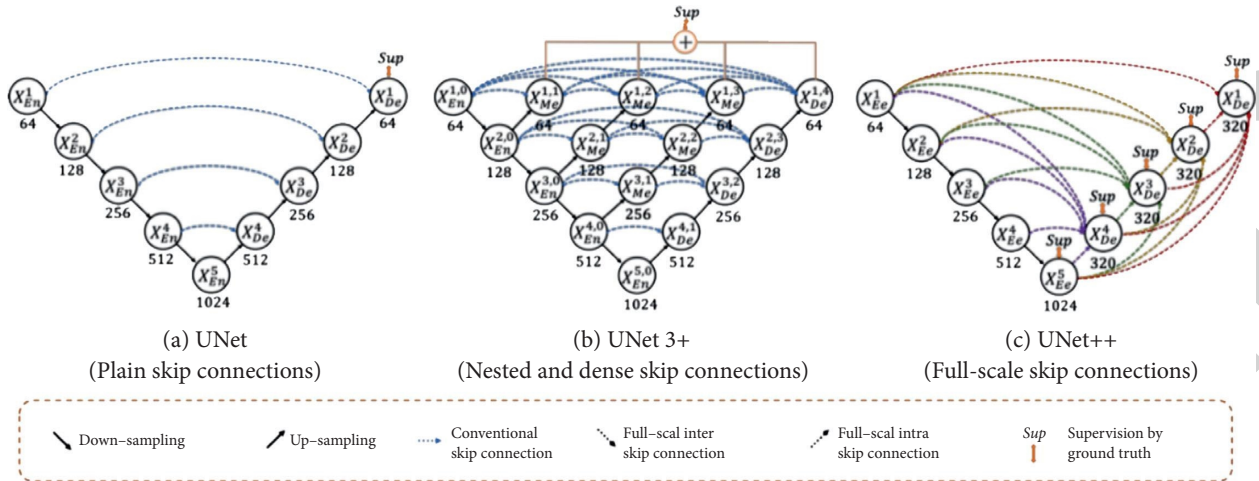
FIGURE 5: A graphic overview of UNet, UNet++, and UNet 3+. By optimizing jump connections and using full-scale depth monitoring, UNet 3+ integrates multiscale features and produces more precise location perception and segmentation maps with clarified boundaries, regardless of the fewer parameters provided [14, 46].

First, the first-level 3D U-Net is trained on the downsampled image and afterward the result is upsampled to the original voxel interval arrangement. The upsampling result is sent to the second-level 3D U-Net as an additional input channel (one-hot encoding) and the image block-based strategy is used for training on the full-resolution image.

The structure of U-Net has negated most of the new network structures in recent years. It is believed that the network structure has been advanced. The more complex the network, the greater the risk of overfitting. More attention should be paid to other factors such as preprocessing, training, reasoning strategies, and postprocessing.

3.8. U2-Net.
Salient object detection (SOD) [52] was designed to segment the most visually attractive objects in the image. It is extensively applied to eye-tracking data [53], image segmentation, and other fields. The recent years have seen a progress in deep CNN especially the emergence of FCN in image segmentation, which substantially enhances the performance of salient target detection. Most SOD network designs share a common pattern, which is to focus on the application of deep features extracted from the present backbone networks, e.g., AlexNet [54, 55], VGG [56], Res-Net [57], ResNeXt [39, 58], and DenseNet [59]. But these backbone networks were proposed for image classification, which extract features that represent semantics instead of local details and global contrast information that are crucial for saliency detection. They must pretrain on the data-inefficient ImageNet data, especially when the target data follows a different distribution from ImageNet.

U2-Net [16, 60] is an uncomplicated and powerful deep network used for salient target detection. It does not use a pretrained backbone model for image classification and could receive training from scratch. It could capture more contextual information because it uses the RSU (ReSidual U-blocks) structure [60, 61], which combines the characteristics of different scales of receptive fields. Meanwhile, it

enhances the depth with entire architecture but without significantly increasing computational cost when the pooling operations are applied to these RSU blocks.

RSU structure: as to SOD and other segmentation tasks, both local and global context information is of great significance. As to modern CNN designs, VGG, Res-Net, DenseNet, 1×1 or 3×3 small convolution filters are the most commonly used feature extraction components. Despite its high computational efficiency and small storage size, its filter experience is too small to capture global information; hence, the shallow output feature map only contains local features. To obtain more global information on the shallow high-resolution topographic map [62, 63], the most direct method is to expand the receiving field.

The existing convolutional block with the smallest receptive field fails to obtain global information, and the output feature map at the bottom layer only contains local features. To obtain richer global information on high-resolution shallow feature maps, the receptive field must be expanded. There are attempts to expand the receptive field by using hole convolution to extract local and nonlocal features. However, performing multiple extended convolutions on the input feature map of the original resolution (especially in the initial stage) requires a large amount of computing and memory resources. Inspired by U-Net, a new RSU is proposed to obtain multiscale features within the stage. RSU is mainly composed of three parts as follows.

(1) Input convolutional layer: convert the input feature map $\text{x}(H \times W \times C_{\text{in}})$ into an intermediate image $F_1(x)$ with the number of C_{out} channels to extract local features.

(2) Use the intermediate feature map $F_1(x)$ as input and learn to extract and encode multiscale context information $U(F_1(x))$. U refers to U-Net. The greater the L, the deeper the RSU and the more pooling operations, the bigger the receptive field and the more local and global features.

(3) Through the summation of $F_1(x)$, local features and multiscale features are merged.

Hence the residual U-block RSU about how to stack and connect these structures is proposed. It results in a completely different method from previous cascade stacking: Un-Net. The exponential notation here means a nested U-shaped structure rather than a cascaded stack. In theory, the index n could be adjusted to any positive integer to realize a single-layer or multilayer nested U-shaped structure. However, to be applied to practical applications. n is set to 2 to form the two-leveled U2-Net. The top layer of it is a large U-shaped structure including 11 stages with each filled with a well-configured RSU. Therefore, the nested U structure could extract the multiscale features in each stage and the multilevel features in the aggregation stage with higher efficiency. Unlike those SOD models which are built on present backbones, U2-Net is constructed on the proposed RSU block that allows training from scratch and different model sizes to be configured according to the constraints of the target environment.

3.9. TransUNet. Due to the inherent locality of convolution operations, U-Net is usually limited in explicitly modeling remote dependencies. Recently, the transformer designed for sequence-to-sequence prediction has emerged as an alternative architecture with a global self-attention mechanism. However, its positioning capabilities are limited by its insufficient underlying details. TransUNet with the advantages of transformer [64] and U-Net was proposed by Chen et al. [17] as a powerful alternative to medical image segmentation. This is because the transformer treats the input as a one-dimensional sequence and only focuses on modeling the global context of all stages, which results in low-resolution features and a lack of detailed positioning information. Direct upsampling to full resolution cannot effectively recover this information, which results in rough segmentation results. In addition, the U-Net architecture provides a way to achieve precise positioning by extracting low-level features and linking them to high-resolution CNN feature maps, which could adequately complement for fine spatial details. An overview of the framework is shown in Figure 6.

The transformer could be used as a powerful encoder for medical image segmentation and combined with U-Net to enhance finer details and restore local spatial information. TransUNet has achieved excellent performance in multi-organ segmentation and heart segmentation. In the design of TransUNet, the issue is how to encode the feature representation directly from the decomposed image patch using the transformer.

In order to complete the purpose of segmentation, that is, to classify the image at the pixel level, the most direct method is to upsample the encoded feature map to predict the full resolution of the dense output. To restore the spatial order, the size of the coding function should first reshape the size of the image from HW/P^2 to $H/P \times W/P$. The next step is to use 1×1 convolution to decrease the channel size of the reshaped feature to the number of classes. Afterward, directly upsampling the feature map to full resolution $H \times W$ is performed to predict the final segmentation result.

In summary, TransUNet mixes CNN and transformer as an encoder and allows the use of medium and high-resolution CNN feature maps in the decoding path, hence more context information can be involved. TransUNet not only uses image features as a sequence to encode strong global context but also makes good use of low-level CNN features through a U-shaped hybrid frame design.

4. Overview of Validation Methods of Resultant Experiments

4.1. Evaluation Parameters. The several U-Net-based extended structure networks introduced above possess different improved structures and characteristics, and their effects in real-world applications vary. Therefore, this paper summarized the corresponding advantages of each by comparing the parameters. The segmentation evaluation parameters play a crucial part in the evaluation of image segmentation performance. This section mainly lists several commonly used evaluation parameters in image segmentation neural networks and illustrates the characteristics of each network in various experiments.

True positive (TP), true negative (TN), false positive (FP), and false negative (FN) are mainly used to count two types of classification problems. There is no doubt that multiple categories could also be counted separately. The samples are divided into positive and negative samples.

4.2. Performance Comparison. The related methods proposed in this paper use almost different data sets including retinal blood vessels, liver, kidney, gastric cancer, and cell sections. The data sets used by various methods are not the same; hence, it is difficult to compare different methods horizontally. This paper listed the data sets to provide an index of data set names. The performance comparison is listed in Table 1.

4.3. Future Development. Medical image segmentation is a popular and developing research field. As an implementation standard of medical segmentation, the U-Net network structure has been in use and improved for many years. Although the work and improvements of U-Net in recent years have begun to solve the challenges presented in Section 2, there are still some unsolved problems. In this part, some promising research discussing those problems will be outlined (accuracy issues, interpretability, and network training issues) and other challenges that may still exist will be introduced.

4.3.1. Higher Generalization Ability. The model is not only required to have a good fit (training error) to the training data set but also to have a good fit (generalization ability) to the unknown data set (prediction set). As for tasks like medical image segmentation, small sample data are usually more prone to overfitting or underfitting. Therefore, the frequently used methods such as early stopping, regularization, feedback, input fuzzification, and dropout have
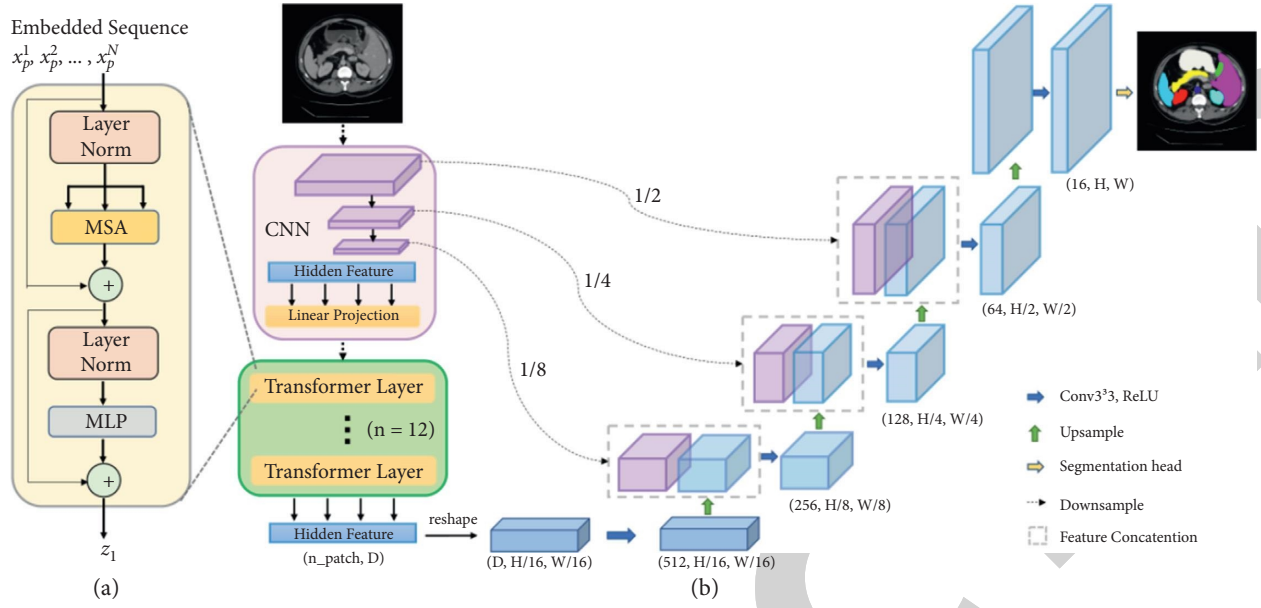
FIGURE 6: Overview of TransUNet's framework. (a) The transformer layer's structure and (b) the entire TransUNet's structure. After the U-Net encoding stage of the network, a transformer structure composed of 12 layers of transformers is added to process the corresponding processed image sequence. Then the number of channels and dimensions of the picture are unified to the standard by redetermining the size [17].

TABLE 1: Performance contrast of the networks listed in this article. Different methods use different data sets for evaluation, which makes it hard to compare various approaches horizontally.

U-net type	Medical image data base	Evaluation parameters	Values
U-Net [1]	DRIVE [1]	Accuracy	0.955 ± 0.003 [1]
	Amazon data set	IoU	0.9530 [64]
3D U-Net [29]	Xenopus kidney embryos	IoU	0.732 [29]
Attention U-Net [7]	Gastric cancer [7]	Dice coefficient	0.767 ± 0.132 [7]
	Amazon data set [64]	IoU	0.9581 [64]
CE-Net [10]	DRIVE [10]	Accuracy	0.975 ± 0.003 [10]
	Lung segmentation CT	IoU	0.9495 [65]
U-Net++ [12]	Cell nuclei [12]	Jaccard/IoU	0.9263 [12]
	Lung segmentation CT [65]	IoU	0.9521 [65]
UNET 3+ [13]	ISBI LiTS 2017	Dice coefficient	0.9552
nnU-Net [14]	BRATS challenge	Dice coefficient	0.8987 ± 0.157
U2 Net [15]	Vienna reading [15]	Dice coefficient	0.8943 ± 0.04 [15]
	CVC-ClinicDB	IoU	0.8611 [66]
TransUNet [16]	MICCAI 2015	Dice coefficient	0.7748
	CVC-ClinicDB	IoU	0.89 [66]

improved the generalization problem of neural networks to varying degrees. But in general, the essence of the neural network is instance learning and the network has the cognition of most instances through limited samples. However, recently it has been suggested to seek innovation and abandon the long-used input vector fuzzification processing method.

4.3.2. Improved Interpretability. As for Interpretability or Explainable Artificial Intelligence (XAI), what always concerns researchers engaged in machine learning is that many current deep neural networks cannot fully understand the decision-making models from human's perspective. We do

not know when there will be an error and what causes it in medical images. Medical images reflect on people's health; hence, interpretability is crucial. Now, people often use sensitivity analysis or gradient-based analysis methods for interpretability analysis. There are many attempts to implement interpretability after training such as surrogate models, knowledge distillation, and hidden layer visualization.

4.3.3. Resolution and Processing of Data Imbalance. Data imbalance often occurs due to inconsistent machine models in medical image segmentation. But in fact, many common imbalance problems can be avoided. Nowadays, the
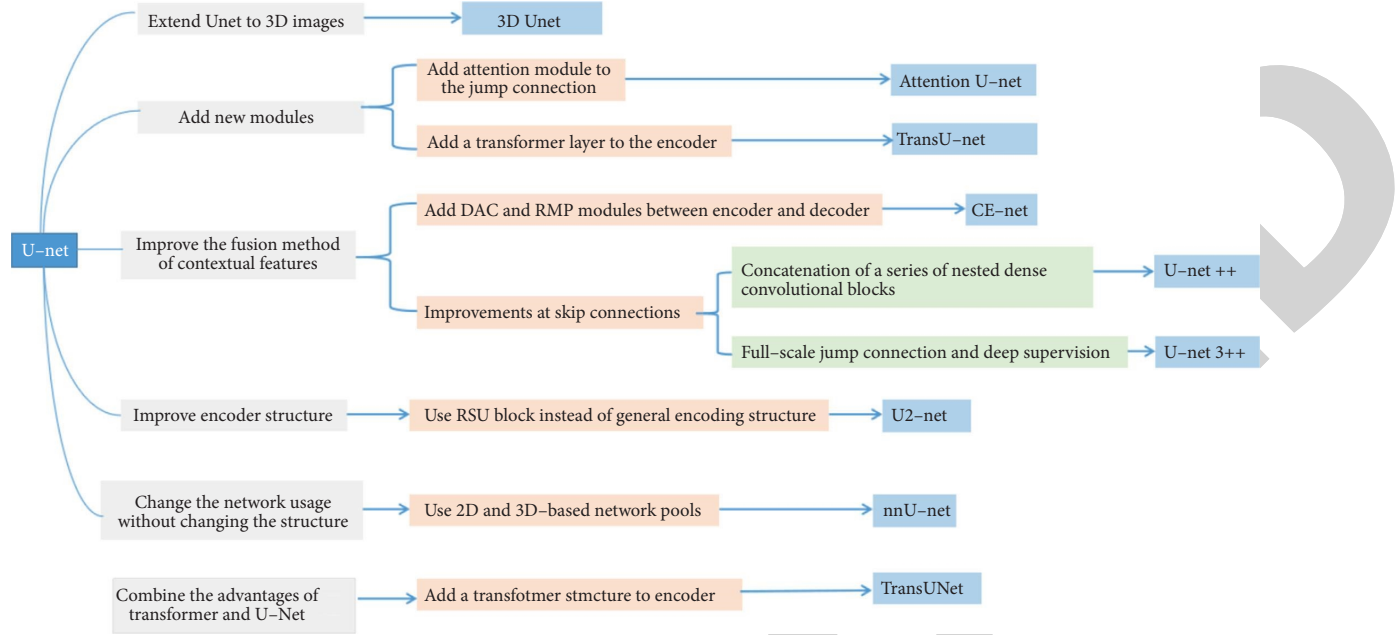
FIGURE 7: U-Net-based extension structure summary diagram.

TABLE 2: The summary of the changes in network structures and adjusted parameters. The number of parameters for a $K \times K (\times K)$ size convolution kernel, C_i input channels, and C_o output channels is a $K \times K (\times K) \times C_i \times C_o$ and is given below for a few U-Net variants.

Model structure	Dimension	Improved structure	Highlights	#Params	Kernel size
U-Net	2D	Fully connected layer (relative to CNN)	Fully connected layer changed to upsampling layer	30M [67]	3×3; 2×2; 1×1
3D U-Net	3D	Encoder, decoder	2D convolution operation replaced with 3D	19M [68]	$1 \times 1 \times 1$; $2 \times 2 \times 2$; $3 \times 3 \times 3$
Attention U-Net	2D	Skip connection	Add the attention module to the skip connection	123M [65]	1×1
CE-Net	2D	Bottleneck between encoder and decoder	DAC and RMP structure	110 [65]	3×3; 1×1
UNET++	2D	Skip connection	Use dense blocks and in-depth supervision	35 [65]	3×3; 1×1
UNET 3+	2D	Skip connection	Full-scale jump connection and deep supervision	26.97 [69]	3×3; $3 \times 3 \times 3$
nnU-Net	2D/3d	Network organization	Multiple ordinary U-Nets form a network pool		$4 \times 4 \times 4$
U2-Net	2D	Encoder and decoder	Use RSU as the decoding and encoding unit	176M [70]	3×3
Trans-U-Net	2D	Encoder	Add the transformer module after the decoder	2.93M [66, 71]	1×1

common ways to solve them include expanding the data, using different evaluation indicators, resampling the data set, trying artificial data samples, and using different algorithms. It was suggested in a recent ICML paper that the increased amount of data could increase the error of the training set with a known distribution and destroys the original training set's allocation, thereby improving the classifier's performance. This paper implicitly used mathematical methods to increase the data without changing the size of the data set. However, we believe that destroying the original distribution is beneficial for dealing with imbalances.

4.3.4. A New Exploration of Transformer and Attention Mechanism. This paper introduced attention and transformer methods that afford an innovative combination of these two mechanisms and U-Net. So far, some research has explored the feasibility of using the Transformer structure which only works on the self-attention mechanism as an

encoder for medical image segmentation without any pre-training. In the future, more novel models will be proposed to solve different problems in medical segmentation with continuous breakthroughs in attention and transformer methods.

4.3.5. Multimodal Learning and Application. Single-modal representation learning is to express information as numerical vectors that could be processed by the computer or further abstracted into higher-level feature vectors, while multimodal representation learning is to eliminate intermodality by taking advantage of the complementarity between multiple modalities. In medical images, multimodal data with different imaging mechanisms could provide information at multiple levels. Multimodal image segmentation is used to fuse information among different modalities for multimodal fusion and collaborative learning. Research on multimodal learning is becoming more popular in recent years and the application of medical images will grow more sophisticated in the future.

5. Discussion and Conclusion

This paper introduces several classic networks with improved U-Net structures to deal with different problems that are encountered in medical image segmentation. We review the paper.

A summary of the technical context based on the U-Net extended structure introduced above is shown in Figure 7.

This paper summarized U-Net network dimensions, improved structure, and structure parameters, along with kernel size. Table 2 summarized these aspects.

U-Net could meet the high-precision segmentation of all lesions with its differentiation of organ structures and the diversification of lesion shapes. With the development and improvement of attention mechanism, dense module, transformer module, residual structure, graph cut, and other modules, different modules based on U-Net have been used recently to achieve precise segmentation of different lesions. Based on the various U-Net extended structures, this paper classifies and analyzes several classic medical image segmentation methods based on the U-Net structure.

It is concluded that U-Net-based architecture is indeed quite ground-breaking and valuable in medical image analysis. However, although U-Net-based deep learning has become a dominant method in a variety of complex tasks such as medical image segmentation and classification, it is not all-powerful. It is essential to be familiar with key concepts and advantages of U-Net variants as well as limitations of it, in order to leverage it in radiology research with the goal of improving radiologist performance and, eventually, patient care. Despite the many challenges remaining in deep learning-based image analysis, U-Net is expected to be one of the major paths forward [72–80].

Conflicts of Interest

The authors declare that they have no conflicts of interest.

References

[1] R. Smith-Bindman, M. L. Kwan, E. C. Marlow et al., "Trends in use of medical imaging in US health care systems and in Ontario, Canada, 2000-2016," *JAMA*, vol. 322, no. 9, pp. 843–856, 2019 Sep 3.

[2] O. Ronneberger, P. Fischer, and T. Brox, "U-net: convolutional networks for biomedical image segmentation," in *Proceedings of the Medical Image Computing and Computer-Assisted Intervention – MICCAI 2015*, N. Navab, J. Hornegger, W. Wells, and A. Frangi, Eds., October 2015.

[3] X. X. Yin, B. W.-H. Ng, and Q. Yang, A. Pitman, K. Ramamohanarao, and D. Abbott, Anatomical landmark localization in breast dynamic contrast-enhanced MR imaging," *Medical, & Biological Engineering & Computing*, vol. 50, no. 1, pp. 91–101, 2012.

[4] X.-X. Yin, S. Hadjiloucas, J.-H. Chen, Y. Zhang, J.-L. Wu, and M.-Y. Su, "Correction: tensor based multichannel reconstruction for breast tumours identification from DCE-MRIs," *PLoS One*, vol. 12, no. 4, p. e0176133, 2017.

[5] P. Radiuk, "Applying 3D U-net architecture to the task of multi-organ segmentation in computed tomography," *Applied Computer Systems*, vol. 25, no. 1, pp. 43–50, 2020.

[6] Q. Tong, M. Ning, W. Si, X. Liao, and J. Qin, "3D deeply-supervised U-net based whole heart segmentation," in *Statistical Atlases and Computational Models of the Heart. ACDC and MMWHS Challenges. STACOM 2017*, M. Pop, Ed., vol. 10663, Cham. Switzerland, Springer, 2018.

[7] C. Wang, T. MacGillivray, G. Macnaught, G. Yang, and D. Newby, "A two-stage U-net model for 3D multi-class segmentation on full-resolution cardiac data," in *Statistical Atlases and Computational Models of the Heart. Atrial Segmentation and LV Quantification Challenges. STACOM 2018*, M. Pop, Ed., vol. 11395, Springer, Cham. Switzerland, 2019.

[8] O. Oktay, J. Schlemper, L. Folgoc et al., "Attention U-Net: Learning where to Look for the Pancreas," in *Proceedings of the 1st Conference on Medical Imaging with Deep Learning*, Amsterdam, The Netherlands, July 2018.

[9] R. Yamashita, M. Nishio, R. K. G. Do, and K. Togashi, "Convolutional neural networks: an overview and application in radiology," *Insights into Imaging*, vol. 9, no. 4, pp. 611–629, 2018.

[10] J. Long, E. Shelhamer, and T. Darrell, "Fully Convolutional Networks for Semantic Segmentation," in *Proceedings of the IEEE conference on computer vision and pattern recognition*, pp. 3431–3440, Boston, MA, USA, June 2015.

[11] P. Jaccard, "The distribution of the flora in the alpine Zone.1," *New Phytologist*, vol. 11, no. 2, pp. 37–50, February 1912.

[12] Z. Gu, J. Cheng, H. Fu et al., "CE-net: context encoder network for 2D medical image segmentation," *IEEE Transactions on Medical Imaging*, vol. 38, no. 10, pp. 2281–2292, 2019.

[13] Z. Zhou, M. M. R. Siddiquee, N. Tajbakhsh, and J. Liang, "UNet++: a nested U-net architecture for medical image segmentation," *Deep Learning in Medical Image Analysis and Multimodal Learning for Clinical Decision Support*, vol. 11045, pp. 3–11, 2018.

[14] H. Huang, L. Lin, R. Tong et al., "UNet 3+: a full-scale connected UNet for medical image segmentation," in *Proceedings of the ICASSP 2020 - 2020 IEEE International Conference on Acoustics, Speech and Signal Processing (ICASSP)*, pp. 1055–1059, Barcelona, Spain, May 2020.

[15] F. Isensee, P. F. Jaeger, S. A. A. Kohl, J. Petersen, and K. H. Maier-Hein, "nnU-Net: a self-configuring method for deep learning-based biomedical image segmentation," *Nature Methods*, vol. 18, no. 2, pp. 203–211, 2021.

[16] X. Qin, Z. Zhang, C. Huang, M. Dehghan, O. R. Zaiane, and M. Jagersand, "U2-Net: going deeper with nested U-structure for salient object detection," *Pattern Recognition*, vol. 106, p. 107404, 2020.

[17] J. Chen, Y. Lu, Q. Yu et al., "TransUNet: Transformers Make Strong Encoders for Medical Image Segmentation," 2021, https://arxiv.org/abs/2102.04306.

[18] X. X. Yin, S. Hadjiloucas, and Y. Zhang, *Pattern Classification of Medical Images: Computer Aided Diagnosis*, Springer-Verlag, Heidelberg, Germany, 2017.

[19] S. Irshad, X. Yin, and Y. Zhang, "A new approach for retinal vessel differentiation using binary particle swarm optimization," *Computer Methods in Biomechanics and Biomedical Engineering: Imaging & Visualization*, vol. 9, no. 5, pp. 510–522, 2021.

[20] X. Yin, S. Irshad, and Y. Zhang, "Classifiers fusion for improved vessel recognition with application in quantification of generalized arteriolar narrowing," *Journal of Innovative Optical Health Sciences*, vol. 13, no. 01, p. 1950021, 2020.

[21] X. X. Yin, L. Yin, and S. Hadjiloucas, "Pattern classification approaches for breast cancer identification via MRI: state-of-the-art and vision for the future," *Applied Sciences*, vol. 10, no. 20, p. 7201, 2020.

[22] D. Pandey, X. Yin, H. Wang, and Y. Zhang, "Accurate vessel segmentation using maximum entropy incorporating line detection and phase-preserving denoising," *Computer Vision and Image Understanding*, vol. 155, pp. 162–172, 2017.

[23] X. X. Yin, S. Hadjiloucas, Y. Zhang et al., "Pattern identification of biomedical images with time series: contrasting THz pulse imaging with DCE-MRIs," *Artificial Intelligence in Medicine*, vol. 67, pp. 1–23, 2016.

[24] T. J. Sejnowski, "The unreasonable effectiveness of deep learning in artificial intelligence," *Proceedings of the National Academy of Sciences*, vol. 117, no. 48, pp. 30033–30038, 2020.

[25] P. J. R Prasad, O. J Elle, F. Lindseth, F. Albregtsen, and R. P. Kumar, "Modifying U-Net for small data set: a simplified U-Net version for liver parenchyma segmentation," in *Proceedings of the SPIE 11597, Medical Imaging 2021: Computer-Aided Diagnosis*, February 2021.

[26] D. Chen, S. Liu, P. Kingsbury et al., "Deep learning and alternative learning strategies for retrospective real-world clinical data," *Npj Digital Medicine*, vol. 2, no. 1, p. 43, 2019.

[27] M. Reyes, R. Meier, S. Pereira et al., "On the interpretability of artificial intelligence in radiology: challenges and opportunities," *Radiology: Artificial Intelligence*, vol. 2, no. 3, p. e190043, 2020.

[28] S. Zheng, X. Lin, W. Zhang et al., "MDCC-Net: multiscale double-channel convolution U-Net framework for colorectal tumor segmentation," *Computers in Biology and Medicine*, vol. 130, p. 104183, 2021.

[29] X. Liu, L. Song, S. Liu, and Y. Zhang, "A review of deep-learning-based medical image segmentation methods," *Sustainability*, vol. 13, no. 3, p. 1224, 2021.

[30] Ö. Çiçek, A. Abdulkadir, S. S. Lienkamp, T. Brox, and O. Ronneberger, "3D U-net: learning dense volumetric segmentation from sparse annotation," in *Proceedings of the Medical Image Computing and Computer-Assisted Intervention – MICCAI 2016*, S. Ourselin, L. Joskowicz, M. Sabuncu, G. Unal, and W. Wells, Eds., October, 2016.

[31] S. Ioffe and C. Szegedy, "Batch normalization: accelerating deep network training by reducing internal covariate shift, ICML'15," in *Proceedings of the 32nd International Conference on International Conference on Machine Learning*, vol. 37, pp. 448–456, Lille, France, July, 2015.

[32] J. Schlemper, O. Oktay, M. Schaap et al., "Attention gated networks: learning to leverage salient regions in medical images," *Medical Image Analysis*, vol. 53, pp. 197–207, 2019.

[33] H. Ma, Y. Zou, and P. X. Liu, "MHSU-Net: a more versatile neural network for medical image segmentation," *Computer Methods and Programs in Biomedicine*, vol. 208, p. 106230, 2021.

[34] B. Jin, P. Liu, P. Wang, L. Shi, and J. Zhao, "Optic disc segmentation using attention-based U-net and the improved cross-entropy convolutional neural network," *Entropy*, vol. 22, no. 8, p. 844, 2020.

[35] C. Han, Y. Duan, X. Tao, and J. Lu, "Dense convolutional networks for semantic segmentation," *IEEE Access*, vol. 7, pp. 43369–43382, 2019.

[36] R. F. Mansour and N. O. Aljehane, *An Optimal Segmentation with Deep Learning Based Inception Network Model for Intracranial Hemorrhage Diagnosis*, Neural Comput & Applic, London, UK, 2021.

[37] C. Szegedy, S. Ioffe, V. Vanhoucke, and A. A. Alemi, "Inception-v4, inception-resnet and the impact of residual connections on learning," in *Proceedings of the Thirty-first AAAI conference on artificial intelligence*, vol. 4, p. 12, San Francisco, California, USA, February, 2017.

[38] K. He, X. Zhang, S. Ren, and J. Sun, "Deep residual learning for image recognition," in *Proceedings of the Computer Vision and Pattern Recognition (CVPR)*, pp. 770–778, IEEE, Las Vegas, Nevada, July, 2016.

[39] M. H. Hesamian, W. Jia, X. He, and P. Kennedy, "Deep learning techniques for medical image segmentation: achievements and challenges," *Journal of Digital Imaging*, vol. 32, no. 4, pp. 582–596, 2019.

[40] T. Zhou, R. Su, and S. Canu, "A review: deep learning for medical image segmentation using multi-modality fusion," *Array*, vol. 3–4, p. 100004, 2016.

[41] T. J. Anchordoquy, Y. Barenholz, D. Boraschi et al., "Mechanisms and barriers in cancer nanomedicine: addressing challenges, looking for solutions," *ACS Nano*, vol. 11, no. 1, pp. 12–18, 2017.

[42] J. Jin, H. Zhu, J. Zhang et al., "Multiple U-Net-Based automatic segmentations and radiomics feature stability on ultrasound images for patients with ovarian cancer," *Frontiers in Oncology*, vol. 10, p. 614201, 2021.

[43] Y. Ma, H. Hao, J. Xie et al., "ROSE: a retinal OCT-angiography vessel segmentation data set and new model," *IEEE Transactions on Medical Imaging*, vol. 40, no. 3, pp. 928–939, 2020.

[44] P. Saivironporn, K. Rodbangyang, T. Tongdee et al., "Cardiothoracic ratio measurement using artificial intelligence: observer and method validation studies," *BMC Medical Imaging*, vol. 21, pp. 1–11, 2021.

[45] Z. Zhou, J. Shin, L. Zhang, S. Gurudu, M. Gotway, and J. Liang, "Fine-tuning convolutional neural networks for biomedical image analysis: actively and incrementally," in *Proceedings of the IEEE Conference on Computer Vision and Pattern Recognition (CVPR)*, pp. 7340–7351, Honolulu, HI, USA, July, 2017.

[46] H. Huang, L. Lin, R. Tong et al., "UNet 3+: a full-scale connected UNet for medical image segmentation," 2020, https://arxiv.org/abs/2004.08790.

[47] G. Mattyus, W. Luo, and R. Urtasun, "DeepRoadMapper: extracting road topology from aerial images," *Proceedings of the IEEE International Conference on Computer Vision (ICCV)*, pp. 3438–3446, Venice, Italy, October, 2017.

[48] P.-T. de Boer, D. P. Kroese, S. Mannor, and R. Y. Rubinstein, "A tutorial on the cross-entropy method," *Annals of Operations Research*, vol. 134, no. 1, pp. 19–67, 2005.

[49] Q. Dou, L. Yu, H. Chen et al., "3D deeply supervised network for automated segmentation of volumetric medical images," *Medical Image Analysis*, vol. 41, pp. 40–54, 2017.

[50] F. Isensee, R. Sparks, and S. Ourselin, "Batchgenerators — a Python Framework for Data Augmentation," 2020, https://zenodo.org/record/3632567#.YkGUnOdBzIU.

[51] Y. Zhang, S. Liu, C. Li, and J. Wang, "Rethinking the dice loss for deep learning lesion segmentation in medical images," *Journal of Shanghai Jiaotong University*, vol. 26, no. 1, pp. 93–102, 2021.

[52] A. Borji, D. N. Sihite, and L. Itti, "Salient object detection: a benchmark," in *Proceedings of the Computer Vision – ECCV 2012*, A. Fitzgibbon, S. Lazebnik, P. Perona, Y. Sato, and C. Schmid, Eds., October, 2012.

[53] F. Xiao, L. Peng, L. Fu, and X. Gao, "Salient object detection based on eye tracking data," *Signal Processing*, vol. 144, pp. 392–397, 2018.

[54] O. Russakovsky, J. Deng, H. Su et al., "ImageNet large scale visual recognition challenge," *International Journal of Computer Vision*, vol. 115, no. 3, pp. 211–252, 2015.

[55] A. Krizhevsky, I. Sutskever, and G. E. Hinton, "ImageNet classification with deep convolutional neural networks," *Advances in Neural Information Processing Systems*, vol. 25, 2012.

[56] S. Liu and W. Deng, "Very deep convolutional neural network based image classification using small training sample size," in *Proceedings of the 2015 3rd IAPR Asian Conference on Pattern Recognition (ACPR)*, vol. 5, pp. 730–734, Kuala Lumpur, Malaysia, November, 2015.

[57] Q. Chen, H. Yue, X. Pang et al., "Mr-ResNeXt: a multi-resolution network architecture for detection of obstructive sleep apnea," in *Neural Computing for Advanced Applications. NCAA 2020. Communications in Computer and Information Science*, H. Zhang, Z. Zhang, Z. Wu, and T. Hao, Eds., vol. 1265, Singapore, Springer, 2020.

[58] S. Xie, R. Girshick, P. Dollar, Z. Tu, and K. He, "Aggregated residual transformations for deep neural networks," in *Proceedings of the 2017 IEEE Conference on Computer Vision and Pattern Recognition (CVPR)*, pp. 5987–5995, Honolulu, HI, USA, July, 2017.

[59] G. Huang, Z. Liu, L. Van Der Maaten, and K. Q. Weinberger, "Densely connected convolutional networks," in *Proceedings of the 2017 IEEE Conference on Computer Vision and Pattern Recognition (CVPR)*, pp. 2261–2269, Honolulu, HI, USA, July, 2017.

[60] J. I. Orlando, P. Seebock, H. Bogunovic et al., "U2-Net: a bayesian U-net model with epistemic uncertainty feedback for photoreceptor layer segmentation in pathological OCT scans," in *Proceedings of the 2019 IEEE 16th International Symposium on Biomedical Imaging (ISBI 2019)*, pp. 1441–1445, Venice, Italy, April 2019.

[61] D. Li, D. A. Dharmawan, B. P. Ng, and S. Rahardja, "Residual U-net for retinal vessel segmentation," in *Proceedings of the 2019 IEEE International Conference on Image Processing*, pp. 1425–1429, ICIP), Taipei, Taiwan, September 2019.

[62] A. J. Kent and A. Hopfstock, "Topographic mapping: past, present and future," *The Cartographic Journal*, vol. 55, no. 4, pp. 305–308, 2018.

[63] A. Kent, "Topographic maps: methodological approaches for analyzing cartographic style," *Journal of Map & Geography Libraries*, vol. 5, no. 2, pp. 131–156, 2009.

[64] D. John and C. Zhang, "An attention-based U-Net for detecting deforestation within satellite sensor imagery," *International Journal of Applied Earth Observation and Geoinformation*, vol. 107, p. 102685, 2022.

[65] R. Su, D. Zhang, J. Liu, and C. Cheng, "MSU-net: multi-scale U-net for 2D medical image segmentation," *Frontiers in Genetics*, vol. 12, p. 639930, 2021.

[66] A.-J. Lin, B. Chen, J. Xu, Z. Zhang, and G. Lu, "DS-TransUNet: Dual Swin Transformer U-Net for Medical Image Segmentation," 2021, https://arxiv.org/abs/2106.06716.

[67] N. Beheshti and L. Johnsson, "Squeeze U-net: a memory and energy efficient image segmentation network," in *Proceedings of the 2020 IEEE/CVF Conference on Computer Vision and Pattern Recognition Workshops (CVPRW)*, pp. 1495–1504, Seattle, WA, USA, June, 2020.

[68] C. Ozgun, A. Abdulkadir, S. S. Lienkamp, T. Brox, and O. Ronneberger, "3D U-net: learning dense volumetric segmentation from sparse annotation," in *Proceedings of the Medical Image Computing and Computer-Assisted Intervention -- MICCAI 2016*, pp. 424–432, Springer International Publishing, Athens, Greece, October, 2016.

[69] H. Huang, L. Lin, R. Tong et al., "UNet 3+: A Full-Scale Connected UNet for Medical Image Segmentation," in *Proceedings of the 2020 IEEE International Conference on Acoustics, Speech and Signal Processing (ICASSP 2020)*, pp. 1055–1059, Barcelona, Spain, May, 2020.

[70] C. Wang, C. Li, J. Liu et al., "U2-ONet: a two-level nested octave U-structure network with a multi-scale Attention mechanism for moving object segmentation," *Remote Sensing*, vol. 13, no. 1, 2021.

[71] Y. Yang and S. Mehrkanoon, "AA-TransUNet: Attention Augmented TransUNet For Nowcasting Tasks," 2022, https://arxiv.org/abs/2202.04996.

[72] X. Jiang, Y. Wang, Y. Wang, W. Liu, and S. Li, "CapsNet, CNN, FCN: comparative performance evaluation for image classification," *International Journal of Machine Learning and Computing*, vol. 9, no. 6, pp. 840–848, 2019.

[73] Z. Wang, E. P. Simoncelli, and A. C. Bovik, "Multiscale structural similarity for image quality assessment," *and Computers*, vol. 2, pp. 1398–1402, 2003.

[74] T. Y. Lin, P. Goyal, R. Girshick, K. He, and P. Dollar, "Focal loss for dense object detection," *IEEE Transactions on Pattern Analysis and Machine Intelligence*, vol. 42, no. 02, pp. 318–327, 2020.

[75] F. Isensee, P. F. Jäger, P. M. Full, P. Vollmuth, and K. H. Maier-Hein, "nnU-net for brain tumor segmentation," in *Brainlesion: Glioma, Multiple Sclerosis, Stroke and Traumatic Brain Injuries. BrainLes 2020*, A. Crimi and S. Bakas, Eds., vol. 12659, Cham. Switzerland, Springer, 2021.

[76] A. Dosovitskiy, L. Beyer, A. Kolesnikov et al., "An image is worth 16x16 words: transformers for image recognition at scale," 2021, https://arxiv.org/abs/2010.11929.

Retraction

Retracted: An Association between EMX2 Variations and Mayer-Rokitansky-Küster-Hauser Syndrome: A Case-Control Study of Chinese Women

Journal of Healthcare Engineering

This article has been retracted by Hindawi following an investigation undertaken by the publisher [1]. This investigation has uncovered evidence of one or more of the following indicators of systematic manipulation of the publication process:

(1) Discrepancies in scope

(2) Discrepancies in the description of the research reported

(3) Discrepancies between the availability of data and the research described

(4) Inappropriate citations

(5) Incoherent, meaningless and/or irrelevant content included in the article

(6) Peer-review manipulation

The presence of these indicators undermines our confidence in the integrity of the article's content and we cannot, therefore, vouch for its reliability. Please note that this notice is intended solely to alert readers that the content of this article is unreliable. We have not investigated whether authors were aware of or involved in the systematic manipulation of the publication process.

Wiley and Hindawi regrets that the usual quality checks did not identify these issues before publication and have since put additional measures in place to safeguard research integrity.

We wish to credit our own Research Integrity and Research Publishing teams and anonymous and named external researchers and research integrity experts for contributing to this investigation.

The corresponding author, as the representative of all authors, has been given the opportunity to register their agreement or disagreement to this retraction. We have kept a record of any response received.

References

[1] H. Li, S. Liao, G. Luo et al., "An Association between EMX2 Variations and Mayer-Rokitansky-Küster-Hauser Syndrome: A Case-Control Study of Chinese Women," *Journal of Healthcare Engineering*, vol. 2022, Article ID 9975369, 6 pages, 2022.

Research Article

An Association between EMX2 Variations and Mayer-Rokitansky-Küster-Hauser Syndrome: A Case-Control Study of Chinese Women

Haiping Li,[1,2] Shi Liao,[3] Guangnan Luo,[3] Haixia Li,[4] Shuai Wang,[5] Zhimin Li,[2] and Xiping Luo [1,2]

[1]*Department of Obstetrics and Gynecology, The First Affiliated Hospital of Jinan University, Guangzhou, Guangdong 511442, China*
[2]*Department of Gynecology, Guangdong Women and Children Hospital, Guangzhou, Guangdong 511442, China*
[3]*Department of Gynecology, The Third Affiliated Hospital of Shenzhen University, Shenzhen, Guangdong 518005, China*
[4]*School of Basic Medical Sciences, Hubei University of Medicine, Shiyan, Hubei 442000, China*
[5]*Department of Obstetrics and Gynecology, The Sixth Affiliated Hospital, South China University of Technology, Foshan, Guangdong 528237, China*

Correspondence should be addressed to Xiping Luo; 2008760228@gzhmu.edu.cn

Mayer-Rokitansky-Küster-Hauser (MRKH) syndrome is characterized by congenital malformations of Müllerian structures, including the uterus and upper two-thirds of the vagina in women. Until now, the etiology of this disease has remained unknown. We hypothesized that EMX2 (the human homologue of *Drosophila* empty spiracles gene (2) might be a candidate gene for MRKH syndrome because it plays an important role in the development of the urogenital system. Through sequence analysis of EMX2 in forty patients with MRKH syndrome and one hundred and forty healthy women controls, we identified eleven variations in total. Four novel variations were only found in MRKH patients, and seven single nucleotide polymorphisms were identified in both patients and controls. In silico analyses suggested that the novel variations in the 5′UTR (untranslated region) and 3′UTR might affect transcriptional activity of the EMX2 promoter or posttranscriptional processing. In conclusion, our study suggests an association between noncoding variations in the EMX2 gene and MRKH syndrome in a Chinese Han population.

1. Introduction

Mayer-Rokitansky-Küster-Hauser (MRKH) syndrome is characterized by congenital malformations of Müllerian structures, including the uterus and upper two-thirds of the vagina. It is also referred to as CAUV (congenital absence of the uterus and vagina) or MA (Müllerian aplasia). This syndrome is a rare disease, affecting 1 in every 4500 female live births [1]. MRKH patients usually have a 46, XX karyotype, normal secondary sexual characteristics and normal ovaries with no sign of androgen excess. Primary amenorrhea is the most prominent feature in these patients [2]. Other malformations that are often associated with this

disorder include renal malformations, skeletal abnormalities, hearing defects, and heart malformations [3].

Although the majority of MRKH cases are sporadic, familial occurrence suggests a genetic cause. Thus, a candidate gene approach has been adopted based on genes involved in Müllerian duct development during embryogenesis or other genetic diseases that share characteristics similar to MRKH syndrome. These candidate genes, such as WNT family members [4–6], HOXA family members [7, 8], TCF2 [9], PAX2 [10], and LHX1 [6], have been studied in patients with MRKH syndrome. Unfortunately, these results are unproductive, and the molecular basis of MRKH syndrome remains to be elucidated. Although WNT4 mutations

were identified in certain patients, all of these patients presented with uterovaginal aplasia and hyperandrogenism, which is considered to be distinct from MRKH syndrome [6, 11, 12]. Moreover, heterozygous mutations of LHX1 were detected in two patients, and it was suggested that LHX1 mutations might be the cause of MRKH syndrome in a subgroup of patients [13]. Additionally, it has been widely accepted to date that MRKH syndrome might occur due to polygenic/multifactorial inheritance [3, 14].

Molecular expression analyses of targeted mutagenesis in mouse models have helped to identify several genes that are involved in the development of the urogenital system. Emx2 (empty spiracles homeobox (2) is a divergent homeobox-containing gene orthologous to the *Drosophila* empty spiracles gene (ems) and is involved in the development of the mammalian brain and urogenital system. Mammalian embryos have both Wolffian ducts and Müllerian ducts, and Müllerian ducts normally develop in parallel with Wolffian ducts approximately 13.0 dpc (day after coitum) in both male and female wild-type mice [15]. Müllerian ducts then differentiate into the oviducts, uterus, cervix, and upper portion of the vagina in females, while they degenerate in males. Emx2 is expressed in the epithelial cells of Wolffian and Müllerian ducts [16]. In homozygous Emx2 mutant mice, the kidneys, ureters, gonads, and genital tracts are completely absent, and Müllerian ducts never form. The phenotype of Emx2 mutant mice is similar to that of MRKH patients. We therefore postulated a connection between the EMX2 gene and MRKH syndrome. We performed a sequence analysis of EMX2 variants in a case-control study. To the best of our knowledge, our study was the first to examine whether MRKH syndrome occurs due to variations in the EMX2 gene in hope of elucidating the pathogenesis of MRKH syndrome.

2. Materials and Methods

2.1. Subjects. Forty Han Chinese patients with sporadic MRKH syndrome and one hundred and forty randomized matched female controls with a normal reproductive history, i.e., at least one normal pregnancy without history of genital abnormalities, were analyzed. All patients were included in this study according to the following criteria: 46, XX karyotype, normal secondary sexual characteristics, primary amenorrhea, and absence of uterus, cervix, and proximal vagina documented by ultrasonography and laparoscopy. Six patients presented with renal abnormalities, including unilateral renal aplasia (five patients) and renal ectopia (one patient). Of the patients with renal abnormalities, one had inguinal hernia and another had thoracic vertebral malformations. This study was approved by the local ethics committee, and informed consent was obtained from each participant before entry into the study.

Total genomic DNA from all participants was isolated from peripheral blood using a QuickGene DNA whole blood kit S (Fujifilm, Japan).

2.2. Polymerase Chain Reaction (PCR) and Sequencing. All three exons and exon-intron boundaries of the human EMX2 gene [reference sequence NM_ 004098.3, hg 19/GRCh 37] were amplified by PCR. The primers were designed using Primer Premier 5 software and are presented in Table 1. Each PCR reaction was performed in a total volume of 25 μl containing 20–50 ng of genomic DNA, 0.4 μM each primer, 10 × LA PCR buffer II (Mg2+ plus), 0.4 mM dNTP mixture, and 1.25U of LA Taq DNA polymerase (TaKaRa, Japan). A touchdown PCR program was used to amplify exon 1, whereas conventional PCR reactions were used for exon 2 and exon 3. The PCR conditions are shown in Table 1. PCR products were subsequently sequenced and analyzed using an ABI 3730XL Genetic Analyzer (Applied Biosystems, USA). To verify whether the detected variations were located in conserved regions, Genome Browser of UCSC (http://genome.ucsc.edu/) was used to render sequence alignments in different species, and constraint scores were calculated by genomic evolutionary rate profiling (GERP) [17, 18]. The DataBase of Transcriptional Start Sites (DBTSS, http://dbtss.hgc.jp) and the MatInspector program were used for transcriptional start site analysis and the identification of binding sites for transcription factor prediction, respectively [19]. Moreover, we determined the effect of genetic variations on RNA folding using GeneQuest and analyzed possible microRNA binding sites using TargetScan-Human 6.2 (http://www.targetscan.org).

2.3. Statistical Analysis. All statistical analyses were conducted using the SPSS statistical package (version 17.0). The Hardy-Weinberg equilibrium for each of the variations in controls was assessed based on a goodness-of-fit χ^2 test. The differences of allelic and genotypic distributions between patients and controls were measured using a χ^2 test. Logistic regression analysis was used to calculate the odds ratio and 95% confidence interval (95% CI) values. The level of significance was taken as $P < 0.05$. Primers and PCR conditions for EMX2 gene amplification ARE shown in Table 1.

3. Results

By sequencing the entire coding region, exon-intron boundaries, 5′UTR and 3′UTR of EMX2, we identified a total of eleven variations; the results are shown in Tables 2 and 3.

Four of these variations were only detected in patients, and the others were present both in patients and controls. The allele and genotype frequencies for all the variants were determined based on the Hardy-Weinberg equilibrium.

We identified four heterozygous variations (c.-621G > C, c.-433_-432insC, c.252 A > G, and c.*950C > T) that were only present in MRKH patients, each with an allelic frequency of 1.25%; the results are shown in Table 2. All of these variations were novel and were not annotated in dbSNP141. The first two variations (c.-621G > C and c.-433_-432insC) were located in the 5′UTR of exon 1. The sequence change c.-621G > C (GERP score: 5.04) is located in a highly conserved region, as verified using the UCSC Genome Browser tool. According to DBTSS, the position of this variation was a possible transcriptional start site of the EMX2 gene. Analysis using the MatInspector program revealed that the region was possibly associated with several transcriptional factors, such as homeobox transcription

Table 1: Primers and PCR conditions for EMX2 gene amplification.

Primer	Primer sequence (5′-3′)	PCR conditions
Exon1F	CGCTAGGCTAGAGGAATCTGTCTGT	3 min at 97°C; 30 s at 97°C, 30s at 68°C (−0.5 °C per cycle), 90 s at 72°C (30 cycles), and
Exon1R	CAACTTCTCCGTTCGCACCC	3 min at 97°C; '30 s at 97°C, 30 s at 61°C, 90 s at 72°C (5 cycles), and 10 min at 72°C
Exon2F	GAGCAGGCGTTCCCTTCGT	3 min at 94°C; 1 min at 94°C, 1 min at 63.4°C, 1 min at 72°C (35 cycles), and 10 min at
Exon2R	GGGCAGATTGGCACTTACAGC	72°C
Exon3F	GCTGGGTCTTTGCTGAGTC	3 min at 94°C; 1 min at 94°C, 45s at 67.3°C, 2 min at 72°C (35 cycles), and 10 min at
Exon3R	TGAGGAGCCTGGGTTTCTT	72°C

Table 2: EMX2 variations detected only in MRKH patients.

Exon/intron	Position	Genotype	No. (%) in patients
Exon 1	c.252 A > G	AG	1 (2.5)
		AA	39 (97.5)
Exon 1	c.-433_-432insC	insC/wt	1 (2.5)
		Wild/wt	39 (97.5)
Exon 1	c.-621G > C	GC	1 (2.5)
		GG	39 (97.5)
Exon 3	c. ∗ 950C > T	CT	1 (2.5)
		CC	39 (97.5)

Table 3: EMX2 variations detected both in MRKH patients and controls.

Exon/intron	dbSNP	Position	GERP score	Genotype	No. (%) in patients	No. (%) in controls
Exon 1	rs12777466	c.-674G > A†	5.07	AA	2 (5)	14 (1)
				AG	16 (40)	37 (26.4)
				GG	22 (55)	89 (72.6)
Intron 1	rs8192644	c.406 + 113G > A	2.04	AA	0 (0)	1 (0.7)
				GA	4 (10)	9 (7.5)
				GG	36 (90)	130 (91.8)
Intron 1	rs142080828	c.407−104G > A	1.23	GA	1 (2.5)	3 (2.1)
				GG	39 (97.5)	137 (97.9)
Intron 2	rs202171958	c.591+6T > C	−6.74	TC	1 (2.5)	1 (0.7)
				TT	39 (97.5)	139 (99.3)
Exon 3z	rs66710107	c. ∗ 317_ ∗ 320del AGAG	—	del/del	40 (100)	40 (100)
				wt/wt	0 (0)	
Exon 3	rs187010704	c. ∗ 925C > T	4.88	CT	1 (2.5)	1 (0.7)
				CC	39 (97.5)	139 (99.3)
Exon 3	rs41284394	c. ∗ 1201T > C	5.79	CC	2 (5)	3 (2.1)
				CT	0 (0)	5 (3.6)
				TT	38 (95)	132 (94.3)

factors. The second variation, c.-433_-432insC, was not located in a highly conserved region, although the region was predicted to interact with at least one of the three specific transcription factors: HMX2, MSX1, and MSX2. The synonymous nucleotide substitution, c.252 A > G, was also not located in a conserved region. Another change, c. ∗ 950C > T, is located in the 3′UTR of exon 3, and analyses using the UCSC Genome Browser tool and GERP test (GERP score: 3.94) suggested that the locus of this variation was conserved among mammals. Analysis using GeneQuest showed that this variation would result in distinctive RNA folding compared with the reference sequence.

Moreover, seven previously reported polymorphisms were found both in patients and controls: one deletion and six single nucleotide polymorphisms, none of which were in coding regions; the results are shown in Table 3. However, no statistically significant associations were found for theses polymorphisms at the allele or genotype levels. We identified

six single nucleotide polymorphisms: rs12777466 in exon 1, rs8192644 and rs142080828 in intron 1, rs202171958 in intron 2, and rs187010704 and rs41284394 in exon 3. The first variation, rs12777466, is located in a highly conserved region, and its GERP score of 5.07 was an indication of evolutionary conservation. However, the intronic variations rs8192644, rs142080828, and rs202171958 were not within highly conserved sequences and had GERP scores of 2.04, 1.23 and, −6.74, respectively.

The UCSC Genome Browser tool showed that the position of rs187010704 (c. ∗ 925C > T) was conserved in other mammals, except for mouse and rat and that of rs41284394 (c. ∗ 1201T > C) was highly conserved in various species, such as zebrafish and *Xenopus tropicalis*. Both of these variations had high GERP scores of 4.88 and 5.79, respectively. Additionally, TargetScanHuman 6.2 analysis predicted that rs41284394 was within the possible binding site

for miR-181abcd/4262. Additionally, the variation might change the RNA-folding process, according to the GeneQuest results. However, rs187010704, the other variation in the 3′UTR, was neither within any possible binding sites for microRNAs nor had an effect on RNA folding. In addition, we detected one deletion, rs66710107 in exon 3, that was not located in a conserved region based on the analysis of multiple sequence alignments.

4. Discussion

Patients with MRKH syndrome suffer from infertility and psychological distress. The disease results in high costs not only to the patient herself but also the whole family. Unfortunately, the etiology, prenatal diagnosis, and effective treatment of MRKH syndrome are currently unavailable. To identify genetic risk factors in MRKH patients, potential pathogenic mechanisms and susceptibility to the disease must be investigated.

There have been many unsuccessful attempts to identify genetic risk factors, and to the best of our knowledge, the implication of EMX2 variations in MRKH syndrome has not been studied. Emx2 plays an important role in urogenital development [15, 20]. In addition, Emx2 mutant mice do not have Müllerian ducts and present a phenotype similar to that observed in MRKH patients. Moreover, Emx2 is also crucial in the morphogenesis of the central nervous system and inner ear development [21, 22]. There are reports of MRKH patients with learning disabilities, mental impairment, hearing loss, and endometriosis, reinforcing the link between the EMX2 gene and MRKH syndrome [3, 23, 24]. To investigate the possibility of a link between EMX2 variations and MRKH syndrome, we screened forty patients with MRKH syndrome and one hundred and forty healthy females for variations in the EMX2 gene. A total of eleven variations were identified.

We detected four heterozygous variations (c.-621G > C, c.-433_-432insC, c.252 A > G, and c. ∗ 950C > T) in MRKH patients. The allele frequency of these variations was 1.25% in MRKH patients, and none of these variations were found in our matching control cohort or dbSNP141. It should be noted that all of these variations are reported in our study for the first time. The 5′UTR variations c.-621G > C and c.-433_-432insC might affect the transcriptional regulation of EMX2. According to in silico analysis using MatInspector, c.-621G > C is located within the potential binding sites for transcriptional factors (including HOXA1, HOXA5, HOXA7, HOXB1, HOXB4, HOXB5, HOXC6, HOXD3, HOXD4, EN2, GSX2, and VAX1), and c.-433_-432insC might be associated with transcription factors of HMX2, HOX7, or HOX8. Interestingly, EMX2 is negatively regulated by HOXA10 binding to a 150 bp EMX2 regulatory element [25, 26]. Furthermore, HOX genes are known to encode transcription factors that play crucial roles in the development of the female reproductive tract. These two 5′UTR variations are not located within the known binding site for HOXA10, although their locations were predicted to interact with other transcriptional modulators, including HOX genes. The HMX2 gene plays an important role in organ development during embryogenesis, especially in inner ear formation [27, 28]. Moreover, bioinformatic analysis showed that c.-621G > C is located in a highly conserved region.

Based on the conservation analyses, this region might be of great importance to the function of the HMX2 gene. It is also possible that the c.-621G > C variation might change the transcriptional start site of the EMX2 gene based on the DBTSS analysis. These variations may change the promoter function and therefore affect the expression of the EMX2 protein. Another synonymous variation, c.252 A > G, is not located in a conserved region and is therefore unlikely to be pathologic. Currently, the important role of the 3′UTR in posttranscriptional regulation, such as mRNA stability and degradation, is well understood [29]. The 3′UTR variation in the EMX2 might also have an effect on gene function. The variation c. ∗ 950C > T is located in a highly conserved region according to the bioinformatic analysis. When compared with the reference sequence, c. ∗ 950C > T resulted in a distinct RNA-folding process. Overall, these variations in regulatory domains might alter the transcriptional activity of the EMX2 promoter or have posttranscriptional effects. Although the low frequency of these variations may be due to small sample size, it should be validated in larger MRKH patient groups.

We also detected seven other previously reported polymorphisms (rs12777466, rs8192644, rs142080828, rs202171958, rs66710107, rs187010704, and rs41284394). The variation rs12777466 is located in the 5′UTR, 674 bp before the start codon in the EMX2 gene. UCSC Genome Browser and GERP score analyses showed that this variation occurs in a conserved region. Its location might be associated with another transcription factor, but not the known binding site for HOXA10. We could not exclude the possibility that the associated transcription factor plays a crucial role during reproductive tract development. Variations in the 5′UTR might affect gene expression at the translational level, and a high level of conversation indicates that this nucleotide residue might be quite important. Three variations (rs8192644, rs142080828, and rs202171958) in the introns and one deletion rs66710107 (c. ∗ 317_320delAGAG) in the 3′UTR were not found to be located in conserved regions. However, the bioinformatic analysis showed that two variations in the 3′UTR of exon 3, rs187010704, and rs41284394, are located in highly conserved regions. It was predicted that rs41284394 lies within the possible binding site for miR-181abcd/4262. Interestingly, previous studies suggested important roles of miR-181 in osteoblastic differentiation and the immune system [30, 31]. Additionally, skeletal abnormalities, such as scoliosis and vertebral anomalies, are associated with MRKH syndrome [1]. Thus, miR-181 might be a link between EMX2 and MRKH syndrome. The GeneQuest analysis also suggested that rs41284394 might alter RNA folding, which might be involved in posttranscriptional regulation. However, the allele and genotype frequencies of all of these variations were not significantly different between MRKH patients and controls. This might be due to our small sample size, and further experimental investigations are needed to determine whether these variations are linked to MRKH syndrome.

5. Conclusions

In conclusion, four variations were reported for the first time in our study, all of which were absent in our control group and dbSNP141. According to in silico analyses, two of these variations (c.-621G > C and c. ∗ 950C > T) in the EMX2 gene might be associated with an increased susceptibility to MRKH syndrome in a Chinese Han population. This study provides the first insight into the involvement of the EMX2 gene in genetic predisposition to MRKH syndrome. Our results do not suggest associations between coding variations in the EMX2 gene and MRKH syndrome. However, we cannot exclude the possibility that regulatory variations in the 5′UTR and 3′UTR might contribute to the polygenic/multifactorial pathogenesis of MRKH syndrome. These findings should be confirmed in large-scale studies, and in vitro functional studies are needed for further evaluation of the association of EMX2 variations with MRKH syndrome.

Data Availability

The simulation experiment data used to support the findings of this study are available from the corresponding author upon request.

Conflicts of Interest

The authors declare that there are no conflicts of interest regarding the publication of this paper.

Acknowledgments

References

[1] M. K. Herlin, M. B. Petersen, and M. Brännström, "Mayer-Rokitansky-Küster-Hauser (MRKH) syndrome: a comprehensive update," *Orphanet Journal of Rare Diseases*, vol. 15, no. 1, p. 214, 2020.

[2] M. A. Hall-Craggs, C. E. Williams, S. H. Pattison, A. P. Kirkham, and S. M. Creighton, "Mayer-Rokitansky-Kuster-Hauser syndrome: diagnosis with MR imaging," *Radiology*, vol. 269, no. 3, pp. 787–792, 2013.

[3] D. S. Bombard and S. A. Mousa, "Mayer-Rokitansky-Kuster-Hauser syndrome: complications, diagnosis and possible treatment options: a review," *Gynecological Endocrinology*, vol. 30, no. 9, pp. 618–623, 2014.

[4] L. S. Williams, D. Demir Eksi, Y. Shen et al., "Genetic analysis of Mayer-Rokitansky-Kuster-Hauser syndrome in a large cohort of families," *Fertility and Sterility*, vol. 108, no. 1, pp. 145–151, 2017, e2.

[5] M. Wang, Y. Li, W. Ma et al., "Analysis of WNT9B mutations in Chinese women with Mayer-Rokitansky-Küster-Hauser syndrome," *Reproductive Biomedicine Online*, vol. 28, no. 1, pp. 80–85, 2014.

[6] R. Tang, Y. Dang, Y. Qin et al., "WNT9B in 542 Chinese women with Müllerian duct abnormalities: mutation analysis," *Reproductive Biomedicine Online*, vol. 28, no. 4, pp. 503–507, 2014.

[7] A. B. Ekici, P. L. Strissel, P. G. Oppelt et al., "HOXA10 and HOXA13 sequence variations in human female genital malformations including congenital absence of the uterus and vagina," *Gene*, vol. 518, no. 2, pp. 267–72, 2013.

[8] X. Chen, G. Li, Y. Qin, Y. Cui, L. You, and Z.-J. Chen, "Mutations in HOXA11 are not responsible for Müllerian duct anomalies in Chinese patients," *Reproductive Biomedicine Online*, vol. 28, no. 6, pp. 739–742, 2014.

[9] L. Bernardini, S. Gimelli, C. Gervasini et al., "Recurrent microdeletion at 17q12 as a cause of Mayer-Rokitansky-Kuster-Hauser (MRKH) syndrome: two case reports," *Orphanet Journal of Rare Diseases*, vol. 4, no. 1, p. 25, 2009.

[10] P. Wang, H. Zhao, M. Sun, Y. Li, and Z.-J. Chen, "PAX2 in 192 Chinese women with Müllerian duct abnormalities: mutation analysis," *Reproductive Biomedicine Online*, vol. 25, no. 2, pp. 219–222, 2012.

[11] A. Biason-Lauber, D. Konrad, F. Navratil, and E. J. Schoenle, "AWNT4Mutation associated with müllerian-duct regression and virilization in a 46,XX woman," *New England Journal of Medicine*, vol. 351, no. 8, pp. 792–798, 2004.

[12] P. Philibert, A. Biason-Lauber, I. Gueorguieva et al., "Molecular analysis of WNT4 gene in four adolescent girls with mullerian duct abnormality and hyperandrogenism (atypical Mayer-Rokitansky-Küster-Hauser syndrome)," *Fertility and Sterility*, vol. 95, no. 8, pp. 2683–2686, 2011.

[13] S. Ledig, S. Brucker, G. Barresi, K. Rall, and P. Wieaker, "Frame shift mutation of LHX1 is associated with Mayer-Rokitansky-Kuster-Hauser (MRKH) syndrome," *Human reproduction*, vol. 27, no. 9, Oxford, England, 2012.

[14] M. Wottgen, S. Brucker, S. P. Renner et al., "Higher incidence of linked malformations in siblings of Mayer-Rokitansky-Kuster-Hauser-syndrome patients," *Human Reproduction*, vol. 23, no. 5, pp. 1226–1231, 2008.

[15] N. Miyamoto, M. Yoshida, S. Kuratani, I. Matsuo, and S. Aizawa, "Defects of urogenital development in mice lacking Emx2," *Development*, vol. 124, no. 9, pp. 1653–1664, Cambridge, England, 1997.

[16] M. Pellegrini, S. Pantano, F. Lucchini, M. Fumi, and A. Forabosco, "Emx 2 developmental expression in the primordia of the reproductive and excretory systems," *Anatomy and Embryology*, vol. 196, no. 6, pp. 427–433, 1997.

[17] G. M. Cooper, E. A. Stone, G. Asimenos, E. D. Green, S. Batzoglou, and A. Sidow, "Distribution and intensity of constraint in mammalian genomic sequence," *Genome Research*, vol. 15, no. 7, pp. 901–913, 2005.

[18] B. J. Raney, T. R. Dreszer, G. P. Barber et al., "Track data hubs enable visualization of user-defined genome-wide annotations on the UCSC Genome Browser," *Bioinformatics*, vol. 30, no. 7, pp. 1003–1005, 2014.

[19] A. Suzuki, S. Kawano, T. Mitsuyama et al., "DBTSS/DBKERO for integrated analysis of transcriptional regulation," *Nucleic Acids Research*, vol. 46, no. D1, pp. D229–D238, 2018.

[20] N. Khoshdel Rad, N. Aghdami, and R. Moghadasali, "Cellular and molecular mechanisms of kidney development: from the embryo to the kidney organoid," *Frontiers in Cell and Developmental Biology*, vol. 8, p. 183, 2020.

[21] M. Holley, C. Rhodes, A. Kneebone, M. K. Herde, M. Fleming, and K. P. Steel, "Emx2 and early hair cell development in the mouse inner ear," *Developmental Biology*, vol. 340, no. 2, pp. 547–556, 2010.

Retraction

Retracted: Effects of the Femoral Nerve Block and Adductor Canal Block on Tourniquet Response and Postoperative Analgesia in Total Knee Arthroplasty

Journal of Healthcare Engineering

This article has been retracted by Hindawi following an investigation undertaken by the publisher [1]. This investigation has uncovered evidence of one or more of the following indicators of systematic manipulation of the publication process:

(1) Discrepancies in scope

(2) Discrepancies in the description of the research reported

(3) Discrepancies between the availability of data and the research described

(4) Inappropriate citations

(5) Incoherent, meaningless and/or irrelevant content included in the article

(6) Peer-review manipulation

The presence of these indicators undermines our confidence in the integrity of the article's content and we cannot, therefore, vouch for its reliability. Please note that this notice is intended solely to alert readers that the content of this article is unreliable. We have not investigated whether authors were aware of or involved in the systematic manipulation of the publication process.

In addition, our investigation has also shown that one or more of the following human-subject reporting requirements has not been met in this article: ethical approval by an Institutional Review Board (IRB) committee or equivalent, patient/participant consent to participate, and/or agreement to publish patient/participant details (where relevant).

Wiley and Hindawi regrets that the usual quality checks did not identify these issues before publication and have since put additional measures in place to safeguard research integrity.

We wish to credit our own Research Integrity and Research Publishing teams and anonymous and named external researchers and research integrity experts for contributing to this investigation.

The corresponding author, as the representative of all authors, has been given the opportunity to register their agreement or disagreement to this retraction. We have kept a record of any response received.

References

[1] D. Jin, Y. Zhu, F. Ji, and X. Kong, "Effects of the Femoral Nerve Block and Adductor Canal Block on Tourniquet Response and Postoperative Analgesia in Total Knee Arthroplasty," *Journal of Healthcare Engineering*, vol. 2022, Article ID 2327753, 6 pages, 2022.

Hindawi

Research Article

Effects of the Femoral Nerve Block and Adductor Canal Block on Tourniquet Response and Postoperative Analgesia in Total Knee Arthroplasty

Di Jin, Yajuan Zhu, Fuhai Ji, and Xiaoqi Kong [iD]

Department of Anesthesiology, First Affiliated Hospital of Soochow University, Jiangsu 215000, China

Correspondence should be addressed to Xiaoqi Kong; 14311010032@stu.cpu.edu.cn

Tourniquet has emerged as an important role in surgical procedures, sixty patients undergoing elective total knee arthroplasty are randomly divided into the nerve block group and adductor duct block group in this paper. The changes of mean arterial pressure (MAP) and heart rate (HR) at different time points during operation, the changes of VAS scores at resting pain and exercise pain, and the changes of quadriceps femur muscle strength at different time points after operation are observed in 2 groups. The experimental results show that compared with adductor duct block, femoral nerve block can better relieve the intraoperative tourniquet reaction without affecting the postoperative analgesic effect and the muscle strength of quadriceps femurs.

1. Introduction

As a simple and practical method of hemostasis, tourniquet plays a very important role in surgical procedures, with the advantages of significantly reducing patient bleeding, providing the surgeon with a clear surgical field, and facilitating surgical operations [1–3]. Presently, it is commonly applied in total knee arthroplasty (TKA) [4]. However, the ischemic pain of the limb caused by the tourniquet also brings some pain and risk to the patient at the same time [5]. When the tourniquet has been used for a long period of time, patients may experience symptoms such as high blood pressure and increased heart beat rates. After the tourniquet is released, there are adverse reactions such as blood pressure drop or shock [6]. Therefore, it is often recommended for doctors to sedate patients with anesthesia, increase the dosage of opioids or other analgesics, or even add vasoactive drugs to alleviate such tourniquet reactions. In addition, for patients with coronary atherosclerosis and other cardiovascular diseases, the tourniquet reaction is more likely to cause myocardial ischemia and arrhythmia [7–9]. Similarly, radicals available in the limb ischemia can cause reperfusion injury which can also cause lung injury, which is not conducive to postoperative recovery of patients.

Simple nerve blocks are often used in anesthesia for lower extremity surgery, but the surgical site does not coincide with the tourniquet binding site and involves different nerves that are innervated by it [10, 11]. Studies shows that a lower limb nerve block can reduce tourniquet response, but the effect of various nerve blocks on tourniquet response is still inconclusive. Both the myocardial blockage and nerve blockage are common measures to control pain during and after TKA surgery.

The rest of this paper is organized as follows: Section 2 discusses related work and analysis, followed by the patient information and research methods in Section 3. Data statistics and comparative analysis are discussed in Section 4. Section 5 concludes the paper with summary and future research directions.

2. Related Work

TKA is an effective surgical procedure for the treatment of advanced knee disease, but TKA often results in severe postoperative pain and impairs early functional exercise. However, TKA often leads to severe postoperative pain, which affects early functional exercise of the knee joint and

increases the risk of postoperative complications such as knee stiffness and deep vein thrombosis, thus affecting the outcome of the surgery [12, 13]. Therefore, adequate postoperative analgesia after TKA is particularly important. The use of a single opioid analgesic dose is large and not ideal. Femoral nerve block and collecting duct block at the time of surgery can significantly reduce the amount of opioids used, which can obtain good analgesic effects and facilitate early postoperative movement of patients [14]. The adductor canal is located from the anterior superior iliac spine to the anterior medial aspect of the middle 1/3 of the patella, between the deep surface of the suture muscle, the greater trochanter and the medial femoral muscle. After the femoral nerve branches from the femoral triangle to innervate the quadriceps, it continues as a sensory branch of the saphenous nerve, which enters the collecting duct at the base of the femoral triangle and travels down the medial side of the knee after exiting the collecting duct and divides into the infrapatellar branch and the sutures muscle branch. The former is distributed on the anterior medial side of the knee joint, and the latter on the medial side of the calf and ankle [15]. When compared with femoral nerve blockage, the advantage of the adductor canal block does not affect quadriceps' muscle strength, which makes it to be a more preferred analgesic method.

The adductor canal is located from the anterior superior iliac spine to the anterior medial aspect of the middle 1/3 of the patella, between the deep surface of the suture muscle, the greater trochanter, and the medial femoral muscle. After the femoral nerve branches from the femoral triangle to innervate the quadriceps, it continues as a sensory branch of the saphenous nerve, which enters the collecting duct at the base of the femoral triangle and travels down the medial side of the knee after exiting the collecting duct and divides into the infrapatellar branch and the sutures muscle branch. The former is distributed on the anterior medial side of the knee joint and the latter on the medial side of the calf and ankle [16].

The current tourniquet reaction can be considered as a systemic reaction which is caused by the ischemia-reperfusion injury as a result of the tourniquet compression of local tissues and the transmission of the injury signal through the local peripheral nerves. The results of this study show that the MAP change in the femoral nerve block group has a higher stability rate as compared to that of the adductor tube block group. This may be due to the fact that the effect of the adductor tube block is lower than the tourniquet binding site, so the compression effect of the tourniquet cannot be relieved. The femoral nerve block can more effectively block the upward conduction of stimulation there, thereby alleviating the tourniquet response. In addition, there is still a difference in MAP between the femoral nerve block group and the adductor tube block group. There is a corresponding change in MAP with the change of the tourniquet time, indicating that the femoral nerve block or the adductor muscle alone cannot completely eliminate the influence of tourniquet reaction. Studies shows that even with sufficient sensory levels in spinal cord and epidural anesthesia, tourniquet pain and high blood pressure will also occur, and the peripheral nerve block has not been proven to be completely effective in preventing blood bands [17, 18]. Therefore, the mechanism of tourniquet reaction remains to be further studied.

Patients with TKA need to start rehabilitation exercises and get out of bed as soon as possible after surgery in order to facilitate their knee function recovery. However, 50% to 60% of patients have severe postoperative pain that interferes with early postoperative functional exercise, which in turn affects the functional recovery of the knee and also increases the risk of deep vein thrombosis and pulmonary embolism. The pain is mainly due to muscle ischemia-reperfusion injury which is caused by quadriceps spasm, intraoperative tourniquet binding, and release of inflammatory mediators. Therefore, effective analgesic treatment after TKA is essential for the recovery of knee function.

3. Patient Information and Research Methods

3.1. Patients and Treatment. Clinical trials are performed on patients undergoing knee arthroplasty who are admitted to the Department of Orthopedic Surgery in the First Affiliated Hospital of Suzhou University from July 2020 to March 2021.

(1) Entry criteria: The American Society of Anesthesiologists (ASA) created two groups, grade I~II, and age 51–80 years old. In the end, about 60 cases are included, and they are randomly divided into the femoral nerve block group and the adductor carnal block group by the random number table method, with 30 cases in each group. There is no statistically significant difference between the two groups of patients in general data such as gender, age, BMI index, and length of operation ($P > 0.05$), and they are comparable, as shown in Table 1.

(2) Exclusion criteria: there are some patients who refuse to participate in this trial, these patients either have medical-related problems such as cognitive dysfunction, poor communication, peripheral neuropathy or potential peripheral neuropathy, local skin infection, clotting dysfunction, drug allergy, and drug addiction. Table 1 shows the comparison of the femoral nerve block group and adductor tube block group.

All patients did not use preoperative medication before entering the room. After a patient enters the room, the peripheral vein is opened, and the monitor is connected to monitor blood oxygen saturation, electrocardiogram, non-invasive blood pressure, and the radial artery puncture method is used to monitor the invasive arterial blood pressure. The patients were administered general anesthesia with endotracheal intubation. The patients are pumped with dexmedetomidine 0.5 μg/kg for 10 minutes before induction. Propofol 1.5–2 mg/kg, sufentanil 0.4–0.6 μg/kg, and cis-atracuron besylate were used at 0.15–0.2 mg/kg for anesthesia induction, sevoflurane inhalation. Anesthesia is maintained by intermittent bolus

TABLE 1: Comparison of the two groups of patients.

n		Age	Height (cm)	Weight (kg)	BMI (kg/m^2)	Operation time (h)	Sex ratio (M : F)	ASA group index I/II
Femoral nerve block group	30	66.37 ± 10.70	158.93 ± 6.59	68.67 ± 10.98	27.15 ± 3.61	2.89 ± 0.90	7/23	10/20
Adductor tube block group	30	68.40 ± 6.84	160.50 ± 7.07	68.40 ± 12.43	26.49 ± 4.17	2.90 ± 0.88	8/22	7/23
t (χ^2)		0.876	0.890	0.089	0.655	0.044	0.089	(0.739)
P		0.386	0.377	0.929	0.515	0.965	0.766	0.390

injection with cis-benzene, and the depth of anesthesia is monitored by inhalation anesthetic concentration monitoring (MAC0.8-1.2Vol%).

After induction, B-ultrasound (Wisonic Huasheng, model: Navi S) guides the nerve block. The patients in the femoral nerve block group are placed in a supine position, and a high-frequency ultrasound probe is placed along the horizontal axis near the groin of the lower extremity on the operating side. The femoral nerve is located outside the femoral artery. The needle is inserted into the outside of the thigh by the in-plane method, and the needle tip reached around the femoral nerve. After confirming that the blood vessel is not inserted, 20 ml of 0.2% ropivacaine is injected. In the adductor tube block group, the inferior sartorius approach is often used. The patient's affected limb is slightly externally rotated. The ultrasound high-frequency probe is placed horizontally on the middle of the thigh on the operating side to confirm the position of the sartorius muscle. 20 ml of 0.2% ropivacaine is injected. The space between the sartorius muscle and its fascia and the artery.

3.2. Observable Indicators

3.2.1. Intraoperative Hemodynamic Changes May Occur in Two Groups of Total Knee Arthroplasty Patients

Observing the intraoperative steps: $T0$ means before anesthesia, $T1$ means upper tourniquet immediately, $T2$ means upper tourniquet for 30 min, and $T3$ means upper tourniquet for 60 min.

The changes of mean arterial pressure MAP and heart rate HR in patients with: $T4$ means 90 minutes from the upper tourniquet, $T5$ means the tourniquet is loosened, and $T6$ means 10 minutes after the tourniquet is loosened.

3.2.2. Postoperative Pain of the Two Groups of Total Knee Arthroplasty Patients. The resting VAS (visual analog scale) score and exercise VAS score of patients at 6 h and 24 h after operation was observed. 0 is painless, (1–3) is mild pain, (4–7) is moderate pain, and (8–10) is severe pain.

3.2.3. Quadriceps Muscle Strength of the Two Groups of Patients Undergoing Total Knee Arthroplasty. It was observed that the quadriceps muscle strength of the patients are affected limb at 6h and 24h after surgery that no muscle contraction at all is level 0. Only muscle contraction cannot. The resulting movement is level 1. The affected limb can

move in the horizontal direction but cannot resist gravity is level 2. It can be lifted off the bed surface but cannot resist resistance is level 3. The resistance that can resist is not completely level 4, and the muscle strength is normal level 5.

3.3. Statistical Processing. The research uses data collection packages such EXCEL2016 and SPSS23.0 for research data analysis. The measurement data in the research data all pass the normality test and are described by the mean $X \pm SD$. The comparison between the two groups is the group t-test or the adjusted Test (statistic is T), and the before and after comparison within the group is the paired t-test (statistic is t). Repeated measurement analysis of variance (statistics is F) + LSD-t test for comparison between two groups (statistics is LSD-t) + pairwise time comparison difference t test (statistics is t). The count data are described by the number of cases, and the comparison between the two groups is the chi-square test or the adjusted chi-square test (the statistic is χ^2). The statistical test level $\alpha = 0.05$, both are two-sided tests. The multiple comparisons of repeated measurement analysis and segmentation test are adjusted according to the Bonferroni correction method, $\alpha' = 0.05/n$, n is the number of multiple comparisons.

4. Data Statistics and Comparative Analysis

4.1. Changes in Mean Arterial Pressure (MAP) at Different Time Points in the Two Groups of Patients. The mean arterial pressure MAP data and data of the two groups of patients at different time points during the operation are listed in the table below. The overall comparison (two-factor repeated measurement variance) shows that between groups (grouping latitude), within groups (time latitude), and interaction (between groups × time), all have a significant significance ($P < 0.05$). Two-by-two fine comparison combined with main data analysis: there is no statistically significant difference in basic MAP between the two groups ($P > 0.05$). The upper tourniquet immediately, 30 min, 60 min, 90 min, the tourniquet immediately, and 10 min at each time point of the two groups of patients The difference in MAP is statistically significant ($P < 0.05$). The MAP during the upper tourniquet in the femoral nerve block group is lower than that in the adductor tube block group. After the tourniquet is released, the MAP is higher than that in the adductor tube block group. In comparison within the group, with the extension of the tourniquet time, the MAP is increased. After the tourniquet is released, the MAP is decreased, which is significantly different from the T_0 time point ($P < 0.008$, $X \pm SD$, $n = 30$), as shown in Table 2.

Table 2: Mean arterial pressure MAP (mmHg) changes at different time points in the two groups of patients during operation.

	Femoral nerve block group	Adductor tube block group
T0	107.878 ± 11.904	108.573 ± 16.352
T1	$91.287 \pm 8.516t$	$98.918 \pm 13.423at$
T2	$88.490 \pm 10.571t$	$96.924 \pm 12.668at$
T3	$91.389 \pm 13.203t$	$102.555 \pm 9.743a$
T4	$93.785 \pm 12.603t$	$106.302 \pm 10.069a$
T5	$87.672 \pm 13.444t$	$75.638 \pm 10.565at$
T6	$85.000 \pm 13.329t$	$73.539 \pm 10.826at$

HF factor is given as 0.9833, P is 5.378 of groups F, P is 40.686 of F in the group, and P is 10.644 of correlations.

Table 3: HR changes at different time points during the operation of the two groups of patients (bpm).

	Femoral nerve block group	Adductor tube block group
T0	71.965 ± 11.755	72.580 ± 8.940
T1	$59.169 \pm 8.534t$	$59.614 \pm 8.133t$
T2	$59.440 \pm 10.254t$	$60.708 \pm 9.314t$
T3	$63.061 \pm 12.079t$	$63.464 \pm 11.201t$
T4	$65.996 \pm 11.916t$	$65.030 \pm 8.646t$
T5	$66.154 \pm 11.162t$	$67.748 \pm 11.779t$
T6	$65.086 \pm 10.470t$	$68.498 \pm 9.541t$

HF coefficient is given as 0.9601, P is 0.763 of groups F, P is 11.468 of F in the group, and P is 0.263 of correlations.

Table 4: Pain scores and quadriceps muscle strength of the two groups of patients 6 hours after surgery.

		Resting VAS score	Exercise VAS score	Quadriceps muscle strength
Femoral nerve block group	Postoperative 6 h	1.63 ± 0.56	2.40 ± 0.56	2.80 ± 0.76
$n = 30$	Postoperative 24 h	1.40 ± 0.56	1.97 ± 0.62	3.53 ± 0.51
	Difference	-0.23 ± 1.21	-0.43 ± 0.47	0.73 ± 0.21
	Paired test, P	1.041, 0.306	5.011, <0.001	19.040, <0.001
Adductor tube block group	Postoperative 6 h	1.60 ± 0.62	2.20 ± 0.81	2.77 ± 0.68
$n = 30$	Postoperative 24 h	1.38 ± 0.57	2.13 ± 0.78	3.57 ± 0.50
	Difference	-0.22 ± 0.94	-0.07 ± 1.72	0.80 ± 1.13
	Paired test t, P	1.282, 0.210	0.223, 0.825	3.878, 0.001
Comparison	Postoperative 6 h	0.197, 0.845	1.112, 0.271	0.161, 0.873
(Group test t, P)	Postoperative 24 h	0.137, 0.892	0.880, 0.382	0.307, 0.760

Table 5: Comparison of sports VAS scores and resting VAS scores in each group.

		Resting VAS score	Exercise VAS score	t	P
Femoral nerve block group	Postoperative 6 h	1.63 ± 0.56	2.40 ± 0.56	5.325	<0.001
$n = 30$	Postoperative 24 h	1.40 ± 0.56	1.97 ± 0.62	3.737	<0.001
Adductor tube block group	Postoperative 6 h	1.60 ± 0.62	2.20 ± 0.81	3.222	0.002
$n = 30$	Postoperative 24 h	1.38 ± 0.57	2.13 ± 0.78	4.252	<0.01

The overall comparison is a two-factor repeated measurement analysis of variance. The fine comparison between groups in latitude is LSD-t test, and the significance markers and *b* are $P < 0.05$ compared with groups A and B, respectively. The fine comparison in time latitude is the difference t-test, and the significance mark t is $PP < \alpha'$ compared with the first time point in the group. $\alpha' = 0.05/6 = 0.008$, 6 is the number of multiple comparisons (Bonferroni correction method).

4.2. Changes of HR in the Two Groups of Knee Patients at Different Times during the Operation. The overall comparison of the simulation upward shows that only within the group (time latitude) has a significant meaning ($P < 0.05$). Two-by-two fine comparison combined with main data analysis: there is no statistically significant difference in heart rate at each time point between the two groups of patients ($P > 0.05$); within each group, there is no change in the snack rate of patients in the femoral nerve block group at each time

significant difference ($P > 0.05$), the difference of HR over time in the adductor tube block group (compared with $T0$) is statistically significant ($P < 0.008$), as shown in Table 3.

4.3. VAS Pain Score and Quadriceps Muscle Strength Changes in the Two Groups of Patients at Different Time Points after Surgery. There is no statistically significant difference in the VAS scores of resting pain between the two groups of patients at 6 h and 24 h after surgery ($P > 0.05$), and there is no significant difference in the VAS scores of exercise pain between the two groups at 6 h and 24 h after surgery ($P > 0.05$). There is no statistically significant difference in quadriceps muscle strength between the group of patients at 6 h and 24 h after surgery ($P > 0.05$). However, the sport VAS score and quadriceps muscle strength of the femoral nerve block group at 24 hours after operation are significantly changed. Compared with 6 hours after operation, the difference is statistically significant. Table 4 shows the pain scores and quadriceps muscle strength of the two groups of patients 6 hours after surgery.

4.4. Comparison of Sports VAS Scores and Resting VAS Scores in Each Group. The sports VAS scores of each group are higher than the resting VAS scores, and the difference is statistically significant ($P < 0.05$), as shown in Table 5.

5. Conclusions

This article intends to comprehensively compare the effects of two nerve block methods on tourniquet response and postoperative analgesia and explore a more favorable nerve block method for TKA patients. There is no significant difference in intraoperative HR changes between the femoral nerve block group and the adductor tube block group, and both are relatively stable, which may be related to the use of dexmedetomidine. Studies show that tourniquet reaction is related to increased sympathetic tone, so the antisympathetic effect of dexamethasone can help alleviate tourniquet reaction. Comparing the two groups, there is no significant change in HR in the femoral nerve block group, and there are statistical differences in HR changes in the adductor tube block group, indicating that the femoral nerve block group could better control the increase in heart rate caused by the tourniquet reaction.

Presently, the adductor tube block is more used for postoperative analgesia after TKA, and the main consideration is that the femoral nerve block will cause the decrease of quadriceps muscle strength and affect postoperative recovery. Theoretically, low concentrations of ropivacaine have little effect on the muscle strength of the blocked area, but studies show that ropivacaine can achieve sufficient analgesic effects within the concentration range of 0.1%– 0.2%, so it with 0.2% ropivacaine for femoral nerve block, there is no significant difference in the analgesic effect and quadriceps muscle strength between the two groups of patients after surgery, which is consistent with the results of the previous study. Therefore, the use of low-concentration ropivacaine for femoral nerve block has no significant

decrease in quadriceps muscle strength compared with adductor tube block, and it will not affect the early functional exercise of patients after knee arthroplasty.

Data Availability

Data from simulated experiments used to support the findings of this study are available from the corresponding author on reasonable request.

Conflicts of Interest

The authors declare that there are no conflicts of interest regarding the publication of this paper.

References

[1] B. A. Parsons, O. Kalejaiye, M. Mohammed, and R. A. Persad, "The penile tourniquet," *Asian Journal of Andrology*, vol. 15, no. 3, pp. 364–367, 2013.

[2] A. A. Magan and F. S. Haddad, "Tourniquet use in knee surgery: is it time to move on?" *The Bone & Joint Journal*, vol. 103-B, no. 5, pp. 805-806, 2021.

[3] A. A. Smith, J. E. Ochoa, S. Wong et al., "Prehospital tourniquet use in penetrating extremity trauma: decreased blood transfusions and limb complications," *Journal of Trauma and Acute Care Surgery*, vol. 86, no. 1, pp. 43–51, 2019.

[4] R. Turan, C. Lin, and C. Jou, "Tourniquet use in total knee arthroplasty: a meta-analysis," *Knee Surgery, Sports Traumatology, Arthroscopy*, vol. 19, pp. 1121–1130, 2011.

[5] R. Turan, H. Yagmurdur, M. Kavutcu, and B. Dikmen, "Propofol and tourniquet induced ischaemia reperfusion injury in lower extremity operations," *European Journal of Anaesthesiology*, vol. 24, no. 2, pp. 185–189, 2007.

[6] P. Zhang, H. Zhang, Y. Li et al., "Improved LHS based cumulant method for probabilistic load flow calculation," *Acta Energiae Solaris Sinica*, vol. 42, no. 1, pp. 14–20, 2021.

[7] L. Helen, B. D. O'Donnell, and E. Moore, "Nerve localization techniques for peripheral nerve block and possible future directions," *Acta Anaesthesiologica Scandinavica*, vol. 59, no. 8, pp. 962–974, 2015.

[8] G. Gao, L. Cao, X. Du et al., "Comparison of minimally invasive surgery transforaminal lumbar interbody fusion and TLIF for treatment of lumbar spine stenosis," *Journal of Healthcare Engineering*, vol. 2022, pp. 1–12, 2022.

[9] F. Canovas and L. Dagneaux, "Quality of life after total knee arthroplasty," *Orthopaedics and Traumatology: Surgery & Research*, vol. 104, no. 1, pp. S41–S46, 2018.

[10] R. Russell, M. Huo, and R. Jones, "Avoiding patellar complications in total knee replacement," *Bone & Joint J*, vol. 97, no. 8, pp. 84–90, 2014.

[11] H.-P. W. van Jonbergen, E. L. Reuver, and R. W. Poolman, "Determinants of anterior knee pain following total knee replacement: a systematic review," *Knee Surgery, Sports Traumatology, Arthroscopy*, vol. 22, no. 3, pp. 478–499, 2014.

[12] T. Ogura, H. Omatsu, H. Fukuda et al., "Femoral nerve versus adductor canal block for early postoperative pain control and knee function after anterior cruciate ligament reconstruction with hamstring autografts: a prospective single-blind randomised controlled trial," *Archives of Orthopaedic and Trauma Surgery*, vol. 141, no. 11, pp. 1927–1934, 2021.

[13] D. Li, Z. Yang, X. Xie, J. Zhao, and P. Kang, "Adductor canal block provides better performance after total knee

Hindawi

Research Article

Correlation between Serum Oxidative Stress Level and Serum Uric Acid and Prognosis in Patients with Hepatitis B-Related Liver Cancer before Operation

Maowen Yu,[1] Chaozhu Zhang,[2] Hongbo Tang,[1] and Chaohui Xiao [3]

[1]*Department of Clinical Lab, Jintang Hospital, West China Hospital, Sichuan University Jintang First People's Hospital,*
 Chengdu 610400, China
[2]*Gastroenterology Department, Chinese PLA Army 951 Hospital, Kuerle 841000, China*
[3]*Department of Hepatobiliary Surgery, Fifth Medical Centre of Chinese PLA General Hospital, Beijing 100039, China*

Correspondence should be addressed to Chaohui Xiao; xch301gd@163.com

Aiming to explore the correlation between preoperative serum oxidative stress level and serum uric acid and prognosis of hepatitis B-related liver cancer, the clinical data of 712 patients with hepatitis B-related liver cancer from January 2019 to December 2020 were retrospectively analyzed. By using the receiver operating curve, the optimal critical values of preoperative superoxide dismutase (SOD), malondialdehyde (MDA), and serum uric acid (SUA) are determined. The single-factor and multifactor Cox models are applied to screen out the suspicious factors affecting the prognosis of patients with hepatitis B-related liver cancer. According to the survival status of patients, the optimal thresholds of SOD, MDA, and SUA before operation were 58.055/mL, 10.825 nmol/L, and 312.77 nmol/L, respectively. The results of univariate analysis show that the prognosis of patients is significantly correlated with preoperative SOD, MDA, and SUA levels and TNM staging ($P < 0.05$). Additionally, multivariate analysis demonstrates that preoperative SOD < 58.055 U/mL and SUA ≥ 312.770 mmol/L and TNM stage III-IV are independent risk factors for postoperative prognosis ($P < 0.05$). Our study suggests that SOD, SUA, and TNM staging have certain value in judging the early prognosis of patients with hepatitis B-related liver cancer. Patients with high preoperative SOD level and low preoperative SUA level can obtain better prognosis.

1. Introduction

Hepatocellular carcinoma (HCC) is one of the common malignant tumors in the Chinese population. According to the 2014 World Health Organization report, the number of new cases and deaths of HCC in China is huge, and it has been ranked first in the world for many years. China has a large population and a high rate of HBV infection, leading to about half of the new cases of liver cancer each year [1]. At present, the staging system of hepatocellular carcinoma (HCC) is not ideal for predicting the prognosis of patients with liver cancer after surgical resection, and the recurrence rate after 5 years is more than 50% [2]. An epidemiological survey showed that patients with hepatitis B-related liver cancer had a lower 5-year survival rate of only 20%, with

poor prognosis and a serious threat to their lives and health [3]. Therefore, early detection and identification of these patients with postoperative recurrence and targeted intervention are essential. In recent years, the role of oxidative stress in tumors has gradually attracted attention.

Studies have shown that patients with cancer have detected an increase in oxidative stress level before treatment, and it is also related to postoperative prognosis, which is conducive to the development of appropriate individualized treatment for patients [4]. In addition, serum uric acid is another important indicator to evaluate the prognosis of cancer. Related studies have confirmed that elevated serum uric acid levels are associated with the incidence and mortality risk of various diseases such as gastric cancer, colon cancer, renal cell carcinoma, and liver cancer [5].

Clinical studies have confirmed that hyperuricemia not only causes gout but also is closely related to kidney disease, cardiovascular disease, and endocrine and metabolic diseases. Hyperuricemia is an important and independent risk factor for cardiovascular disease and cardiovascular risk factors, such as hypertension, hyperlipidemia, type 2 diabetes, obesity, insulin resistance, and metabolic syndrome [6]. Many studies have shown that the increase of SUA level is an independent risk factor for malignant tumor occurrence and poor prognosis [7, 8]. The proinflammatory properties of SUA may play an important role in the occurrence and development of cancer [9].

Therefore, the analysis of serum oxidative stress and uric acid levels in patients with hepatitis B-related lung cancer is of great significance to understand the occurrence and development of the disease. In this study, the serum oxidative stress and uric acid levels in patients with hepatitis B-related lung cancer before operation were detected to analyze the relationship between the two and the prognosis and survival of patients after operation, so as to use them as effective indicators for prognosis judgment in clinical practice.

2. Related Work

Existing works demonstrate that the infection of hepatitis B virus (HBV) in patients with chronic infection is an important reason for the transformation of liver cirrhosis into hepatocellular carcinoma. China is a big country with hepatitis B, in which 60% to 80% of liver cirrhosis is caused by HBV infection and 45% of patients with liver cancer caused by HBV infection [10]. Although many new treatments, such as transcatheter arterial chemoembolization, have been developed in recent years, surgical resection of tumor lesions in recent decades is still the first choice for patients with primary liver cancer. However, the prognosis of patients remains unsatisfactory due to the high rates of postoperative recurrence and metastasis. Determined prognostic biomarkers facilitate the development of individualized treatment strategies for patients. In recent years, with the continuous development of biomedicine and immunopathology, the markers used for diagnosis, disease evaluation, and prognosis have gradually increased. Among them, alpha-fetoprotein (AFP) is a commonly used serum tumor marker, although it has certain specificity. However, there is still a phenomenon of underdiagnosis [11]. Some existing works found that the dynamic changes of immune, nervous, and endocrine systems in patients from HBV infection to tumor formation play an important role [12]. Above achievements lay a theoretical foundation for finding meaningful markers.

Oxidative stress is the state of imbalance between cell oxidation and antioxidation, excessive promotion of oxides, exceeding the scavenging capacity of antioxidants, leading to the accumulation of free radicals in cells and the oxidative damage of biological macromolecules such as proteins, lipids, and DNA, resulting in cell or tissue damage [13]. In previous studies, they found that oxidative stress is involved in the formation of a variety of diseases, such as cancer, diabetes, and cardiovascular and neurological diseases, and in cancer research, others found that oxidative stress may have a high probability of joining in the formation of HCC [14, 15]. Interleukin 6 (IL-6) can inhibit tissue inflammation and cell apoptosis [16], and one of the important functions of tumor necrosis factor α (TNF-α) is to activate the cell apoptosis pathway. Oxidative stress can induce hepatocyte injury, produce multiple cytokines and chemokines such as IL-6 and TNF-α, promote the occurrence of fibrosis, and affect liver inflammation and cell apoptosis [17]. In addition, mitochondrial dysfunction caused by oxidative stress can affect many important functions of hepatocytes, leading to the development of cells towards cancer. Mitochondria are the main endogenous source of ROS in human body. Excessive ROS in human body will directly attack mitochondria. Because mitochondrial DNA (mtDNA) lacks histone protection and complete repair mechanism, mtDNA is sensitive to oxidative stress and vulnerable to ROS interference, resulting in mtDNA mutations, respiratory chain complex degeneration, and oxidative phosphorylation dysfunction. In addition, mitochondrial dysfunction caused by oxidative stress can affect many important functions of hepatocytes, leading to the development of cells towards cancer. A large amount of ROS accumulation would increase the deposition of oxidized lipids, thereby inducing more lipid peroxidation, inhibiting the respiratory electron transport chain, and forming a vicious cycle [18]. The excessive ROS generated in the body attacks the lipid and oxidizes the lipid on the cell membrane surface, resulting in changes in the structure and properties of the cell membrane. MDA is the lipid peroxide formed by ROS attacking the lipid and oxidizing the lipid on the cell membrane surface. Its level can reflect the oxidative stress state of the body. As a natural free radical scavenging system in human body, SOD maintains a dynamic balance with oxygen free radicals under normal conditions and changes with the change of oxygen free radical level and membrane lipid peroxidation under pathological conditions. Uric acid is the product of hydrolysis, deamination, and oxidation of purine nucleotides in human body. Its content is related to the catabolism rate of nucleic acid and excretion function of kidney. Acute kidney injury after advanced liver disease is a common syndrome in clinical practice. Relevant research evidence shows that there is a complex correlation between the liver and kidney [19].

3. Object and Method

3.1. Source of Research Object. The patients with hepatitis B-related liver cancer treated in our hospital from January 2019 to December 2020 were retrospectively analyzed. The following criteria were included. The pathological diagnosis of liver cancer was confirmed after operation. The patient had a history of hepatitis B and had no other causes of liver cancer such as hepatitis C and alcoholic liver disease. The biochemical indexes of the patient were detected within one week before operation, and the radical resection of liver cancer was performed in our hospital, with complete clinical data and follow-up data. Exclusion requirements combined

with the following criteria, patients with severe underlying diseases and other tumors, received other antitumor treatment. All the contents of this study are with the informed consent of patients.

3.2. Data Collection and Specific Research Methods.

The data collected contain basic information of patients, gender, age, tumor size, tumor number, TNM stage, and BCLC stage. Next, the last blood biochemical examination within a week before surgery, including superoxide dismutase (SOD), malondialdehyde (MDA), and serum uric acid (SUA) are selected as laboratory indicators. The preoperative blood biochemical examination and corresponding clinical pathological data of the patients were collected and included through the hospital case data system. The receiver operating characteristic curve (ROC) was used to analyze and calculate the blood indexes before treatment, followed by the optimal cutoff value for survival prediction. With the cutoff value as the critical value, it was divided into two categories of variables. Single-factor Cox regression model was used to screen the factors affecting the overall survival (OS) of patients and construct the survival curve. The survival differences at different levels of indicators were compared. Finally, multivariate Cox regression analysis was performed.

3.3. Follow-Up Method.

All cases included in the study were followed up, including outpatient follow-up and telephone follow-up. Liver ultrasound, chest X-ray examination, serum AFP detection, and CT comparison were performed every 6 months after operation [20, 21]. Tumor recurrence and death were recorded within 3 years. Patients who lost follow-up or died for other reasons are defined as deletion. Tumor recurrence is defined by clinical, radiological, or pathological diagnosis [22]. Follow-up continued until death or the deadline for follow-up was December 2021. OS is defined as the time to start treatment to any cause of death [23]. The time of survival or loss of follow-up at the end of follow-up was counted as the final deadline for statistical analysis.

3.4. Statistical Methods.

The specific steps of statistical methods are as follows.

(i) Step 1: SPSS 21.0 is applied to analysis data. The collected data that conform to the normal distribution are expressed as mean ± standard deviation. In order to meet the comparison between the standard groups, t-test is used.

(ii) Step 2: after K–S test, M(P25, P75) should be adopted to deal with the measurement data that do not conform to the normal distribution. The enumeration data will be replaced, and chi-square (χ^2) test can be used for comparison between groups of those data.

(iii) Step 3: the cutoff values of SOD, MDA, and SUA will be selected as binary variables for Cox regression analysis.

(iv) Step 4: univariate and multivariate Cox regression analysis on the prognostic factors of patients will be performed, and Kaplan-Meier method and log-rank correction test were used. $P < 0.05$ was used as the criterion for statistical difference in the whole study.

4. Results and Discussion

4.1. Clinical Data of Included Patients.

Finally, the study collected 712 patients, including 520 males and 192 females. The age range was 39–73 years old, and the average age was (51.36 ± 8.23) years old. The number of tumors in patients was multiple (≥2), and the average tumor size was (5.12 ± 1.49) cm. The overall survival rates of patients 1 and 3 years after operation were 68.56% and 53.09%, and the total survival time was 2–36 months. The median survival time of patients with large logarithm was 24 months. As of the follow-up date, there were 363 patients with disease recurrence, of which 334 died. There were 323 patients who did not appear the outcome of this study, 26 patients were lost, and the loss rate was 3.65%, as shown in Table 1.

4.2. Determination of Optimal Cutoff Values for Preoperative SOD, MDA, and SUA.

Referring to the patient's final survival status, the optimal cutoff values of preoperative SOD, MDA, and SUA were 58.055 U/mL, 10.825 nmol/L, and 312.77 nmol/L, respectively. The sensitivity is 0.844, 0.838, and 0.719, respectively. The specificities were 0.778, 0.761, and 0.701, respectively, as shown in Table 2 and Figure 1. According to the preoperative SOD, MDA, and SUA cutoff values, they were divided into high SOD group (≥58.055 U/mL), low SOD level group (<58.055 U/mL), and MDA high level group (≥10.825 nmol/mL), MDA low level group (<10.825 nmol/L), SUA high level group (≥312.77 nmol/L), and SUA low level group (<312.77 nmol/L).

4.3. Univariate Analysis of Patient Prognostic Factors.

Univariate analysis showed that preoperative TNM stage, SOD < 58.055 U/mL, MAD ≥ 10.825 nmol/L, and SUA ≥ 312.770 mmol/L were the main factors affecting the OS of patients ($P < 0.05$), as shown in Table 3.

4.4. Comparison of Survival Curves between Groups.

In NM stage group, high and low SOD, MDA group, and high and low SUA group, compared with Log-rank test, we found that the overall survival time was statistically significant among them ($\chi^2 = 17.213$, $\chi^2 = 26.433$, $\chi^2 = 7.548$, $\chi^2 = 26.683$). Figures 2 and 3 show the results of OS comparison by SOD stratification and results of OS comparison by MDA stratification, respectively. In Figure 4, the results of OS comparison in 712 patients with TNM classification can be observed. Besides, Figure 5 demonstrates the results of OS hierarchical comparison by SUA.

4.5. Prognostic Factors of 712 Patients Screened by Multivariate Cox Regression Model.

Cox multivariate analysis showed that the survival time of patients with SOD < 58.055 U/mL was

TABLE 1: Clinical data of 712 patients.

Factors	$(\bar{\chi} \pm s)/n(\%)/M(P25, P75)$
Sexuality	
Males	520 (73.03)
Female	192 (26.97)
Age (years old)	51.36 ± 8.23
Tumor size (cm)	5.12 ± 1.49
Number of tumors	
1	164 (23.03)
≥2	548 (76.97)
TNM staging	
I ~ II	413 (58.01)
III ~ IV	299 (41.99)
BCLC staging	
0 ~ A	85 (11.94)
B	313 (75.97)
C	314 (12.09)
SOD (U/mL)	60.12 ± 14.36
MDA (nmol/L)	8.89 ± 1.02
SUA (mmol/L)	312.45 ± 89.36
OS (month)	24 (11, 36)

TABLE 2: ROC curve parameters of preoperative SOD, MDA, and SUA prompting the prognosis of patients.

Factors	AUC	Sensitivity	Specificity	Youden index	Cut-off	P value
SOD	0.844	0.851	0.778	0.629	58.055	<0.001
MDA	0.838	0.842	0.761	0.603	10.825	<0.001
SUA	0.719	0.683	0.701	0.390	312.770	<0.001
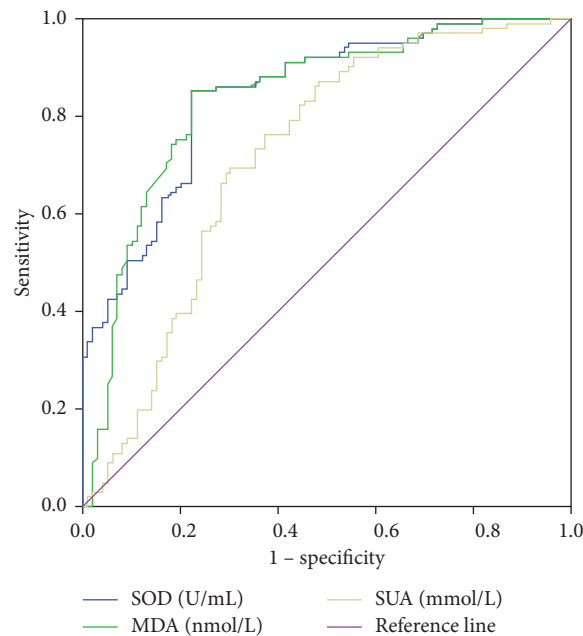
FIGURE 1: ROC curve of preoperative SOD, MDA, and SUA as data variables.

shorter than that of patients with SOD ≥ 58.055 U/mL, and the survival time of patients with SUA ≥ 312.770 mmol/L was shorter than that of patients with SUA < 312.770 mmol/L. It was confirmed that patients with low levels of SOD and high levels of SOD had worse prognosis. At the same time, TNM staging also had a certain impact on the prognosis of liver cancer. The larger the staging is, the shorter the survival time of patients after operation will be, as shown in Table 4.

TABLE 3: Univariate analysis of overall survival of patients.

Factor	HR	95% CI	P value
Sexuality			
Male	1		
Female	1.094	0.816, 1.467	0.548
Age (years old)			
<51	1		
≥51	1.033	0.770, 1.387	0.828
Tumor size(cm)			
<5	1		
≥5	1.494	1.110, 2.013	0.066
Number of tumors			
1	1		
≥2	1.715	1.011, 2.654	0.062
TNM staging			
I ~ II	1		
III ~ IV	1.830	1.109, 3.020	0.018
BCLC staging			
0 ~ A	1		
B			
C	1.997	0.432, 9.242	0.376
SOD (U/mL)			
<58.055	1		
≥58.055	4.471	2.217, 9.017	<0.001
MDA (nmol/L)			
<10.825	1		
≥10.825	1.704	1.014, 2.863	0.044
SUA (mmol/L)			
< 312.770	1		
≥312.770	1.874	1.108, 3.170	0.019

Log-rank X2 =26.443 P = 0.001

SOD (U/mL)
— < 58.055
— ≥ 58.055
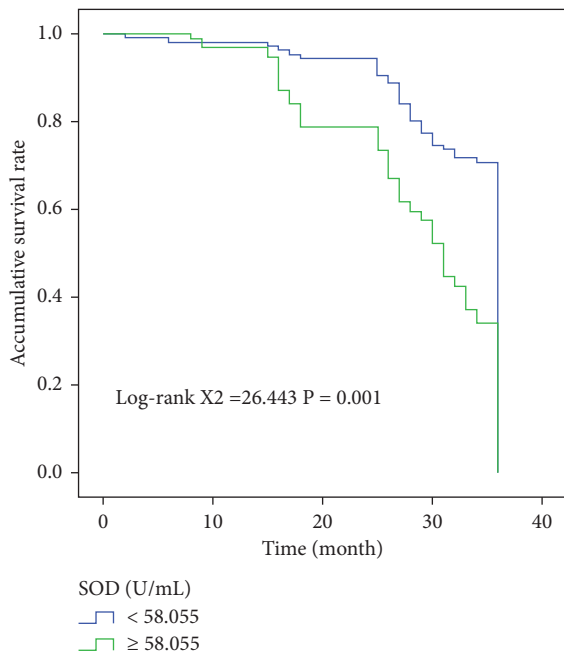
FIGURE 2: Results of OS comparison by SOD stratification in 712 patients.

Log-rank X2 = 7.548 P = 0.006

MDA (nmol/L)
— < 10.825
— ≥ 10.825
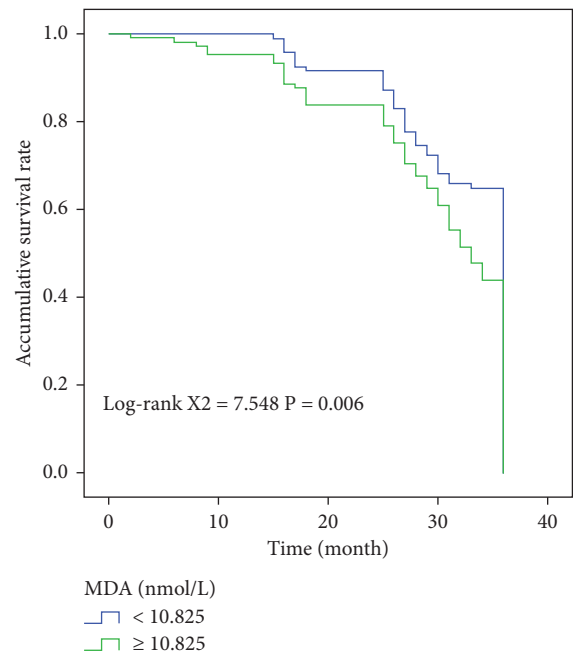
FIGURE 3: Results of OS comparison by MDA stratification in 712 patients.

Log-rank X2 = 17.213 P < 0.001

TNM staging
I ~ II
III ~ IV
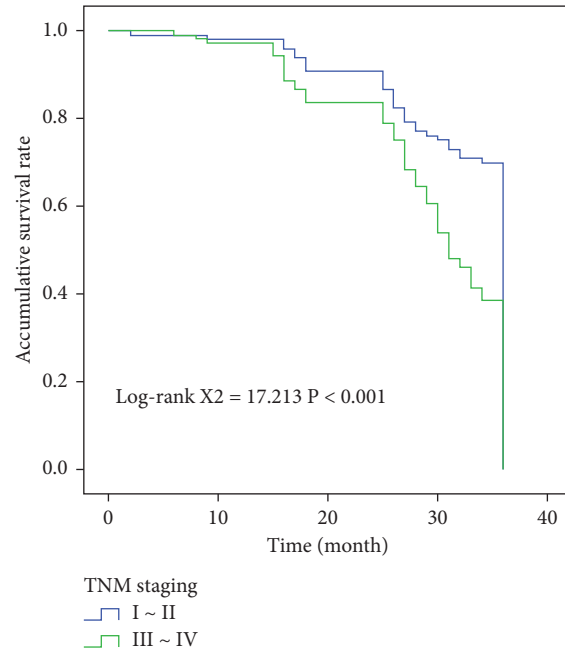
Figure 4: Results of OS comparison in 712 patients with TNM classification.

Log-rank X2 = 26.683 P < 0.001

SUA (mmol/L)
< 312.770
≥ 312.770
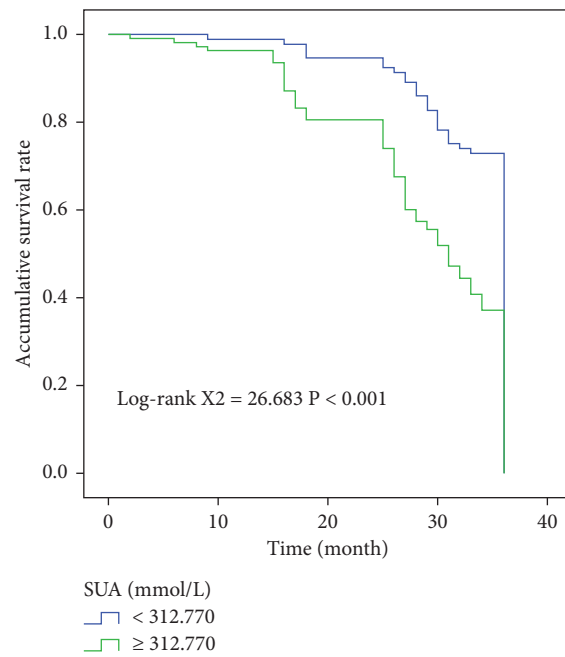
Figure 5: Results of OS hierarchical comparison by SUA in 712 patients.

Table 4: Prognostic factors of 712 patients screened by multivariate Cox regression model.

Factor	HR	95% CI	P value
TNM staging (I ~ II are controls)	1.555	1.172, 2.063	0.002
SOD (<58.055 U/mL are controls)	1.533	1.154, 2.036	0.003
MDA (<10.825 nmol/L are controls)	1.300	0.978, 1.728	0.071
SUA (<312.770 mmol/L are controls)	1.612	1.215, 2.138	0.001

5. Conclusions

In this study, the ROC curve was used to analyze the optimal truncation values of MDA, SOD, and SUA, which were 10.825 nmol/L, 58.055 U/m, and 312.77 mmol/L, respectively. The patients were analyzed according to different truncation points. From the survival curve, it can be found that the postoperative survival time of patients with MDA < 10.825 nmol/L and SUA < 312.77 mmol/L was higher than that of patients with MDA ≥ 10.825 nmol/L and SUA ≥ 312.77 mmol/L. The overall survival time of patients with SOD ≥ 58.055 U/m was higher than that of patients with SOD < 58.055 U/m. Single-factor results showed that MDA, SOD, SUA, and TNM staging were correlated with prognosis, and Log-rank test results confirmed that the above indicators were correlated with the prognosis of patients. The results of multivariate analysis also showed that pre-operative SOD < 58.055 U/mL and SUA ≥ 312.770 mmol/L and TNM staging III-IV were independent risk factors affecting the postoperative prognosis of patients, indicating that the prognosis of these liver cancer patients after radical resection may be poor and the survival time may be shortened.

In general, the preoperative oxidative stress level and serum uric acid are closely related to the death of patients with hepatitis B-related liver cancer after surgical resection. In the future, it is worth paying attention to the preoperative oxidative stress level and serum uric acid in clinical work. Research and detection of SOD and SUA levels in patients before surgery have been carefully evaluated and selected treatment options, which have important clinical significance for judging the prognosis of liver cancer after surgery. It should be noted that more prospective large sample studies are also needed to further explore the optimal predictive thresholds of SOD and SUA for predicting the death of patients and postoperative so as to further improve the predictive efficiency.

Data Availability

The data used in the paper are available from the corresponding author upon request due to requirements of permission and consent.

Conflicts of Interest

The authors declare that there are no conflicts of interest regarding the publication of this paper.

References

[1] W. Q. Qiu, J. F. Shi, L. W. Guo et al., "Medical expenditure for liver cancer in urban China: a 10-year multicenter retrospective survey (2002-2011)," *Journal of Cancer Research and Therapeutics*, vol. 14, no. 1, pp. 163–170, 2018.

[2] C. Akateh, S. M. Black, L. Conteh et al., "Neoadjuvant and adjuvant treatment strategies for hepatocellular carcinoma," *World Journal of Gastroenterology*, vol. 25, no. 28, pp. 3704–3721, 2019.

[3] C. C. N. Chong, G. L. Wong, and P. B. Lai, "Impact of antiviral therapy on post-hepatectomy outcome for hepatitis B-related hepatocellular carcinoma," *World Journal of Gastroenterology*, vol. 20, no. 20, pp. 6006–6012, 2014.

[4] A. Sharma, M. Rajappa, A. Saxena, and M. Sharma, "Antioxidant status in advanced cervical cancer patients undergoing neoadjuvant chemoradiation," *British Journal of Biomedical Science*, vol. 64, no. 1, pp. 23–27, 2007.

[5] D. B. Trindade, V. A. de Araújo, E. P. Franco, R. C. Fernandes, A. P. P. F. Carvalho, and G. D. Pimentel, "Serum uric acid concentration is not associated with handgrip strength, lean body mass or survival in gastrointestinal cancer patients," *Clinical Nutrition ESPEN*, vol. 37, no. 11, pp. 75–79, 2020.

[6] F. Chong, J. J. Huang, N. N. Huang et al., "Associations between serum uric acid and hepatobiliary-pancreatic cancer: a cohort study," *World Journal of Gastroenterology*, vol. 26, no. 44, pp. 157–171, 2020.

[7] K. D. Yadav, B. A. Patil, S. A. Raheel et al., "Serum uric acid levels in patients with oral cancer, leukoplakia and submucous fibrosis: a cross-sectional study," *Translational Cancer Research*, vol. 9, no. 4, pp. 22–32, 2020.

[8] M. Jiang, L. Ren, S. Chen, and G Li, "Serum uric acid levels and risk of eight site-specific cancers: a mendelian randomization study," *Frontiers in Genetics*, vol. 22, no. 12, pp. 1–11, 2021.

[9] R. Lombardi, G. Pisano, and S. Fargion, "Role of serum uric acid and ferritin in the development and progression of NAFLD," *International Journal of Molecular Sciences*, vol. 17, no. 4, pp. 548–555, 2016.

[10] F. S. Wang, J. G. Fan, Z. Zhang, B. Gao, and H. Y. Wang, "The global burden of liver disease: the major impact of China," *Hepatology*, vol. 60, no. 6, pp. 2099–2108, 2014.

[11] P. Luo, S. Wu, Y. Yu et al., "Current status and perspective biomarkers in AFP negative HCC: towards screening for and diagnosing hepatocellular carcinoma at an earlier stage," *Pathology and Oncology Research*, vol. 26, no. 2, pp. 599–603, 2020.

[12] S. D'souza, K. C. Lau, C. S. Coffin, and T. R. Patel, "Molecular mechanisms of viral hepatitis induced hepatocellular carcinoma," *World Journal of Gastroenterology*, vol. 26, no. 38, pp. 5759–5783, 2020.

[13] S. K. Saha, S. B. Lee, J. Won et al., "Correlation between oxidative stress, nutrition, and cancer initiation," *International Journal of Molecular Sciences*, vol. 18, no. 7, pp. 1544–1555, 2017.

[14] J. Lee, S. Giordano, and J. Zhang, "Autophagy, mitochondria and oxidative stress: cross-talk and redox signalling," *Biochemical Journal*, vol. 441, no. 2, pp. 523–540, 2012.

[15] Z. Wang, Z. Li, Y. Ye, L. Xie, and W. Li, "Oxidative stress and liver cancer: etiology and therapeutic targets," *Oxidative Medicine and Cellular Longevity*, vol. 2016, Article ID 7891574, 10 pages, 2016.

[16] H. Yu, D. Pardoll, and R. Jove, "STATs in cancer inflammation and immunity: a leading role for STAT3," *Nature Reviews Cancer*, vol. 9, no. 11, pp. 798–809, 2009.

[17] J. Djordjevic, A. Djordjevic, M. Adzic, A. Niciforovic, and M. Radojcic, "Chronic stress differentially affects antioxidant enzymes and modifies the acute stress response in liver of Wistar rats," *Physiological Research*, vol. 59, no. 5, pp. 729–736, 2010.

[18] S. T. Ahmad, W. Arjumand, S. Nafees et al., "Hesperidin alleviates acetaminophen induced toxicity in Wistar rats by abrogation of oxidative stress, apoptosis and inflammation," *Toxicology Letters*, vol. 208, no. 2, pp. 149–161, 2012.

[19] W. Chancharoenthana and A. Leelahavanichkul, "Acute kidney injury spectrum in patients with chronic liver disease: where do we stand?" *World Journal of Gastroenterology*, vol. 25, no. 28, pp. 3684–3703, 2019.

[20] R. J. DeBerardinis and N. S. Chandel, "Fundamentals of cancer metabolism," *Science Advances*, vol. 2, no. 5, Article ID 1600200, 2016.

[21] T. Y. Yu, S.-M. Jin, J. H. Jee, J. C. Bae, M.-K. Lee, and J. H. Kim, "The protective effects of increasing serum uric acid level on development of metabolic syndrome," *Diabetes & Metabolism Journal*, vol. 43, no. 4, pp. 504–520, 2019.

[22] H. Wang, H. Zhang, L. Sun, and W. Guo, "Roles of hyperuricemia in metabolic syndrome and cardiac-kidney-vascular system diseases," *American Journal of Tourism Research*, vol. 10, no. 9, pp. 2749–2763, 2018.

[23] A. Oral, T. Sahin, F. Turker, and E. Kocak, "Relationship between serum uric acid levels and nonalcoholic fatty liver disease in non-obese patients," *Medicina (Rijeka)*, vol. 55, no. 9, pp. 600–606, 2015.

Retraction

Retracted: Knowledge-Based Discovery of the Role and Mechanism of Resveratrol in Improving Glomerular Tether Cell Proliferation and Apoptosis in Diabetic Nephropathy

Journal of Healthcare Engineering

This article has been retracted by Hindawi following an investigation undertaken by the publisher [1]. This investigation has uncovered evidence of one or more of the following indicators of systematic manipulation of the publication process:

(1) Discrepancies in scope

(2) Discrepancies in the description of the research reported

(3) Discrepancies between the availability of data and the research described

(4) Inappropriate citations

(5) Incoherent, meaningless and/or irrelevant content included in the article

(6) Peer-review manipulation

The presence of these indicators undermines our confidence in the integrity of the article's content and we cannot, therefore, vouch for its reliability. Please note that this notice is intended solely to alert readers that the content of this article is unreliable. We have not investigated whether authors were aware of or involved in the systematic manipulation of the publication process.

In addition, our investigation has also shown that one or more of the following human-subject reporting requirements has not been met in this article: ethical approval by an Institutional Review Board (IRB) committee or equivalent, patient/participant consent to participate, and/or agreement to publish patient/participant details (where relevant).

Wiley and Hindawi regrets that the usual quality checks did not identify these issues before publication and have since put additional measures in place to safeguard research integrity.

We wish to credit our own Research Integrity and Research Publishing teams and anonymous and named external researchers and research integrity experts for contributing to this investigation.

The corresponding author, as the representative of all authors, has been given the opportunity to register their agreement or disagreement to this retraction. We have kept a record of any response received.

References

[1] Y. Chi, S. Liu, X. Wu et al., "Knowledge-Based Discovery of the Role and Mechanism of Resveratrol in Improving Glomerular Tether Cell Proliferation and Apoptosis in Diabetic Nephropathy," *Journal of Healthcare Engineering*, vol. 2022, Article ID 9705144, 8 pages, 2022.

Hindawi

Research Article

Knowledge-Based Discovery of the Role and Mechanism of Resveratrol in Improving Glomerular Tether Cell Proliferation and Apoptosis in Diabetic Nephropathy

Yangfeng Chi, Shuang Liu, Xinye Wu, Bingbing Zhu, Hao Wang, Yongping Liang, and Yunman Wang (iD)

Department of Nephrology, Putuo Hospital, Shanghai University of Traditional Chinese Medicine, ShangHai 200062, China

Correspondence should be addressed to Yunman Wang; yunmanwang2217@shutcm.edu.cn

To investigate the effects and mechanisms of resveratrol on glucolipid metabolism in diabetic humans. In this paper, we introduced the knowledge discovery theory into the data processing of the factors related to the pathogenesis of type 2 diabetes for the first time, and identified valid, potentially useful, and understandable pathogenesis patterns from a large amount of measured data. A data mining C4.5 algorithm was used to classify 17072 validated cross-sectional health survey data from the whole population according to the characteristics of type ρ diabetes data. A human model of diabetes mellitus was prepared by high sugar and high fat diet plus low dose streptozotocin (STZ, 35 mg/kg) and randomly grouped into four groups: the normal control group, the model group, the resveratrol group, and the pioglitazone group. 8 animals in each group were treated with the corresponding drugs for 8 weeks. Hepatic steatosis and damage were significantly reduced compared with the model group as observed by HE staining. Resveratrol has obvious effects on regulating glucolipid metabolism, and its mechanism of action is associated with its ability to increase the antioxidant activity of the body, activate the Akt signaling pathway, and improve liver pathological damage.

1. Introduction

With socioeconomic progress and development, the spectrum of diseases that threaten human health is changing. Chronic noncommunicable diseases are a growing threat to the health of the population, especially the elderly, and most notably, the prevalence of type 2 diabetes mellitus is on the rise in a near epidemic worldwide. Type 2 diabetes mellitus occurs due to a combination of genetic and environmental factors, and the interplay of these factors is complex [1]. Many factors associated with the onset of diabetes have been proposed by applying current research tools, but it is difficult to establish further linkages and identify patterns among these factors. In the face of the limitations of traditional statistical studies with huge and complex data, this paper attempts to investigate this problem through bioinformatics. Knowledge discovery is one of the main techniques in bioinformatics. It is an advanced process of identifying valid,

potential, and understandable patterns from large amount of data and is a class of deep data analysis methods [2, 3]. It can extract the regular content hidden behind the data from large-scale data and is widely used in decision support and scientific research. Based on the database and data preparation, we introduced the knowledge discovery theory into the data processing of type 2 diabetes, and used the data mining C4.5 algorithm to automatically build a decision classification tree according to the characteristics of the data. The system was trained to identify the relationship between the prevalence factors of type 2 diabetes and determine whether the disease was present [4, 5]. The application of this algorithm laid the foundation for further exploration of the pathogenesis of type 2 diabetes and the development of disease prediction models.

GSK-3β is a key enzyme involved in hepatic glucose metabolism, inhibiting its activity by phosphorylating glycogen synthase, decreasing hepatic glycogen synthesis and

increasing blood glucose concentration in the body, with abnormally high expression in diabetic and obese humans [6]. -3β is a downstream signaling molecule directly regulated by Akt, and when the upstream Akt signaling molecule is activated, GSK-3β is inhibited, preventing its inhibition of hepatic glycogen synthesis and thus facilitating the conversion of glucose uptake by the body after meals. Inhibition of GSK-3β activity plays a crucial role in glycogen synthesis [7, 8].

Hepatic glycogen is the main form of glucose storage in the body, and the body converts excess glucose in the blood into glycogen stored in the body through a series of enzymatic reactions mediated by signaling pathways, thus reducing blood glucose concentration. Therefore, increased hepatic glycogen synthesis facilitates the reduction of hepatic glycogen output for the purpose of lowering blood glucose. The experimental results showed that resveratrol could promote hepatic glycogen synthesis and lower blood glucose levels by increasing Akt phosphorylation activity, inhibiting downstream GSK-3β phosphorylation activity, and promoting downstream GCK protein levels in diabetic model animals [9, 10]. It is suggested that resveratrol may achieve the effect of lowering blood glucose by upregulating Akt activity.

Diabetic fatty liver is a common and frequent chronic complication that seriously endangers the health of diabetic patients during the onset, development, and treatment of diabetes. Some clinical studies have confirmed that liver lesions can be as high as 46% in diabetic patients. Patients who develop fatty liver can further aggravate the pathological conditions such as insulin resistance and glucose metabolism disorders, which in turn promote the deterioration of diabetes. Abnormal liver function, which affects the normal glucose metabolism function and the inability to convert excess blood glucose into hepatic glycogen for storage, can result in persistently high blood glucose levels and aggravate diabetes [11, 12]. Resveratrol can significantly regulate the body's disorders of glucose and lipid metabolism, improve the body's antioxidant activity, delay liver damage, and improve the formation and development of diabetic complications. Resveratrol has obvious antioxidative stress effects and can avoid oxidative stress damage induced by high sugar and high fat, thus playing an important role in the prevention and treatment of diabetes and its chronic complications, especially in the early stages of diabetes to delay the development of diabetic complications and protect other organ tissues. It can play an important role in the prevention and treatment of diabetes and its chronic complications, especially in the early stages of diabetes to delay the development of diabetic complications and protect other organ tissues [13–15]. Resveratrol is a natural drug with great potential, and the prospect of clinical application needs further study.

2. Data Sources, Scale, and Preprocessing Methods

The measured data were obtained from a cross-sectional survey of a whole cohort sample of 17,946 people in our hospital, from which 17,072 valid data were selected. Each data record was divided into five sections: general personal data, living and working habits, past and family medical history, physical examination data, and laboratory test data. The investigators who participated in the data collection were trained in a standardized way and used a standardized questionnaire to collect personal data; life and work habits; and medical history to determine height, weight, abdominal circumference, and blood pressure by a standardized method. Blood glucose and lipids (cholesterol, triglycerides, LDL, and HDL) were measured in a strictly quality-controlled laboratory. The diagnostic criterion for diabetes mellitus was fasting blood glucose >7.0 mmol/l [16].

The abovementioned raw data were entered into the computer and a database was established. Raw data preprocessing was used to improve the quality of the data for incomplete, noisy, and inconsistent raw data, and thus improve the quality of the excavation results. The data preprocessing process used in this paper mainly includes data cleaning, data transformation, and data statute (the specific method is published in a separate paper). The data (11,400 items) were randomly extracted from the preprocessed data by the C4.5 algorithm as the training data of the C4.5 algorithm, and the rest of the data were used as the test data. The operating system is Solaris8, and the C++ compiler is c.

In order to make the program run on the laris platform, a Makefile file for the Solaris platform was written in addition to the ANSI C implementation. After compiling and linking with cc, the executable version for the Solaris platform is generated.

3. Choice of Algorithm

The data in this paper are characterized by the predictive and continuous nature of the classifications, and it is known whether each set of data corresponds to a classification of diseased or undiseased data. The main task of this paper is to learn the classification patterns in the data. Based on the categorical nature of the mining task, the decision tree algorithm, which is least affected by the record fields, easy to understand the model, easy to train the model, easy to implement the model, has the most generality, and highest usefulness, was selected for mining. The C4.5 algorithm is a very effective decision tree algorithm, which can handle continuous data items. Therefore, the C4.5 algorithm is the preferred algorithm for data mining in this work [17].

4. C4.5 Principle of the Decision Tree Classification Algorithm

C4.5 is an algorithm for constructing decision tree classifiers, which is an extension of the ID3 algorithm. While the I3 algorithm can only handle discrete descriptive attributes, the C4.5 algorithm can also handle cases where the descriptive attributes are continuous. This algorithm uses a comparison of the magnitude of the information gain value of each descriptive attribute to select the attribute with the largest gain value for classification. If there are continuous

TABLE 1: Comparison of glycolipid metabolic indexes in each group after drug administration and treatment ($\overline{x} \pm s$, $n = 8$).

Group	FBG	TC	TG	LDL-C	HDL-C
Normal group	4.52 ± 0.44	1.32 ± 0.19	0.73 ± 0.25	0.27 ± 0.13	0.59 ± 0.04
Model group	24.6 ± 2.31	12.1 ± 0.68	3.48 ± 0.43	7.13 ± 3.65	0.54 ± 0.2
Resveratrol group	14.3 ± 3.4	2.71 ± 0.41	1.08 ± 0.31	0.75 ± .33	0.81 ± 0.12
Pioglitazone group	13.6 ± 3.01	2.42 ± 0.52	0.92 ± 0.49	0.69 ± 0.15	0.91 ± .13

descriptive attributes, then the values of these continuous attributes are first divided into different zones, i.e., "discretized". The method of "discretizing" continuous attributes is as follows:

$$A_i = \text{MIN} + \frac{\text{MAX} - \text{MIN}}{N} \times i, \ i = 1, 2, \ldots, N. \quad (1)$$

AK, the largest F57C value, is selected as the breakpoint for this continuous attribute, and the attribute value to [MIN,AK] and (AK, MAN) interval values is set[18].

$$S = - \sum_I \left(p_i^* \log(p_i) \right). \quad (2)$$

The information gain described in the paper is the effective reduction of information entropy, according to which it is possible to determine what variables at what level to classify the algorithm in the application by two processes a training process to derive the classification algorithm, and a testing process, i.e., to derive the correct recognition rate. The experiment is to select about two-thirds of the 17072 valid data, i.e., 11400 as training data and the remaining 5672 as test data.

5. Case Study

5.1. General Materials. Healthy Wistar male rats, SPF class, 50 rats, body weight (120 ± 15) g, were purchased from the Guangdong Experimental Animal Center, and the experiments were performed in an SPF class laboratory at 20–25°C, 40%–70% relative humidity, and 10–15 air changes/h. Resveratrol (purity = 95.1%, HPLC) was provided by Shaanxi Saide Hi-Tech Biological Co. Ltd. High-fat and high-sugar feed formula: 0.5% bile salt, 1% cholesterol, 1% egg yolk powder, 10% lard, 20% sucrose, 67.5% common feed.

5.2. Main Reagents. Trace malondialdehyde (MDA), liver glycogen, and other measurement kits were purchased from Nanjing Jiancheng Institute of Biological Engineering; concentrated sulfuric acid (AR) was purchased from Guangzhou Chemical Reagent Factory; p-Akt, p-GSK-3β, GSK-3β, and GAPDH antibodies were purchased from Cell Signaling, USA; Akt and GCK antibodies were purchased from Santa Cruz, USA; and streptozotocin (STZ) was purchased from Sigma, USA.

5.3. Results. Compared with the normal group, the diabetic humans showed the typical symptoms of diabetes, such as fasting blood glucose, serum TC, TG, and LDL-C levels, and the difference was statistically significant (P < 0.05). After 8 weeks of treatment, the symptoms of "three more and one
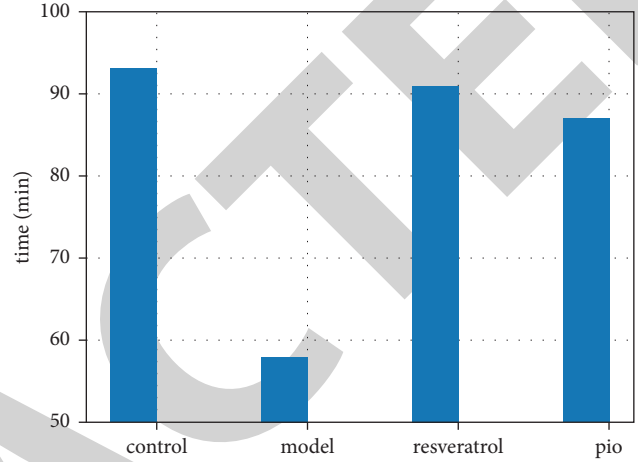
FIGURE 1: Effect of liver glycogen content in liver tissue.

less" in all diabetic groups were improved, and the levels of fasting blood glucose, TC, TG, and LDL-C were significantly reduced, and the levels of HDL-C were increased in each group, and the difference was statistically significant (P < 0.05) [19]. It is suggested that resveratrol has the effect of lowering blood glucose and also has a certain effect on lipid regulation (Table 1).

The liver of the model group showed a significant decrease in liver glycogen content compared with the normal group, and the difference was statistically significant ($P < 0.05$). In the resveratrol and pioglitazone groups, the liver glycogen content increased significantly compared with the model group, and the difference was statistically significant ($P < 0.05$) [20]. This suggests that resveratrol has the effect of significantly increasing the liver glycogen content and promoting the storage of glycogen in the body, which not only promotes the utilization of blood sugar but also plays an important role in preventing the occurrence of multiorgan complications in the body (Figure 1).

The level of SOD activity reflects the ability of the body to scavenge oxygen free radicals, while the level of MDA content reflects the severity of free radical attack on the body cells. The results of SOD activity and MDA content were used to analyze the ability of the organism to resist oxygen stress. In the model group, SOD activity decreased and MDA content increased compared with the normal group, and the difference was statistically significant ($P < 0.05$); in the drug administration group, SOD activity increased and MDA content decreased compared with the model group, and the difference was statistically significant ($P < 0.05$) [21]. The effect of the resveratrol group has significantly improved the level of oxidative stress in the
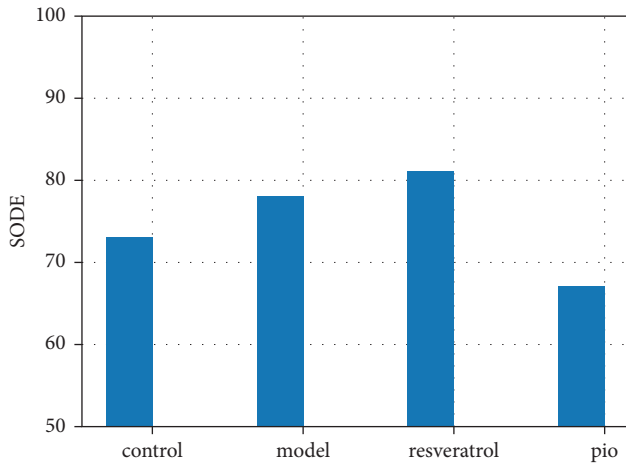
FIGURE 2: Effect of resveratrol on SOD activity and MDA content in diabetic human serum.

FIGURE 3: Effect of resveratrol on the phosphorylation level of Akt in diabetic human liver.
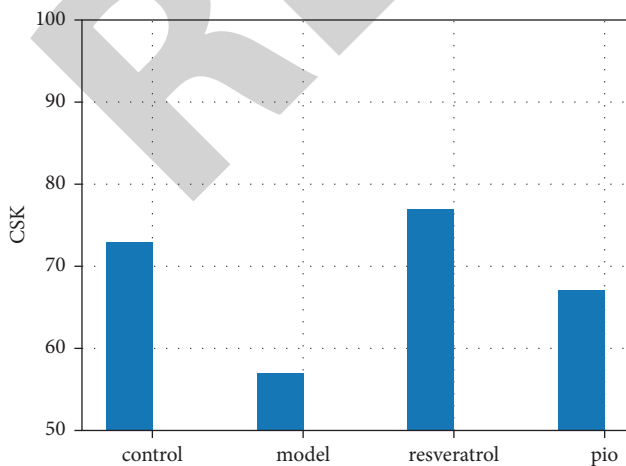
FIGURE 4: Effect of resveratrol on GSK-3β activity in diabetic humans.

FIGURE 5: Effect of resveratrol on diabetic human glucose kinase (GCK) protein expression.

body, thus controlling the occurrence of diabetic complications (Figure 2).

The protein expression of phosphorylated Akt was significantly reduced in the model group rats relative to total Akt, and the phosphorylated expression of Akt protein was inhibited, while resveratrol and pioglitazone could effectively increase the phosphorylated expression level of Akt protein in the livers of model animals (Figure 3).

The active form of GSK-3β in the model group, phosphorylated-GSK-3β relative to total-GSK-3β protein expression level, was significantly higher than that in the normal group, and the difference was statistically significant ($P < 0.05$). The resveratrol group could significantly reduce the protein expression of p-GSK-3β compared with the model group, and the difference was statistically significant ($P < 0.05$), suggesting that resveratrol could effectively inhibit the phosphorylated expression level of GSK-3β protein in the liver (Figure 4).

The protein expression level of glucokinase in the model group was significantly decreased compared with the normal group, and the difference was statistically significant ($P < 0.05$). The resveratrol group could significantly increase the protein expression of GCK in the diabetic human liver, and the difference was statistically significant ($P < 0.05$). The difference was statistically significant ($P < 0.05$) [22], suggesting that resveratrol could effectively increase the protein expression level of GCK in the diabetic human liver based on the activation of liver Akt protein phosphorylation expression (Figure 5).

In the resveratrol group, the morphology of hepatocytes was normal, the nuclei were clear, small lipid droplets were still visible in the plasma of some hepatocytes, and the boundaries of local cells were unclear. The hepatocyte cords were arranged neatly and radially, the hepatic sinusoids were normal, and some of the hepatic cords were disordered. The degree of hepatic steatosis and damage was significantly reduced compared with that of the hyperlipidemic diabetic human model group. In the pioglitazone group, the degree of hepatic steatosis and damage was reduced compared with that in the hyperlipidemic diabetic human model group, but a large
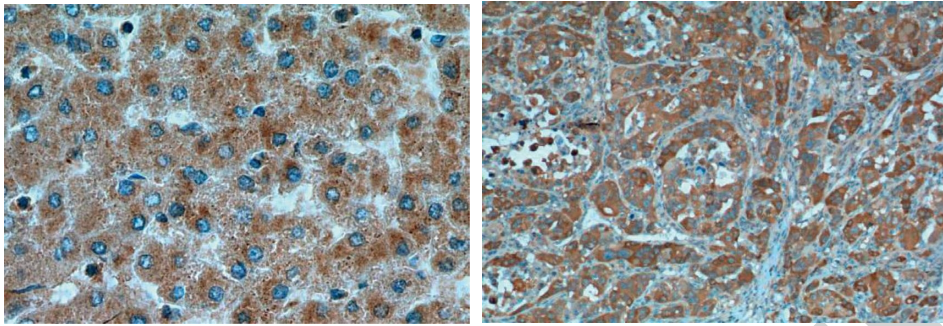
FIGURE 6: HE staining of human liver tissue in each group.

Three blobs

Gaussian divided into three quantiles
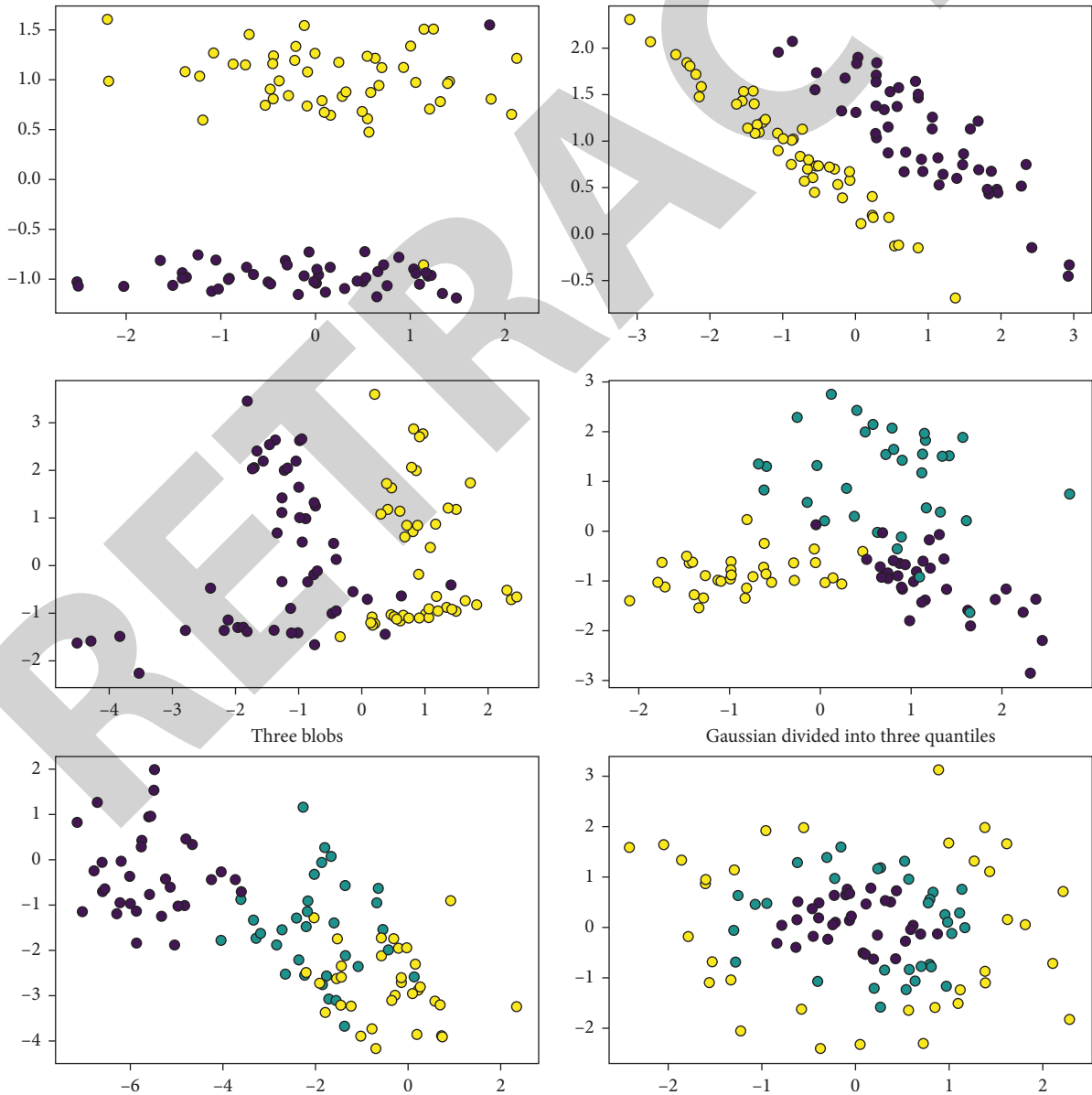
FIGURE 7: Clustering subcases of different methods.
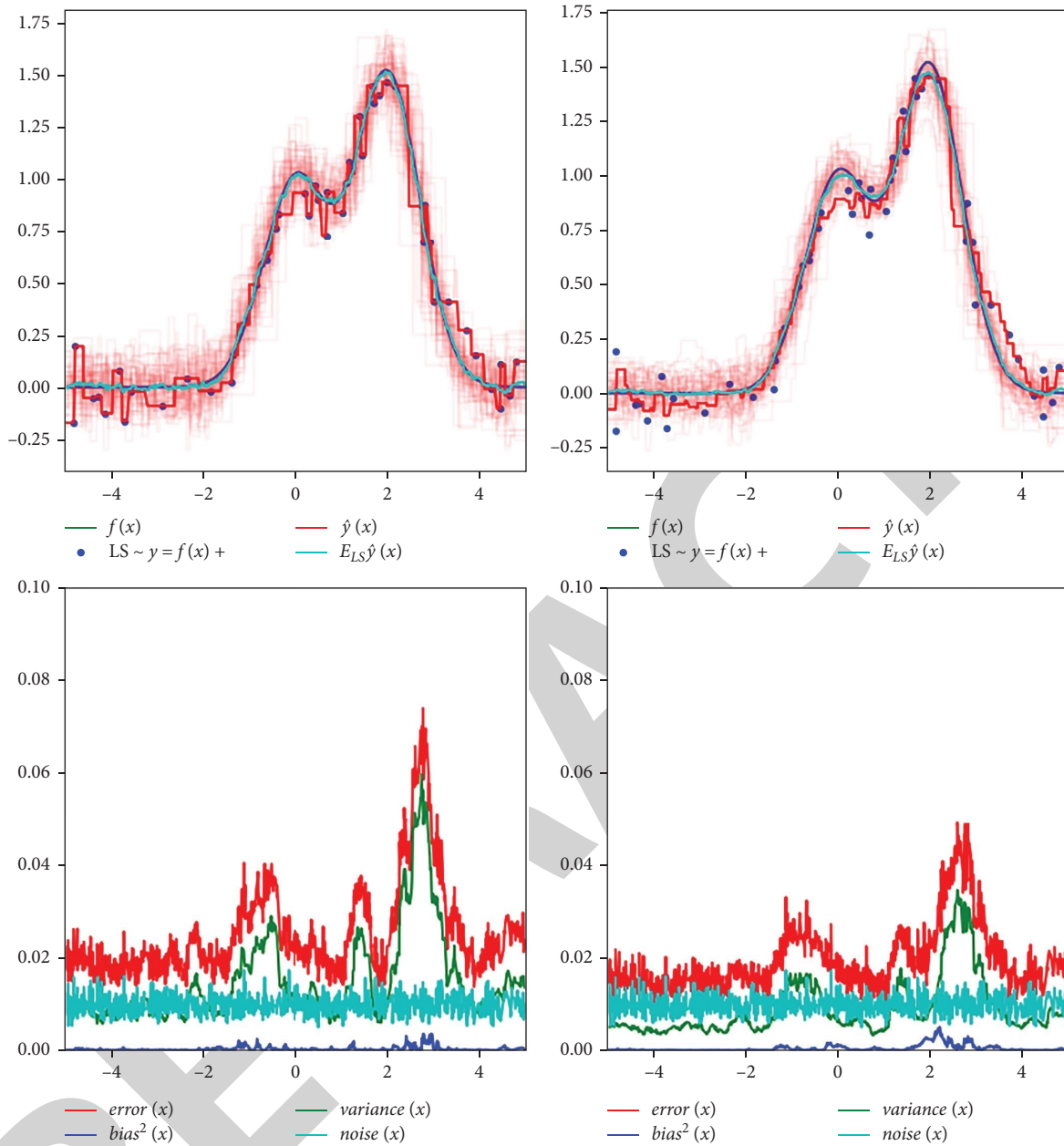
FIGURE 8: Recognition efficiency.

number of fat vacuoles of different sizes and uneven cytoplasmic staining were still visible in the hepatocytes (Figure 6).

6. Experimental Results

By using the C4.5 algorithm, the following decision classification tree was derived, where N indicates no disease and Y indicates disease (the main reason for giving this type of classification decision tree is that the values in the classification can be directly observed, such as the blood glucose value (GLU) of 5.85, as the threshold value of the main classification is very important, the value tends to be consistent with the medical understanding), as shown in Figure 7.

As shown in Figure 7, a total of 31 nodal parameters entered into the decision tree accounted for 66% of all investigated parameters, classified according to the larger information gain value (information gain value) determined by this algorithm. Among them, there were 10 node parameters in the first 5 levels, including age, family history of diabetes, dietary habits, hyperlipidemia, etc. The nodal parameters in the first 10 levels were 30, including abdominal circumference, body weight, blood pressure, and lipids. The composition of these parameters tended to be consistent with the known risk factors in medicine, especially the threshold value of 5.85 for the classification of blood glucose, which is of great importance for the classification of risk factors of diabetes in medicine. Finally, the classification accuracy was tested by randomly dividing the given data into two independent sets, i.e., the training set and the test set, and specifically, 5672 test

samples were used in the experiment, including 340 diseased samples.

As shown in Figure 8, this is consistent with the domestic report of Geng [4], and also with the foreign study of Young et al. [3] in diabetic rats in vivo. And they found that the cause of the proliferation of diabetic glomerular tract cells was related to the paracrine secretion of PDGF and bFGF. In contrast, studies in the commonly used high glucose model (normal glomerular thylakoid cells in culture stimulated by high glucose) showed that high glucose promoted ECM secretion but inhibited MC proliferation. This suggests that a brief high glucose stimulation (a few days) cannot mimic the glomerular thylakoid cells in vivo (there are other pathogenic factors besides high glucose, and it is a chronic pathological process), which also suggests that a diabetic model followed by MC culture is a good way to study glomerular thylakoid cells in DM.

7. Conclusions

The common approaches to knowledge discovery mainly include techniques such as artificial neural networks, decision trees, genetic algorithms, nearest neighbor algorithms, rule derivation, fuzzy theory methods, and visualization. Although almost all data mining techniques can be described as data-driven rather than user-driven, i.e., the user only needs to give the data when using these algorithms and does not have to tell the algorithm what to do and what results to expect; everything is found by the algorithm itself from the given servant data. Based on the ID3 algorithm, a variety of decision tree algorithms have been developed, and the C4.5 algorithm is one of them. It is an extension of the I3 algorithm.

Data Availability

The data underlying the results presented in the study are available within the manuscript.

Conflicts of Interest

The authors declare no conflicts of interest.

Authors' Contributions

Yangfeng Chi and Shuang Liu made equal contributions to the manuscript.

Acknowledgments

References

[1] A. Yarahmadi, S. Z. Shahrokhi, Z. Mostafavi-Pour, and N. Azarpira, "MicroRNAs in diabetic nephropathy: from molecular mechanisms to new therapeutic targets of treatment," *Biochemical Pharmacology*, vol. 189, Article ID 114301, 2021.

[2] S. Rovira-Llopis, C. Bañuls, N. Diaz-Morales, A. Hernandez-Mijares, M. Rocha, and V. M. Victor, "Mitochondrial dynamics in type 2 diabetes: pathophysiological implications," *Redox Biology*, vol. 11, pp. 637–645, 2017.

[3] M. Yetisgen-Yildiz and W. Pratt, "Using statistical and knowledge-based approaches for literature-based discovery," *Journal of Biomedical Informatics*, vol. 39, no. 6, pp. 600–611, 2006.

[4] A. Yarahmadi, N. Azarpira, and Z. Mostafavi-Pour, "Role of mTOR complex 1 signaling pathway in the pathogenesis of diabetes complications; A mini review," *Int J Mol Cell Med Summer*, vol. 10, no. 3, p. 2, 2021.

[5] A. Muzzi, V. Masignani, and R. Rappuoli, "The pan-genome: towards a knowledge-based discovery of novel targets for vaccines and antibacterials," *Drug Discovery Today*, vol. 12, no. 11-12, pp. 429–439, 2007.

[6] S. Sheng, M. Zou, Y. Yang et al., "miR-23a-3p regulates the inflammatory response and fibrosis in diabetic kidney disease by targeting early growth response 1," *In Vitro Cellular & Developmental Biology - Animal*, vol. 57, no. 8, pp. 763–774, 2021.

[7] J. Strycharz, Z. Rygielska, E. Swiderska et al., "SIRT1 as a therapeutic target in diabetic complications," *Current Medicinal Chemistry*, vol. 25, no. 9, pp. 1002–1035, 2018.

[8] D. L. Galvan, N. H. Green, and F. R. Danesh, "The hallmarks of mitochondrial dysfunction in chronic kidney disease," *Kidney International*, vol. 92, no. 5, pp. 1051–1057, 2017.

[9] C. Tang, M. J. Livingston, Z. Liu, and Z. Dong, "Autophagy in kidney homeostasis and disease," *Nature Reviews Nephrology*, vol. 16, no. 9, pp. 489–508, 2020.

[10] A. K. Maiti, "Development of biomarkers and molecular therapy based on inflammatory genes in diabetic nephropathy," *International Journal of Molecular Sciences*, vol. 22, no. 18, p. 9985, 2021.

[11] H. J. Zheng, X. Zhang, J. Guo et al., "Lysosomal dysfunction-induced autophagic stress in diabetic kidney disease," *Journal of Cellular and Molecular Medicine*, vol. 24, no. 15, pp. 8276–8290, 2020.

[12] J. Wada and A. Nakatsuka, "Mitochondrial dynamics and mitochondrial dysfunction in diabetes," *Acta Medica Okayama*, vol. 70, no. 3, pp. 151–158, 2016.

[13] Y. Yao, X. Zhao, J. Xin, Y. Wu, and H. Li, "Coumarins improved type 2 diabetes induced by high-fat diet and streptozotocin in mice via antioxidation," *Canadian Journal of Physiology and Pharmacology*, vol. 96, no. 8, pp. 765–771, 2018.

[14] K. R. Hallows, P. F. Mount, N. M. Pastor-Soler, and D. A. Power, "Role of the energy sensor AMP-activated protein kinase in renal physiology and disease," *American Journal of Physiology - Renal Physiology*, vol. 298, no. 5, Article ID F1067, 2010.

[15] N. Apostolova and V. M. Victor, "Molecular strategies for targeting antioxidants to mitochondria: therapeutic implications," *Antioxidants and Redox Signaling*, vol. 22, no. 8, pp. 686–729, 2015.

[16] M. Guerrero-Hue, V. Farre-Alins, A. Palomino-Antolin et al., "Targeting Nrf2 in protection against renal disease," *Current Medicinal Chemistry*, vol. 24, no. 33, pp. 3583–3605, 2017.

[17] A. V. Cybulsky, R. J. Quigg, and D. J. Salant, "Experimental membranous nephropathy redux," *American Journal of Physiology - Renal Physiology*, vol. 289, no. 4, pp. F660–F671, 2005.

Retraction

Retracted: Impact of High-Flux Hemodialysis on Chronic Inflammation, Antioxidant Capacity, Body Temperature, and Immune Function in Patients with Chronic Renal Failure

Journal of Healthcare Engineering

This article has been retracted by Hindawi following an investigation undertaken by the publisher [1]. This investigation has uncovered evidence of one or more of the following indicators of systematic manipulation of the publication process:

(1) Discrepancies in scope

(2) Discrepancies in the description of the research reported

(3) Discrepancies between the availability of data and the research described

(4) Inappropriate citations

(5) Incoherent, meaningless and/or irrelevant content included in the article

(6) Peer-review manipulation

The presence of these indicators undermines our confidence in the integrity of the article's content and we cannot, therefore, vouch for its reliability. Please note that this notice is intended solely to alert readers that the content of this article is unreliable. We have not investigated whether authors were aware of or involved in the systematic manipulation of the publication process.

Wiley and Hindawi regrets that the usual quality checks did not identify these issues before publication and have since put additional measures in place to safeguard research integrity.

We wish to credit our own Research Integrity and Research Publishing teams and anonymous and named external researchers and research integrity experts for contributing to this investigation.

The corresponding author, as the representative of all authors, has been given the opportunity to register their agreement or disagreement to this retraction. We have kept a record of any response received.

References

[1] S. Li, H. Li, J. Wang, and L. Yin, "Impact of High-Flux Hemodialysis on Chronic Inflammation, Antioxidant Capacity, Body Temperature, and Immune Function in Patients with Chronic Renal Failure," *Journal of Healthcare Engineering*, vol. 2022, Article ID 7375006, 7 pages, 2022.

Research Article

Impact of High-Flux Hemodialysis on Chronic Inflammation, Antioxidant Capacity, Body Temperature, and Immune Function in Patients with Chronic Renal Failure

Sufang Li,[1] Hongwei Li,[2] Jun Wang,[3] and Lianliang Yin [1]

[1]*Department of Blood Purification Room, Dalian No. 3 People's Hospital, Dalian 116033, China*
[2]*Department of Laboratory, Dalian No. 3 People's Hospital, Dalian 116033, China*
[3]*Department of Cardiology, Dalian Fifth People's Hospital, Dalian 116033, China*

Correspondence should be addressed to Lianliang Yin; yinlianlianga@163.com

In order to probe into the impact of high-flux dialysis and hemodiafiltration on patients with chronic rental failure, this paper selects in total 92 cases with chronic renal failure receiving hemodialysis from November 2018 to July 2021, allocating them into two groups based on the random table, each with 46 cases. The control group received hemodiafiltration, the observation group is given high-flux hemodialysis, and we compared serum inflammatory factor level and antioxidant factor level before and after treatment, as well as cellular immune factor level (CD3+, CD4+) and humoral immune factor level (IgE) before and after treatment in the two groups; the renal function, serum total calcium ion level, and serum phosphorus ion level in the two groups were compared before and after treatment, as well as the proportion of metabolic abnormalities in calcium and phosphorus ion levels during treatment; the trend of changes in axillary temperature during treatment in the two groups is analyzed. After treatment, serum inflammatory factor level (hs-CRP & TNF-α) is lower than that in the control group ($P < 0.05$), antioxidant factor level (MDA) is lower than that in the control group ($P < 0.05$), and SOD level is higher than that in the control group ($P < 05$). After treatment CD3+ and CD4+ levels in the observation group are higher than those in the control group ($P < 0.05$). For patients with chronic renal failure, high-flux hemodialysis is available to better reduce inflammatory response, improve antioxidant and immune capacity in the body, and help maintain calcium and phosphorus metabolic balance.

1. Introduction

Chronic kidney-related diseases will inevitably result in rental failure with the end of the course of disease research [1]. Under the current medical conditions, the most effective way to improve life quality for patients with chronic renal failure is kidney transplantation, but which is difficult to find and expensive, and most patients are still receiving long-term hemodiafiltration [2]. Studies have said that for those with chronic renal failure receiving long-term hemodiafiltration, combined with exogenous microorganisms and even endotoxin, immune complexes accumulated in the body by chronic kidney disease will activate the mononuclear macrophage system as well as other immune systems, resulting in the body a long-term obvious state of chronic inflammatory response and reduced antioxidant capacity [3, 4]. Long-term hemodiafiltration will also have a certain impact on the patient immune function, calcium, and phosphorus metabolism in the body [5].

In recent years, as people increasingly apply PS membrane for high-flux dialysis machine, they can better coordinate the balance between hydrophilicity and hydrophobicity, effectively improving the compatibleness between molecular biofilms and blood. In comparison with the conventional hemodiafiltration in the past, it has a greater ultrafiltration coefficient, while having a stronger adsorption capacity, which can better remove the endotoxins, inflammatory metabolites, and immuno-complexes in patients [6]. Although high-flux hemodialysis has been applied and popularized in patients with chronic renal

failure, the research on inflammation, oxidative stress, and immunity of patients after high-flux hemodialysis needs to be further studied, and no study has been seen on the impact of high-flux dialysis on changes in body temperature [7]. Therefore, our work mainly explores the clinical effect of high-flux hemodialysis on patients with chronic renal failure and its impact on inflammation, oxidative stress, immune function, and body temperature.

2. Information and Methods

2.1. General Information. Our team selected 92 patients receiving hemodialysis for chronic renal failure from November 2018 to July 2021 as our research subjects; they signed a consent form before joining the experiment, and we declared for the Ethics board approval.

Inclusion criteria include diagnosed of chronic renal failure clear and renal failure over 1 year; need to receive regular hemodialysis; 40–60 years old [8–11].

Exclusion criteria include those who combined with blood system-borne diseases, malignant tumors, bloodstream infections, chronic cardiopulmonary dysfunction, hepatic insufficiency, receiving immunosuppressants 1 month before joining the group, allogeneic blood transfusion within 3 months before joining, mental illness, during fever phase for body infection, pregnancy, and lactation [12–14].

In accordance with random table, we allocated them into two groups, 46 cases each. Observation group includes 22 male, 24 female, 40–60 years old, average (50.2 ± 1.5), and history of chronic renal failure lasting for 1–3 years, average (2.3 ± 0.2) [15–17].

Causes are as follows: 10 cases with nephrotic syndrome, 10 cases with obstructive kidney failure, 5 cases with immunoglobulin A (IgA) nephropathy, 16 cases with diabetic nephropathy, and 5 cases with interstitial nephritis.

Control group includes the following: 23 male, 23 female, 40–60 years old, average (50.3 ± 1.6), and history of chronic renal failure lasting for 1–3 years, average (2.4 ± 0.2).

Causes include the following: 10 cases with renal syndrome, 10 cases with obstructive kidney failure, 4 cases with IgA nephropathy, 16 cases with diabetic nephropathy, and 6 cases with interstitial nephritis. There is no statistically significant difference between the two groups in comparing sex, age, chronic renal failure history, and causes ($P > 0.05$).

2.2. Method. All participants received low molecular weight heparin sodium anticoagulant, with dehydration volume of 3000 to 6000 ml/time, and the sodium concentration in dialysis solution is 14 mmol/L, with flow rate set at 500 ml/min. The control group received hemodiafiltration, using dialysis machine 4008S and its matched hemodialysis FX80 from Fresenius Medical Care (USA), with the parameters setting as follows: ultrafiltration coefficient of 59 ml/(h mmHg), filter membrane area of 1.8 m^2, and blood flow of 200–250 ml/min. The observation group received high-flux hemodialysis, using dialysis machine 4008B and its matched hemodialysis 18UC from AsahiKASEI (Japan), with the

parameters setting as follows: ultrafiltration coefficient of 60 ml/(h mmHg), filter membrane area of 1.8 m^2, and blood flow of 280–360 ml/min. Our team performed the above treatment for 4 h each time every 2 to 3 days.

2.3. Observational Indicators. Our team compared serum inflammatory factor level and antioxidant factor level before and after treatment, as well as changes in cellular immune factor level (CD3+, CD4+) and humoral immune factor level (IgE) before and after treatment. Later, we compared the changes in renal function, total serum calcium ion level, serum phosphorus ion level before and after treatment, as well as the proportion of metabolic abnormalities in calcium and phosphorus ion levels during treatment, and analyzed the trend of changes in axillary temperature and the remaining clinical manifestations in the two groups after treatment.

2.4. Standard. Our work is based on the changes in serum inflammatory factors as the standard, like hypersensitive C-reactive protein (hs-CRP, ELISA, <100 ng/L) and tumor necrosis factor-α (TNF-α, ELISA, 5 ng/L–100 ng/L). Oxidative stress indicators included malondialdehyde (MDA, 3.52 mmol/L-4.78 mmol/L) and superoxide dismutase (SOD, 0.242 U/L–0.620 U/L). Cellular immune indicators included CD3+T (flow cytometry, reference value for adult: 955–2860/UL) and CD4+T count (flow cytometry, reference value for adult: 450–1440/0 UL). Humoral immune indicators mainly included IgE (flow cytometry, reference value for adult: 277 U/ml–759 U/ml); L) and serum creatinine (reference value for adult: 2.86 mmol/L–7.14 mmol/L); serum electrolyte level determination included serum total calcium ions (reference value for adult: 2.08 mmol/L–2.60 mmol/L) and serum phosphorus ions (reference value for adult: 0.97 mmol/L–1.61 mmol/L). Changes in body temperature during treatment are represented by axillary temperature (reference value for adult: 36.0°C~37.0°C). Clinical manifestations during treatment mainly included pruritus, renal osteoporosis, nausea and vomiting, abdominal distention and pain, and restless leg syndrome.

2.5. Statistical Processing. Through SPSS 20.0, our team expressed the data as mean ± standard deviation (SD) and compared the mean between the two groups via t-test, and the intergroup rate through χ^2 test. $P < 0.05$ mean difference is significant.

3. Results before and after Treatment

3.1. Comparison of Serum Inflammatory Factor Level and Antioxidant Factor Level before and after Treatment. There is no statistical significance in comparing serum inflammatory factor level (hs-CRP &TNF-α) with antioxidant factor level (MDA & SOD) between the two groups before treatment ($P > 0.05$). After treatment, serum inflammatory factor (hs-CRP and TNF-α) level in the

two groups is lower than that before treatment ($P < 0.05$), serum inflammatory factor (hs-CRP and TNF-α) level in the observation group is lower than that in the control group ($P < 0.05$), antioxidant factor (MDA) level in the two groups is lower than that before treatment ($P < 0.05$), SOD level is higher than that before treatment ($P < 0.05$), antioxidant factor (MDA) level in the observation group is lower than that in the control group ($P < 0.05$), and SOD level is higher than that in the control group ($P < 0.05$), as shown in Table 1. Figure 1 is the comparison of serum inflammatory factor and antioxidant factor levels before and after treatment.

3.2. Comparison of Cellular Immune Factor Level (CD3+, CD4+) and Humoral Immune Factor Level (IgE) before and after Treatment.

The difference between CD3+ and CD4+ levels and IgE level is not significant ($P > 0.05$); CD3+ and CD4+ levels are higher than those before treatment ($P < 0.05$); IgE level is lower than that before treatment ($P < 0.05$). After treatment, CD3+ and CD4+ levels in the observation group are higher than those in the control group ($P < 0.05$) and IgE level is lower than that in the control group ($P < 0.05$), as shown in Table 2. Figure 2 presents the comparison of CD3+, CD4+ levels, and humoral immune factor IgE level before and after treatment.

3.3. Comparison of Renal Function before and after Treatment.

The differences in urea nitrogen and creatinine levels in the two groups before treatment are not significant ($P > 0.05$); urea nitrogen and creatinine levels in the two groups after treatment are lower than before ($P < 0.05$); and the levels of urea nitrogen and creatinine levels in the observation group after treatment are lower than those in the control group ($P < 00.05$), as shown in Table 3. Figure 3 displays the comparison of renal function before and after treatment between the two groups.

3.4. Comparison of Serum Total Calcium Ion and Serum Phosphorus Ion Levels between the Two Groups after Treatment.

The serum total calcium ion level in serum is higher than that in the control group ($P < 0.05$), and the serum phosphorus ion level is lower than that in the control group ($P < 0.05$), as shown in Table 4.

Proportion of hypercalcemia, hypocalcemia, hyperphosphatemia, and hypophosphatemia in the observation group during treatment is lower than that in the control group ($P < 0.05$), as shown in Table 5.

3.5. Changes in Axillary Temperature during Treatment in the Two Groups.

The difference in pretreatment temperature is not significant ($P > 0.05$). Axillary temperature during treatment and after treatment in 30min in the observation group is normal and higher than that in the control group, as shown in Table 6. Figure 4 illustrates the axillary temperature in the two groups during treatment.

3.6. Comparison of Clinical Manifestations That Still Existed after Treatment between the Two Groups.

The proportion of pruritus, renal osteoporosis, nausea and vomiting, abdominal distension, and pain as well as restless leg syndrome in the observation group is signally lower than that in the control group ($P < 0.05$), as shown in Table 7.

4. The Clinical Result Analysis

Chronic renal failure, a clinically universal nephrology-related disease, with the progress of renal dysfunction, will result in metabolic abnormalities in hydrolytic electrolytes and alkaloid and increase in immunological complexes, inflammatory factors, endotoxins, and microorganisms. If not timely and effective treated, it even results in death. At present, giving hemodialysis to patients with chronic renal failure is the most effective intervention to prolong the survival time of patients other than kidney transplantation, in which hemodiafiltration and high-flux hemodialysis are the most universally applied methods, both of which have certain clinical efficacy. Among them, hemodiafiltration is mainly to disperse the impact of removing metabolic products in the blood but with limited impact on removing the molecular products in macromolecule nucleus so that it cannot effectively reduce the body's inflammatory response and improve antioxidant capacity. Long-term hemodiafiltration also has certain damage to patient's immune function. Convection and dispersion are the basic function mechanism of high-flux hemodialysis, which is available to remove endotoxins, immune complex and other medium-molecule and large-molecule substances more effectively than conventional hemodiafiltration, thus improving the clinical effect.

For patients receiving hemodialysis for chronic renal failure, the observation group in this work received high-flux hemodialysis, in comparison with hemodiafiltration given to the control group. Our team compared the serum inflammatory factors, antioxidant factors, CD3+ and CD4+, and IgE levels before and after treatment of the two groups; we found that after treatment, inflammatory factors hs-CRP and TNF-α levels in the t observation group are lower than those in the control group, antioxidant factor MDA level in the observation group is lower than that in the control group, SOD level is higher than that in the control group, CD3+ and CD4+ levels are higher than those in the control group, and IgE level is lower than that in the control group. It is suggested that applying high-flux hemodialysis for patients with chronic renal failure can more effectively reduce inflammatory response, improve antioxidant ability, and reduce the damage to immune function in comparison with conventional hemodiafiltration. Additionally, the changes in renal function before and after the treatment in the two groups are compared. After treatment, urea nitrogen and creatinine levels in the observation group are lower than those in the control group. Although both groups had improved renal function after treatment, the impact of high-flux hemodialysis is more pronounced in the observation group. At the same time, our team compared the total serum calcium ion and serum phosphorus ion levels after treatment and the proportion of metabolic abnormalities in calcium

Table 1: Comparison of serum inflammatory factor level and antioxidant factor level before and after treatment ($\overline{x} \pm s$).

		hs-CRP (mg/L)	TNF-α (g/L)	MDA (mol/L)	SOD (U/L)
Observation group	Before treatment	12.5 ± 1.4	135.6 ± 10.2	6.6 ± 0.4	0.4 ± 0.1
	After treatment	6.9 ± 0.5▲★	41.2 ± 4.3▲★	2.6 ± 0.1▲★	1.1 ± 0.2▲★
Control group	Before treatment	12.6 ± 1.5	135.7 ± 10.1	6.7 ± 0.5	0.5 ± 0.1
	After treatment	9.6 ± 1.1▲	60.4 ± 5.1▲	4.2 ± 0.2▲	0.8 ± 0.1▲

▲ Compared with pretreatment, $P < 0.05$; ★in comparison with the control group, $P < 0.05$.
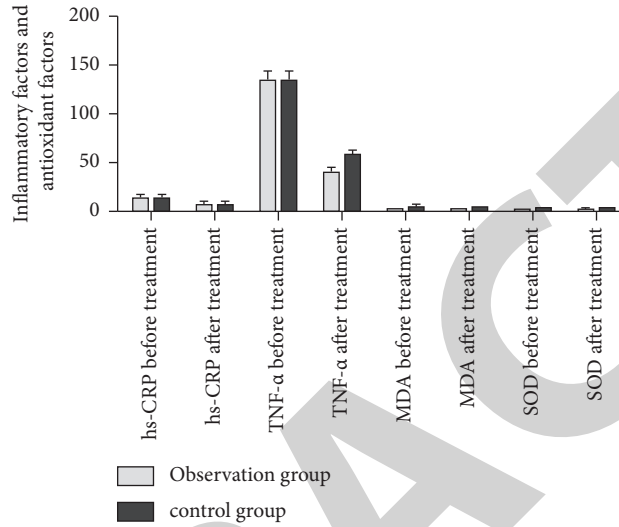
Figure 1: Comparison of serum inflammatory factor and antioxidant factor levels before and after treatment.

Table 2: Comparison of CD3+, CD4+ levels+, and IgE level before and after treatment $\overline{x} \pm s$.

		CD3+ (%)	CD4+ (%)	IgE (U/ml)
Observation group	Before treatment	24.5 ± 1.5	14.7 ± 1.0	475.9 ± 38.8
	After treatment	51.5 ± 3.5▲★	42.3 ± 2.9▲★	158.7 ± 12.4▲★
Control group	Before treatment	24.6 ± 1.6	14.8 ± 1.1	475.8 ± 38.9
	After treatment	40.4 ± 2.0▲	25.5 ± 1.6▲	323.8 ± 22.6▲

▲ Compared with pretreatment, $P < 0.05$; ★in comparison with the control group, $P < 0.05$.
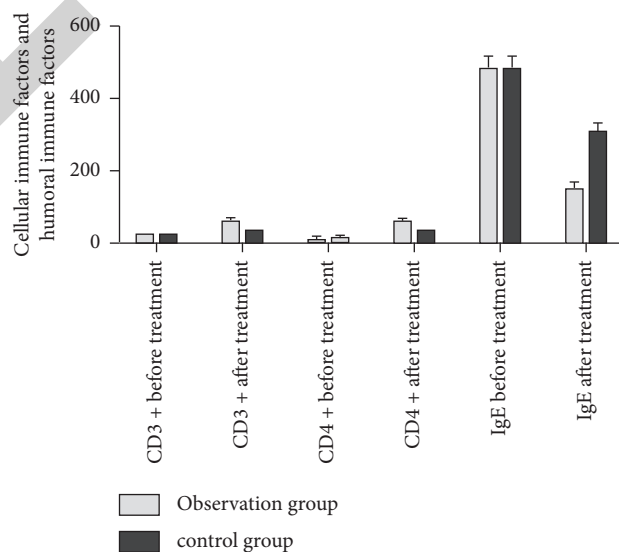
Figure 2: Comparison of CD3+, CD4+ levels, and humoral immune factor IgE level before and after treatment.

Table 3: Comparison of renal function before and after treatment between the two groups ($\overline{x} \pm s$).

		Urea nitrogen (mmol/L)	Creatinine (mmol/L)
Observation group	Before treatment	35.5 ± 3.8	447.9 ± 15.2
	After treatment	5.8 ± 0.7▲★	88.8 ± 6.3▲★
Control group	Before treatment	35.6 ± 3.9	448.0 ± 15.3
	After treatment	12.5 ± 2.7▲	119.8 ± 18.7▲

▲ Compared with pretreatment, $P < 0.05$; ★in comparison with the control group, $P < 0.05$.
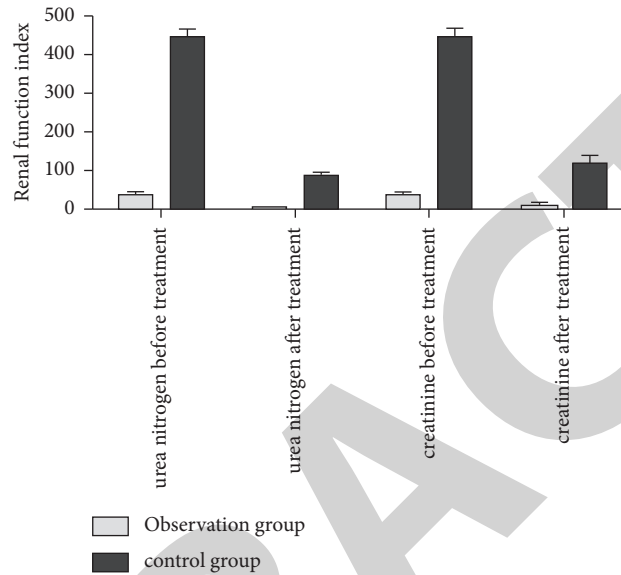
Figure 3: Comparison of renal function before and after treatment between the two groups.

Table 4: Comparison of serum calcium ion level with serum phosphorus ion level before and after treatment (mmol/L, $\overline{x} \pm s$).

	Serum total calcium ion	Serum phosphorus ion
Observation group	2.21 ± 0.04	1.28 ± 0.04
Control group	1.91 ± 0.03	1.69 ± 0.05
T	111.503	43.428
P	0.000	0.000

Table 5: Proportion of metabolic abnormalities in calcium and phosphorus ion levels occurring during treatment in both groups (cases, %).

	Hypercalcemia	Hypocalcemia	Hyperphosphatemia	Hypophosphatemia	Total occurrence
Observation group	1	0	1	0	2 (4.3%)
Control group	7	2	6	1	16 (34.8%)
χ^2			—		11.673
P			—		0.001

Table 6: Changes in axillary temperature in the two groups during treatment (°C, $\overline{x} \pm s$).

	Before treatment	During treatment	After treatment in 30 min
Observation group	36.6 ± 0.3	36.8 ± 0.2	36.7 ± 0.2
Control group	36.5 ± 0.2	35.5 ± 0.7	36.1 ± 0.6
T	1.881	12.111	6.434
P	0.063	0.000	0.000

and phosphorus ion level during treatment. It is found that the serum total calcium ion level in the observation group is higher than that in the control group, the serum phosphorus ion level is lower than that in the control group, and the total proportion of hypercalcemia, hypocalcemia, hyperphosphatemia, and hypophosphatemia in the observation group during treatment is lower than that in the control group. It is explained that applying high-flux
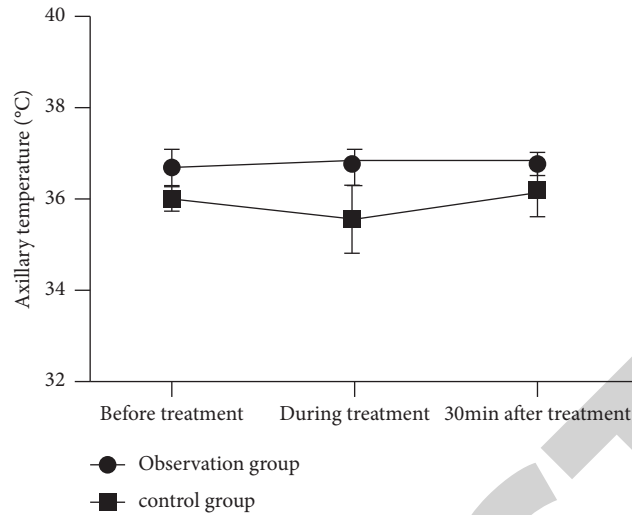
FIGURE 4: Axillary temperature in the two groups during treatment.

TABLE 7: Comparison of clinical manifestations that still existed after treatment between the two groups

	Pruritus	Renal osteoporosis	Nausea and vomiting	Abdominal distension and pain	Restless leg syndrome
Observation group	11/46	8/46	5/46	7/46	3/46
Control group	28/46	26/46	29/46	20/46	18/46
χ^2	12.863	15.116	26.872	8.859	12.094
P	0.000	0.000	0.000	0.003	0.001

hemodialysis for patients with chronic renal failure, in comparison with conventional hemodiafiltration, has a positive impact on maintaining calcium and phosphorus metabolic balance, improving the total calcium ion level after hemodialysis, as well as reducing serum phosphorus ion level. Moreover, the research also compared the changes in axillary temperature in the two groups during treatment and found that the axillary temperature during treatment and 30 min after treatment in the observation group is normal and higher than that in the control group. It is suggested that applying high-flux hemodialysis for patients with chronic renal failure is of great value for maintaining the body temperature during treatment. Finally, our group compared the clinical manifestations that still existed after the treatment in the two groups; it is found that the proportion of pruritus, renal osteoporosis, nausea and vomiting, abdominal distension, and pain and restless leg syndrome is signally lower than that in the control group after treatment. It is further explained that applying high-flux hemodialysis for patients with chronic renal failure can better improve the clinical symptoms, ensure the clinical effect, and improve life quality for patients after treatment in comparison with conventional hemodialysis.

In the past, the hemodiafiltration used small aperture membrane and low-flux dialysis machine, with a certain filter impact on small molecular substances such as uric acid, urea nitrogen, and creatinine in the blood, but for medium and large molecular substances, such as inflammatory factors, immune complex, its filter effect is limited, and long-term repeated application also has a significant negative impact on immune function and antioxidant capacity. High-flux dialysis is through high-flux dialysis machine, using Helixone nanocontrolled filament dialysis membrane, with higher biocompatibility and molecular mechanical effect. And, its pore membrane diameter is relatively large, combined with the new cover seamless design, significantly improves adsorption effect for layer cracking turbulence substances, and has important value reduce blood leakage rate. Through the diffusion-convection-absorption circulating mode, it effectively filtrates and removes large, middle, and small molecular toxins in the blood at the same time. In contrast to conventional hemodialysis, it promotes the removal range of toxin species in the body to expand, especially for the effective removal of large molecular toxins with weight of 32M and above, thus preventing their accumulation, further reducing kidney load, and improving renal function.

5. Conclusion

Applying high-flux hemodialysis for patients with chronic renal failure, in comparison with conventional hemodiafiltration, can better reduce inflammatory response and improve antioxidant capacity and immunity in the body. It is conducive to maintaining the calcium and phosphorus metabolic balance, with a small impact on the body temperature during treatment, thus have a positive impact on improving clinical symptoms.

Data Availability

The simulation experiment data used to support the findings of this study are available from the corresponding author upon request.

Retraction

Retracted: The Impact of a Knowledge Discovery-Based Psychoanalytic Intervention in the Treatment of Tuberculosis in University Students with Different Doses of Isoniazid

Journal of Healthcare Engineering

This article has been retracted by Hindawi following an investigation undertaken by the publisher [1]. This investigation has uncovered evidence of one or more of the following indicators of systematic manipulation of the publication process:

(1) Discrepancies in scope

(2) Discrepancies in the description of the research reported

(3) Discrepancies between the availability of data and the research described

(4) Inappropriate citations

(5) Incoherent, meaningless and/or irrelevant content included in the article

(6) Peer-review manipulation

The presence of these indicators undermines our confidence in the integrity of the article's content and we cannot, therefore, vouch for its reliability. Please note that this notice is intended solely to alert readers that the content of this article is unreliable. We have not investigated whether authors were aware of or involved in the systematic manipulation of the publication process.

In addition, our investigation has also shown that one or more of the following human-subject reporting requirements has not been met in this article: ethical approval by an Institutional Review Board (IRB) committee or equivalent, patient/participant consent to participate, and/or agreement to publish patient/participant details (where relevant).

Wiley and Hindawi regrets that the usual quality checks did not identify these issues before publication and have since put additional measures in place to safeguard research integrity.

We wish to credit our own Research Integrity and Research Publishing teams and anonymous and named external researchers and research integrity experts for contributing to this investigation.

The corresponding author, as the representative of all authors, has been given the opportunity to register their agreement or disagreement to this retraction. We have kept a record of any response received.

References

[1] Z. Xia, Y. Tan, and Y. Yang, "The Impact of a Knowledge Discovery-Based Psychoanalytic Intervention in the Treatment of Tuberculosis in University Students with Different Doses of Isoniazid," *Journal of Healthcare Engineering*, vol. 2022, Article ID 5610469, 8 pages, 2022.

Research Article

The Impact of a Knowledge Discovery-Based Psychoanalytic Intervention in the Treatment of Tuberculosis in University Students with Different Doses of Isoniazid

Zhihui Xia,[1] Youping Tan,[2] and Yumei Yang [3]

[1]*North China Electric Power University Hospital, Health Care Department, Changping, Beijing 102206, China*
[2]*Department of Hematology, Guangdong Second People's Hospital, Guangzhou, Guangdong 510310, China*
[3]*Medical and Nursing College, Wuhan Railway Vocational and Technical College, Wuhan, Hubei 430205, China*

Correspondence should be addressed to Yumei Yang; meiziyz23@sina.com

Tuberculosis (TB) is an infectious disease that poses a serious threat to the health of the population in China, and TB outbreaks in universities have aroused great concern in society. Psychological emotions have a large impact on the academic lives of university students, and nowadays it is not only labour-intensive but also slow to monitor and analyse and deal with the psychology of university students' daily lives in a uniform manner. If psychological problems are not detected and given feedback in a timely manner, they can have a series of negative effects on the individual university student. In this paper, we apply the Bi-LSTM model and the CNN model neural network algorithm to learn the text data, and finally have 95.55% and 90.03% accuracy in the sentiment analysis experiment, respectively, which provides a feasible solution to solve the batch rapid analysis of the psychological changes reflected in the daily text of university students. Risk communication for TB emergencies should emphasize public participation, timely release of information about the epidemic, and good monitoring of public opinion.

1. Introduction

Tuberculosis (TB) is a chronic respiratory infectious disease. It ranks second in China in terms of the incidence of infectious diseases and has become one of the major diseases that seriously affect the health of the population [1]. In recent years, the prevention and control of *tuberculosis* in schools has attracted a great deal of attention from all sectors of society, especially from university students, who have a high incidence of *tuberculosis* and the potential for outbreaks due to factors such as relocation, changes in the social environment, and increased pressure from studies and employment [2].

The important role of risk communication [3] in emergency situations has gradually been recognized by the society in recent years. Knowledge discovery is included in the Ministry of Health document: "Strengthen risk communication and crisis communication. The importance of

risk communication in daily work and information dissemination in the management of emergencies should be fully recognized" [4]. The purpose and significance of risk communication in the management of university *tuberculosis* outbreaks are as follows: in the event of a public health emergency, focusing on the reactions of all parties to the risk of disease and disseminating strategic measures for prevention and control by government or health management departments [5]. The most important purpose of risk communication is to build trust between the parties involved in an epidemic. This is where risk communication differs from general mass communication; the establishment and strength of trust is mutually dependent on the success or failure of risk communication and ultimately plays an important role in the development of effective risk decision-making, risk management, and risk early warning [6].

In the case of university TB outbreaks, the role of risk communication is to enable universities, education

authorities, health authorities, students, staff, parents, the media, and the public to understand the facts of the incident, form a common understanding, establish a relationship of mutual trust, and work together to overcome risks. Risk communication is an integral part of the management of a TB outbreak and is important for the effectiveness of the management measures [7].

Identify the stakeholders in the management of a TB outbreak at the university so as to define the scope for the selection of communication targets. Risk communication can be divided into the following: internal communication, media communication, and public communication [8–10]. Internal communication is mainly aimed at medical and nursing staff, disease prevention and control staff, and health administration staff. Health administrative departments are responsible for organising internal communication, clarifying their respective responsibilities and scope of work in epidemic management, and coordinating conflicts, while medical workers should make full use of their professional advantages to audit the accuracy of the information released [11].

Sentiment analysis [12], also known as sentimental disposition analysis, is a direction of natural language processing, which is the process of analysing, generalizing, and reasoning through subjective texts with emotional overtones. In recent years, the development of the Internet has brought a large amount of data, making the advantages of natural language processing in terms of extracting features, classification speed, etc., increasingly significant. It is widely used in areas such as bulk user prediction and opinion induction. Deep learning is a type of machine learning that analyses and predicts data by using multiple nonlinear transformation structures to abstract the data at a higher order from large amounts of data. Convolutional neural network (CNN) [13] has been improved from image recognition and speech recognition to natural language processing in recent years and has achieved great success in processing short segments of speech. Gradient disappearance is based on bidirectional processing that can be analysed in conjunction with the context. In this paper, we compare and analyse the advantages and disadvantages of Bi-LSTM models and CNN models, and find a number of feasible features [14].

2. Theoretical Background

The dissemination of health information in advance will not only give all parties at the university sufficient time to make psychological adjustments in the event of an epidemic, but will also prepare public opinion and lay the groundwork for prevention and control of the epidemic in advance [15]. A good system of morning and afternoon check-ups and information sharing on the management of student sick leave registration should be implemented, and information between the universities should be shared.

The establishment of daily communication channels and mechanisms for health information between doctors and class teachers, between class teachers and class cadres, and between department heads and university leaders also has a positive effect on the early detection and reporting of epidemics, while the development and rehearsal of emergency plans should also incorporate risk communication to lay a good foundation for public health emergency work [16].

After a university *tuberculosis* outbreak, risk communication should be closely focused on the actual aspects and specific measures of university *tuberculosis* outbreak management, in line with the implementation of various prevention and control measures [17]. The development of strategies for risk communication in university TB epidemics; the timely release of epidemic information in university TB epidemic management; risk communication should also do a good job of monitoring public opinion and using monitoring data as an important basis for strategy development; paying attention to the amount of information released and the frequency of information release; and risk communication should make use of all possible means of communication. The epidemic management always also needs to deal with the following two contradictions: first, dealing with the timeliness and accuracy of risk; and second, the contradiction between timeliness and accuracy of information dissemination. On the basis of timeliness, acknowledging the uncertainty of the development of the epidemic, efforts should be made to ensure the relative accuracy of information in order to avoid filling the information vacuum before the release of "official" information with misinformation on the one hand, and to leave room for future policy adjustments on the other [18].

3. Related Technologies

3.1. Word Vectors. Computer deep learning requires the text to be segmented and then transformed into a vector form. One-hot representation [19] represents a word as a vector of length equal to the size of the lexicon, with only one padded 1 on the vector, indicating the position in the lexicon, and all the rest padded 0. The Euclidean distance between each vector is $\sqrt{2}$. One-hot encoding is simple to set up, but results in slow training due to an explosion of parameters in the text. One-hot encoding is simple to set up, but results in an explosion of parameters in the text, which leads to slow training. Moreover, discrete representation cannot represent the relationship between two words, and each word is isolated from each other, resulting in the inability to distinguish between synonyms in natural language processing work [20].

3.2. Neural Network Models. Neural networks are machine learning algorithms that mimic the human brain and are highly expressive and good fits for data. By setting up multiple hidden layers, it can automatically learn from the bottom features of the training data to the top features, as shown in Figure 1 [21]. The expression of the neural network is as follows:

$$y = NN(x), \tag{1}$$

where x is the input vector, and y is the task-related output.
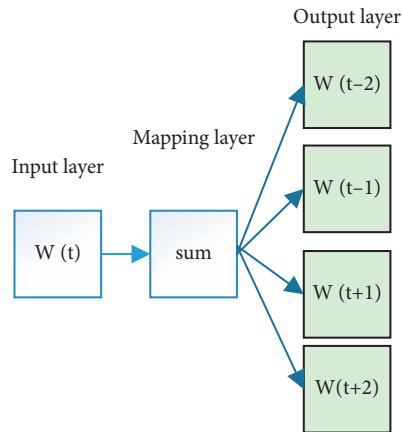
Figure 1: Skip-gram model.

4. Models in This Paper

The model will be trained by the above process to obtain the final neural network parameters suitable for the needs of this paper. (1) The text is transformed into one-hot encoding using Python's Jieba library; (2) the one-hot encoding is pretrained by word2vec and transformed into word embedding vectors as input to the neural network; (3) the model is trained by Bi-LSTM network or CNN model to obtain; and (4) multiplying by fully connected layers and multiclassifying by software function to obtain sentiment tendency results. In this paper, we summarize the comparison between Bi-LSTM and CNN models on the basis of this process, as shown in Figure 2.

5. Case Studies

5.1. Information. In this study, 85 patients with TBM with mild anxiety symptoms admitted to our hospital between August 2016 and August 2019 were selected as the main study subjects. Inclusion criteria were as follows: patients with meningeal enhancement on cranial CT or MRI, confirmed by cerebrospinal fluid (CSF) and clinical features, and meeting the diagnostic criteria for tuberculous meningitis in the 2003 edition of Tuberculosis [22]; with a mean SAS score of 54.67 ± 1.85 and a mean SDS score of 57.31 ± 1.60. 42 patients had different degrees of headache, 42 patients had increased cranial pressure, and 40 patients had meningeal irritation.

Patients in both groups were treated according to the WHO recommended antituberculosis quadruple regimen and given oral paroxetine tablets at 20 mg/d, which could be increased to 40 mg/d depending on the patient's condition. INH 200 mg + dexamethasone 5 mg intrathecally in the low-dose group and INH 200 mg + dexamethasone 5 mg in the high-dose group.

Intrathecal injections were administered at the time of infusion. Once a week, the number of injections was adjusted according to the level of cerebrospinal fluid biochemical parameters. Both groups were treated continuously for 3 months, and the treatment effects were compared.

According to the modern hospital practice, the effect of TBM treatment in this study was evaluated [23, 24]. Clinical signs and symptoms of TBM improve slightly, and CSF levels improve to some extent on cerebrospinal fluid examination, but are not satisfactory.

6. Results

At the end of 3 months of treatment, the clinical efficacy was evaluated according to the "Modern Hospital Treatment Practice." 18 cases were clinically cured, 12 cases were effective, 7 cases were effective, and 5 cases were ineffective in the small-dose group; 21 cases were clinically cured, 15 cases were effective, 6 cases were effective, and 1 case was ineffective in the high-dose group. The total effective rate of the high-dose group was 97.67% (42/43), higher than that of the small-dose group, which was 88.10% (37/42) ($\chi 2 = 0.9417$, $P < 0.05$).

6.1. Comparison of SAS and SDS Scores between the Two Groups. After treatment, the SAS and SDS scores of patients in both groups were significantly lower than before, and the scores of patients in the high-dose group were significantly lower than those in the low-dose group ($P < 0.05$), as shown in Table 1.

Before treatment, there was no statistically significant difference in the cell count, chloride level, protein content, and glucose of the cerebrospinal fluid between the two groups ($P > 0.05$). After treatment, the cell count, chloride level, protein content, and glucose in both groups improved significantly compared with before, and the improvement in biochemical indexes was better in the high-dose group than in the low-dose group ($P < 0.05$), as shown in Table 2.

During the treatment period, one case each of electrolyte abnormality, mild liver injury, and mild peripheral neuritis occurred in the low-dose group; two cases of electrolyte abnormality, and one case of mild hearing impairment, one case each of mild peripheral neuritis and liver injury occurred in the high-dose group. The incidence of drug-related adverse reactions was 9.30% in the high-dose group and 7.14% in the low-dose group, with no statistically significant difference ($x^2 = 16910$, $P > 0.05$).

7. Experiment

7.1. Experimental Setup. In this paper, the dataset is obtained from the public dataset of IMDB, with 50,000 items and a positive to negative sample ratio of 1 : 1. After preprocessing, it is divided into a training set of 20,000 items, a development set of 5,000 items, and a test set of 25,000 items. The training set was used to train the neural network model. Then, the data from the development set were used for model selection and parameter tuning, and finally, the test set was used to evaluate the generalisation ability of the model [25, 26].

The experimental parameters directly affect the experimental results of the models. In this paper, we compare the number of hidden layers, the optimisation function, the dropout, filter size, and filter number of the CNN for
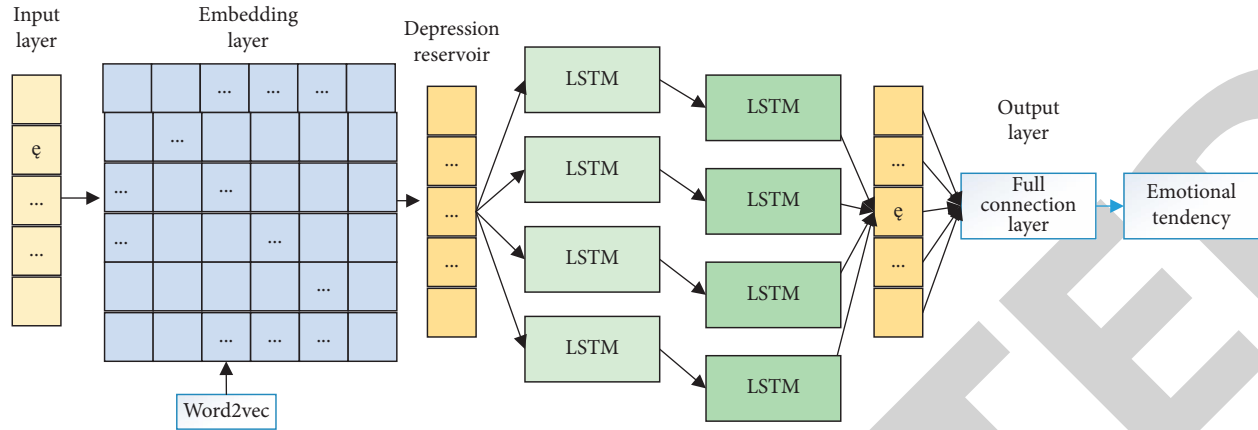
Figure 2: Flowchart of our model.

Table 1: Comparison of SAS and SDS scores before and after treatment between the two groups ($\overline{x} \pm s$, scores).

Group	Number of cases	SAS score		SDS score	
		Before treatment	After treatment	Before treatment	After treatment
Low-dose group	42	54.67 ± 1.85	44.92 ± 1.67	57.31 ± 1.6	43.27 ± 1.55
High-dose group	43	54.62 ± 1.81	39.33 ± 1.65	57.29 ± 1.59	36.81 ± 1.56

Table 2: Comparison of cerebrospinal fluid biochemical indicators between the two groups before and after treatment ($\overline{x} \pm s$).

Group	Number of cases	Cell count (10^6/L)		Chloride level (mmol/L)		Protein content (g/L)		Glucose (mmol/L)	
		Before treatment	After treatment	Before treatment	After treatment	Before treatment	After treatment	Before treatment	After treatment
Low-dose group	42	436.25 ± 55.19	177.49 ± 39.92	97.71 ± 10.31	102.99 ± 10.54	6.65 ± 1.27	4.88 ± 1.19	1.11 ± 0.25	1.49 ± 0.28
High-dose group	43	436.33 ± 55.26	115.07 ± 36.22	98.75 ± 5.66	97.78 ± 10.29	116.43 ± 10.63	6.67 ± 1.28	1.12 ± 0.24	1.94 ± 0.29

different Bi-LSTMs after repeated experiments to arrive at the optimal initial parameters for the two models. Table 3 shows the parameters of the Bi-LSTM, and Table 4 shows the parameters of the CNN.

7.2. Experimental Results. This paper not only compares the accuracy of the Bi-LSTM and CNN models, but also trains the classical RNN model and the LSTM model to help analyse the strengths and weaknesses of the models for the application in this paper. The experimental results are shown in Table 5.

It can be seen that the Bi-LSTM has a better result than the LSTM in terms of contextual analysis and a 5.52% higher accuracy than the CNN model. The prediction is that CNN does not have a high accuracy rate in the analysis of long passages due to the varying sentence lengths in the dataset. The LSTM is better than the RNN but still cannot make accurate predictions due to the inability to incorporate the following content. The results of this paper indirectly suggest that the daily textual expressions of university students are scattered among the segments, which is likely to be missed if

manual analysis is conducted. The 95.55% accuracy of Bi-LSTM is good enough for batch text processing [27, 28].

This paper presents a comparative study of the performances of Bi-LSTM models, CNN models, and traditional neural network models to solve the psychological problem of batch analysis of university students. A feasible solution is proposed for the back analysis of daily texts of university students. For daily sentiment analysis, this paper starts with the natural language processing aspect of text, but can also be evaluated comprehensively with various aspects such as image and speech processing. In the future, the image literacy algorithm will be invoked to filter out some suitable computational nodes and then sort them so as to select an optimal node host, as showed in Figure 3 Different sentiment analysis effects.

The performance test is based on the response time and throughput of creating one virtual machine instance and the maximum number of virtual machines that can be successfully created by a single server, as shown in Figure 4.

In the current environment, up to 32 virtual machines can be created; it takes 320s to create the first instance of a virtual machine, and thereafter about 15 to 20 s to create

TABLE 3: Bi-LSTM parameters.

Parameter	Value	Parameter	Value
Batch size	64	Learning rate	0.001
Unit num	32	Loss function	Cross entropy
Bi-LSTM	32	Optimization function	Random gradient descent
Epoch	6	Word vector dimension	256
Activation function	LeakyReLU		

TABLE 4: CNN parameters.

Parameter	Value	Parameter	Value
Filter size	$3 * 3$	Dropout rate	0.5
Number of filters	100	Epoch	6
Activation function	ReLU	L2	3
Pooling method	Max	Word vector dimension	256

TABLE 5: Comparison of experimental results.

Model	Acc
Bi-LSTM	95.55
CNN	90.03
LSTM	85.07
RNN	81.33
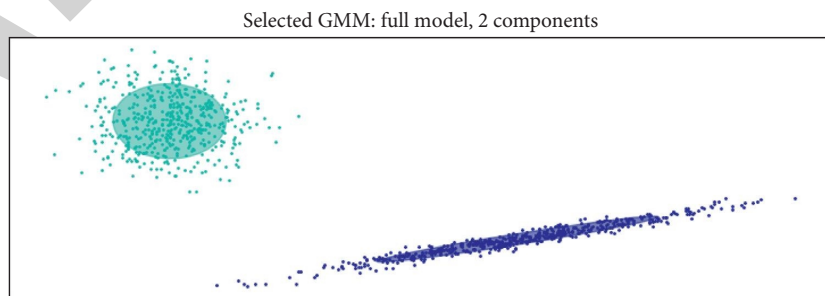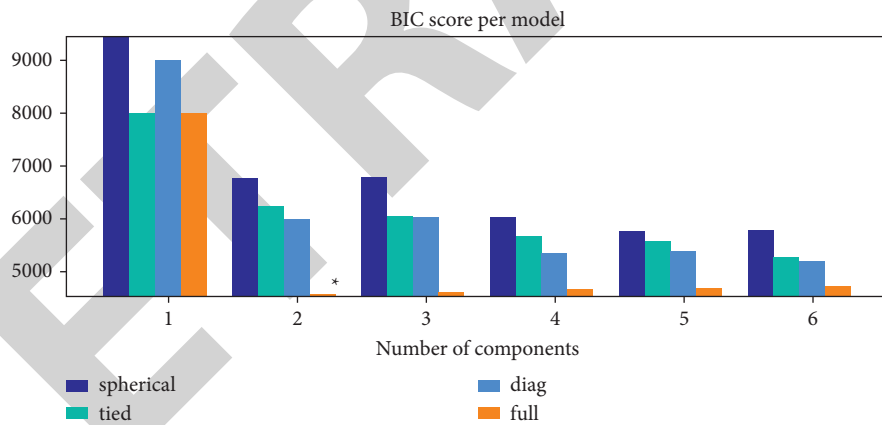
FIGURE 3: Effect of different sentiment analysis.

virtual machines of the same image, as shown in Figure 5 for mental comfort when creating virtual machines in bulk. The first virtual machine takes longer as it needs to be found and copied when it is created. After the first VM is created, VMs are created quickly and the time remains relatively constant [29].
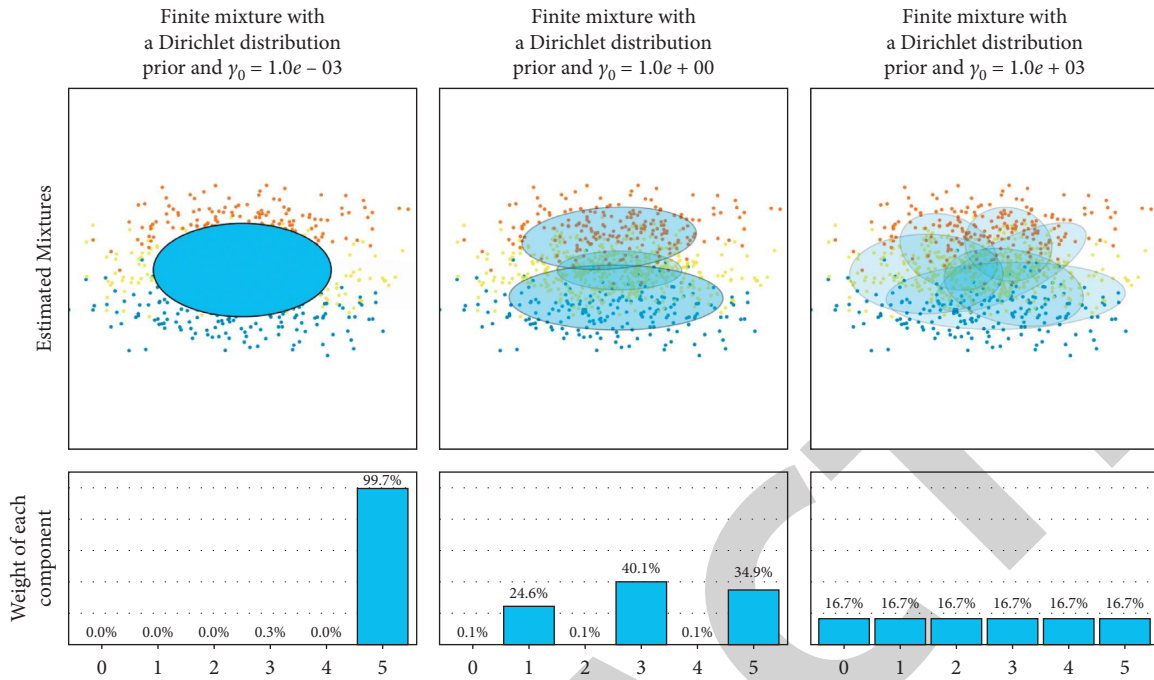
FIGURE 4: The effect of psychological comfort at different nodes.
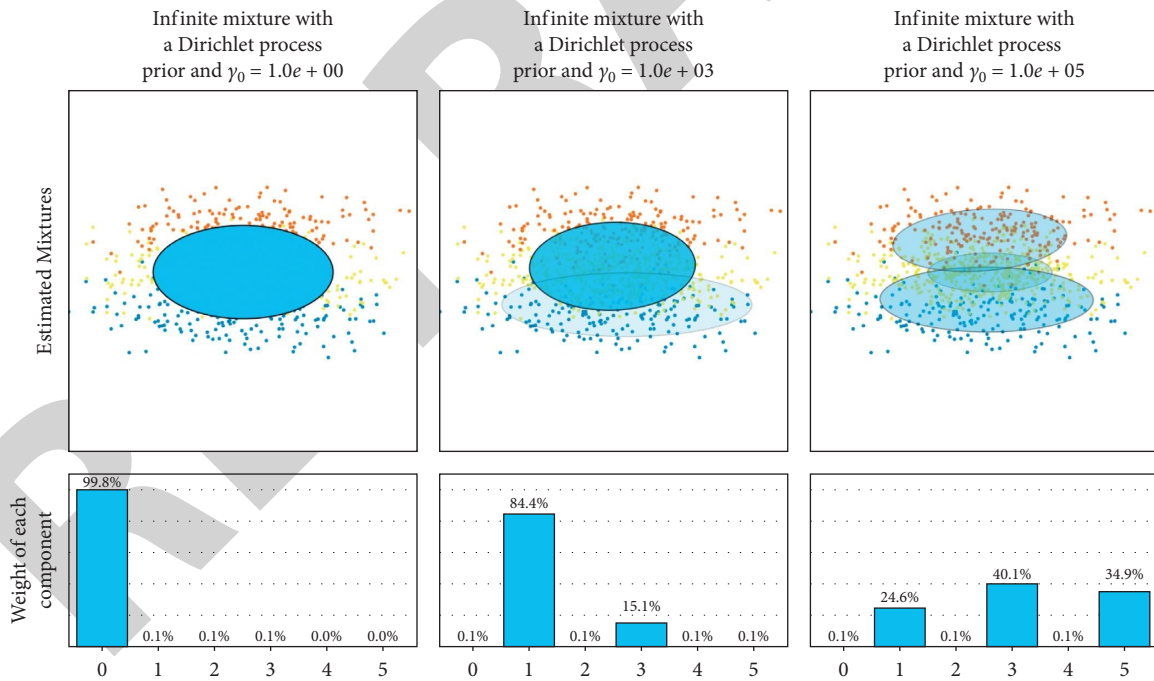
FIGURE 5: Optimised psychological comfort effect.

8. Discussion

Modern medicine has confirmed [30] that TBM is highly infectious, disabling, and fatal, and that if intervention is not timely during the acute phase, it can easily turn into chronic meningoencephalitis, with pathological changes such as basal ganglia exudate and hydrocephalus causing lesions to be deposited at the base of the skull and eventually causing permanent neurological complications, especially when symptoms of parenchymal damage appear at 4–8 weeks of onset, manifesting as mental depression, apathy, indifference, delirium, or delusions. Delirium or delusions, and even varying degrees of anxiety, depression, lethargy, confusion, or partial

epilepsy. Therefore, treatment of patients with TB meningitis with anxiety and depression should be initiated early with antituberculosis and antianxiety and depression treatment.

Isoniazid (INH), a commonly used antituberculosis drug, can rapidly penetrate the blood-brain barrier and penetrate into the cerebrospinal fluid regardless of whether the patient has meningitis. Modern pharmacogenetics studies have shown that high concentrations of INH can kill *Mycobacterium tuberculosis* in the reproductive phase and that it is equally effective against *Mycobacterium tuberculosis* in the stationary phase if the blood concentration is increased or the contact time with the bacteria is prolonged. In this study, the total effective rate was 97.67% (42/43) in the high-dose group, which was higher than the total effective rate of 88.10% (37/42) in the low-dose group ($P < 0.05$). It was suggested that the INH 200 mg + dexamethasone 5 mg regimen was more effective than the INH 100 mg + dexamethasone 5 mg intrathecal injection, which was generally consistent with the results of [25] studies.

The mental status of patients with TBM is closely related to *tuberculosis* intoxication, meningeal irritation, increased cranial pressure, cerebral nerve injury, and brain parenchymal damage. INH was considered the first antidepressant, but was withdrawn from the market because of its high hepatotoxicity [27]. In this study, both treatment regimens reduced the SAS and SDS scores of patients after treatment, but the high-dose group reduced the SAS and SDS scores to a greater extent than the control group ($P < 0.05$), suggesting that oral paroxetine tablets combined with intrathecal INH could significantly improve the patients' mental status.

In conclusion, INH 200 mg intrathecal injection combined with paroxetine tablets significantly improved the mental status, cerebrospinal fluid cell count, chloride level, protein level, and glucose level in patients with TBM with anxiety and depression, which is important in improving the prognosis.

9. Conclusion

The university will play an important role in the management of the *tuberculosis* epidemic. With the substantial increase in computer computing power, deep learning natural language processing can help people analyse and solve previously unsolvable problems in productive life. Psychological emotions have a large impact on the academic lives of university students. Nowadays, unified monitoring and analysis of the psychology of university students' daily lives is not only labour-intensive but also slow. This paper applies the Bi-LSTM model and CNN model neural network algorithm to learn text data, and finally has a 95.55% and 90.03% accuracy rate, respectively, in the sentiment analysis experiment, which provides a feasible solution to solve the batch rapid analysis of the psychological changes reflected in the daily text of university students.

Data Availability

The data underlying the results presented in the study are available within the manuscript.

Conflicts of Interest

The authors declare no conflicts of interest.

References

[1] K. v. q. Luong and L. T. H. Nguyen, "Impact of vitamin D in the treatment of tuberculosis," *The American Journal of the Medical Sciences*, vol. 341, no. 6, pp. 493–498, 2011.

[2] E. Hopper, "On the nature of hope in psychoanalysis and group analysis," *British Journal of Psychotherapy*, vol. 18, no. 2, pp. 205–226, 2010.

[3] J. F. García-Goez, G. A. Munera, V. Rojas, R. Pacheco, J. A. Cayla, and J. M. Miro, "Tuberculosis in recipients of solid-organ transplants during 1995–2015 in Cali, Colombia," *The International Journal of Tuberculosis and Lung Disease*, vol. 21, no. 11, pp. 1155–1159, 2017.

[4] M. Smolovic, D. Pesut, M. Bulajic, and M. Simic, "Knowledge and attitudes towards tuberculosis in non medical students University of Belgrade," *Pneumologia*, vol. 61, no. 2, pp. 88–91, 2011.

[5] A. Manoharan, V. G. Chellaiyan, J. Maruthappapandian, and F. Liaquathali, "Impact of educational intervention on the tuberculosis knowledge among the medical students, Chennai," *International Journal of Community Medicine and Public Health*, vol. 6, no. 12, Article ID 5317, 2019.

[6] D. M. Castaeda-Hernández, A. Mondragón-Cardona, C. F. Campo-Betancourth, and D. Tobon-Garcia, "Impact of a training activity in knowledge, attitudes and perceptions on tuberculosis of medical students from the University of Risaralda, Colombia," *Gaceta Medica de Caracas*, vol. 120, no. 1, pp. 40–47, 2012.

[7] B. J. Cohler and D. H. Friedman, "Guidelines: updated guidelines for the use of rifamycins for the treatment of tuberculosis in HIV-infected patients taking protease inhibitors or non-nucleoside reverse transcriptase inhibitors," *Southern African Journal of HIV Medicine*, vol. 13, no. 2, pp. 237–254, 2005.

[8] K. Dua, V. K. Rapalli, S. D. Shukla et al., "Multi-drug resistant *Mycobacterium tuberculosis* & oxidative stress complexity: emerging need for novel drug delivery approaches," *Biomedicine & Pharmacotherapy*, vol. 107, pp. 1218–1229, 2018.

[9] G. F. Araj, R. S. Talhouk, L. Y. Itani, W. Jaber, and G. W. Jamaleddine, "Comparative performance of PCR-based assay versus microscopy and culture for the direct detection of *Mycobacterium tuberculosis* in clinical respiratory specimens in Lebanon," *International Journal of Tuberculosis & Lung Disease*, vol. 4, no. 9, pp. 877–881, 2000.

[10] E. Shorter, "Anxiety: a short history by allan V. Horwitz," *Bulletin of the History of Medicine*, vol. 88, no. 2, pp. 375-376, 2014.

[11] O. Bottasso, Y. M. L. Ba, H. Besedovsky, and A. del Rey, "The immuno-endocrine component in the pathogenesis of tuberculosis," *Scandinavian Journal of Immunology*, vol. 66, no. 2-3, pp. 166–175, 2010.

[12] J. R. Furnal, "Film, lacan and the subject of religion: a psychoanalytic approach to religious film analysis - by steve nolan," *Reviews in Religion and Theology*, vol. 18, no. 1, pp. 117–120, 2011.

Retraction

Retracted: Application of a Nursing Data-Driven Model for Continuous Improvement of PICC Care Quality

Journal of Healthcare Engineering

This article has been retracted by Hindawi following an investigation undertaken by the publisher [1]. This investigation has uncovered evidence of one or more of the following indicators of systematic manipulation of the publication process:

(1) Discrepancies in scope

(2) Discrepancies in the description of the research reported

(3) Discrepancies between the availability of data and the research described

(4) Inappropriate citations

(5) Incoherent, meaningless and/or irrelevant content included in the article

(6) Peer-review manipulation

The presence of these indicators undermines our confidence in the integrity of the article's content and we cannot, therefore, vouch for its reliability. Please note that this notice is intended solely to alert readers that the content of this article is unreliable. We have not investigated whether authors were aware of or involved in the systematic manipulation of the publication process.

In addition, our investigation has also shown that one or more of the following human-subject reporting requirements has not been met in this article: ethical approval by an Institutional Review Board (IRB) committee or equivalent, patient/participant consent to participate, and/or agreement to publish patient/participant details (where relevant).

Wiley and Hindawi regrets that the usual quality checks did not identify these issues before publication and have since put additional measures in place to safeguard research integrity.

We wish to credit our own Research Integrity and Research Publishing teams and anonymous and named external researchers and research integrity experts for contributing to this investigation.

The corresponding author, as the representative of all authors, has been given the opportunity to register their agreement or disagreement to this retraction. We have kept a record of any response received.

References

[1] J. Zhou and L. Wang, "Application of a Nursing Data-Driven Model for Continuous Improvement of PICC Care Quality," *Journal of Healthcare Engineering*, vol. 2022, Article ID 7982261, 8 pages, 2022.

Research Article

Application of a Nursing Data-Driven Model for Continuous Improvement of PICC Care Quality

Juzhen Zhou[1] and Lihua Wang [2]

[1]*Department of Oncology, Dushu Lake Hospital, Soochow University, Suzhou 215000, Jiangsu, China*
[2]*Department of Oncology, The First Affiliated Hospital of Soochow University, Suzhou 215000, Jiangsu, China*

Correspondence should be addressed to Lihua Wang; lemonwlh2@sina.com

A PICC catheter maintenance network was established and managed to monitor the maintenance of catheters in placed patients throughout the process, providing homogeneous PICC catheter continuity of care for patients. Model-driven thinking is an idea for simulation system development. Model-driven architecture (MDA) is a design methodology that implements model-driven thinking and is widely used in simulation system development. Based on the requirements of nursing, the data-driven model is mainly divided into interface layer and functional service layer; this study adopts MDA technology which can detach the functions of the system from the platform, based on domain knowledge, and the metamodel adopts XSD-based data model to generate the PIM model, which is stored in the model library. The results showed that the number of nurses at maintenance sites increased from 79 to 232, the PICC placement rate for oncology patients increased from 35.0% to 76.0%, the nurse maintenance operation pass rate increased from 53.9% to 88.4%, and the maintenance default rate decreased from 40.0% to 10.9%.

1. Introduction

Peripherally inserted central catheters (PICC) are catheters placed via peripheral venous puncture into the superior or inferior vena cava at the tip. PICCs are widely used in clinical practice because they can avoid repeated punctures, reduce patient pain, reduce the occurrence of mechanical phlebitis, reduce the impact of chemotherapeutic drug extravasation on peripheral vessels, are simple and safe to operate, and provide intravenous access to oncology patients for medium-to long-term chemotherapy [1]. Catheter maintenance needs to be performed locally, and if timely and correct PICC maintenance cannot be achieved during discharge, it will cause complications such as blockage, phlebitis, and infection and prolong the PICC retention time, resulting in an increased rate of unplanned extubation [1].

PICC catheters have important application value for patients who need to receive long-term treatment such as intravenous injection, which can effectively reduce the number of venipuncture of patients, thus appropriately

reducing the pain caused by frequent punctures and to a certain extent reducing the workload of nursing staff [2], which has high feasibility and efficiency in clinical care. However, in the actual application, patients are prone to various accidents during intubation, resulting in adverse events and complications, which have a serious impact on their therapeutic effects and physical and mental health. Therefore, continuous quality improvement of care during PICC placement is necessary and has a positive clinical effect on the effectiveness and safety of clinical treatment [3].

PICC not only effectively avoids direct contact between drugs and arm veins but also has become an important way of clinical treatment and parenteral nutrition because of its simple operation, easy maintenance, and long retention time [4]. However, in practice, improper care is likely to lead to the occurrence of accidents such as catheter blockage and dressing dislodgement, resulting in complications such as prolonged retention time and mechanical phlebitis, which seriously affects the clinical treatment of patients [5]. In this study, we applied the management method of intravenous

therapy care team to the continuous quality improvement of PICC care, and the results showed that the observation group had a significantly higher rate of successful primary puncture and a significantly shorter retention time and lower complication rate than the control group. This shows that the intravenous therapy nursing team has significant application effect in continuous improvement of PICC nursing quality and is worth promoting [6].

As a typical nursing information application system, the development of simulation software for nursing data-driven model faces many problems such as uncertain requirements and rapid changes in the application environment [7], and new software development ideas and methods need to be explored. At present, the range constructs multiple sets of nursing data-driven models, which are applied to different simulation implementation platforms, such as RT-Space platform and DWK platform [8], resulting in serious waste of resources and increasing many repetitive tasks, and the main reason for this phenomenon is because the system does not have portability and reusability [9].

Therefore, in order to ensure the effectiveness and safety of PICC treatment, this study applies the intravenous therapy care team to the continuous improvement of PICC care quality and discusses the effect of its application.

2. Knowledge Background

2.1. PICC Catheter Maintenance Behavior. After the placement of PICC catheters, catheter maintenance can take several to dozens of times and weeks [10], and the safety and standardization of catheter maintenance is related to the length of catheter retention. Many patients need to travel long distances to return to our hospital for catheter maintenance after catheter placement, so it is especially important to establish a PICC maintenance site for patients nearby.

The regional collaborative care model of PICC maintenance, which was found during the preliminary piloting process, is a phased establishment of an integrated urban-rural PICC maintenance network, which, on the one hand, facilitates maintenance in the vicinity of patients (the return maintenance rate decreased from 71.9% in 2014 to 29.2% in 2017), and on the other hand, reduces catheter maintenance costs, reduces discomfort caused by long-distance travel, alleviates patient pain, and protects patient safety. For medical workers, it can realize the rational division of nursing work, improve work efficiency, enhance operational skills, decrease the rate of missing PICC maintenance ($P < 0.01$), increase the rate of qualified PICC maintenance, increase team cohesion, and improve nursing quality; for hospitals, it can reduce the incidence of nursing disputes, improve the rate of PICC placement, improve patient satisfaction, and enhance the overall brand image of hospitals; for society [11], it can reduce the incidence of nursing disputes, improve the rate of PICC placement, and improve the overall brand image of hospitals. For the hospital, it can reduce nursing disputes, improve PICC placement rate, improve patient satisfaction, and enhance the overall brand image of the hospital; for the society, it can effectively build a medical regional collaboration network, provide a reference

for subsequent medical regional collaboration, alleviate the problem of concentration and uneven distribution of medical resources today, and achieve a win-win situation for both economic and social benefits [12].

2.2. PICC Maintains Regional Collaborative Care Model. Facilitating catheter maintenance for patients between treatments PICC reduces the number of venipunctures, avoids PICC has been widely accepted and used by oncology chemotherapy patients because it reduces the number of venous punctures, avoids damage to blood vessels from extravasation of chemotherapy drugs, reduces patients' psychological stress, and provides a safe intravenous access for treatment [13]. And the maintenance of catheters is related to whether patients can safely complete their treatment. The use of online platforms such as WeChat can strengthen the connection between nurses and between nurses and patients and ensure the continuity of care [14]. Before the catheter is placed, the PICC maintenance network allows for quick and easy access to the location of each maintenance site and informs patients of the maintenance site near their place of residence; after the catheter is placed, patients can receive efficient and standardized homogeneous nursing services at the nearest maintenance site through the regional nursing collaboration model, saving patients' time and expenses such as travel and accommodation costs so that patients can enjoy "home" maintenance services. At the same time, patients can enjoy "doorstep" maintenance services, reduce their economic burden and psychological pressure, receive homogeneous services, reduce the risk of catheter-related complications, indirectly promote their physical recovery, and meet the needs of discharged patients for extended care services [15, 16], which is a safe and feasible nursing service model. This model improves patient satisfaction and win-win situation for both nurses and patients and promotes the development of the out-of-hospital care model [17].

2.3. PICC Maintains Regional Collaborative Care Model. The regional resource allocation was optimized by building a PICC maintenance network, leading from point to point, expanding the coverage of PICC maintenance to a certain extent, and breaking through the limitations of the original method; at the same time, through the development of relevant systems, the workflow of nurses at maintenance points was standardized, their knowledge of PICC was strengthened, the safety of nursing services was ensured, the qualification rate of catheter maintenance was improved, and the maintenance of catheters was improved. Quality prolongs the service life of PICCs, promotes the clinical application of PICC technology in oncology chemotherapy patients, and promotes the development of PICC specialist nurses [18]. In addition, the use of this nursing model has saved nurses' PICC maintenance time in tertiary hospitals, allowing nurses to have more energy to take care of inpatients, further improving inpatient satisfaction, enhancing the quality of departmental care and the overall image of

hospitals, and also promoting the promotion of the graded diagnosis and treatment system.

3. Data-Driven Model Development Ideas

As a typical nursing information application system, the development and exploitation of its simulation software faces many problems such as uncertain requirements and rapid changes in the application environment [5], and new software development ideas and methods need to be explored. At present, the range constructs multiple sets of nursing data-driven models, which are applied to different simulation implementation platforms, such as RT-Space platform and DWK platform, resulting in serious waste of resources and increasing many repetitive tasks, and the main reason for this phenomenon is because the system does not have portability and reusability. The application of data model-driven development technology can realize the separation of application logic and underlying changes of the care data-driven model and increase the reuse of application logic and even application subsystems at large granularity, thus enhancing the adaptability and changeability of the software system and realizing that one modeling can be applied to different technical environments [7].

The requirements of the nursing data-driven model are mainly divided into the interface layer and the functional service layer. In this study, MDA technology can be used to detach the functions of the system from the platform, based on domain knowledge, and the metamodel is used to generate PIM models based on the XSD data model, which is deposited in the model library. The models proposed in the model library can all be mapped to different platforms, including RT-Space platform, DWK platform, HLA, and other specific platforms, and realize automatic code generation and rely on component technology to finally realize the development of the whole system; the main implementation framework is shown in Figure 1.

The combat system interface protocol-aided design tool was introduced in [6], which proposed a model-driven approach by converting the stored relevant combat system interface protocol unit data into an XML schema file (XSD). Therefore, the realization of a data model-centric simulation system development method in the MDA environment and the construction of a care data-driven model data model is a very important element.

4. Nursing Data-Driven Model

The nursing data-driven model is a very complex system, and the data model of the system plays a crucial role in the simulation development. During the development of the system using a model-driven approach, modifications to the data model can be automatically reflected in all phases of the design, such as updating system object properties, updating system interface protocols, updating the simulation model, and updating the implementation code of the simulation system.

4.1. XSD-Based System Data Model. In the development process of the nursing data-driven model, even though there is a better top-level design, the system design will still be adjusted as the user needs keep changing, the interface will keep changing, and the interface parsing needs to be adjusted significantly. The use of XML Schema definitions (XSD) to build the data model can solve the problem of adapting to such interface changes in the system development process, in order to improve the system development efficiency, reduce development costs, and make the interface with strong adaptability.

For the information units and related data fields defined in the nursing data-driven model interface protocol, the XSD is used to build a data model, which mainly describes the basic information of the model, the data types, and the component information of the model and describes the structural relationships between the information elements and the detailed information used to constrain each element, for example, the name, type, length, maximum value, and minimum value of the data fields. The information structure of the nursing data-driven model data model is shown in Figure 2.

4.1.1. Model Basic Information. The basic information of the model describes the management class information such as the name of the nursing data-driven model simulation program model in English, the development language of the model, and the model development platform, and its information structure is shown in Figure 3.

4.1.2. Model Component Information. Model component information describes model information such as model component description information, desired initialization parameters, attribute class input information, attribute class output information, event class input information, and event class output information of the care data drive model. The information structure is shown in Figure 4.

Among them, thought initialization information is used to describe the inherent properties of the simulation objects, such as the heading and speed of the target trajectory object of the care data-driven model. Attribute class information is used to describe the object class information of the interaction between simulation objects, such as the target trajectory information reported by radar. Event class information is used to describe the interaction class information between simulation objects, such as hard weapon target indication messages and radar status reporting messages [14].

4.2. Application of the Data Model in Interface Description. Combined with SOA thinking, the concept of service is introduced. A service can accept requests and send response results, and the format of the received request messages and the feedback response messages are defined from the XSD-based data model. When implementing a specific service, the distribution of that service over the network needs to be bound to a specific network
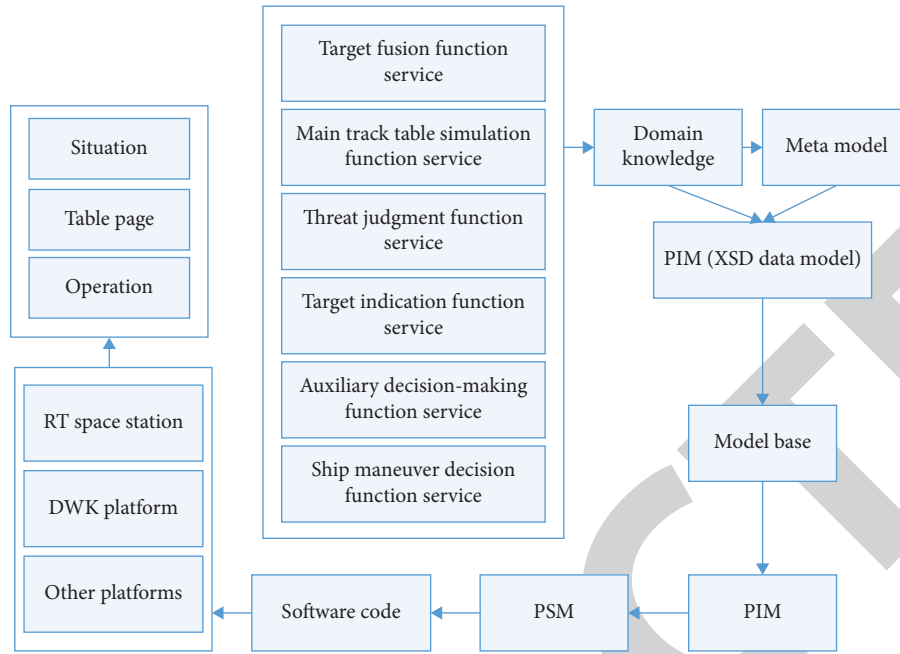
FIGURE 1: Block diagram of the simulation development of the nursing data-driven model.
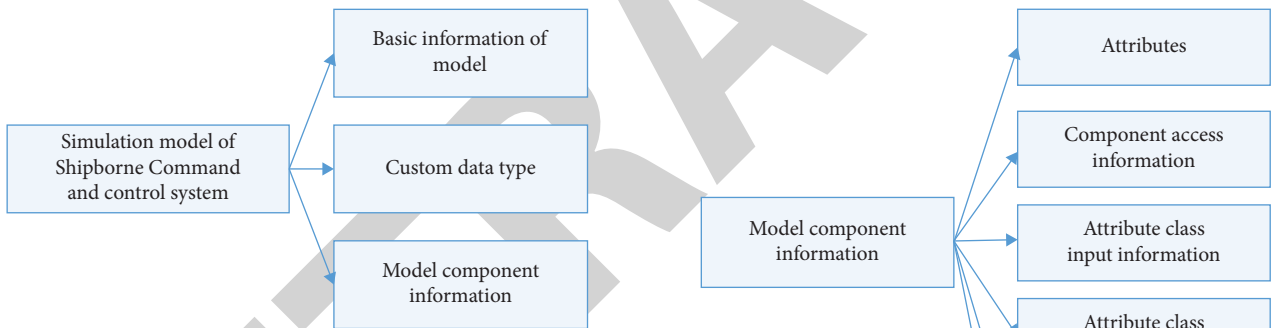
FIGURE 2: Information structure of the nursing data-driven model.
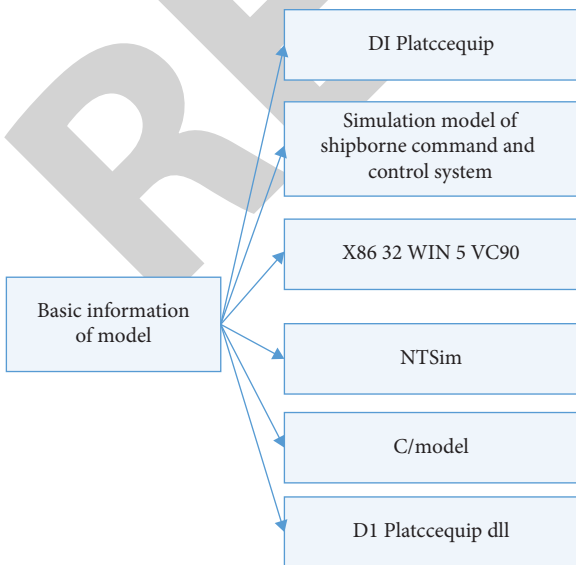
FIGURE 3: Information structure of the basic information of the model.

FIGURE 4: Model component information structure.

communication protocol. The data model mainly describes the format and content of the messages in the interface, but it is necessary to add a description of the service interface information, i.e., a description of the operation, port, and protocol binding information.

5. A Data-Driven Model Approach to Nursing Data-Driven Model Development

Generally speaking, software code can be divided into three parts: generic code, personality code, and structural repetitive code. In the nursing data-driven model simulation

software, the generic code is the basic code that contains the basic framework of the software and implements the simulation system; the personalized code is the code that implements the specific functions of the nursing data-driven model, and the structural repetitive code mainly contains the code that describes the specific format of the nursing data-driven model information messages and the message parsing procedure, and through further research, it is found that this part of the code is the structural repetitive code which contains code that describes the specific format of the nursing data-driven model messages and the message parsing procedure.

In the previous sections, the data model of the nursing data-driven model describes mainly the information related to messages. During the development process, there will be many structural repetitive codes in the nursing data-driven model, which can be generated by the conversion of the data model of the system. By establishing a mapping relationship between the data model and the structural repetitive codes and applying model-driven ideas to guide the automatic generation of this part of the code, the development efficiency of the nursing data-driven model can be greatly improved.

5.1. XSD-Based Message Parsing Code Generation.
In order to realize the data-driven model code development, it is actually the realization of the conversion from PIM to actual code in MDA idea.

The XML file is defined in a tree-like structure, which is characterized by good structure and facilitates program analysis, and can be processed by tree traversal and generation algorithms. In order to improve the efficiency of the interface code development, the idea is based on the one shown in Figure 5. After reading the XSD file, the XSD file structure is first analyzed and the parsing code is generated according to the file structure.

5.2. PIM to PSM Conversion.
The platform-independent model (PIM) is designed without considering the middleware platform on which the final implementation is made or the platform on which the final code will run; it is a model that describes the functions and structure of the system and does not include any platform technologies. The design of the platform-related model (PSM) is closely related to the specific platform, which depends on the functions and services provided by the platform and involves the implementation details of the system on the platform.

Examples of platforms include HLA, CORBA, and DWK, which are used in the simulation of the data-driven model of care. Converting PIM to PSM, that is, from a conceptual analytical model to a computer simulation, the implementation of the model can be automated by the PSM automatic conversion tool.

The conversion from a nursing data-driven model PIM to a PSM that satisfies the DWK platform implementation protocol requires the PIM to achieve the conversion to PSM in accordance with the object model structure, simulation
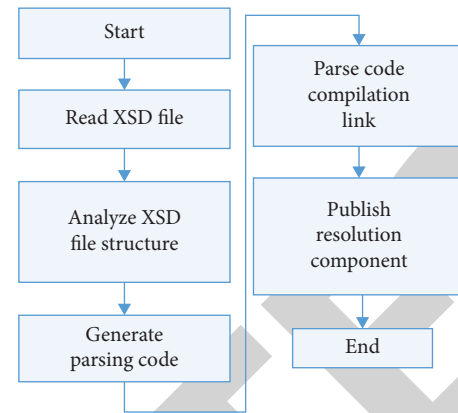
FIGURE 5: Code generation parsing method.

drive method, service acquisition method, and exception mechanism and parameter type specified by DWK.

6. Case Study

6.1. PICC Maintenance Point Quality Control.
The nursing department arranges for members of the sedation team to be assigned to the PICC maintenance sites in each region of Suzhou, forming one-to-one hospital commissioner-to-hospital contact, understanding the training needs of local nurses through PICC exchange groups, making training plan, and going to local hospitals to organize training every year. Every six months, the nursing department of the hospital takes the lead in conducting network theoretical and operational assessments for the nurses of PICC maintenance sites to ensure the correctness of nursing operations of the nurses at the maintenance sites and to ensure that the maintenance sites can provide quality services to patients. ① Network theory assessment: the theory assessment scores 100 points, 90 points, and makes up those who fail to pass the test. The system automatically closes after the time is up, and the test taker submits the test paper and the system automatically scores it to avoid the errors in the manual correction of the paper. Those who fail the examination have a chance to make up the

6.2. Effectiveness of PICC Maintenance Network Implementation.
According to the statistics of the Department of Medical Oncology of our hospital, the establishment of the regional PICC maintenance network has led to the increase in the number of PICC insertion year by year, and the triage of maintenance points has realized the maintenance of patients in the vicinity, which effectively reduces the rate of patients returning to the hospital for maintenance. The triage of maintenance points has enabled patients to be maintained close to each other and effectively reduced the rate of patients returning to the hospital for maintenance, as shown in Table 1.

The operation of nurses at maintenance sites in 2019 (the initial stage of PICC maintenance network construction) and 2020 (the middle stage of PICC maintenance network construction) was compared, and PICC maintenance videos

Table 1: PICC placement rate and return maintenance rate in medical oncology department.

| Particular year | Actual number of catheters | Catheterization | | Maintain | |
		Number of persons to be placed	Catheterization rate (%)	Number of returned maintenance personnel	Return to hospital maintenance rate (%)
2014	432	1235	35	311	71.9
2015	480	942	51	245	50.1
2016	521	766	68	188	63.1
2017	589	775	76	172	29.2

Table 2: PICC maintenance point and nurse maintenance operation assessment pass rate.

Particular year	Number of nurses	Qualified persons (person)	Pass rate (%)
2019	78	42	53.9
2020	232	205	88.4
x^2		42.948	
P		<0.001	

Table 3: PICC with tube patient maintenance absence rate and satisfaction survey.

| Particular year | Number of patients examined | Maintenance missing | | Satisfaction | |
		Number of cases	Incidence (%)	Number of cases	Satisfaction rate (%)
2015	195	78	40	124	63.6
2016	238	26	10.9	229	96.3
x^2		49.651		79.756	
P		<0.001		<0.001	
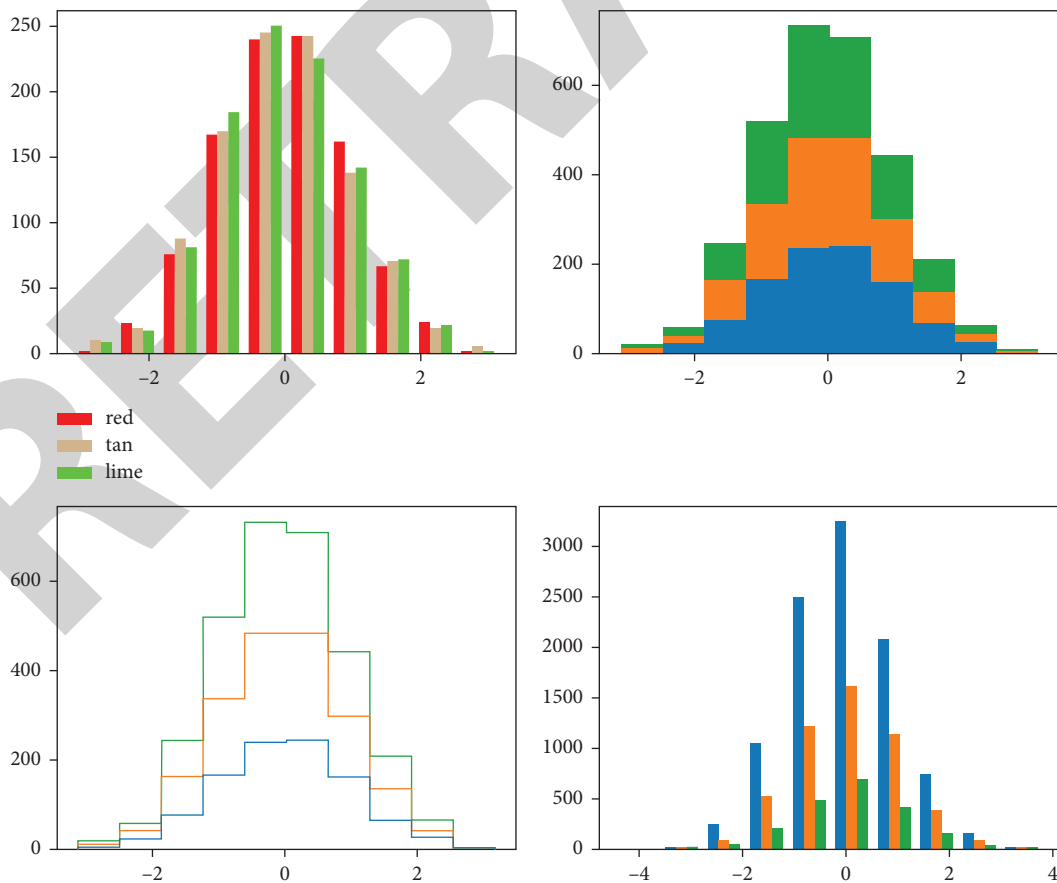
Figure 6: PICC of different partition implementation effects.

Figure 7: Effectiveness of PICC care for different patient households.

were filmed by one to two nurses qualified in PICC maintenance at maintenance sites by means of online operation assessment. All participating nurses signed the informed consent form, and the operation videos were rated by our PICC specialist nurses, and the results showed that the operation level of nurses at the PICC maintenance site improved and the operation assessment pass rate increased ($P < 0.01$), see Table 2.

By comparing the rate of missing PICC maintenance with the rate of patient satisfaction, we surveyed patients who returned to the hospital for maintenance after PICC discharge in the medical oncology and radiotherapy departments, and the results showed that the rate of missing catheter maintenance decreased, various catheter-related complications decreased, and patient satisfaction increased year by year during the interval between treatments (Table 3).

Extended care service refers to the provision of nursing care and health guidance services for discharged patients with nursing needs, which is an extension of inpatient services [19]. The establishment of PICC maintenance network has solved the worries of discharged patients and provided patients with "home" care services. The "Health China 2030" plan outlines the establishment of information sharing and interconnection mechanisms, the continuous improvement of service networks, the improvement of the treatment-rehabilitation-long-term care service chain, and the standardization and promotion of "Internet + health care" services to realize the Health China Cloud Health Plan. The service plan is shown in Figure 6.

Although the establishment of PICC maintenance network based on regional nursing coordination has

achieved the above results, there are still shortcomings; the regional distribution of PICC maintenance points has not yet fully covered all hospitals, especially some more remote areas. The effect of different PICCs is shown in Figure 7, and the future should strengthen the publicity, optimize the management of PICC maintenance network, gradually strengthen the maintenance team, while strengthening their own strength, and further expand the coverage of PICC maintenance network to further meet the needs of patients in rural areas. This model provides a reference for the subsequent implementation of graded diagnosis and treatment, incorporating more nursing content and medical models and realizing the sharing of medical and nursing resources.

7. Conclusions

The effectiveness of an intravenous therapy care team is continuously improving the quality of PICC care. A PICC catheter maintenance network was established and managed to monitor the maintenance of catheters in patients with catheters placed throughout the process, providing homogeneous PICC catheter continuity of care for patients. At the same time, PICC quality management standards are formulated for the actual situation, and the quality of placement is regularly supervised and evaluated; at the same time, the team is responsible for organizing training and assessment of relevant staff, conducting comprehensive discussions on difficult cases, proposing solutions, and conducting joint consultations when necessary.

Research Article

Study on the Grading Model of Hepatic Steatosis Based on Improved DenseNet

Ruwen Yang,[1] Yaru Zhou,[1] Weiwei Liu,[2] and Hongtao Shang [ID][2]

[1]*First Clinical Medical College, Nanjing University of Chinese Medicine, Nanjing 210004, China*
[2]*Affiliated Hospital, Nanjing University of Chinese Medicine, Nanjing 210004, China*

Correspondence should be addressed to Hongtao Shang; shanghongtao@njucm.edu.cn

To achieve intelligent grading of hepatic steatosis, a deep learning-based method for grading hepatic steatosis was proposed by introducing migration learning in the DenseNet model, and the effectiveness of the method was verified by applying it to the practice of grading hepatic steatosis. The results show that the proposed method can significantly reduce the number of model iterations and improve the model convergence speed and prediction accuracy by introducing migration learning in the deep learning DenseNet model, with an accuracy of more than 85%, sensitivity of more than 94%, specificity of about 80%, and good prediction performance on the training and test sets. It can also detect hepatic steatosis grade 1 more accurately and reliably, and achieve automated and more accurate grading, which has some practical application value.

1. Introduction

The liver, as an important organ of the body, is the key to regulating lipid metabolism in the body. When the body's lipid metabolism is abnormal, it will lead to lipid accumulation in the liver and liver steatosis. Severe liver steatosis is irreversible and threatens human life and health, while milder liver steatosis can be completely cured by treatment. Therefore, early screening for hepatic steatosis is of clinical importance. At present, the degree of hepatic steatosis is mainly determined by manual grading, in which the imaging physician analyzes the patient's imaging data to score the grade of hepatic steatosis. This approach suffers from subjective grading bias and low efficiency. In recent years, with the widespread use of deep learning in medicine, new opportunities for intelligent grading of hepatic steatosis have been presented. For example, Qiblawey Yazan and Montalbo Francis Jesmar P. proposed a cascade system to detect, localize, and quantify COVID-19 infection from CT images using encoder-decoder convolutional neural networks (ED-CNNs), UNet, and feature pyramid network (FPN) [1, 2]. Ben Jabra Marwa used 16 deep learning classifiers to diagnose the validity of COVID-19 from chest X-ray images

and found that the combination of deep learning models and integrated classification techniques resulted in the highest confidence level for class 3 classification [3]. Liu Zhenguo et al. identified patients with myasthenia gravis effectively based on the 3D DenseNet deep learning (DL) model of preoperative CT of patients as a complement to the conventional diagnostic criteria for identifying thymoma-associated MG [4]. Riasatian Abtin et al. used a DenseNet topology with four dense blocks, fine tuned and trained with different structures to propose a KimiaNet histopathology image recognition model, and tested KimiaNet using three publicly available datasets of TCGA, endometrial cancer images, and colorectal cancer images to verify the effectiveness of the model [5]. The model has certain search and classification performance when used for image representation. Considering the correlation of multilead ECG, systematically mining the correlation of interlead signals, and enhancing the multiplexing of feature information between interlead and intralead signals by using the dense connection of DenseNet, Xiong Peng et al. proposed a novel multilead myocardial infarction localization method based on a densely connected convolutional network (DenseNet), which automatically captures valid myocardial infarction,

improves its recognition rate, and can be introduced into clinical practice to assist in the diagnosis of myocardial infarction [6]. Albahli Saleh et al. proposed three different BiT models: the DenseNet, InceptionV3, and Inception-ReNetV4 for the diagnosis of coronavirus pneumonia patients by X-ray chest radiographs, and the results showed that the pretrained DenseNet model had the highest classification efficiency of 92%, the accuracy of Inception V3 was 83.47% and that of Inception-ResNetV4 was 85.57%. This is sufficient to show the advantages of the DenseNet algorithm [7]. Wang Gaihua et al. proposed an image classification model with a residual attention mechanism based on the improved DenseNet, extracting image features from the training set, which can improve the accuracy of DenseNet algorithm by 8.89% [8]. It can be seen that deep learning has been effective in identifying various diseases in medicine, and it has certain auxiliary functions for physicians to diagnose diseases. Therefore, based on the above research studies, this paper combines the DenseNet algorithm of deep learning with transfer learning to propose a migration learning-based method for grading hepatic steatosis with the improved DenseNet model.

2. Basic Methods

2.1. Introduction to DenseNet Algorithm. The DenseNet algorithm is a neural network that uses feature combinations and set bypasses to improve the performance of the network, which enables the summation of the features of the two pathways before and after the block by means of dense connections [9], which in turn improves the reuse of the features by the network. One L-layer DenseNet network includes $L(L + 1)/2$ connections to ensure that model short-circuit values occur in blocks. However, to ensure no short circuiting between blocks, the model adds a pooling layer to approximately reduce the parameters, while ensuring a relatively small model size. The DenseNet model block is shown in Figure 1. The input of layer i is X_t, which can be expressed as

$$X_t = H_t([X_0, X_1, ..., X_{t-1}]),\tag{1}$$

where H is the nonlinear transform, usually a combination of $BN + ReLU + Conv(3 * 3)$; X_0 and X_{t-1} are all layers before the i-th layer; [ ] is the stitching, indicating that all outputs from X_0 to X_{t-1} are stitched.

2.1.1. DenseNet Algorithm Improvements. The DenseNet model extracts features by training from scratch, which tends to lead the model fall into local optimum. In addition, to obtain the best prediction, the model often needs a large amount of data support, which leads to a deepening network, and a too deep network will reduce the learning ability of the model, which in turn is prone to overfitting. At the same time, the radio image used for liver steatosis grading is usually small compared to conventional image datasets so that the model is less effective in classification recognition. To solve the above problems, the DenseNet model is improved in this paper. According to the literature [10, 11], if

two domains have commonality, their "knowledge" can be transferred; i.e., the knowledge learned from one domain can be used in the other domain. Therefore, this paper improves the DenseNet model by combining transfer learning. In this paper, we improve the training accuracy of the model by transferring the pretrained model from the world's largest image recognition library (ImageNet dataset) into the DenseNet model [12].

When training a DenseNet model based on transfer learning, the amount of data (batch-size) fed into each iteration is only a small fraction of all the data, and the larger the batch-size, the less time it takes to train the model for one round (epoch). After increasing the batch size n times, the time per batch is $\sqrt{n}$. Considering the existence of a local minimum in the design training, the objective of the training is to minimize the softmax function. During the training process, the learning rate determines the update step of the iterations, and if its value is too large, it tends to cause the loss function not to converge, too small to fall more slowly. The best value can be selected by observation.

The regular model gradient descent update weight is as follows [13]:

$$w' = w - a \cdot \nabla c,\tag{2}$$

where w' and w denote the connection weights after and before the update, a denotes the learning rate, and ∇c denotes the backpropagation gradient. After adding the momentum, the above equation can be rewritten as

$$v' = \text{momentum} \cdot v - a \cdot \nabla c,\tag{3}$$

$$w' = w + v',\tag{4}$$

where v denotes the iterative gradient cumulative information and momentum is the momentum coefficient, which usually takes the value of 0.9 to 0.99 [14].

3. Deep Learning for Liver Steatosis Grading Practice

Based on the above analysis of the DenseNet model related to transfer learning, the specific method of using deep learning for liver steatosis grading study in this paper is as follows:

(1) Dataset construction. All patients' clinical information is concealed, the grade of hepatic steatosis is labeled and used as a tag, and the dataset with their corresponding ROI is constituted.

(2) Data preprocessing. To improve the convergence speed of the network, the datasets are dealt with normalization, the patient MRI image pixels are normalized to [0, 1] without changing the stored information of images, and the training set and test set are divided in a certain ratio [15].

(3) Model construction and training. Based on the basic structure of DenseNet, a DenseNet model is built and transfer learning feedforward and backpropagation algorithms are trained on low-level weights and
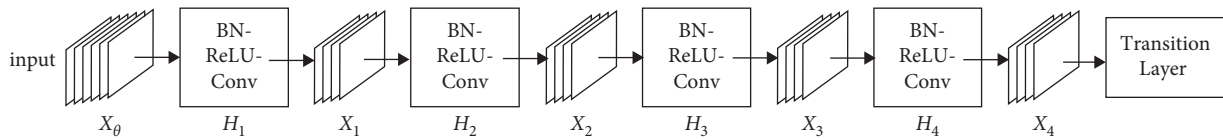
FIGURE 1: Dense connection of DenseNet blocks.

high-level weights, respectively, to identify the features of the discovered structures and specific images in the images. In this paper, 1.28 million natural images from the ImageNet dataset are selected for pretraining the model.

(4) Model fine tuning. Model fine tuning usually includes by training the whole network, freezing the convolutional base, and freezing some layers to train some layers [16]. Considering the difference in data volume between the experimental dataset and the ImageNet dataset on the hepatic steatosis study in this paper, it was decided to choose the approach of freezing some layers to train some layers for model fine tuning[17]. After the model is pretrained, the fully connected layer is removed, 2 dense blocks are frozen, and 1 untrained dense block and the fully connected layer are added immediately afterwards, with the aim of extracting and classifying advanced features, which then connected by batch normalization and pooling layers [18]. Ultimately, the model structure used in this paper for liver steatosis grading study is shown in Figure 2. In the figure, Dense Block1, Dense Block2, and Dense Block3 are densely connected in 4, 4, and 32 layers, respectively.

4. Simulation Experiments

4.1. Experimental Environment Setup.
The experiments were conducted on an Nvidia GeForce RTX 2080 Ti GPU, implemented through the Keras deep learning framework, and programmed in Python 3.6.

4.2. Data Source and Preprocessing.
The data of this experiment were obtained from abdominal MR imaging data and clinical information of 50 patients from June to July 2020 in a hospital in Beijing. Among them, hepatic fat grade grading was done independently by two professional imaging physicians based on patient imaging data, and hepatocellular steatosis was divided into four degree scores, noting hepatocellular adipocyte deformation 0–5% as 0, 5–33% as 1, 34%–66% as 2, and more than 66% as 3, respectively [19]. The statistics of patients' hepatic steatosis grade shows that there were 38 patients with grade 0, 24 male patients and 14 female patients; 12 patients with grade 1, 6 male patients and 1 female patient; there were no patients with grade 2 or 3.

Figure 2 shows an example of an MR abdominal mDixon imaging slice of a patient. Six square ROI regions were set for each MR sequence of DICOM images under the premise of avoiding large blood vessels, focal liver lesions, and significant liver artifacts [20]. Four of the ROIs were located in the
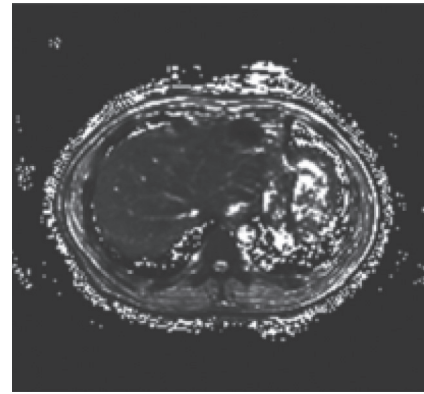
FIGURE 2: Example of mDixon slice image.

parenchyma of the right lobe of the patient's liver, i.e., segments V, VI, VII, and VIII of the liver, and the other two ROIs were located in the parenchyma of the left lobe of the patient's liver, i.e., segments II and III of the liver. Each region of the liver parenchyma has $16 * 16$ pixels.

Considering the small amount of experimental data, only 300 ROIs of 50 patients, it is difficult to meet the demand of deep learning data volume, so the experiment uses panning, rotation, mirroring, and other enhancement processing on the data [21]. In addition, since the difference in the number of data between samples with liver fat deformation as grade 0 (38 cases) and grade 1 (12 cases) is more obvious, if directly input into the depth model, it will easily lead to the neglect of the minority class samples, which are of important research value in medical image analysis. Therefore, to avoid the effect of unbalanced data samples on the results, the experiments combined the actual number of minority class samples and majority class samples and used the method of oversampling minority class samples to deal with unbalanced data samples [22, 23]. The 648 ROIs with grade 1 hepatic steatosis were amplified twice with 2-fold data to obtain a total of 2,592 cases of grade 1 hepatic steatosis ROI data. Finally, 2,052 cases of grade 0 ROI data and 2,592 cases of grade 1 ROI data of hepatic steatosis were obtained in this experiment, where 3,766 and 878 ROIs were used for model training and testing, respectively, and Adam was selected as the optimization algorithm during the modeling process.

4.3. Evaluation Indexes.
In this experiment, precision, sensitivity, specificity, and AUC were chosen as the indexes to evaluate the model performance. Precision reflects the probability that the model predicts correctly for all samples and is calculated as in equation (5). Sensitivity is a measure of the probability that the model predicts correctly for positive class samples and is calculated as in equation (6).

The specificity is a measure of the probability that the model correctly predicts the negative class samples and is calculated as in equation (7). The higher the values of precision, sensitivity, and specificity, the better the model performance. AUC, the probability of predicting a positive case before a negative case, is an important index of the predictive effectiveness of a dichotomous classification model. The closer its value is to 1, the better the model performance is indicated [24].

$$\text{precision} = \frac{TP}{(TP + FP)}, \tag{5}$$

$$\text{sensitivity} = \frac{TP}{P}, \tag{6}$$

$$\text{specificity} = \frac{TN}{N}, \tag{7}$$

where TP denotes true positive; FP denotes false positive; P denotes all positive; TN denotes true negative; N denotes all negative. The accuracy and the loss function were selected to evaluate the metrics for evaluating the change of the model during training and testing. The accuracy rate reflects the probability of correct prediction during the model iteration and is calculated as in equation (8). The closer its value is to 1, the higher the model prediction accuracy is. The loss function reflects the difference between the predicted label and the true label, and is calculated as in equation (9). The closer its value is to 0, the better the model prediction is, and the closer the predicted value is to the true value [25].

$$\text{accuracy} = \frac{TP + TN}{P + N}, \tag{8}$$

$$\text{loss} = [y \log \hat{y} + (1 + y)\log(1 - \hat{y})]. \tag{9}$$

In equation (9), y and $\hat{y}$ denote the true label and the predicted label, respectively.

4.4. Experimental Results

4.4.1. Model Validation.
To verify the effectiveness of the proposed model transfer learning for model improvement, the experiments compare the training error of the model before and after the transfer learning with the test set accuracy, and the results are shown in Figure 3, where a and b are the model training error and test set accuracy before transfer learning, with the number of iterations, respectively, and c and d are the model training error and test set accuracy after transfer learning, with the number of iterations, respectively. As can be seen from the figure, before transfer learning, the model reached convergence at about 100,000 iterations and its accuracy on the test set was 80%; after transfer learning, the model converged at about 30,000 iterations and its accuracy on the test set was 83.4%. It shows that transfer learning can improve the model convergence speed and prediction accuracy.

To further validate the effectiveness of transfer learning, the confusion matrix of the model's prediction of each grade

of hepatic steatosis after transfer learning was experimentally analyzed, as shown in Figure 4, where the horizontal and vertical coordinates are the sample prediction and the true grade, respectively, and the diagonal line is the proportion of correct predictions. As can be seen from the figure, the proposed model has a high accuracy in predicting the grade of hepatic steatosis, which is more than 80%.

In addition, the experiments also compared the prediction effects of the proposed model with other models before and after transfer learning, and the results are shown in Table 1. As can be seen from the table, the accuracy of the model after transfer learning is improved in different degrees on the test set compared with the model before transfer learning; the proposed model has a higher accuracy of 83% on the test set compared with other transfer learning models, and the smaller the model size is, the shorter the time to predict a single image, which shows that the proposed model has certain superiority.

4.4.2. Model Prediction Results.
To verify the validity of the proposed model for liver steatosis grading practice, the accuracy, sensitivity, specificity, and AUC values of the model on the training and test sets were collected experimentally, and the results are shown in Table 2. As shown in the table, the accuracy of the model on the training and test sets was more than 85%, the sensitivity was more than 94%, the specificity was about 80%, and the AUC value was more than 0.8, which is closer to 1. This indicates that the proposed model has good predictive performance and can predict the grade of hepatic steatosis of patients more accurately. The sensitivity and specificity indicate that the model has a strong ability to detect positive cases, indicating that the model can detect hepatic steatosis grade 1 more reliably and has some practical application value.

Figure 5 shows the changes of loss and accuracy curves on the training and testing sets during the iterations of the model. From the figure, it can be seen that with the increase of iterations, the loss and accuracy curves gradually leveled off and reached a stable state after 400 iterations; the model did not show any overfitting phenomenon during the whole training and testing process, which indicates that the proposed model exhibits good prediction performance through transfer learning.

4.4.3. Statistical Analysis.
Spielman correlation analysis was performed using MATLAB R2018b on the obtained clinical information, such as gender and age of the patients, and the grade of hepatic steatosis, and the results are shown in Table 3, where $P < 0.05$ indicates a statistically significant difference, and $*$ indicates a significant correlation at the 0.05 level. The table shows that the p value of pancreatic steatosis grade and hepatic steatosis grade was 0.003, and the correlation between them was significant; the p value of other clinical information such as patient age and gender and hepatic steatosis grade was larger than 0.05, indicating that the correlation between them was not significant.

Correlation analysis between clinical information and hepatic steatosis grade in patients of different genders

(a)

(b)

(c)

(d)
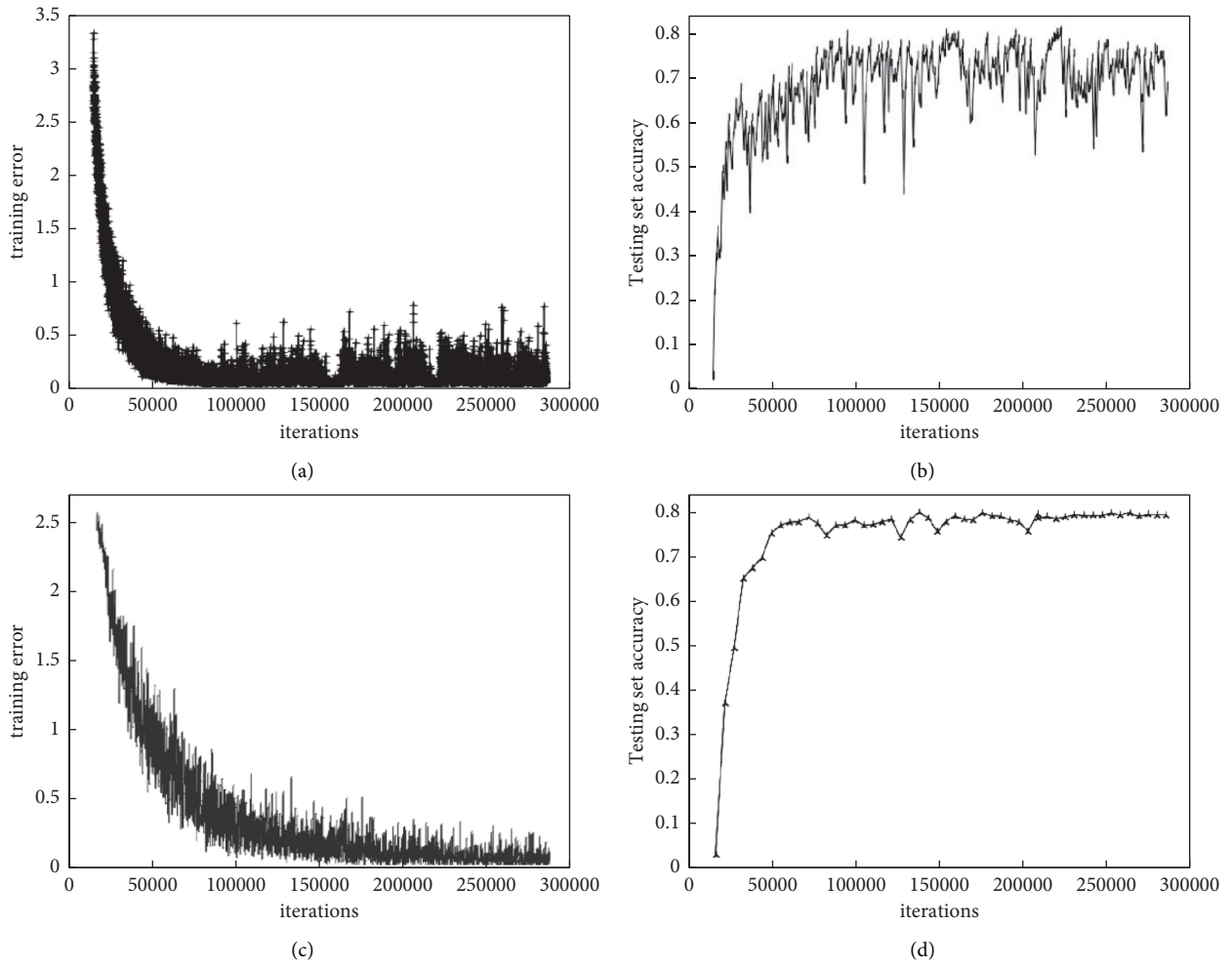
Figure 3: Performance comparison before and after model transfer learning.
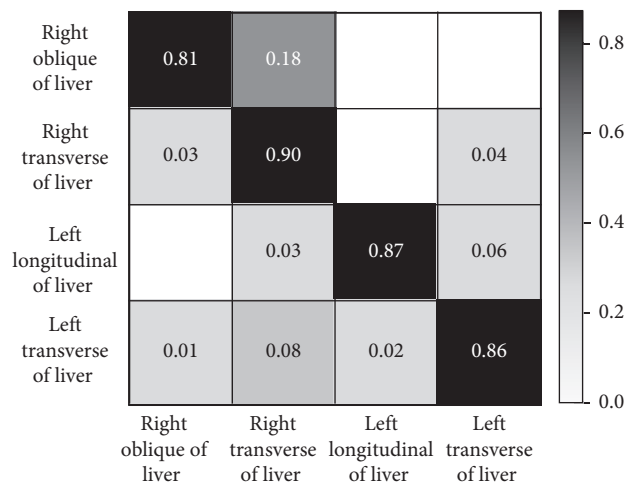
Figure 4: Confusion matrix of model prediction results.

revealed significant correlations between hepatic steatosis grade and metabolic syndrome and pancreatic steatosis grade in female patients $P = 0.007$ and $P = 0.002$, while there was no correlation between hepatic steatosis grade and its

clinical information in male patients. The change in liver fat content with age of the patients was analyzed, and the results are shown in Figure 6. As can be seen from the figure, there was no correlation between liver fat content and the age of

TABLE 1: Comparison of prediction results of different models.

| Network name | Testing set accuracy | | Model size (MB) | The time of predicting single image(s) |
	Nontransferable learning (%)	Transfer learning (%)		
ResNet52	68.34	70.33	235	0.2447
VGG16	77.25	79.48	521	0.0630
VGG19	77.31	80.27	561	0.0704
SqueezeNet	73.09	77.36	2.77	0.0072
GoogleNet-inception V1	78.42	80.46	39.4	0.0221
DenseNet 16	80.27	83.46	101	0.2721

TABLE 2: Model performance.

Items	Accuracy (%)	Sensitivity (%)	Specificity (%)
Training sets	88.49	95.44	81.6
Test sets	85.79	94.55	79.82

(a)

(b)
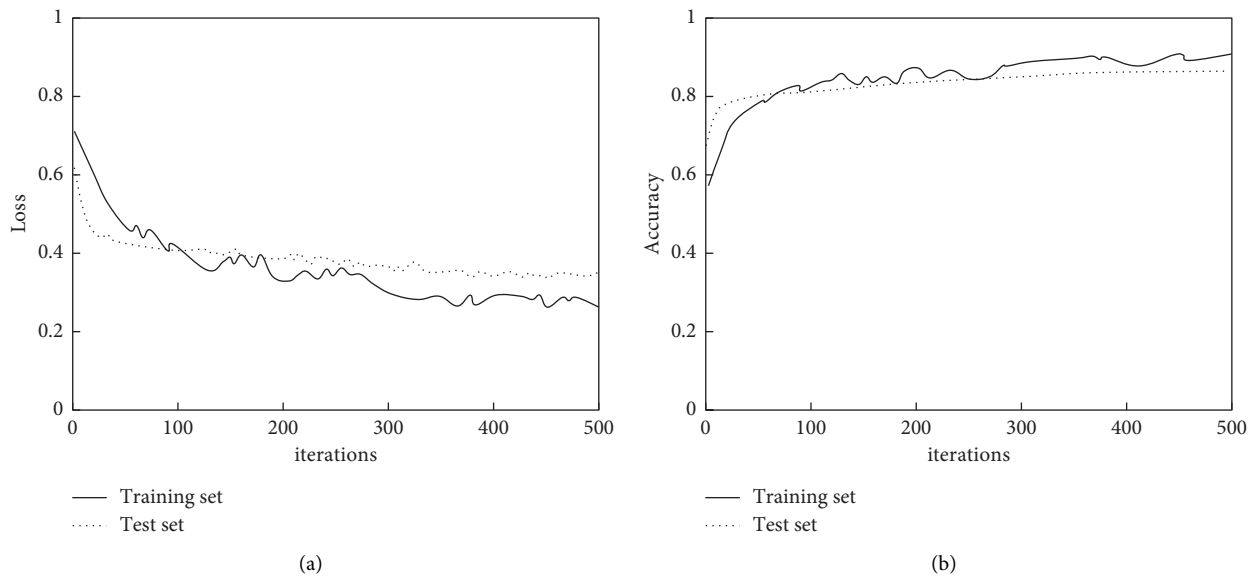
FIGURE 5: Model performance iteration curve.

TABLE 3: Analysis results of clinical information and hepatic steatosis grade of patients.

Clinical information	Correlation coefficient	P value
Age	0.003	0.959
Gender	0.035	0.570
Pancreatic steatosis grade	0.702 ∗	0.003
Metabolic syndrome	0.890	0.147
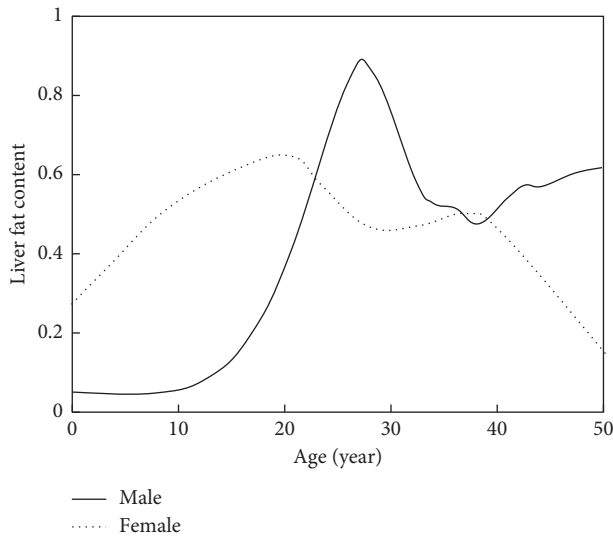
Figure 6: Variation curve of liver fat content with age.

the patients, but there was a peak between the ages of 50 and 60 years for women and one peak each between the ages of 40 and 50 years and 70 to 80 years for men.

5. Conclusion

In summary, applying deep learning to liver steatosis time can achieve automated and more accurate grading, and by introducing transfer learning into the deep learning DenseNet model, the number of model iterations can be significantly reduced and the model convergence speed and prediction accuracy can be improved, which has some potential application value. Applying it to the practice of liver steatosis grading, the accuracy of the proposed model on the training and test sets reached more than 85%, the sensitivity exceeded 94%, the specificity was about 80%, and the AUC value reached more than 0.8, which is closer to 1. It has good predictive performance and can detect liver steatosis grade 1 more accurately and reliably, which has some practical application value. Statistical correlation analysis shows that hepatic steatosis correlates significantly with pancreatic steatosis and has some correlation with metabolic syndrome; hepatic steatosis was correlated with age and metabolic syndrome in women only. However, due to the limitations, there are still some shortcomings in this paper; the amount of patient data is too small, the preliminary results obtained need to be further validated, and among the 50 patients with hepatic steatosis, there are no patients with grade 1 or higher, which leads to the accuracy and generalization ability of the model to be demonstrated. Therefore, the amount of hepatic steatosis imaging data will be further collected and expanded in the next study.

Data Availability

The experimental data used to support the findings of this study are available from the corresponding author upon request.

Conflicts of Interest

The authors declare that they have no conflicts of interest regarding this work.

References

[1] Q. Yazan, A. Tahir, M. E. H. Chowdhury et al., "Detection and Severity classification of COVID-19 in CT images using deep learning[J]," *Diagnostics*, vol. 11, no. 5, p. 893, 2021.

[2] F. J. P. Montalbo, "Diagnosing Covid-19 chest x-rays with a lightweight truncated DenseNet with partial layer freezing and feature fusion," *Biomedical Signal Processing and Control*, vol. 68, pp. 102583–102589, 2021.

[3] B. J. Marwa, A. Koubaa, B. Benjdira, A. Ammar, and H. Hamam, "COVID-19 diagnosis in chest X-rays using deep learning and majority Voting[J]," *Applied Sciences*, vol. 11, no. 6, pp. 2884–2887, 2021.

[4] Z. Liu, Y. Zhu, Y. Yuan et al., "3D DenseNet deep learning based preoperative Computed Tomography for detecting myasthenia gravis in patients with thymoma," *Frontiers in Oncology*, vol. 11, p. 631964, 2021.

[5] R. Abtin, M. Babaie, D. Maleki et al., "Tizhoosh. Fine-tuning and training of DenseNet for histopathology image Representation using TCGA diagnostic Slides[J]," *Medical Image Analysis*, vol. 69, pp. 102032–102036, 2021.

[6] P. Xiong, Y. Xue, J. Zhang et al., "Localization of myocardial infarction with multi-lead ECG based on DenseNet," *Computer Methods and Programs in Biomedicine*, vol. 203, pp. 106024–106029, 2021.

[7] S. Albahli, N. Ayub, and S. Muhammad, "Coronavirus disease (COVID-19) detection using X-ray images and enhanced DenseNet," *Applied Soft Computing*, vol. 110, pp. 107645–107648, 2021.

[8] G. Wang, Z. Guo, X. Wan, and Xu Zheng, "Study on image classification algorithm based on improved DenseNet[J]," *Journal of Physics: Conference Series*, vol. 1952, no. 2, pp. 1742–1749, 2021.

[9] J. Zhang, C. Wu, X. Yu, and X. Lei, "A novel DenseNet Generative Adversarial network for Heterogenous low-Light image enhancement," *Frontiers in Neurorobotics*, vol. 15, pp. 700011–700019, 2021.

[10] M. Z. Alom, T. M. Taha, C. Yakopcic et al., "A state-of-the-Art Survey on deep learning theory and Architectures," *Electronics*, vol. 8, no. 3, pp. 292–296, 2019.

[11] J. Balajee and M. A. Saleem Durai, "Detection of water availability in SAR images using deep learning architecture [J]," *International Journal of System Assurance Engineering and Management*, vol. 62, pp. 1–10, 2021.

[12] X. Hu, Y. Liu, Z. Zhao et al., "Real-time detection of uneaten feed pellets in underwater images for aquaculture using an improved YOLO-V4 network[J]," *Computers and Electronics in Agriculture*, vol. 185, pp. 186–192, 2021.

[13] C. Dewi, R.-C. Chen, Y.-T. Liu, and S.-K. Tai, "Synthetic Data generation using DCGAN for improved traffic sign recognition[J]," *Neural Computing & Applications*, vol. 86, pp. 1–16, 2021.

[14] H. Jeyaprakash, S. Roseline, S. Geetha, S. Kadry, and R. Damaševičius, "An efficient DenseNet-based deep learning model for malware detection[J]," *Entropy*, vol. 23, no. 3, pp. 344–348, 2021.

[15] D. Yu, J. Yang, Y. Zhang, and S. Yu, "Additive DenseNet: dense connections based on simple addition operations,"

Journal of Intelligent and Fuzzy Systems, vol. 40, no. 3, pp. 5015–5025, 2021.

[16] G. Zhang, L. Lin, and J. Wang, "Lung Nodule classification in CT images using 3D DenseNet," *Journal of Physics: Conference Series*, vol. 1827, no. 1, pp. 012155–012159, 2021.

[17] H. Hong Hai and T. H. Hieu, "Improvement for convolutional neural networks in image classification using Long Skip connection[J]," *Applied Sciences*, vol. 11, no. 5, pp. 2092–2098, 2021.

[18] J. Fu, K. Singhrao, X. S. Qi, Y. Yang, D. Ruan, and J. H. Lewis, "Three - dimensional multipath DenseNet for improving automatic segmentation of glioblastoma on pre - operative multimodal MR images," *Medical Physics*, vol. 48, no. 6, pp. 2859–2866, 2021.

[19] S. Qamar, P. Ahmad, and L. Shen, "Dense Encoder-Decoder–based architecture for Skin lesion segmentation[J]," *Cognitive Computation*, vol. 96, pp. 1–12, 2021.

[20] S.R. Braulio and V.F. Ricardo, "A low-Cost three-dimensional DenseNet neural network for Alzheimer's disease early Discovery †[J]," *Sensors*, vol. 21, no. 4, pp. 1302–1309, 2021.

[21] Y. Pan, D. Pi, I. A. Khan, Z. U. Khan, J. Chen, and H. Meng, "DenseNetFuse: a study of deep unsupervised DenseNet to infrared and visual image fusion," *Journal of Ambient Intelligence and Humanized Computing*, vol. 12, no. 11, pp. 10339–10351, 2021.

[22] J. Zhang, J. Yu, S. Fu, and X. Tian, "Adoption value of deep learning and serological indicators in the screening of atrophic gastritis based on artificial intelligence," *The Journal of Supercomputing*, vol. 77, no. 8, pp. 8674–8693, 2021.

[23] H. Li, G. Wang, Z. Dong et al., "Identifying Cotton Fields from Remote sensing images using Multiple deep learning networks," *Agronomy*, vol. 11, no. 1, pp. 174–178, 2021.

[24] Yu-D. Zhang, S. Chandra Satapathy, X. Zhang, and S.-H. Wang, "COVID-19 diagnosis via DenseNet and optimization of transfer learning Setting[J]," *Cognitive Computation*, vol. 69, pp. 1–17, 2021.

[25] X. Fu, C. Chen, and D. Li, "Survival prediction of patients suffering from glioblastoma based on two-branch DenseNet using multi-channel features[J]," *International Journal of Computer Assisted Radiology and Surgery*, vol. 16, no. 2, pp. 1–11, 2021.

Retraction

Retracted: Random Forest and LightGBM-Based Human Health Check for Medical Device Fault Detection

Journal of Healthcare Engineering

This article has been retracted by Hindawi following an investigation undertaken by the publisher [1]. This investigation has uncovered evidence of one or more of the following indicators of systematic manipulation of the publication process:

(1) Discrepancies in scope

(2) Discrepancies in the description of the research reported

(3) Discrepancies between the availability of data and the research described

(4) Inappropriate citations

(5) Incoherent, meaningless and/or irrelevant content included in the article

(6) Peer-review manipulation

The presence of these indicators undermines our confidence in the integrity of the article's content and we cannot, therefore, vouch for its reliability. Please note that this notice is intended solely to alert readers that the content of this article is unreliable. We have not investigated whether authors were aware of or involved in the systematic manipulation of the publication process.

Wiley and Hindawi regrets that the usual quality checks did not identify these issues before publication and have since put additional measures in place to safeguard research integrity.

We wish to credit our own Research Integrity and Research Publishing teams and anonymous and named external researchers and research integrity experts for contributing to this investigation.

The corresponding author, as the representative of all authors, has been given the opportunity to register their agreement or disagreement to this retraction. We have kept a record of any response received.

References

[1] W. Wang, "Random Forest and LightGBM-Based Human Health Check for Medical Device Fault Detection," *Journal of Healthcare Engineering*, vol. 2022, Article ID 2847112, 7 pages, 2022.

Research Article

Random Forest and LightGBM-Based Human Health Check for Medical Device Fault Detection

Weiwei Wang [ID]

Department of Equipment Pingdu People's Hospital, Pingdu, Qingdao, Shandong 266700, China

Correspondence should be addressed to Weiwei Wang; qdpdwww@sina.com

Medical devices are items used directly or indirectly in the human body and are a prerequisite for hospital treatment of patients, and their quality can have a direct impact on the health of patients, so strengthening the quality control of medical device use is a hot spot of concern in the clinic. Current medical device testing can reduce the occurrence of adverse events, but it cannot be completely avoided, and its work still needs to be further strengthened. In this paper, we design a two-way feature selection algorithm based on PSO_RF. We use random forest to calculate the importance of the feature attributes of the sample data and sort the results in descending order, where a particle swarm algorithm is introduced to optimize the parameters of the random forest algorithm. The 245 medical device adverse event reports received by the testing center were selected, the occurrence and types of adverse events were analyzed retrospectively, and quality control countermeasures for medical device use were formulated.

1. Introduction

With the rapid development of science and technology in the medical field, the medical equipment used is becoming more and more sophisticated and complex and the normal and stable operation of the equipment becomes more and more important in the process of using the instruments and equipment. The problem of accidental failure of the equipment will cause a great loss of scientific research results and reduce the efficiency of using the equipment [1].

Now, most universities, in the actual experiments, mostly use the way of regular testing and maintenance. Such testing cannot be based on the state of the equipment itself for maintenance and repair but according to people's own experience, which means that the equipment's potential failure points cannot be accurately maintained and, at the same time, will lead to a serious waste of funds and time [2–4]. With the development of complex and sophisticated instruments and equipment, the traditional manual detection method becomes infeasible and the manual fault detection method has the problems of difficult fault detection, time consumption, inaccuracy, and

high cost. In addition, especially for some precision instruments, it is more difficult for the management personnel of the equipment to accurately understand the operation of the equipment, so that the equipment is not timely maintained and repaired, which may have certain impact on the resulting experimental outcomes, affecting the final results of the experiment [5, 6]. At the same time, this also caused the low utilization rate of instruments and equipment, maintenance and repair costs, and other problems. Therefore, traditional testing methods have become difficult to adapt to the development of current instrumentation.

For the aforementioned problems, equipment failure detection technology was proposed. As early as the 1960s, the National Aeronautics and Space Administration of the United States set up a failure prediction team, specializing in data collection and calculation, etc., so as to make up for the shortcomings of the traditional manual mode to a certain extent [7]. Then, the United Kingdom and other countries also followed the research of equipment failure detection technology. With the continuous development of technologies, the stability of the equipment becomes more and more

high and the fault detection technology is constantly moving forward. Nowadays, the computing power of computers has been improved as never before, and the data from the operation of the equipment are constantly collected, so how to use the collected information to achieve effective management of the operation of equipment has become a popular issue [8–11].

Most of those who use medical devices are clinical healthcare workers, so those in control of their quality should actively communicate with clinicians to understand the potential problems that exist in their use and put forward certain adjustment suggestions [12]. At the same time, it is necessary to establish a perfect quality of medical equipment use rules and regulations, requiring that each contact with the use of medical equipment can follow the rules and regulations to reduce the adverse events of medical devices caused by human factors [13]. Routine and regular maintenance of equipment can prolong the service life of hospital equipment. For example, after clinicians use it, maintenance personnel needs to fill in maintenance records [14]. The contents of the records can dynamically grasp the use of medical equipment, analyze the adverse events that may occur, and exclude failures in the dangerous period, which in turn can ensure the normal operation of the instruments and equipment [15]. At the same time, the equipment should be regularly dusted and cleaned, its performance should be tested, the vulnerable parts should be replaced in a timely manner, and all records should be made. And a direct responsible person for medical devices should be established, so that adverse events that occur during maintenance or use can be traced directly by the individual, which in turn improves the requirements of each person in contact with medical equipment for themselves [16].

In summary, analysis of medical device adverse events and strengthening control over the quality of their use can reduce the occurrence of adverse events.

2. Related Work

Fault detection methods can be broadly classified into three categories: model-based, knowledge-based, and data-driven. Among them, model-based fault detection methods can provide a deeper understanding of the system nature and more real-time fault detection. In [17], a generalized graceless Kalman filter algorithm was used to detect and separate faults in the phase current and rotor position sensors of a three-phase permanent magnet synchronous motor, which handled the nonlinear data well [18]. By using the fault identification model of a knowledge vector machine, a hybrid reasoning model of knowledge reasoning and information fusion can be obtained. The authors of [19] used least squares support vector machine for fault detection and classification of regulating valves. Firstly, cleaning the experimental data and then using LS-SVM multiplicative for classification experiments on regulating valve samples achieved better results.

The machine learning method is a method that gives a computer a human way of thinking so that it can have the ability to process complex data, by training the algorithm model, using test data to verify the accuracy of the algorithm, and finally using the trained model to make effective decisions. In [20], the original data were subjected to feature extraction by PCA algorithm to obtain the feature vector of the original data, and finally, a multiclassification algorithm combining binary tree and SVM was used to achieve fault detection during vibration sensor operation, whose experimental results showed that the improved method not only increased the accuracy of fault detection but also accelerated the classification speed. In [21], a multimodal SVM learning method was proposed and applied to the fault detection problem of gearboxes, and the effectiveness of the method was verified in experiments on gearboxes with two structures: straight gearboxes and helical gearboxes.

3. Fault Detection Based on Random Forest and LightGBM

3.1. Analysis of Equipment Failure Detection Problems. LightGBM is chosen for its higher efficiency and accuracy, lower memory usage, and support for parallelized learning, so it is chosen to build the equipment fault detection model and to test the effectiveness of the PSO_RF-based bidirectional feature selection method based on the accuracy and precision of the confusion matrix [22]. The data after feature selection are then input to the LightGBM algorithm for learning, and a grid search method is used to optimize the parameter search process to produce the final classification results. In this paper, an equipment fault detection model is developed through the following steps:

Step 1: data preprocessing, including the deletion of sample data with problems such as missing and duplicate data, data transformation, and other operations

Step 2: feature selection using PSO_RF's bidirectional feature selection method

Step 3: Initializing the parameters of LightGBM, inputting the processed data into the model for training, and performing parameter optimization using the grid method

Step 4: inputting the test data into the model and then evaluating and analyzing the final output results

The flow chart of the model is shown in Figure 1.

3.2. Data Acquisition and Normalized Preprocessing. To detect equipment failure problems, the first thing to do is to conduct a comprehensive study of the equipment's failure information and the factors that affect it. The first step is to conduct a comprehensive study of the equipment fault information and its influencing factors. However, there are various problems in the data that do not meet the requirements as input variables for the model [23]. The data are preprocessed according to the following four steps.

Data collection: the real data used in the model come from the laboratory's independent project "Large-Scale instrument sharing platform," which mainly solves the problem of low
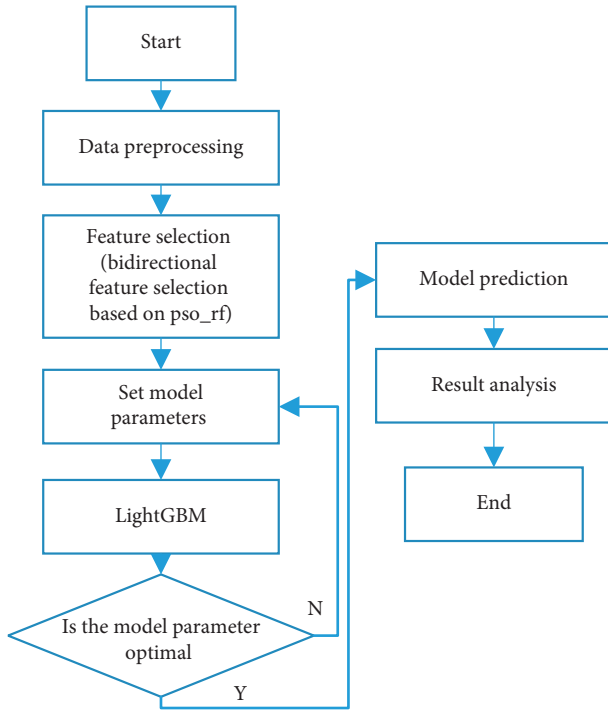
Figure 1: Flow chart of equipment fault detection algorithm.

utilization rate of instruments in universities and is currently serving many universities. The data set contains 1200 pieces of X-ray camera usage information, including 955 pieces of faulty data and 245 pieces of normal data. There is more information in the design, and although there are many factors to consider [24], there are some uncontrollable and other reasons that cannot be considered, such as improper human operation and other factors that are not included in the study. In summary, this data set can be used for the training of the equipment fault detection model.

Based on the analysis of the intuitive factors affecting the equipment, a total of 16 attribute values, E, F, G, H, I J, K, L, M, N, O|, P, Q, R, S, and T, are extracted as influencing factors [25].

The data in the sample have problems such as missing and duplicate data. Due to the relatively small amount of data, this paper fills in the values of the missing attributes by calculating the mean values of the attributes, and for the duplicate data, they are deleted because there are few duplicates. The same method of calculating the mean value of attributes is used to fill in the case of handling abnormal values.

Although the features are reduced using intuitive factors such as knowledge and experience in the previous section, there is still redundancy among the features. Redundant features can have a great impact on the model results and training efficiency during the model building process, so it is necessary to analyze the data and remove the useless information in this step. If an attribute value has a large range of values, then it will have a certain impact on the training of the model, so the transformation of the data is needed. In the experiments for E, F, G, H, I, J, K, L, M, N, O, P, Q, R, S, and T, data were normalized using the Max-Min (maximum-minimum) approach to normalize their attribute values. The

attribute values are normalized to the interval from 0 to 1. For the fault types, Err1, Err2, Err3, Err4, and Err5 are used for power failure, dome failure, heat dissipation failure, imaging failure, and cable failure, respectively. Normal is N.

After the above four steps, the problems of data duplication, missing values, and inconsistency in the original data are solved. This improves the quality of the data to a large extent, which is important for the subsequent performance improvement of the model [26].

3.3. Bidirectional Feature Selection Algorithm for Random Forests. The main idea is to add noise to a relevant feature and then judge the importance of a feature based on the change of the result before and after adding noise to the feature. The main idea is to add noise to a relevant feature and then judge the importance of a feature based on the change of the result before and after adding noise [27]. The procedure for calculating the importance of the random forest attribute X is as follows:

Step 1: for each tree, use its corresponding out-of-bag (OOB) data.

Step 2: among all samples of out-of-bag (OOB) data, randomly select the feature attribute X, add some noise to it, then calculate the out-of-bag error once again, and record it as errOOB.

Step 3: if the random forest is composed of N trees, then the importance of the feature X is

$$importance = \frac{\sum(errOOB2 - errOOB1)}{N}. \quad (1)$$

If the accuracy of attribute X is significantly lower after adding noise than before, then it can be said that feature X has a great influence on the learning effect of the model.

The random forest algorithm has many parameters, but there is no fixed method of parameter selection for different sample data. In order to solve this problem, this paper uses particle swarm algorithm to optimize the parameter search process of the random forest algorithm, so that the random forest can find the optimal combination of parameters more quickly and efficiently and the algorithm can further improve the performance of the model; the process of the algorithm is as follows:

Step 1: initialize the parameters of the random forest and particle swarm based on experience

Step 2: Generate a decision tree by randomly selecting k samples from the sample data according to the bootstrap algorithm

Step 3: Compute the output of the model

Step 4: The above classification results are used as the fitness values, and the particle swarm algorithm is used to continuously iterate, perform parameter optimization, and compare with historical results to finally output the optimal model parameters

Step 5: Based on the obtained model parameters, the random forest is trained and the importance score of feature attributes are finally derived

In this paper, a two-way feature selection algorithm based on PSO_RF is used to calculate the importance of the feature attributes of the sample data using random forest and the results are sorted in descending order. Then, the search starts from the full set of sample features, and each time, the features with the lowest degree of importance are removed from the current subset of features to form a new subset; finally, the part of backward selection is performed, and the accuracy of the current subset of features is calculated using LightGBM based on the confusion matrix; if the accuracy of the final result decreases after removing the features, the features just removed are recycled and so on until the end of the cycle. In this way, we can reduce the volatility of feature attributes and ensure that the selected subset has less redundancy and does not lose classification accuracy by adding the prediction results of the current subset as a factor to evaluate the feature subset on top of the feature importance [28].

4. Case Study

4.1. General Information. 245 cases of medical device adverse event reports received by the testing center were selected for retrospective analysis of the occurrence and types of adverse events and implementation of quality control countermeasures for medical device use. These included five major categories of medical devices: nonwoven surgical gowns, mercury thermometers, monitors, single-use sterile syringes, and OCU intrauterine devices, and all personnel involved in testing, maintenance, and quality control were in the same group.

245 cases of medical device adverse events were analyzed, including nonwoven surgical gowns, mercury thermometers, monitors, single-use sterile syringes, and OCU IUDs, and the total number of medical device adverse events from September 2018 to August 2019 and from September 2019 to August 2020 was counted [29].

4.2. Results. Among the 245 medical device adverse events, nonwoven surgical gowns accounted for 22.1%, mercury thermometers accounted for 35.5%, monitors accounted for 14.7%, single-use sterile syringes accounted for 16.7%, and OCU IUDs accounted for 10.4%, as shown in Table 1. The number of cases of medical device adverse events after the implementation of quality control in September 2019 ~ August 2020 was significantly less than the number of cases that occurred in September 2018 ~ August 2020. The number of cases occurring without implementation from September 2019 ~ August 2019 ($P < 0.05$) is shown in Table 2.

5. Fault Detection Model Training and Evaluation

In this paper, a particle swarm algorithm is used to optimize the bidirectional feature selection based on random forest and LightGBM for device fault detection. In this paper, we use the bidirectional feature selection algorithm based on the particle swarm optimization random forest described in this paper for feature selection. After collecting and preprocessing the original data in the above section, the processed data are input to the model as the input variables, 70% of the data set is used as training data for model training, and the remaining data are used as test data for model testing. In the experiments, CFS (correlation-based feature selection) is used as a comparison experiment, the search strategy of CFS for feature subsets is best-first search, the respective feature subsets are selected by both the feature selection algorithm and CFS, and then the results are predicted using LightGBM. Table 3 shows the results of the feature selection process using the two algorithms to select subsets separately and then using LightGBM for training, where X_{num} indicates the number of features.

As shown in Figure 2, the curves in the figure specifically represent the line graph of the variation of the accuracy of the fault detection model constructed from the data processed by the two feature selection algorithms with the number of features.

As can be seen from Table 3, the classification accuracy of the fault detection model built by the particle swarm optimized random forest bidirectional feature selection method selected in this paper is 89.73% and the F1 value is 90.26%, which is higher than that of the CFS feature selection method in terms of accuracy and F1 value, and the time cost of the feature selection algorithm used in this paper is smaller in terms of model time overhead. Finally, 12 features that have an impact on the device are selected as the input of the final model, including 12 features such as temperature, tube voltage, current, half-valence layer, and output repeatability.

The optimal feature subset was selected through the above experiments, then the fault detection model was constructed using the LightGBM algorithm and trained and tested in groups using the ten-fold cross-validation method, LightGBM, GBDT, and random forest were used for training and testing, and the average value was taken as the final result.

Figure 3 shows the accuracy of random forest, GBDT, and LightGBM algorithms using cross-validation each time, where the horizontal coordinates indicate the serial number of cross-validations and the vertical coordinates indicate the classification accuracy.

As shown in Table 4 and Figure 3, LightGBM achieves a good level of accuracy and F1 value in prediction results, which are better than the other two models, and the training efficiency of the model is also better than the other two models. In summary, the equipment fault detection method used in this paper is more accurate and reliable in terms of results through feature selection and fault model building and it effectively improves the computational efficiency of the fault detection model and improves the performance of the model.

TABLE 1: 245 medical device adverse event occurrence comparison.

Group	Number of cases	%
Nonwoven surgical garment	55	22.1
Mercury thermometer	87	35.5
Monitor	36	14.7
Disposable sterile syringe	41	16.7
OCU IUD	26	10.4

TABLE 2: Comparison of the number of cases of adverse events after the implementation of quality control (n).

Group	Number of cases
2018.9–2019.8	245
2019.9–2020.8	184
X^2	4.894
P	<0.05

TABLE 3: Analysis of the operation results of different feature selection algorithms.

	X_{num}	Accuracy rate	F1 value
CFS	13	0.8625	0.8589
Bidirectional feature selection based on PSO RF	12	0.8972	0.9025
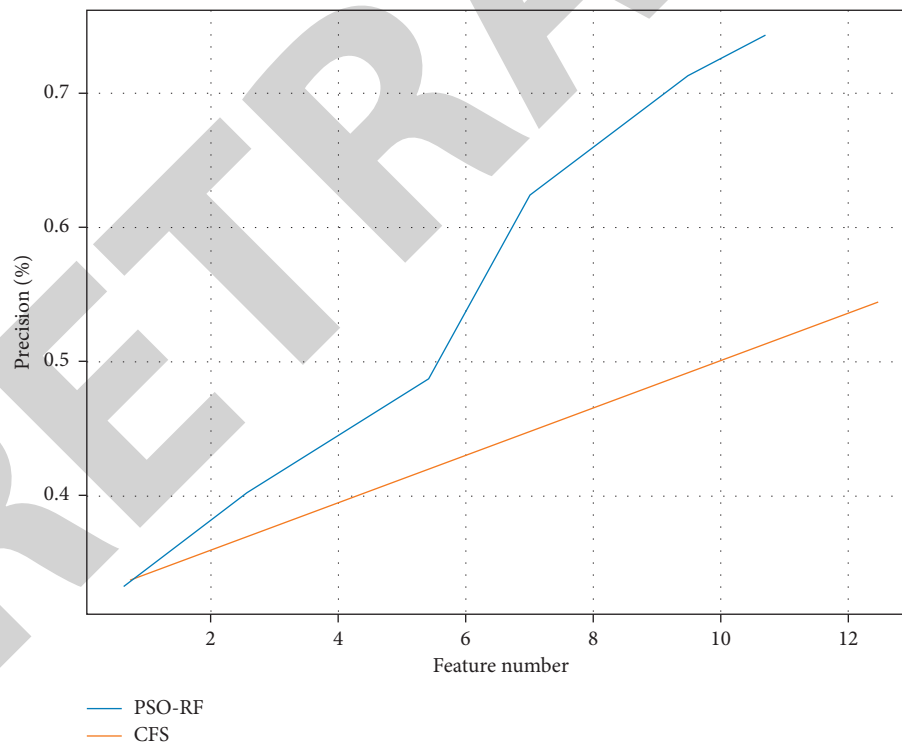
FIGURE 2: Effect of the number of features of the two algorithms on the results.
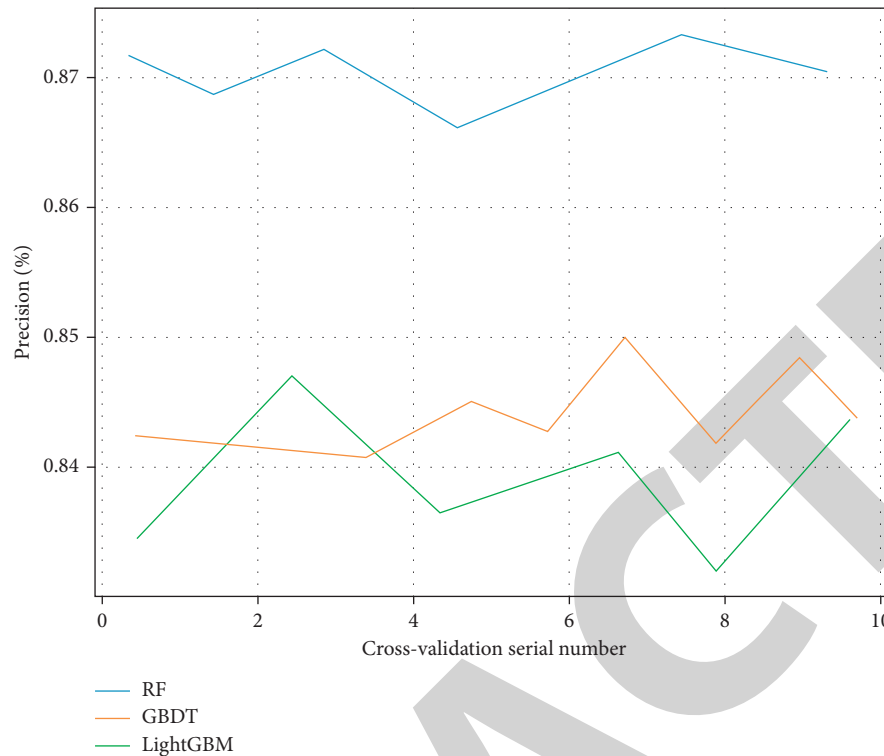
FIGURE 3: Comparison of classification results of different models.

TABLE 4: Comparison of fault diagnosis results of different models.

Model name	Accuracy rate	Recall	F1 value	Running time (s)
Random forest	0.8652	0.8957	0.8788	0.3257
GBDT	0.8554	0.9442	0.892	1.0041
LightGBM	0.9025	0.9259	0.9142	0.2689

6. Conclusions

This paper presents the complete process of building a fault detection model for equipment, firstly preprocessing the data, then selecting the optimal feature subset by a two-way feature selection method based on PSO_RF, finally using the selected feature subset as input to build a fault detection model, and verifying that the fault detection model used in this paper is realistic and effective by comparing and analyzing with other algorithms.

Data Availability

The data underlying the results presented in the study are included within the manuscript.

Conflicts of Interest

The author declares no conflicts of interest.

Authors' Contributions

The author has seen the manuscript and approved for submission.

References

[1] D. D. Rufo, T. G. Debelee, A. Ibenthal, and W. G. Negera, "Diagnosis of diabetes mellitus using gradient boosting machine (LightGBM)," *Diagnostics*, vol. 11, no. 9, p. 1714, 2021.
[2] L. Kopitar, P. Kocbek, L. Cilar, A. Sheikh, and G. Stiglic, "Early detection of type 2 diabetes mellitus using machine learning-based prediction models," *Scientific reports*, vol. 10, no. 1, pp. 11981–12012, 2020.
[3] S. H. Kassania, P. H. Kassanib, M. J. Wesolowskic, K. A. Schneidera, and R. Detersa, "Automatic detection of coronavirus disease (COVID-19) in X-ray and CT images: a machine learning based approach," *Biocybernetics and Biomedical Engineering*, vol. 41, no. 3, pp. 867–879, 2021.
[4] C. H. Cao, Y. N. Tang, D. Y. Huang, and W. Gan, "IIBE: An improved identity-based encryption Algorithm for WSN security," *Security and Communication Networks*, pp. 2021–8, Article ID 8527068, 2021.
[5] D. Wu, C. Zhang, L. Ji, R. Ran, H. Wu, and Y. Xu, "Forest fire recognition based on feature extraction from multi-view images," *Traitement du Signal*, vol. 38, no. 3, pp. 775–783, 2021.
[6] L. Wang, C. Zhang, Q. Chen, S. Liu, Z. Yang, and H. Li, "A communication strategy of proactive nodes based on loop theorem in wireless sensor networks," in *Proceedings of the 2018 9th International Conference on Intelligent Control and*

Review Article

A Review on the Rule-Based Filtering Structure with Applications on Computational Biomedical Images

Xiao-Xia Yin [ID],[1] **Sillas Hadjiloucas,**[2] **Le Sun,**[3] **John W. Bowen** [ID],[2] **and Yanchun Zhang**[1]

[1]*Cyberspace Institute of Advanced Technology, Guangzhou University, Guangzhou 510006, China*
[2]*Biomedical Engineering, School of Biological Sciences, University of Reading, Reading RG6 6AY, UK*
[3]*Engineering Research Center of Digital Forensics, Ministry of Education,*
 Nanjing University of Information Science and Technology, Nanjing, China

Correspondence should be addressed to Xiao-Xia Yin; xiaoxia.yin@gzhu.edu.cn

In this paper, we present rule-based fuzzy inference systems that consist of a series of mathematical representations based on fuzzy concepts in the filtering structure. It is crucial for understanding and discussing different principles associated with fuzzy filter design procedures. A number of typical fuzzy multichannel filtering approaches are provided in order to clarify the different fuzzy filter designs and compare different algorithms. In particular, in most practical applications (i.e., biomedical image analysis), the emphasis is placed primarily on fuzzy filtering algorithms, with the main advantages of restoration of corrupted medical images and the interpretation capability, along with the capability of edge preservation and relevant image information for accurate diagnosis of diseases.

1. Introduction

From a biomedical image reconstruction perspective, fuzzy filtering is particularly useful because it enables the denoising of extremely corrupted color images [1]. As a result, future knowledge-based systems for biomedical imaging are likely to incorporate fuzzy operators in their software [2]. Various noise forms impair color pictures in various approaches, and this poses a major challenge to the design of multichannel filters [3–6].

In order to successfully address the problem of color image denoising, the challenge is to (a) trace the origins and account for the diversity of the noise characteristics and (b) take into consideration the nonstationary statistics of the underlying image structures [7]. The above considerations have fueled current academic exertions aimed at merging structure or noise estimation approaches alongside filtering techniques regarding color image restoration. There are three main objectives that need to be fulfilled when designing filters for color image restoration: noise attenuation, chromaticity retention, and edge detail preservation [8].

Numerous signal processing issues, particularly those involving the nonlinearities of the picture creation process, cannot be successfully treated using linear approaches. Additionally, one must consider the human visual system's nonlinear nature [9]. Fuzzy modelling provides a bridge between linear and nonlinear techniques by integrating conventional linear and nonlinear filters with fuzzy logic. Since information extracted from data may also be corrupted by noise, a precise mathematic model of a nonlinear system is more difficult to establish because it requires a deterministic component in the model and a separate stochastic one, increasing the number of parameters that need to be evaluated. Fuzzy reasoning is particularly well suited from this perspective as it enables the choice of soft thresholds that can adapt better to the nonlinearities in the model inputs [9, 10].

The method of applying fuzzy logic to formulate a mapping to an output from a given input is fuzzy inference. This mapping then serves as a foundation for decision-making and pattern recognition [11]. In modelling, the fuzzy rule-based method considers orally defined rules that

overlap in the parameter space [12, 13]. In the fuzzy modelling process, the aim is to derive a fuzzy rule base that is appropriate for the task at hand. As a fuzzy filter takes into account selected patterns in the neighbourhood of the element to be processed, the filtered output is capable of adapting to information present in the vicinity of the pixels being processed. To restore and correct a corrupted pixel locally, a window-based fuzzy filter is normally used, where the fuzzy rule acts directly on the signal elements within the operational window.

However, a significant number of rules is often needed, and the designer must strike a balance between rule count and performance because even a modest processing window frequently requires a huge number of rules [14]. To address these issues, data-dependent filters based on fuzzy reasoning have been developed. To derive fuzzy rules automatically, two fundamental problems concerning fuzzy system modelling should be addressed: one is fuzzy rule parameter optimization and the other is the identification of an appropriate system structure in relation to the number of membership functions and fuzzy rules [15]. A three-step approach is applied to achieve the fuzzy inference process; this involves the right choice of membership functions, fuzzy logic operators, and if-then rules [11].

Concluding, the basic motivation behind this work is not to elaborate into new ideas in fuzzy logic theory but to use effectively fuzzy logic techniques into the filtering of multidimensional data and color images with biomedical applications. The presented method can be generalized to any dimension and can be used effectively to other types of correlated multidimensional/multichannel data as well.

This paper is organized as follows. Section 2 addresses the generation of suitable membership functions for fuzzy variables. Identification of optimized equation parameters through fuzzy rule modelling is also reviewed in this section. Section 3 discusses the use of a membership function to restore the corrupted pixels in a color image. Section 4 contains various fuzzy filter construction through fuzzy inferences. Section 5 discusses how the fuzzy reduction approach may be used to analyze, restore, and repair biomedical imaging. Finally, Section 6 provides a concise summary of the most important aspects in each section.

2. Fuzzy Variables and Fuzzy Rules for a Color Image

It is widely accepted that color conveys additional information beyond that conveyed in greyscale imaging. As a result, color and multispectral imaging systems are used in most scientific applications. The origins of such advantage may be traced to Fellgett's multiplex advantage in astronomy, which states that a multispectral system has an advantage over its monochromatic counterpart because of higher throughput per unit time associated with the different separate channels conveying the acquired information. Within the context of acquiring information from different channels, noise filtering is one of the most common image processing tasks and forms an essential part of any image processing system [16, 17].

Instead of adopting traditional vector filters for a fixed amount of smoothing or noise removal [3], it is possible to adapt the smoothing criterion to local image statistics. Two basic assumptions play an important role in filtering techniques development [18]. One is that a noise-free image should be locally and smoothly varying while at the same time also separated by edges [19]. The other is that, normally, a noise pixel possesses a gray value that is much more or lesser than that of its neighbors [20]. Any fuzzy rule is associated with a local representation over a region defined in the input space [21]. A particular window, as illustrated in Figure 1, can thus be designed to define a region with pixels corrupted by impulse noise.

To design a fuzzy filter, it is important to clarify where and how a particular membership function arises, how it is used and its effect is quantified, and how it can be tailored according to the imaging problem at hand in order to provide meaningful results. Different interpretations of fuzziness result in a multiplicity of solutions to graded membership and membership definition problems [22]. The following sections review some basic concepts and defines fuzzy (logic) variables concerning color images. The adopted approaches to calculating specific fuzzy variables are represented as special cases tailored to specific problems. They lead to relevant membership functions suitable for achieving the outputs of the ruled fuzzy filters.

2.1. Adaptive Fuzzy Hybrid Approaches.

The adaptive fuzzy hybrid multichannel (AFHM) filter [23] provides the generic framework that incorporates the ideas from the following three filters: the vector median (VM) filter, the vector directional (VD) filter, and the identity filter [23].

Let d_{VM} and $d_{\xi,VM}$ denote the aggregated Euclidean distances corresponding to $\mathbf{y}_{VM}$ and $\mathbf{y}_\xi$ (the central vector-valued pixel), respectively. In addition, let $d_{BV\ D}$ and $d_{\xi,BV\ D}$ denote the aggregated angular distances corresponding to $\mathbf{y}_{BV\ D}$ and $\mathbf{y}_\xi$, respectively. It is obvious that $d_{VM} < d_{\xi,VM}$ and $d_{BV\ D} < d_{\xi,BV\ D}$.

Let μ and ν denote two measures as fuzzy varieties for detecting the possibility whether the central vector-valued pixel is contaminated or not. A big μ-value suggests the substantial probability of contamination of the center vector-valued pixel. A big ν-value indicates the center vector-valued pixel's direction to be more possibly a directional outlier [24]. We define μ and ν as fuzzy varieties, which satisfy the following equations, respectively.

$$\begin{aligned} \mu &= \left| d_{VM} - d_{\xi,VM} \right|, \\ \nu &= \left| d_{BV\ D} - d_{\xi,BV\ D} \right|. \end{aligned} \tag{1}$$

When both μ and ν are large, this indicates that the chance of corrupting the center vector-valued pixel $\mathbf{y}_\xi$ is significantly high. The aggregated distance between a corrupted vector-valued pixel and the median vector should be large [23]. When only μ is small, this indicates that $\mathbf{y}_\xi$ is regarded as an uncorrupted vector by the VM filter but a corrupted vector by the BVD filter. When only ν is small, the situation is opposite. When both μ and ν are small, there is
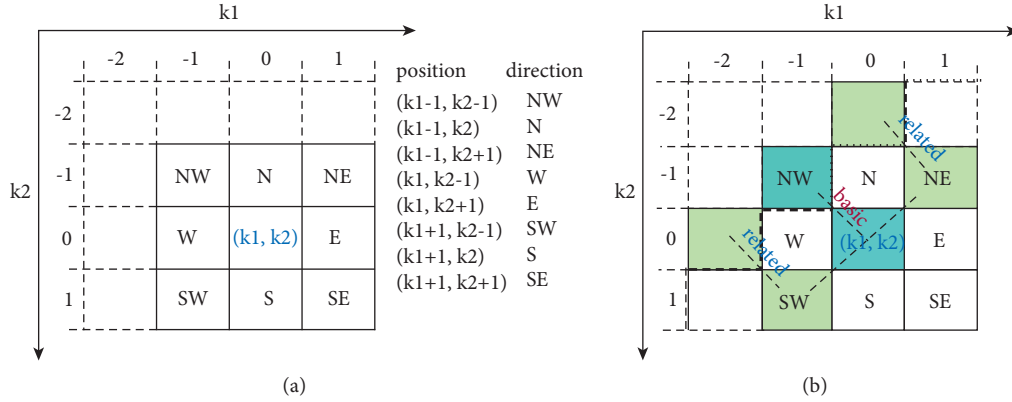
Figure 1: (a) Illustration of the neighborhood of a central pixel (**k**) within a 3×3 window demonstrated by a thick solid black line. (b) Illustration of centers for the calculation of the basic and related gradient values in the NW-direction and an example of an edge related to the local area inside the window. The latter is represented by a thick dash line.

high possibility that the center pixel is not corrupted by noise.

2.2. Applications of the Fuzzy Derivative.

It has been shown that fuzzy derivatives are useful for fuzzy filtering. A simple derivative at the central pixel position (k_1, k_2) in the direction $\mathbf{D}$ ($\mathbf{D} \varepsilon \mathbf{DIR} = \{\mathbf{NW, W, SW, S, SE, E, NE, N}\}$) is defined as the difference between the pixel at (k_1, k_2) and its neighbor in the direction $\mathbf{D}$. This derivative value is denoted by $\nabla_{\mathbf{D}}(k_1, k_2)$. This can be expressed as follows:

$$\nabla_{\mathbf{D}}(k_1, k_2) = \mathbf{x}(k_1 - 1, k_2 - 1) - \mathbf{x}(k_1, k_2). \tag{2}$$

The fuzzy derivative's principal idea considers this observation. Assume an edge that runs in the $\mathbf{SW-NE}$ direction across the neighborhood of a pixel (k_1, k_2). The derivative gains a big value. Additionally, the derivative values of nearby pixels perpendicular to the direction of the edge might be rather considerable. To carry out the edge detection procedure, one basic gradient value and two associated gradient values (specified in the same direction) are generated for each direction. These correspond to the two parameters $\nabla_{\mathbf{D}}(k_1, k_2), \nabla_{\mathbf{D}}(k_1 + 1, k_2 - 1), \nabla_{\mathbf{D}}(k_1 - 1, k_2 + 1)$, respectively; see Figure 1(b). The objective is to cancel out the influence of a single high derivative value caused by noise. Thus, if two of the three derivative values are small, it is generally reasonable to believe that the considered direction lacks an edge. The stated assumption is considered when the fuzzy rule for computing fuzzy derivative values is developed [25]. For an overview of how the pixels are used to calculate the fuzzy derivative for each direction, one can refer to [25]. Figure 1(a) illustrates the neighborhood of a central pixel (k_1, k_2). In Figure 1(b), pixel values indicated in gray are used to compute the "fuzzy derivative" of the central pixel (k_1, k_2) for the NW-direction [25].

In [26], the fuzzy gradient (derivative) value, associated with a noisy component of a center pixel (e.g., the red component), $\nabla_D^F C_R(k_1, k_2)$ can be defined according to a fuzzy fusion function which has a span between the basic gradient value and the two related gradient values in the direction D.

$$\nabla_D^F C_R(k_1, k_2)^{\text{noise}}$$
$$= \left|\nabla_D C_R(k_1, k_2)\right|^S \cap \left|\dot{\nabla}_D C_R(k_1, k_2)\right|^L \cap \left|\ddot{\nabla}_D C_R(k_1, k_2)\right|^L \cup \left|\nabla_D C_R(k_1, k_2)\right|^L \cap \left|\dot{\nabla}_D C_R(k_1, k_2)\right|^S \cup \left|\ddot{\nabla}_D C_R(k_1, k_2)\right|^S. \tag{3}$$

This way, it is possible to obtain the fuzzy gradient (derivative) value regarding the free noisy (red) component of a center pixel in the direction D.

$$\nabla_D^F C_R(k_1, k_2)^{\text{noisefree}}$$
$$= \left|\nabla_D C_R(k_1, k_2)\right|^L \cap \left|\dot{\nabla}_D C_R(k_1, k_2)\right|^L \cap \left|\ddot{\nabla}_D C_R(k_1, k_2)\right|^L \cup \left|\nabla_D C_R(k_1, k_2)\right|^S \cap \left|\dot{\nabla}_D C_R(k_1, k_2)\right|^S \cap \left|\ddot{\nabla}_D C_R(k_1, k_2)\right|^S. \tag{4}$$

The sign $\nabla_D C_R(k_1, k_2)$ is the basic gradient value (for the red component); $\dot{\nabla}_D C_R(k_1, k_2)$ and $\ddot{\nabla}_D C_R(k_1, k_2)$ are the two related gradient values in the direction D. The fuzzy sets *large* and *small* are denoted as $|\cdot|^L$ and $|\cdot|^S$, respectively.

The fuzzy gradient (derivative) value regarding the noisy red component of a center pixel, $\nabla_D^F C_R(k_1, k_2)$ can also be defined using a fuzzy set *large*, *small*, *big positive* and *big negative*, denoted as $|.|^L$ and $|\cdot|^S$, respectively.

$$
\begin{aligned}
&\nabla_D^F C_R(k_1, k_2)^L \\
&= \left|\nabla_D C_R(k_1, k_2)\right|^L \cap \left|\dot{\nabla}_D C_R(k_1, k_2)\right|^S \cup \left|\nabla_D C_R(k_1, k_2)\right|^L \\
&\quad \cap \left|\ddot{\nabla}_D C_R(k_1, k_2)\right|^S \cup \left|\nabla_D C_R(k_1, k_2)\right|^{BP} \cap \left(\dot{\nabla}_D C_R C_R(k_1, k_2) \cap \ddot{\nabla}_D C_R(k_1, k_2)\right)^{BN} \\
&\quad \cup \nabla_D C_R C_R(k_1, k_2)^{BN} \cap \left(\dot{\nabla}_D C_R C_R(k_1, k_2) \cap \ddot{\nabla}_D C_R(k_1, k_2)\right)^{BP}.
\end{aligned}
\tag{5}
$$

Further details on the formulation of these fuzzy sets can be found in [27].

Using fuzzy rules, the red component of a central pixel $C_R(k_1, k_2)$ can therefore be identified as being corrupted with impulse noise, if more than half of the fuzzy gradient values (more than four for a nonborder placed pixel) are part of a $\alpha \in (0, 1]$ (weak) level of the fuzzy set *large* [28]. The application of local directional gradients using fuzzy logic to detect an outlier pixel and calculate the outputs of such a fuzzy filter is also discussed by [9].

The fuzzy derivative method mentioned above can be used to achieve perform uniformly distributed (random valued) impulse noise detection [26, 27]. Another approach for identifying random valued impulse noise pixels is to investigate the state of the neighborhood around a pixel. The detection process requires the construction of suitable fuzzy sets' *noise* for each color component at each position of an image [26, 27]. This method achieves random valued impulse noise detection.

In the current method, the mean difference in a $H \times S$ window denoted as $g(k_1, k_2)$ is calculated:

$$
g(k_1, k_2) = \frac{\sum_{h=-H}^{H} \sum_{s=-S}^{S} \left|\mathbf{x}(k_1 + h, k_2 + s) - \mathbf{x}(k_1, k_2)\right|}{(2H + 1)(2S + 1) - 1}.
\tag{6}
$$

Corrupted impulse noise pixels generally cause large $g(k_1, k_2)$ values because impulse noise pixels normally occur as outliers in a small neighborhood around the pixel. On the other hand, the $g(k_1, k_2)$ value could be relatively large in the case of an edge pixel. Therefore, the following two values denoted as $\mathrm{obs}_1(k_1, k_2)$ and $\mathrm{obs}_2(k_1, k_2)$ are considered:

$$
\mathrm{obs}_1(k_1, k_2) = \frac{\sum_{h=-H}^{H} \sum_{s=-S}^{S} g(k_1 + h, k_2 + s)}{(2H + 1)(2S + 1)},
\tag{7}
$$

$$
\mathrm{obs}_2(k_1, k_2) = g(k_1 + h, k_2 + s).
\tag{8}
$$

If both values $\mathrm{obs}_1(k_1, k_2)$ and $\mathrm{obs}_2(k_1, k_2)$ are large, then the pixel can be considered as an edge pixel instead of a noisy one. So, when the two values $\mathrm{obs}_1(k_1, k_2)$ and $\mathrm{obs}_2(k_1, k_2)$ are very similar, it is concluded that the pixel is noise free. Otherwise, if the difference between $\mathrm{obs}_1(k_1, k_2)$ and $\mathrm{obs}_1(k_1, k_2)$ is large, then the pixel is considered as noisy.

Agrawal et al. [29] conducted fuzzy derivative and fuzzy smoothing based on fuzzy rules, which make use of membership functions for removal of narrow-tailed and medium narrow-tailed noise in medical images. Iteratively applying the filter significantly reduces background noise. The form of the membership functions is modified depending on the residual level of noise following every iteration, taking use of the image's homogeneity distribution. A statistical model for noise distribution may be used to connect the homogeneity of the membership functions to their adaptation method. Experiments are conducted to demonstrate the practicality of the suggested technique. Additionally, these findings are compared to those obtained from other filters using numerical metrics and ocular examination.

In addition, Ma et al. [4] proposed an improved version of the partition filter that takes advantage of partition-based trimmed vector median, instead of center-weighted vector median as a fuzzy reference estimate can be considered. Partition-based trimmed vector median is different from center-weighted trimmed vector median in that the latter replaces the threshold value of center-weighted trimmed vector median with $(N - 1)/2$. The resultant algorithm of this improved version of the fuzzy partition filter simplifies computation and adapts well to the local properties of image structures.

As an important extension of fuzzy derivative, the fuzzy nth-order derivative and fuzzy differential equations of fractional order using Laplace and integral transforms are investigated by Ahmadi et al. [30] and Salahshour et al. [31], respectively. The most important advantage of this fuzzy differential procedure is the significantly reduced computational complexity in dealing with the fractional/nth-order derivative.

3. Membership Function

One of the most difficult aspects of designing fuzzy systems is generating appropriate fuzzy variables' membership functions [32]. A fuzzy constraint to single parameter is normally defined by a fuzzy membership function with values within [0,1] [33]. Each response input and output has a unique membership function.

Generally, the membership function $\mu_{\mathscr{A}}(x)$ describes the membership of the elements x of the base set $\mathscr{X}$ in the fuzzy set $\mathscr{A}$, whereby for $\mu_{\mathscr{A}}(x)$ a large class of functions can be taken assumed. In other words, a fuzzy set is formed on the basis of a membership function that generates the membership degree [34]; this enables the progressive evaluation of the membership of set components [35].

Membership functions with reasonable membership are typically piecewise linear functions, including trapezoidal or triangular functions. Certain applications require continuously differentiable curves and, consequently, smooth transitions. Smoothness is often achieved using Gaussian and other bell-shaped membership functions. In addition, for certain applications, it is also important to define asymmetric membership functions. Asymmetric and closed sigmoidal membership functions can be generally synthesized using two sigmoidal functions.

For many other applications, these membership functions mentioned above are insufficient because they are not accurately representative of the linguistic terms being modelled; thus, they must be elicited directly from experts, either through a "statistical" way or through an automatic generation of specific pass- and reject-band filter shapes. This is an emergent topic in the current artificial intelligence literature, as the aim is to develop automated fuzzy inference engines. Before discussing such approaches, however, it is worthwhile to consider traditional (manual) approaches.

3.1. Similarity Measurements. Consideration of membership values as similarity indicators is typically utilized in prototype theory, where membership is defined as the state of being similar to a category's representative [36]. Therefore, a membership function value may be utilized to measure an element's degree of resemblance to a given set [22].

3.1.1. Adaptive Color Pixel Similarity Function. Based on [7], in robust signal processing, sample rank ordering is often utilized. Recent breakthroughs in fuzzy set theory have integrated sample rank ordering in the temporal domain or the spatial ordering of observations [37–41]. Given two color pixels, x and y, there exists a wide range of functions [5, 17, 38, 42, 43], $\mu(x, y)$, which can be used to assess their physical similarity and meet the constraints of a fuzzy membership function; that is,

(i) $\mu(\mathbf{x}, \mathbf{y}) \longrightarrow 1$ if $\|\mathbf{x} - \mathbf{y}\| \longrightarrow 0$

(ii) $\mu(\mathbf{x}, \mathbf{y}) \longrightarrow 0$ if $\|\mathbf{x} - \mathbf{y}\| \longrightarrow \infty$

(iii) $\mu(\mathbf{x}_1, \mathbf{y}_1) \geq \mu(\mathbf{x}_2, \mathbf{y}_2), \forall \|(\mathbf{x}_1 - \mathbf{y}_1) \geq \|\mathbf{x}_2 - \mathbf{y}_2\|$

The objective is to choose an acceptable Gaussian function to express similarities between two color pixels, which is facilitated by the exponential nature of perceptual distance measurements [5, 44]. The ideal sample spread associated with each kind of Gaussian function may be determined using the mean absolute error (MAE) criteria as described in [45]. Additionally, in [7, 46], a resolution to noise deviation estimates is proposed. This strategy is used in

[7], which compares two different forms of Gaussian functions. The first is a scalar Gaussian function μ_1 based on the vectors' Euclidean distance, and the second is a vector of component-wise Gaussian functions μ_2 in the YCbCr or RGB color space. Compared to the simpler μ_1 scalar function, the μ_2 function provides additional flexibility in modelling the similarity membership, but its performance in various color spaces is weak in the RGB space, running a risk of an expensive computation cost due to its component-wise sample spread. As new expanded color spaces are introduced by industry, this can be an interesting approach.

3.1.2. A Self-Adaptive Algorithm. A new way of defining the similarity function is introduced in [17]. There is an attempt to achieve nonascending, *convex* similarity measures, with the use of a natural normalization of the similarity function, satisfying $\mu(0) = 1$, $\mu(\infty) = 0$.

The *convex* membership functions for the similarity measures can be treated as kernels of nonparametric density estimation, as illustrated in [17, 47, 48]. The expression in (10) is shown to be particularly effective as discussed in [17, 49, 50].

$$\mu(\mathbf{x}_i, \mathbf{x}_j) = \begin{cases} 1, & -\dfrac{\rho(\mathbf{x}_i, \mathbf{x}_j)}{h} \text{ for } \rho(\mathbf{x}_i, \mathbf{x}_j) < h, \\ \\ 0, & \text{otherwise,} \end{cases} \tag{9}$$

where $\rho\{\mathbf{x}_i, \mathbf{x}_j\} = \|\mathbf{x_i} - \mathbf{x_j}\|$.

The parameter h is determined on the basis of the image structure and noise statistics. It influences the severity of the filtering process so that a decreasing function of h related to the fraction of pixels is replaced. Compared with the vector median filter (VMF), corresponding to $h = 0$, the resultant filter shows enhanced performance. Performance can be tuned by specifying positive values of h, compelling the filter to maintain uncorrupted original pixels to a greater or lesser extent, while still enabling the removal of corrupted ones.

Using the $\mathbf{L}_2$ norm of the Euclidean distance between two pixels in the RGB color space, it is possible to estimate the fraction of corrupted pixels. Thus, among eight neighboring pixels around a center pixel, there exists at least m pixels that have a $\mathbf{L}_2$ norm less than a predefined constant d.

3.1.3. Fuzzy Color Correlation. An alternative approach to traditional vector-based approaches is the idea by [51], which achieves similarity measurements in each color component between the central pixel $\mathbf{x}_0$ and each color neighbour $\mathbf{x}_k$, separately, the approach also assesses whether the local differences in one, for example, the *R* component, neighborhood corresponds to the differences found in the *G* and *B* components. We denote these two memberships with S_1 and S_2.

The aim is to first to develop membership function that may be used to check these differences of neighbor component, which can be represented through a fuzzy set *small*.

$$1 - S(x) = S_1 = \begin{cases} 1, & x \leq \alpha_1, \\\\ 1 - 2\left(\dfrac{x - \gamma_1}{\gamma_1 - \alpha_1}\right)^2, & \alpha_1 < x < \dfrac{\alpha_1 + \gamma_1}{2}, \\\\ 2\left(\dfrac{x - \gamma_1}{\gamma_1 - \alpha_1}\right)^2, & \dfrac{\alpha_1 + \gamma_1}{2} < x < \gamma_1, \\\\ 0, & x > \gamma_1, \end{cases} \tag{10}$$

where $\alpha_1 = 10$ and $\gamma_1 = 70$ can achieve experimentally satisfying results of noise filtering. The second item element of equation (10) shows a large membership degree with a relatively small difference and a slow decrease in the membership degree. The third item element is a parameter used to decrease the membership degree faster for each larger difference after a certain point. As a result, the membership function defined in equation (10) is also utilized to calculate the absolute value of the membership degree differences in the fuzzy set S_1 for the green and red components, as well as the blue and red components. If one denotes the relevant membership function as S_2, the membership function equation (10) is calculated, with $\alpha_1 = 0.01$ and $\gamma_1 = 0.15$.

A further interest in this work is that it enables the identification of noise-free center pixels in a different color channel. The noise-free degree of x_0^R, denoted as $NF_{x_0^R}$, is calculated as follows by utilizing the product triangular norm representing both the fuzzy OR (disjunction) operator and the fuzzy AND (conjunction) operator.

$$NF_{x_0^R} = \mu^R \mu^{RG} \mu^G + \mu^R \mu^{RB} \mu^B - \mu^R \mu^{RG} \mu^G \mu^R \mu^{RB} \mu^B, \tag{11}$$

where the standard negation operation is used to derive the membership degree in the fuzzy set *noise free* for each color component. Here, μ^R and μ^{RG} are the conjunction of $S_1(\Delta F_k^R)$ and μ_k^{RG} in the distance measurement of a red component and the difference between the membership degrees in the fuzzy set S_1 for the red and the blue components. A similar computation can be performed for the other color components. The noise-free degrees of blue $NF_{x_0^B}$ and green $NF_{x_0^G}$ components of the center pixel can thus be achieved.

3.2. Histogram-Based Approaches.

In order to establish connections among different smaller membership functions, in [52], it is proposed to calculate the slope difference of each selected intensity value from a color image. This approach uses the histogram approach described earlier to establish a separate membership function (denoted as $\mu_{\text{noise}_{p^k}}$). Given each selected integer value p^k, the membership function can be expressed as follows:

$$\mu_{\text{noise}_{p_k}} \begin{cases} 0, & (\forall x \leq a_k) \text{ or } (\forall x \geq d_k), \\\\ 2\left(\dfrac{x - a_k}{b_k - a_k}\right)^2, & \forall x \in \left(a_k, \dfrac{a_k - b_k}{2}\right], \\\\ 1 - 2\left(\dfrac{x - b_k}{b_k - a_k}\right)^2, & \forall x \in \left(\dfrac{a_k + b_k}{2}, b_k\right), \\\\ 1, & \forall x \geq [b_k, c_k], \\\\ 1 - 2\left(\dfrac{x - c_k}{d_k - c_k}\right)^2, & \forall x \in \left(c_k, \dfrac{c_k + d_k}{2}\right], \\\\ 2\left(\dfrac{x - d_k}{d_k - c_k}\right)^2, & \forall x \in \left(\dfrac{c_k + d_k}{2}, d_k\right). \end{cases} \tag{12}$$

The membership function *impulse noise* (for the red component) μ_{impulse}^R then becomes

$$\mu_{\text{impulse}}(C_R(k_1, k_2)) = \max_{k \in \{1, \dots, n\}} \mu_{\text{noise}/p_k}(C_R(k_1, k_2)). \tag{13}$$

The parameters used in expression (13) are related to the slope of each the selected intensity value. There exist two different types of noise histograms. The histograms containing only peaks normally have a very small slope and the histograms containing peaks with some other features normally have a larger slope. These are treated as a relation with the low estimated standard deviation and large estimated standard deviation, respectively. Based on the edge image produced by the Sobel operator [53], the following expressions are proposed to calculate these parameters:

$$a_k = p^k - \vartheta_a,$$
$$b_k = p^k - \vartheta_b,$$
$$c_k = p^k + \vartheta_c,$$
$$d_k = p^k + \vartheta_d,$$
$$\vartheta_b = \frac{2}{3\vartheta_a}, \tag{14}$$
$$\vartheta_c = \frac{2}{3\vartheta_d}$$
$$\vartheta_a = \vartheta_d = \min(25, \lfloor \sigma \rfloor),$$

where $\lfloor \sigma \rfloor$ is the largest integer value that is smaller than the standard deviation (variance) σ. This method of parameter selection is especially well suited for denoising pictures that have been damaged by a combination of impulse and Gaussian noise. When $\lfloor \sigma \rfloor > 20$, to prevent overfiltering, ϑ_a and ϑ_d are then restricted to be a value of 20. Further

discussion regarding the histogram based methods can be found in [26].

Based on [26], with existing fixed-value impulse noise, histograms are initially created from most likely corrupted impulse noise color components. Since pixels that have been damaged by fixed-value impulse noise are often very dissimilar to their neighbors, they are usually identified in a local window by their minimum and maximum intensity values, denoted as p_{max} or p_{min}. In order to calculate histograms for each image component, a two-step process is involved: (a) the corrupted greyscale images are divided into small blocks from each color channel, with a suggested block size of 5×5; and (b) the determination of the values of the two intensity levels p_{max} or p_{min} to be adopted for the calculation of the histogram depends on the following conditions being simultaneously satisfied:

(i) If p_{max} is involved, then $|m_1 - p_{max}| > |m_1 - m_2|$ or $|m_2 - p_{max}| > |m_1 - m_2|$

(ii) If p_{min} is involved, then $|m_1 - p_{min}| > |m_1 - m_2|$ or $|m_2 - p_{min}| > |m_1 - m_2|$

(iii) Defining the membership degrees $\mu^{noise}(p_R)$ for the intensity value p_R^k of a red component in the fuzzy set *noise*, if $(h_R^{noise}(k)/\sum_{l=0}^{255} h_R^{noise}(l))$, then k is a noise red intensity

In the case of fixed-value impulse noise, at least a single intensity value with a membership degree of one in the fuzzy set *noise* is anticipated; or else, the picture is not damaged by fixed-value impulse noise. The random valued impulse noise detection technique does not need to be used in this circumstance.

In the case of a random valued impulse noise, the color difference, between, for example, the red and green components, in each direction D of this window around the center position is calculated and denoted as ϱ_{RG}^D. For each color difference ϱ_{RG}^D, $D \in [1, 8]$, bell-shaped membership functions are defined as η_{small}, η_{medium}, and η_{large} that represent the degree of membership in the corresponding fuzzy sets *small*, *medium*, and *large*:

$$\eta_{small}\left(\varrho_{RG}^D\right) = \begin{cases} 1, & \text{if } \varrho_{RG}^D \leq c_1, \\ \dfrac{1}{1 + \left(\varrho_{RG}^D - c_1/a_1\right)^2 b_1}, & \text{if } \varrho_{RG}^D > c_1 k = 1, 2, \ldots, 9. \end{cases}$$

$$\eta_{medium}\left(\varrho_{RG}^D\right) = \dfrac{1}{1 + \left(\varrho_{RG}^D - c_2/a_2\right)^2 b_2}, \quad k = 1, 2, \ldots, 9,$$

$$\eta_{small}\left(\varrho_{RG}^D\right) = \begin{cases} \dfrac{1}{1 + \left(\varrho_{RG}^D - c_3/a_3\right)^2 b_3}, & \text{if } \varrho_{RG}^D \leq c_3 k = 1, 2, \ldots, 9, \\ 1, & \text{if } \varrho_{RG}^D > c_3. \end{cases}$$

(15)

Histogram adaptive filtering in [54, 55] is applied to achieve a solution to the parameter space. The parameters $b1 = b2 = b3 = 17$ are adopted and experimentally validated. They are set to be excessively larger than c_1, c_2, and c_3, respectively, in order to adaptively filter out impulsive noise by the membership functions. The calculation of the parameters $(a1, c1)$, $(a2, c2)$, and $(a3, c3)$ takes advantage of statistics of the estimated histograms, in relation to intensity differences between red and green values. The calculation of the parameters for the other color differences is very similar. The following calculations of fuzzy sets regarding centroids *small* (denoted as CEN_{small}^{RG}), *medium* (denoted as CEN_{medium}^{RG}), and *large* (denoted as CEN_{large}^{RG}) are the functions of the total histogram h_{RG}, and two divided histograms $P\,DF_{part_1}^{RG}$ and $P\,DF_{part_2}^{RG}$ by the splitting point $M = [2(2^m - 1) \cdot CEN_{medium}^{RG} - (2^m - 1)]$, where $[x]$ is the largest integer value smaller than x.

$$PDF^{RG}(z) = \frac{h_{RG}(z)}{\sum_{k=-(2^m-1)}^{2^m-1} h_{RG}(k)},$$

$$CEN_{medium}^{RG}(z) = \sum_{k=-(2^m-1)}^{2^m-1} \frac{k}{2^{m+1} - 1} P\,DF_{RG}(k), \quad CEN_{small}^{RG}(z) = \sum_{k=-(2^m-1)}^{M} \frac{k}{2^{m+1} - 1} P\,DF_{part1}^{RG}(k), \quad CEN_{large}^{RG}(z) = \sum_{k=M+1}^{2^m-1} \frac{k}{2^{m+1} - 1} P\,DF_{part2}^{RG}(k),$$

(16)

where $P\,DF_{RG}(z)$ is the potential density function of the histogram h_{RG} for index z ($z \in [-(2m - 1), 2m - 1]$) (with m being the amount of bits used to store a single intensity value (mostly $m = 8$)). The index k varies from 1 to $H \times S$ in order to select one of the window values.

The calculation of the mass that corresponds to the support of a fuzzy set is a function of the subdivided histogram h_{RG} with three equal parts.

$$MASS_{small}^{RG} = \frac{\sum_{k=-(2^m-1)}^{M_1} h_{RG}(k)}{\sum_{k=-(2^m-1)}^{2^m-1} h_{RG}(k)},$$

$$MASS_{medium}^{RG} = \frac{\sum_{k=M_1+1}^{M_2} h_{RG}(k)}{\sum_{k=-(2^m-1)}^{2^m-1} h_{RG}(k)},$$

(17)

$$MASS_{large}^{RG} = \frac{\sum_{k=M_2+1}^{2^m-1} h_{RG}(k)}{\sum_{k=-(2^m-1)}^{2^m-1} h_{RG}(k)},$$

where $M_1 = [2(2^m - 1) \cdot \text{CEN}_{\text{medium}}^{\text{RG}} + \text{CEN}_{\text{small}}^{\text{RG}}/2 - (2^m - 1)]$ and $M_2 = [2(2^m - 1) \cdot (\text{CEN}_{\text{medium}}^{\text{RG}} + \text{CEN}_{\text{large}}^{\text{RG}}/2) - (2^m - 1)]$.

The values MASS and CEN obtained from the estimated histogram h_{RG} are, respectively, used for the parameters a and c, with $c_1 = \text{CEN}_{\text{SMALL}}^{\text{RG}}$, $c_2 = \text{CEN}_{\text{MEDIUM}}^{\text{RG}}$, $c_3 = \text{CEN}_{\text{LARGE}}^{\text{RG}}$ and $a_1 = \text{MASS}_{\text{SMALL}}^{\text{RG}}$, $a_2 = \text{MASS}_{\text{MEDIUM}}^{\text{RG}}$, $a_3 = \text{MASS}_{\text{LARGE}}^{\text{RG}}$. Thus, the membership functions are completely specified.

The procedure of the histogram estimation h_{RG} can be used to estimate the histograms of all the other color differences (red-green, red-blue, and green-blue). The histogram estimation ranges between −255 and +255. Each red-green difference (i.e., $RG(i, j)$), for example, is included in the histogram h_{RG} if and only if the membership degree in the fuzzy set noise for both components is zero, in other words if $\mu_{\text{noise}}(C_R(i, j)) = 0$ and $\mu_{\text{noise}}(C_G(i, j)) = 0$.

The fuzzy set noise μ_{noise} is represented by a membership degree as follows:

$$\mu_{\text{noise}}(C_R(i, j)) = \begin{cases} \eta_{\text{noise}}(C_R(i, j)), & \text{if cond}_1, \\ 0, & \text{otherwise}, \end{cases} \qquad (18)$$

with

$$\text{cond}_1 = \sum_{D \in \{N, \ldots, S\}} \tau_{\text{noise}}^D \geq \tau_{\text{free}}^D. \qquad (19)$$

The overall membership degrees to the fuzzy sets $\tau_{\text{noise}}^D(C_R(i, j))$ and $\tau_{\text{noise}}^D(C_R(i, j))$ are calculated on the basis of the eight membership degrees in the relevant fuzzy sets impulse noise-free for the eight directions around a certain central pixel position (i, j), respectively. The membership function of a fuzzy set $\tau_{\text{noise}}(C_R(i, j))$ is illustrated in Figure 2. The parameters a and b are equal to

$$a = \frac{\left(\sum_{h=-H}^{H} \sum_{s=-S}^{S} g(k_1 + h, k_2 + s)\right) - g(k_1, k_2)}{(2H + 1)(2S + 1) - 1}, \qquad (20)$$

where g satisfies (6).

$$b = 1.2a. \qquad (21)$$

The standard negator $N_s(x) = 1 - x$ is used to calculate a fuzzy set impulse noise-free.

If cond_1 is satisfied, the membership function $\eta_{\text{noise}}(C_R(i, j))$ has a similar shape to Figure 2, but with $\min_{h \in \{-H, \ldots, H\}; s \in \{-S, \ldots, S\}} g(i + h, j + s)$. This is used to define a central pixel $C_R(i, j)$ with fuzzy set large, and define η_{noise}; that is, $\eta_{\text{noise}}(C_R(i, j)) = \mu_{\text{large}}(\text{obs}_1 - \text{obs}_2)$. In this figure, the horizontal axis corresponds to all possible differences between obs_1 and obs_2. Detailed explanation regarding $(\text{obs}_1 - \text{obs}_2)$ can be found in equations (7) and (8).

The most homogeneous region around $C_R(i, j)$ results in the $g(i + k, j + l)$ value, which corresponds to a. This region has the smallest amount of impulse-noise corrupted pixels. Experimental results have shown that the best choice for parameter b is $b = 1.2a$, the larger the parameter a is, the larger the uncertainty interval (a, b) should be.

Several fuzzy rules are used in the aforementioned algorithm:
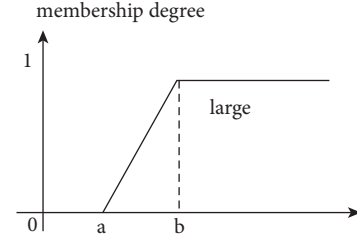
Figure 2: Illustration of the membership function large.

(i) Membership degrees for the elements ϱ_{RG}^D in the fuzzy set noise-free:

IF (C_{RD} is not noise) AND ((C_{RD} is not noise) THEN ϱ_{RG}^D is noise-free

(i) A corrupted central pixel $C_R(i, j)$ with impulse noise:

IF $\text{obs}_1 - \text{obs}_2$ is large

THEN the central pixel $C_R(i, j)$ is an impulse noise pixel

Two additional fuzzy rules related to the central pixel $C_R(i, j)$ that is defined as an impulse noise and impulse free pixel in the direction D are represented in equations (3) and (4). The other two noise-corrupted color channels have analogous fuzzy rules. The second fuzzy rule can be transferred used to calculate the third via fuzzy rule from the evaluation of the relevant histograms.

Histogram-based fuzzy color filter is particularly effective for reducing high-impulse noise in digital images while preserving edge sharpness. Different from applying a greyscale algorithm on each color component separately, vector-based filtering methods can overcome artefacts introduced especially on edge or texture pixels when dealing with noisy color images [26]. The major improvement achieved by the histogram-based fuzzy color filter (HFC) is demonstrated in Figure 3. This figure illustrates the visual performance of a magnified part of the "Lena" image with 20% salt-and-pepper noise. It is clearly observed that HFC shows the best performance in the noise removal and detail preservation; meanwhile, it does not introduce new colors (especially in texture elements of an image) in contrast to many of the compared filters, including the fuzzy impulse noise detection and reducing method (FIDRM), the adaptive-weighted fuzzy mean filter (AWFM) from [56], the histogram adaptive fuzzy filter (HAF), dual-step fuzzy inference ruled by else-action filter (DSFIRE) [57], the tristate median filter (TSM) from [58], and vector mean filter (VMF). An objective evaluation is performed using the peak signal-to-noise ratio (PSNR) (Figure 4).

3.3. Fuzzy Peer Group-Based Algorithms. Following the traditional peer group filters, the authors in [59] claim that traditional methods adopt crisp ways to calculate distance threshold d; however, the similarity measurements are not that easy. Furthermore, the number of peer group members is determined using Fisher's linear discriminant (FLD), which often turns out not to be a desired peer group since

(a)

(b)

(c)

(d)

(e)

(f)
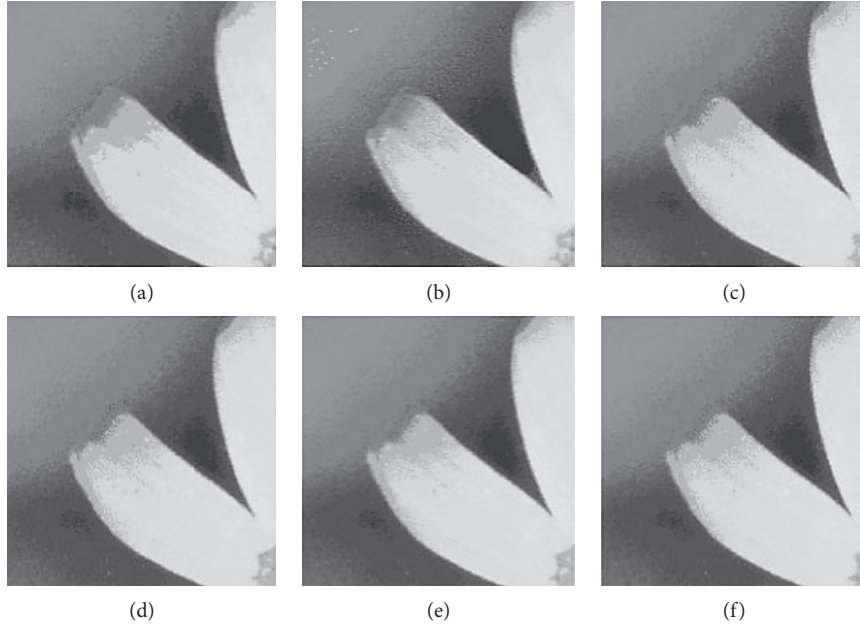
FIGURE 3: (a) Original image, (b) classical error diffusion (MSE = 67.4), (c) fuzzy error diffusion (MSE = 48.3), (d) L-filter with common memberships (MSE = 50.5), (e) L-filter with four fixed membership values (0.82, 0.14, 0.03, and 0.01) (MSE = 49.8), and (f) L-filter with two fixed membership values (0.85 and 0.15) (MSE = 51.8) [65].

(a)

(b)

(c)

(d)

(e)

(f)

(g)

(h)

(i)
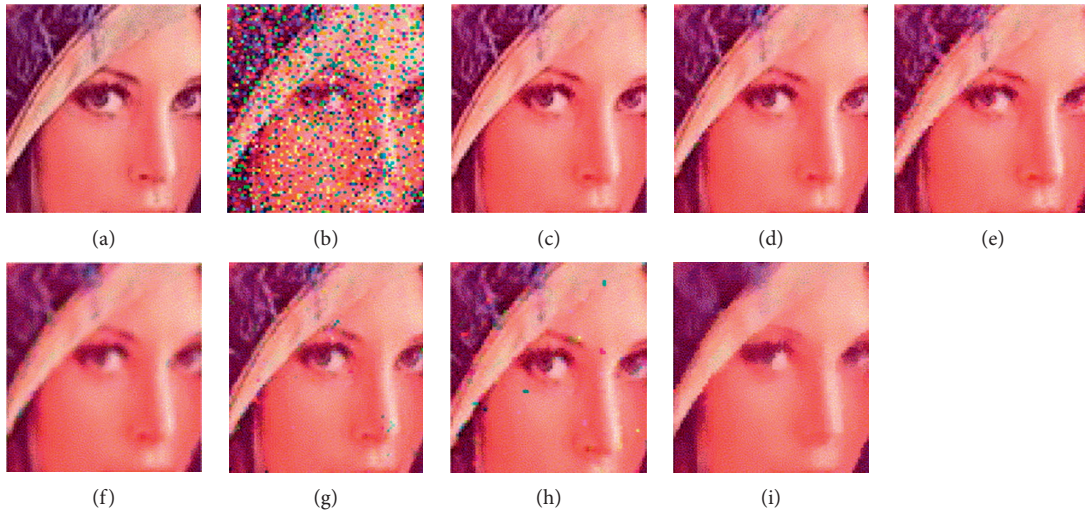
FIGURE 4: From top left to bottom right, (a) a part of the original colored Lena image and (b) the part corrupted with 20% salt-and-pepper noise (PSNR: 12.29). (c) After the proposed HFC (PSNR: 46.84). (d) After the FIDRM (PSNR: 34.97). (e) After the AWFM (PSNR: 30.58). (f) After the HAF (PSNR: 29.19). (g) After the DSFIRE (PSNR: 30.75). (h) After the TSM (PSNR: 28.05). (i) After the VMF (PSNR: 29.12) [26].

more than the necessary number of clusters is always obtained.

To overcome this problem, a similarity membership function μ is introduced:

$$\mu_1\left(\mathbf{x}_i, \mathbf{x}_j\right) = e^{-\left(\|\mathbf{x}_i - \mathbf{x}_j\|/\Psi\right)}, \quad \text{for } i, j = \left\{0, \ldots, n^2 - 1\right\}, \quad (22)$$

where $\Psi > 0$ is a fuzzy matrix [60, 61], and $\mu_1 = 1$ if $\mathbf{x}_0 = \mathbf{x}_{(i)}$ so that

$\mu_1\left(\mathbf{x}_0, \mathbf{x}_{(0)}\right) \geq \mu_1\left(\mathbf{x}_0, \mathbf{x}_{(1)}\right) \geq \cdots \geq \mu_1\left(\mathbf{x}_0, \mathbf{x}_{(n^2-1)}\right)$. And an accumulated similarity (fuzzy distance) metric $d_{\text{PG}}\left(\mathbf{x}_0, \mathbf{x}_{(i)}\right)$ between $\mathbf{x}_0$ and $\mathbf{x}_i$ is used:

$$d_{\text{PG}}\left(\mathbf{x}_0, \mathbf{x}_{(i)}\right) = \sum_{k=0}^{i} \mu_1\left(\mathbf{x}_0, \mathbf{x}_{(k)}\right), \quad \text{for } i = \left\{0, \ldots, n^2 - 1\right\},$$

$$(23)$$

where $1 \leq d_{\text{PG}}\left(\mathbf{x}_0, \mathbf{x}_{(i)}\right) \leq n^2$, for $i = \left\{0, \ldots, n^2 - 1\right\}$.

A fuzzy set *large* $(\cdot)^{\mathscr{L}}$ is used to represent the fuzzy variable $d_{\text{PG}}(\mathbf{x}_0, \mathbf{x}_{(i)})$ *large*:

$$
\begin{aligned}
\left(d_{\text{PG}}\left(\mathbf{x}_0, \mathbf{x}_{(i)}\right)\right)^{\mathscr{L}} &= \mu_2\left(d_{\text{PG}}\left(\mathbf{x}_0, \mathbf{x}_{(i)}\right)\right) \\
&= -\frac{1}{\left(n^2 - 1\right)^2}\left(d_{\text{PG}}\left(\mathbf{x}_0, \mathbf{x}_{(i)}\right) - 1\right) \\
&\quad \times \left(\left(d_{\text{PG}}\left(\mathbf{x}_0, \mathbf{x}_{(i)}\right) - 2n^2 + 1\right)\right), \\
&\quad \text{for } i = \left\{0, \ldots, n^2 - 1\right\}.
\end{aligned}
\tag{24}
$$

In order to better distinguish between noisy and noise-free pixels, it is more appropriate in establishing peer group cardinality differences. A quadratic function is normally used as it shows sensitivity in low values of cardinality more than in the high values. In the determination of membership function, there is no need to adjust further the parameter of the membership function.

A further idea discussed in that work is to calculate the parameter r of the *peer group* of the filter using fuzzy logic. So, the best number of members $\tilde{r}$ corresponds to the value $r = \{0, \ldots, n^2 - 1\}$ that maximizes the certainty of the resulting expression. By using the product T-norm as the conjunction operator, the certainty $\mathscr{C}_{(r)}$ of r that corresponds to the best number of members for $\mathscr{P}(\mathbf{x}_0, r, d)$ satisfies the following fuzzy reasoning argument:

$$
\mathscr{C}_{(r)} = \mu_1\left\{\mathbf{x}_0, \mathbf{x}_{(r)}\right\}\left(d_{\text{PG}}\left(\mathbf{x}_0, \mathbf{x}_{(r)}\right)\right)^{\mathscr{L}},
\tag{25}
$$

where $\mathscr{C}_{(r)}$ represents the certainty of "$\mathbf{x}_0$ is similar to $\mathbf{x}_{(r)}$"; $\mu_1\left\{\mathbf{x}_0, \mathbf{x}_{(r)}\right\}$ represents the extent to which the farthest pixel in $\mathscr{P}(\mathbf{x}_0, r, d)$ is similar to the center pixel $\mathbf{x}_0$; and $\left(d_{\text{PG}}\left(\mathbf{x}_0, \mathbf{x}_{(i)}\right)\right)^{\mathscr{L}}$ gives the certainty of "$\left(d_{\text{PG}}\left(\mathbf{x}_0, \mathbf{x}_{(r)}\right)\right)$ is *large*". The best number $\tilde{r}$ of members for $\mathscr{P}(\mathbf{x}_0, r, d)$ is given by the function

$$
\tilde{r} = \underset{r \in \omega}{\arg\max}, \quad \text{for } \omega = \left\{1, \ldots, n^2 - 1\right\}.
\tag{26}
$$

This reasoning is used to check for each value r, whether the increment from $\left(d_{\text{PG}}\left(\mathbf{x}_0, \mathbf{x}_{(r-1)}\right)\right)$ to $\left(d_{\text{PG}}\left(\mathbf{x}_0, \mathbf{x}_{(r)}\right)\right)$ is sufficiently large to include in the fuzzy peer group. Since the proposed method allows the operator to ignore the number of clusters in the particular neighborhood, which are always the results from Fisher's linear discriminant approach, this is in its essence a statistics based algorithm for designing peer group filters.

Finally, the fuzzy peer group is formulated by a similarity fuzzy set $f\mathscr{P}(\mathbf{x}_0, \mathbf{x}_{(i)}) = \mu_1\left(\left\{\mathbf{x}_0, \mathbf{x}_{(i)}\right\}\right)$, with peer group members $\mathbf{x}_{(0)}, \mathbf{x}_{(1)}, \ldots, \mathbf{x}_{(\tilde{r})}$.

For summarization, membership functions characterize the fuzzy sets. In a fuzzy logic system (FLS), membership functions are associated with terms that appear as the antecedents or the consequences of fuzzy rules. FLS is one of the tools used to model a multi-input, multioutput system. Type-1 membership functions have been the focus in this paper.

One important issue is the derivation of membership functions that achieve fuzzy similarity measurements of the color pixels of an image. According to [7], the rank ordering

of samples approach is a good starting point. A Gaussian function may be used to describe the similarity between two color pixels; this approach is more commonly adopted mainly due to its extensive use in fuzzy ranked filters.

Another way of evaluating the similarity function is introduced by [17]. A number of *convex* membership functions for evaluating the degree of similarity have been introduced in their works. A simple linear similarity function with parameter h is only required to be determined, which reflects the similarity of image structure. Compared to the vector median filter (VMF) approach, the resultant filter shows enhanced performance.

Exploring color similarity measurements is discussed in [51]. It is claimed that a membership function is applied to firstly achieve color component correlation; this includes both the Euclidean distance measurements associated with each color component and the measurements of the Euclidean distance difference from different pairs of color components.

As mentioned, histogram-based approaches have been developed to also derive membership functions. One interest is to link small membership function depending on slope varieties of each selected intensity value [52]. Another approach in [26] has the following two focal points: one is to establish a membership function with adaptation to a fixed-value impulse-noise, and the other is to establish a membership function to random-value impulse-noise. In the fixed-value impulse-noise case, the extreme values are compared with mean values for noise detection. For a random-value impulse-noise, the histogram algorithm achieves parameter estimation for membership function constructions.

4. Fuzzy Filters' Design

If a color pixel or component is considered noisy (not noise-free), it should be filtered or smoothed proportionally. The estimated value is computed using the information of its local neighbourhood or the other color components of the filtered pixel in order to better estimate the original value while preserving edge information without introducing color artefacts.

4.1. Proposed L-Filter. The work carried out by [62] presents a switching rule-based filter that can be switched between the identity filter (denoted as $\mathbf{y}_\xi$) and a modified L-filter design (denoted as $\mathbf{y}_{L_{\text{mod}}}$). Following the detecting method, this is utilized to calculate the ideal output for the pixel's intensity and color. The suggested filter is distinguished from most L-filters because it integrates just two pixels from the vector ordered set; this significantly decreases the time required for both output calculation and coefficient training. The following is the expression for the switching scheme filter.

$$
\mathbf{y}_i = \begin{cases} \mathbf{y}_\xi, & \text{if clean}, \\ \mathbf{y}_{L_{\text{mod}}}, & \text{otherwise}, \end{cases}
\tag{27}
$$

where $\mathbf{y}_i$ denotes the intermediate output with index i in a color image, corresponding to intensity or color. The

switching operation is finally carried out by a combination of the outputs between intensity $|v|$ and color θ with optimal magnitude and optimal direction:

$$\tilde{\mathbf{y}}_i = |v_i|\theta_i, \tag{28}$$

where

$$|v_i| = \left(y_{\mathrm{R}i}^2 + y_{\mathrm{G}i}^2 + y_{\mathrm{B}i}^2\right)^{1/2},$$
$$\theta_i = \cos^{-1}\left(\frac{y_{\mathrm{R}i} \cdot y_{\mathrm{G}i} \cdot y_{\mathrm{B}i}}{|v_i|}\right), \tag{29}$$

where $y_{\mathrm{R}i}$, $y_{\mathrm{R}i}$, and $y_{\mathrm{R}i}$ denote the red, green, and blue components of the intermediate pixel vector.

The suggested L-filter is constructed by combining two pixels from the vector median ordered set linearly.

$$\mathbf{y}_{\mathrm{L_{mod}}} = \sum_{i=1}^{2} c_i \tilde{\mathbf{y}}_{j_i}. \tag{30}$$

Here c_i corresponds to the ith coefficient in the vector median ordered set. The subscript j denotes the index of the pixel selected from the ordered set. For a $n \times n$ filter window with the center position at $C = (n \times n + 1)/2$, j_1 will be $C - 2$ and j_2 will be $C - 1$. In the calculation, the center pixel is considered to be noise from the detection result, without being included as a possible output.

The constrained least mean square (LMS) algorithm optimized the coefficients using a set of target and purposely distorted pictures supplied by the user [63]. Optimization is performed to reduce the direction and amount of the inaccuracy in the color and intensity values, respectively. For more details related to the LMS algorithm, one needs to refer to [63].

In [64], through the fuzzy model, an $l2 - l\infty$ filter has been constructed for nonuniformly sampled nonlinear systems. Compared with the classical filter (i.e., Kalman filter), the $l2 - l\infty$ filter is more applicable because the requested peak value of the estimation error for the external noise is less than a certain level that often requires to be satisfied. Hence, it shows the advantage of the fuzzy modelled filter in achieving a prescribed noise attenuation level.

While the error-diffusion dither produces a relatively high-quality image, it is computationally expensive. In [65], a new approach to error diffusion dithering through a fuzzy error diffusion algorithm is proposed. To speed up the fuzzy error diffusion process, an L-filter approach is developed by determining a fixed set of membership values. The fuzzy error diffusion algorithm is performed to achieve drastic improvements of color images quality, resulting in superior-quality dithered images and significantly lower mean squared error values (MSE). Figure 3(c) illustrates the result of fuzzy error diffusion and compares it with the classical approaches in Figures 3(d) and 3(e) along with classical error diffusion that has been used to produce the image in Figure 3(b). The original image is given in Figure 3(a). Color impulses are observed as white dots on uniformly gray colored regions. The result of the fuzzy error diffusion algorithm is given in Figure 3(c), where fuzzy error diffusion

reduces the occurrence of color impulses drastically. A significantly lower MSE value for the fuzzy error diffusion algorithm is 48.3 for Figure 3(c) versus 67.4 for Figure 3(b).

4.2. Fast Adaptive Similarity Filter. Considering the information associated with the central pixel, [17] proposed the design of nonlinear filters to establish similarity measures in a fast, adaptive manner on the basis of the correlation between the different image channels. The algorithm benefits from a lower computational complexity than that of the vector median filter.

Following Section 3.1.2, according to equation (9), a modified cumulative distance function R_k can be established:

$$R_k = \begin{cases} -h + \sum_{j=1}^{n} \rho\left(\mathbf{x}_k, \mathbf{x}_j\right), & \text{for } k = 0, \\ \sum_{j=1}^{n} \rho\left(\mathbf{x}_k, \mathbf{x}_j\right) & \text{for } k = 1, \ldots, n. \end{cases} \tag{31}$$

For convenience of representation, here we relabel the center pixel as $\mathbf{x}_0$ in this equation. The filter construction is quite similar to the standard VMF. The major difference is the omission of the central pixel $\mathbf{x}_0$ when calculating $\mathbf{x}_k$, $k > 0$.

The condition for retaining the original image pixel is $R_0 < R_k$, $k = 1, \ldots, n$, which leads to the condition

$$-h + \sum_{j=1}^{n} \rho\left(\mathbf{x}_0, \mathbf{x}_j\right) \leq \sum_{j=1}^{n} \rho\left(\mathbf{x}_k, \mathbf{x}_j\right). \tag{32}$$

That means

$$R_0 \leq R_k \, if \, h \geq \sum_{j=1}^{n} \left[\rho\left(\mathbf{x}_0, \mathbf{x}_j\right) - \rho\left(\mathbf{x}_0, \mathbf{x}_j\right)\right], \tag{33}$$

where $k = 1, \ldots, n$.

This technique, which is based on the basic leave-one-out strategy, is the new algorithm's most significant feature. The central pixel is only replaced when it is really noisy; this approach aims to preserve as much as possible the original information in the images.

As is commonly known, the VMF method has the problem of replacing an excessive number of uncorrupted picture pixels. This problem is addressed in the existing filter design by specifying positive h values, compelling the filter to retain as many uncorrupted, original pixels as possible while still allowing for the removal of corrupted ones. Additionally, h may be fine-tuned further based on noise statistics and image structure.

The filtering process follows three steps. (a) The fractions of corrupted pixels are estimated. As mentioned in Section 3.1.2, it is possible to find two "close" pixels among its eight neighbors and a filtered center located pixel, according to a predefined L_2 distance constant d and the number of pixels m within the distance range. Outside that distance range, the pixel is considered noisy. (b) An optimal value of h is found. Consequently, the constant h is established to the value that

results in the filter changing the same proportion of pixels as the predicted noise fraction p.

To quickly create a filter, the well-known bisection approach may be employed [66]. This approach permits the root of an equation $g(x) = 0$ in [a, b] to be determined, provided that $g(x)$ is continuous and $g(a)g(b) < 0$. In the case considered here,

$$g(h) = \lambda(h) - p, \tag{34}$$

where $\lambda(h)$ is the fraction of pixels changed by the filter, depending on h. For the majority of standard color images, a sufficiently long interval is considered as [0, 4], where $g(0)g(4) < 0$. (c) Filtering of an image using the obtained optimal value of h is subsequently performed. The algorithm incorporates the following steps: (1) Set $r := a$, $s := b$. (2) Set $z := (r + s)/2$. (3) If $g(z) = 0$, then output $\bar{\beta} = z$ and exit. In any other case, (a) if $g(z)g(r) < 0$, then set $s := z$ and go to 2. (b) If $g(z)g(r) > 0$, then set $r := z$ and go to 2. Although the described process may be of infinite length and may not give an exact value, it provides a sufficiently good approximation of $\bar{\beta}$, after a limited number of iterations.

4.3. Histogram-Based Fuzzy Color Filter. Referring to histogram adaptive filtering in [54, 55], the differences between intensity values in the different components can be transformed from the unit interval into the $[-(2m+1), +(2m+1)]$ interval for a real gray intensity distribution. We denote this as $\triangle'$. The filtering procedure only processes those components that have a nonzero membership degree in the fuzzy set *noise* (i.e., for the red components $\mu_{\text{noise}}(C_R(k_1, k_2)) > 0$). The filtering method distinguishes four different cases, which can be illustrated for a noisy red component pixel $(C_R(k_1, k_2))$ (i.e., $\mu_{\text{noise}}(C_R(k_1, k_2))$), where $y_{R(k_1,k_2)}$ denotes the filtered output value.

Case 1. $\mu_{\text{noise}}(C_G(k_1, k_2)) > 0$ and $\mu_{\text{noise}}(C_B(k_1, k_2)) > 0$ $y_R(k_1, k_2)) = (\sum_{k=1}^{9}(1 - \mu_{\text{noise}}(C_{Gk}))C_{Rk} / \sum_{k=1}^{9}(1 - \mu_{\text{noise}}(C_{Gk})))$.

Case 2. $\mu_{\text{noise}}(C_G(k_1, k_2)) = 0$ and $\mu_{\text{noise}}(C_B(k_1, k_2)) > 0$ $y_R(k_1, k_2) = C_G(k_1, k_2) + \triangle'_{RG}C(k_1, k_2)$.

Case 3. $\mu_{\text{noise}}(C_G(k_1, k_2)) > 0$ and $\mu_{\text{noise}}(C_B(k_1, k_2)) = 0$ $y_R(k_1, k_2) = C_B(k_1, k_2) + \triangle'_{RB}C(k_1, k_2)$.

Case 4. $\mu_{\text{noise}}(C_G(k_1, k_2)) = 0$ and $\mu_{\text{noise}}(C_B(k_1, k_2)) = 0$ $y_R(k_1, k_2) = 0.5(C_G(k_1, k_2) + \triangle'_{RG}C(k_1, k_2)) + 0.5(C_B(k_1, k_2) + \triangle'_{RB}C(k_1, k_2))$.

In the first case it is possible that $\sum_{k=1}^{9}(1 - \mu_{\text{noise}}(C_{Rk})) = 0$ (which is exceptional). In this situation, the output value $F_R(k_1, k_2)$ is assumed to be equal to the median of all the associated pixel intensity values.

Additionally, Fotinos et al. [67] designed a multidimensional filtering technique using fuzzy logic ideas and based on local statistics, the maximum and minimum of the histogram as parameters for signal shape description. Experimental results, conducted in true color images, show improved performance in the suppression of different types of noise and the preservation of the image details compared with other popular filtering techniques in literature, such as the arithmetic mean filter (AMF), vector median filter (VMF), the mean filter, and the fuzzy multichannel filter [68].

5. Fuzzy Filters in the Restoration of Medical Images and Signals

The large number of sensors and hyperspectral imaging modalities adopted in medical imaging leads to different types of noise [69, 70], which may coexist when the images are the result of data fusion procedures. Noise that is not informative may impair visual interpretation process and affect the fidelity of automated analysis source [71]. Numerous fuzzy techniques have been investigated for restoring corrupted magnetic resonance imaging (MRI) data, including those from the brain and the heart [72–77].

5.1. Filtering Heart MRI Data. In [72], a unique postprocessing approach is introduced via considering phasecontrast magnetic resonance imaging. Automatic vessel segmentation is accomplished using active contours [78, 79], while the segmented velocity field is filtered by applying multidimensional fuzzy adaptive vector median filtering. Accordingly, the processed MRI data is from children born with congenital single-ventricle heart abnormalities. The study demonstrates the algorithm's capability of visualizing and quantifying hemodynamics, as well as identifying patients with heart failure risks.

Random noise is introduced during segmentation as a consequence of a fuzzy vessel edge. A hybrid multichannel filter architecture is suggested to identify and replace this noise.

$$y(\vec{k}) = \mu(\vec{k})x(\vec{k}) + (1 - \mu(\vec{k}))M(\vec{k}), \tag{35}$$

where x denotes the input vector, $\vec{k}(k_1, k_2)$ signifies the pixel coordinate vector, M is the selected filter value to replace the vector's noisy component, and μ denotes a continuous fuzzy membership determining the extent of x being a flow pixel. Vector median filtering is presented for the analysis of a segmented PC MRI dataset, a vector field having three components for each data point. Due to the physical properties of flow and noise, the parameters used to establish these rules are as follows: (i) VDH or vector direction homogeneity; (ii) DVM or the distance of the given pixel from the vector median within the interrogation window; (iii) MI or magnitude image intensity; and (iv) SD or the standard deviation of the vector field. As a result, a set of generic principles for characterizing flow and noise may be defined as follows.

  (i) *Rule 1.* DVM is high for noise and low for flow

  (ii) *Rule 2.* VDH is low for noise and high for flow

  (iii) *Rule 3.* SD is high for noise and low for flow

  (iv) *Rule 4.* MI is low for noise and high for flow

Then, using fuzzy fusion, a membership function μ is assessed to estimate the chance of a pixel being noise. Figure 5 shows an example of noise used in active contour-based segmentation. Along the vessel walls, noise vectors are readily visible inside this segmented vessel, as shown by the oval [72].

5.2. Filtering Brain MRI Data.

Additionally, [80] included a switch mode fuzzy adaptive median filter (SMFAMF), which is used to reduce noise in MR images distorted by significant impulse (salt and pepper) noise without damaging picture edges and features. The authors next examined the same issue using a fuzzy adaptive median filter with adaptive membership parameters (FAMFAMP) [81]. It was discovered that it outperformed the SMFAMF when it came to suppressing salt-and-pepper noise and other noise of impulse type.

Bappy and Jeon [82] restored medical X-ray pictures using total variation (TV) minimisation and a hybrid median filter (HMF), with the goal of preserving edges and essential image information for accurate illness identification by doctors or radiologists. The resulting experiment demonstrates increased convergence speed and the restoration of high-quality medical X-ray pictures, with the staircase effect and spurious edges erased.

5.3. Filtering Multimodality Medical Images.

Today there have been several medical imaging modalities, including structural modalities and functional modalities. Functional modalities include single-photon emission CT (SPECT), positron emission tomography (PET), and functional magnetic resonance imaging (fMRI) images that provide more information about functional tissues like blood flow in a vein. On the other hand, structural modalities include magnetic resonance imaging (MRI) and computed tomography (CT) that render high-resolution structural information about an organ. Each modality has its respective advantages and disadvantages.

Ullah et al. [83] coupled Sum-Modified-Laplacian (SML) algorithms and local featured fuzzy sets in the non-subsampled Shearlet Transform (NSST) domain to develop color medical picture fusion that effectively restrains color distortion and improves visual quality. The technique involves decomposing two registered pictures of the same scene into a single Low-Frequency Subband (LFS) and numerous High-Frequency Subbands (HFS). On the LFS, the weights of each pixel are determined using Fuzzy Pixel-based fusion algorithms. To extract more meaningful information, merged HFS coefficients are chosen based on the SML coefficients of each HFS. Finally, the appropriate fused picture is obtained using inversed NSST. To evaluate performance, 256×256 MRI, PET, and SPECT images are picked for the fused MRI/PET and MRI/SPECT images. The obtained results demonstrate that the proposed approach is not only better in terms of contour and edge detection, visual feature recognition, and computing performance, but also in terms of quantitative parameters when compared to other state-of-the-art offered systems, such as Fuzzy Transform
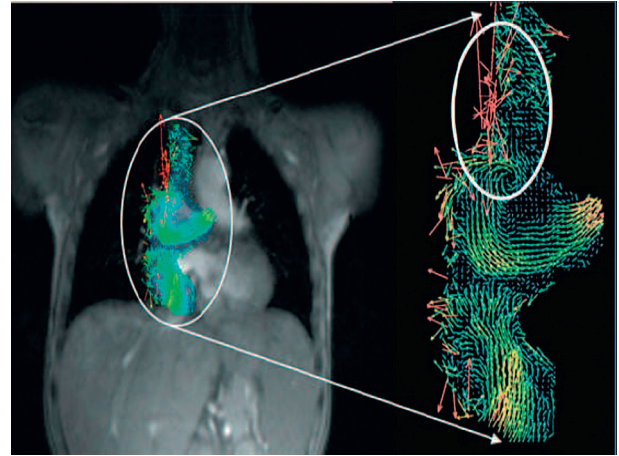

FIGURE 5: An example of noise being embedded into active contour-based segmentation [72].

with uniform sinusoidal membership fusion [84], PCNN model [85, 86] for the fusion of LFS and HFS, local Laplacian filtering (LLF) [87] for image decomposition, contourlet transform (COT) [88], nonsubsampled contourlet transform (NSCT) [88], moving frame based decomposition framework (MFDF) [89], and sparse representation (SR) based approach [90].

5.4. Fuzzy Rule-Based Methods for Earlier Cancer Diagnosis.

Currently, Fuzzy rule-based systematic approaches have been developed for early cancer diagnosis with the analysis of medical images. Mammogram images are being acquired to aid the breast cancer diagnosis of the suspected patients. Rao et al. [91] implemented fuzzy rules with minimum phases for the analysis of mammographic images that consist of 320 images coming from 160 patients with each of 1024×1024 resolutions. We calculate statistical metrics such as the Correct Detection Ratio (CDR), the Undersegmentation Error (USE), and the Similarity Index (SI). The suggested method gives quicker, more accurate findings that are more helpful in diagnosing and classifying aberrant tumors or masses while incurring less processing costs.

Tiwari et al. [92] defined medical entities as fuzzy sets and reasoning as rule-based systems in order to explore the likelihood of incidence of lung infection. It is regarded to be a safe and cost-effective method of treating lung disorders. Additionally, fuzzy logic implementation gives a set of approaches for obtaining dependable solutions. Kumar et al. [93] created a Combined Fuzzy-Rough-Set-Based F-Information and Water Swirl Algorithm with the goal of automating the discovery of cancer-associated genes (FRFI-WSA). There are two phases of gene selection: filtering and embedding, which are used to identify prospective genes and the most important cancer genes. The suggested technique is assessed on 9 binary and 13 multicategory cancer gene expression datasets. In the global cancer map with repeated measurements (GCM-RM) dataset, FRFI-WSA identified the 16 most significant genes linked with cancer with the fewest possible compact rules and the maximum classification accuracy of 96.45%.

For an extended application in biomedicine, Harsha and Vajpai [94] illustrate a Fuzzy Inference System that is used for the analysis and classification of electroencephalogram (EEG) signals. Statistical analysis of dynamical properties of the EEG signals is performed and the outcome of this analysis is used to create a fuzzy inference model. The final aim is to differentiate between brain states and zones they belong to, for example, healthy zone, epileptic zone, and nonepileptic zone. Encouraging results have been obtained from this pilot project. Further generalization of the rules is possible with the help of more data and inputs from neurophysiological experts.

6. Conclusion

This paper is focused on fuzzy filtering with type-I fuzzy reasoning, using some well-known fuzzy filter design approaches. Different fuzzy variable designs using different fuzzy rules were considered. Furthermore, different membership functions with optimized parameters were also discussed. Advances in the design of multichannel hybrid filters originally proposed in [23] have been considered, and their evolution all the way until the development of fuzzy peer group filter designs, which were introduced in 2009 [59], has been summarized. These designs have over the years been gradually simplified and evolved to variants requiring less computational complexity. What must be stressed out, however, is that these ideas form an important intellectual scaffolding for further developments in this field. Finally, within the context of biomedical imaging applications, what is particularly attractive is that these filters can be adapted to provide resilient energy-to-peak filter designs for each pixel or voxel, when nonlinearities in the image need to be preserved after assuming a Takagi–Sugeno fuzzy model where the designed filter is assumed to have additive gain variations [95]. Furthermore, these designs complement well existing wavelet parametrizations with adaptive filtering [96, 97], so it is thus envisaged that the fuzzy filtering techniques may also be soon applied to wavelet parametrizations (at different decomposition levels) so as to significantly improve filtering and signal reconstruction. Fuzzy filters are especially promising in MRI image denoising and have applications to hyperspectral imaging, and in cases when combining terahertz (THz) imaging with images from different parts of the electromagnetic spectrum (e.g., near infrared, visible, or ultraviolet parts of the spectrum). In addition, they have applications in magnetic resonance imaging (MRI) [73, 75, 97–103], retinal fundus photography [104, 105], face recognition [106], and video analysis [107].

Furthermore, they have important applications in optical coherence tomography and fundus imaging [108], in electroencephalogram (EEG) analysis [109, 110], and in other tomographic applications (e.g., in 3-dimensional reconstruction of brain images [111] or X-ray computed axial tomography [112] or ultrasound [113, 114]). The collective discussion of the various fuzzy filtering approaches in this article should lead to a better understanding of what has been achieved so far by the fuzzy filtering community and provides some further directions for research. From an applications perspective, an adaptation and evaluation of these algorithms for the different biomedical imaging modalities mentioned is urgently needed.

Conflicts of Interest

The authors declare that they have no conflicts of interest.

Acknowledgments

References

[1] S. Masood, A. Hussain, M. A. Jaffar, and T.-S. Choi, "Color differences based fuzzy filter for extremely corrupted color images," *Applied Soft Computing*, vol. 21, pp. 107–118, 2014.

[2] L. H. Son and N. T. Thong, "Intuitionistic fuzzy recommender systems: an effective tool for medical diagnosis," *Knowledge-Based Systems*, vol. 74, pp. 133–150, 2015.

[3] R. Lukac, B. Smolka, K. Martin, K. N. Plataniotis, and A. N. Venetsanopoulos, "Vector filtering for color imaging," *IEEE Signal Processing Magazine*, vol. 22, no. 1, pp. 74–86, 2005.

[4] Z. Ma, H. R. Wu, and D. Feng, "Partition-based vector filtering technique for suppression of noise in digital color images," *IEEE Transactions on Image Processing*, vol. 15, no. 8, pp. 2324–2342, 2006.

[5] K. N. Plataniotis and A. N. Venetsanopoulos, *Color Image Processing and Applications*, Springer, Berlin, Germany, 2000.

[6] J. Astola and P. Kuosmanen, *Fundamentals of Nolinear Digital Filtering*, CRC, Boca Raton, FL, USA, 1997.

[7] Z. Ma, H. R. Wu, and D. Feng, "Fuzzy vector partition filtering technique for color image restoration," *Computer Vision and Image Understanding*, vol. 107, no. 1-2, pp. 26–37, 2007.

[8] H.-H. Tsai and P.-T. Yu, "Genetic-based fuzzy hybrid multichannel filters for color image restoration," *Fuzzy Sets and Systems*, vol. 114, no. 2, pp. 203–224, 2000.

[9] D. Chen and C. Zhao, "Data-driven fuzzy clustering based on maximum entropy principle and PSO," *Expert Systems with Applications*, vol. 36, no. 1, pp. 625–633, 2009.

[10] F. Russo, "FIRE operators for image processing," *Fuzzy Sets and Systems*, vol. 103, no. 2, pp. 265–275, 1999.

[11] S.-M. Guo, C.-S. Lee, and C.-Y. Hsu, "An intelligent image agent based on soft-computing techniques for color image processing," *Expert Systems with Applications*, vol. 28, no. 3, pp. 483–494, 2005.

[12] M. Setnes, R. Babuska, U. Kaymak, and H. R. van Nauta Lemke, "Similarity measures in fuzzy rule base simplification," *IEEE Transactions on Systems, Man and Cybernetics, Part B (Cybernetics)*, vol. 28, no. 3, pp. 376–386, 1998.

[13] J. C. Bezdek, J. Keller, R. Krisnapuram, and N. R. Pal, *Fuzzy Models and Algorithms for Pattern Recognition and Image Processing (The Handbooks of Fuzzy Sets)*, Springer-Verlag New York Inc., Secaucus, NJ, USA, 2005.

[14] F. Russo and G. Ramponi, "Nonlinear fuzzy operators for image processing," *Signal Processing*, vol. 38, no. 3, pp. 429–440, 1994.

[15] H. Pomares, I. Rojas, J. Ortega, J. Gonzalez, and A. Prieto, "A systematic approach to a self-generating fuzzy rule-table for function approximation," *IEEE Transactions on Systems, Man and Cybernetics, Part B (Cybernetics)*, vol. 30, no. 3, pp. 431–447, 2000.

[16] I. Pitas and A. N. Venetsanopoulos, *Nonlinear Digital Filters, Principles and Applications*, Springer, Kluwer, Norwell, MA, 1990.

[17] B. Smolka, R. Lukac, A. Chydzinski, K. N. Plataniotis, and W. Wojciechowski, "Fast adaptive similarity based impulsive noise reduction filter," *Real-Time Imaging*, vol. 9, no. 4, pp. 261–276, 2003.

[18] C.-C. Kang and W.-J. Wang, "Fuzzy reasoning-based directional median filter design," *Signal Processing*, vol. 89, no. 3, pp. 344–351, 2009.

[19] T. Sun and Y. Neuvo, "Detail-preserving median based filters in image processing," *Pattern Recognition Letters*, vol. 15, no. 4, pp. 341–347, 1994.

[20] D. Zhang and Z. Wang, "Impulse noise removal using polynomial approximation," *Optical Engineering*, vol. 37, no. 4, pp. 1275–1282, 1998.

[21] J. S. R. Jang, C. T. Sun, and E. Mizutani, *Neuro Fuzzy and Soft Computing*, Rentice-Hall, Englewood Cliffs, NJ, 1997.

[22] K. N. Plataniotis, D. Androutsos, and A. N. Venetsanopoulos, "Adaptive fuzzy systems for multichannel signal processing," *Proceedings of the IEEE*, vol. 87, no. 9, pp. 1601–1622, 1999.

[23] H.-H. Tsai and P.-T. Yu, "Adaptive fuzzy hybrid multichannel filters for removal of impulsive noise from color images," *Signal Processing*, vol. 74, no. 2, pp. 127–151, 1999.

[24] P. E. Trahanias, D. Karakos, and A. N. Venetsanopoulos, "Directional processing of color images: theory and experimental results," *IEEE Transactions on Image Processing*, vol. 5, no. 6, pp. 868–880, 1996.

[25] D. Van De Ville, M. Nachtegael, D. Van der Weken, E. E. Kerre, W. Philips, and I. Lemahieu, "Noise reduction by fuzzy image filtering," *IEEE Transactions on Fuzzy Systems*, vol. 11, no. 4, pp. 429–436, 2003.

[26] S. Schulte, V. De Witte, M. Nachtegael, D. Van der Weken, and E. E. Kerre, "Histogram-based fuzzy colour filter for image restoration," *Image and Vision Computing*, vol. 25, no. 9, pp. 1377–1390, 2007.

[27] S. Schulte, V. De Witte, M. Nachtegael, D. Van der Weken, and E. E. Kerre, "Fuzzy two-step filter for impulse noise reduction from color images," *IEEE Transactions on Image Processing*, vol. 15, no. 11, pp. 3567–3578, 2006.

[28] E. E. Kerre, *Fuzzy Sets and Approximate Reasoning*, Xian Jiaotong University Press, Xian, China, 1998.

[29] A. Agrawal, A. Choubey, and K. Nagwanshi, "Development of adaptive fuzzy based image filtering techniques for efficient noise reduction in medical images," *International Journal of Computer Science and Information Technologies*, vol. 2, pp. 1457–1461, 2011.

[30] M. B. Ahmadi, N. A. Kiani, and N. Mikaeilvand, "Laplace transform formula on fuzzy nth-order derivative and its application in fuzzy ordinary differential equations," *Soft Computing*, vol. 18, no. 12, pp. 2461–2469, 2014.

[31] S. Salahshour, A. Ahmadian, and C. S. Chan, "A novel technique for solving fuzzy differential equations of fractional order using laplace and integral transforms," in *Proceedings of the 2016 IEEE International Conference on Fuzzy Systems (FUZZ-IEEE)*, pp. 1473–1477, Vancouver, Canada, July 2016.

[32] M. Makrehchi, O. Basir, and M. Kamel, "Generation of fuzzy membership function using information theory measures and genetic algorithm," in *Book Series Lecture Notes in Computer Science 2715/2003*, pp. 603–610, Springer, Berlin, Germany, 2003.

[33] H. Zimmermann, *Fuzzy Set Theory and its Applications, 4th Edition*, Kluwer Academic Publishers, Boston, Dordrecht, London, 2001.

[34] L. A. Zadeh, "Fuzzy sets," *Information and Control*, vol. 8, no. 3, pp. 338–353, 1965.

[35] G. J. Klir and B. Yuan, *Sets and Fuzzy Logic Theory and Applications*, Prentice-Hall, UpperSaddle River, NJ, 1995.

[36] T. Bilgic and I. B. Turksen, "Elicitation of membership functions: how far can theory take us," in *Proceedings of the 6th Int. Conf. Fuzzy Systems III*, pp. 1321–1325, Barcelona, Spain, July 1997.

[37] A. Flaig, K. E. Barner, and G. R. Arce, "Fuzzy ranking: theory and applications," *Signal Processing*, vol. 80, no. 6, pp. 1017–1036, 2000.

[38] Y. Nie and K. E. Barner, "Fuzzy rank LUM filters," *IEEE Transactions on Image Processing*, vol. 15, no. 12, pp. 3636–3654, 2006.

[39] J. H. Lee and K. H. You, "A fuzzy ranking method for fuzzy numbers, IEICE Transactions on Fundamentals of Electronics," *Communications and Computer Sciences*, vol. E86A, no. 10, pp. 2650–2658, 2003.

[40] T. K. Ho, K. H. Ip, and C. W. Tsang, "Service bid comparisons by fuzzy ranking in open railway market timetabling," *Expert Systems with Applications*, vol. 36, no. 7, pp. 10334–10343, 2009.

[41] A. Baykasoglu and T. Gocken, "Solution of a fully fuzzy multi-item economic order quantity problem by using fuzzy ranking functions," *Engineering Optimization*, vol. 39, pp. 919–939, 2007.

[42] L.-C. Ma and H. L. Li, "A fuzzy ranking method with range reduction techniques," *European Journal of Operational Research*, vol. 184, no. 3, pp. 1032–1043, 2008.

[43] L. Tran and L. Duckstein, "Comparison of fuzzy numbers using a fuzzy distance measure," *Fuzzy Sets and Systems*, vol. 130, no. 3, pp. 331–341, 2002.

[44] H. R. Wu and K. R. Rao, *Digital Video Image Quality and Perceptual Coding*, CRC Press, Boca Raton, FL, USA, 2005.

[45] K. E. Barner, Y. Nie, and W. An, "Fuzzy ordering theory and its use in filter generalization," *EURASIP Journal on Applied Signal Processing*, pp. 206–218, 2001.

[46] M. Shao and K. E. Barner, "Optimization of partition-based weighted sum filters and their application to image denoising," *IEEE Transactions on Image Processing*, vol. 15, no. 7, pp. 1900–1915, 2006.

[47] B. W. Silverman, *Density Estimation for Statistics and Data Analysis*, Chapman & Hall, London, 1986.

[48] D. W. Scott, *Multivariate Density Estimation, 2nd Edition*, Wiley, New York, 1992.

[49] B. Smolka, A. Chydzinski, K. Wojciechowski, K. Plataniotis, and A. N. Venetsanopoulos, "On the reduction of impulsive noise in multichannel image processing," *Optical Engineering*, vol. 40, no. 6, pp. 389–402, 2001.

[50] B. Smolka, K. N. Plataniotis, A. Chydzinski, M. Szczepanski, A. N. Venetsanopoulos, and K. Wojciechowski, "Self-adaptive algorithm of impulsive noise reduction in color images," *Pattern Recognition*, vol. 35, no. 8, pp. 1771–1784, 2002.

[51] S. Schulte, S. Morillas, V. Gregori, and E. E. Kerre, "A new fuzzy color correlated impulse noise reduction method,"

IEEE Transactions on Image Processing, vol. 16, no. 10, pp. 2565–2575, 2007.

[52] S. Schulte, M. Nachtegael, V. De Witte, D. Van der Weken, and E. E. Kerre, "A fuzzy impulse noise detection and reduction method," *IEEE Transactions on Image Processing*, vol. 15, no. 5, pp. 1153–1162, 2006.

[53] R. C. Gonzalez and R. E. Woods, *Digital Image Processing*, Prentice-Hall, New Jersey, 2002.

[54] J. H. Wang and H. C. Chiu, "An adaptive fuzzy filter for restoring highly corrupted images by histogram estimation," *Proceedings of the National Science Council ROC(A)*, vol. 23, pp. 630–643, 1999.

[55] J. H. Wang, W. J. Liu, and L. D. Lin, "Histogram-based fuzzy filter for image restoration," *IEEE Transactions on Systems, Man and Cybernetics, Part B (Cybernetics)*, vol. 32, no. 2, pp. 230–238, 2002.

[56] C.-S. Lee, Y.-H. Kuo, and P.-T. Yu, "Weighted fuzzy mean filters for image processing," *Fuzzy Sets and Systems*, vol. 89, no. 2, pp. 157–180, 1997.

[57] F. Russo and G. Ramponi, "Removal of impulse noise using a fire filter," in *Proceedings of the 3rd IEEE International Conference on Image Processing*, vol. 2, pp. 975–978, Lausanne, Switzerland, September 1996.

[58] T. Chen, K. Ma, and L. H. Chen, "Tri-state median filter for image denoising," *IEEE Transactions on Image Processing*, vol. 8, no. 12, pp. 1834–1838, 1999.

[59] S. Morillas, V. Gregori, and A. Hervas, "Fuzzy peer groups for reducing mixed Gaussian-impulse noise from color images," *IEEE Transactions on Image Processing*, vol. 18, no. 7, pp. 1452–1466, 2009.

[60] A. George and P. Veeramani, "On some results in fuzzy metric spaces," *Fuzzy Sets and Systems*, vol. 64, no. 3, pp. 395–399, 1994.

[61] V. Gregori and S. Romaguera, "Characterizing completable fuzzy metric spaces," *Fuzzy Sets and Systems*, vol. 144, no. 3, pp. 411–420, 2004.

[62] E. S. Hore, B. Qiu, and H. R. Wu, "Improved vector filtering for color images using fuzzy noise detection," *Optical Engineering*, vol. 42, no. 6, pp. 1656–1664, 2003.

[63] C. Kotropoulos, I. Pitas, and L. M. S. Adaptive, "Adaptive LMS L-filters for noise suppression in images," *IEEE Transactions on Image Processing*, vol. 5, no. 12, pp. 1596–1609, 1996.

[64] G. Mustafa and T. Chen, "Filtering for nonuniformly sampled systems: a Markovian jump systems approach," *Systems & Control Letters*, vol. 60, no. 10, pp. 871–876, 2011.

[65] D. Ozdenir and L. Akarun, "Fuzzy error diffusion," *IEEE Transactions on Image Processing*, vol. 9, no. 4, pp. 683–690, 2000.

[66] D. M. Young and R. T. Gregory, *A Survey of Numerical Mathematics*, Vol. 1, Dover Publications, New York, 1988.

[67] A. Fotinos, N. Laskaris, G. Economou, and S. Fotopoulos, "Multidimensional fuzzy filtering using statistical parameters," *Multidimensional Systems and Signal Processing*, vol. 10, no. 4, pp. 415–424, 1999.

[68] K. N. Plataniotis, D. Androutsos, S. Vinayagamoorthy, and A. N. Venetsanopoulos, "Color image processing using adaptive multichannel filters," *IEEE Transactions on Image Processing*, vol. 6, no. 7, pp. 933–949, 1997.

[69] J. G. Sled and G. B. Pike, "Standing-wave and RF penetration artifacts caused by elliptic geometry: an electrodynamic analysis of MRI," in *IEEE Transactions on Medical Imaging*vol. 17, no. 4, pp. 653–662, IEEE, 1998.

[70] C. Studholme, V. Cardenas, E. Song, F. Ezekiel, A. Maudsley, and M. Weiner, "Accurate template based correction of brain mri intensity distortion with application to dementia and aging," *Medical Image Analysis*, vol. 2, no. 1, pp. 299–110, 2004.

[71] A. Ogier, P. Hellier, and C. Barillot, "Restoration of 3D medical images with total variation scheme on wavelet domains (TVW)," *Proceedings of the SPIE Medical Imaging 2006: Image Processing*, vol. 6144, pp. 465–473, 2006.

[72] K. S. Sundareswaran, D. H. Frakes, M. A. Fogel, D. D. Soerensen, J. N. Oshinski, and A. P. Yoganathan, "Optimum fuzzy filters for phase-contrast magnetic resonance imaging segmentation," *Journal of Magnetic Resonance Imaging*, vol. 29, no. 1, pp. 155–165, 2009.

[73] H. Khotanlou, O. Colliot, J. Atif, and I. Bloch, "3D brain tumor segmentation in MRI using fuzzy classification, symmetry analysis and spatially constrained deformable models," *Fuzzy Sets and Systems*, vol. 160, no. 10, pp. 1457–1473, 2009.

[74] N. R. Pal, K. Pal, and J. C. Bezdek, "A mixed c-mean clustering model," in *Proceedings of the IEEE International Conference on Fuzzy Systems*, vol. 1, pp. 11–21, Barcelona, Spain, July 1997.

[75] O. Colliot, O. Camara, and I. Bloch, "Integration of fuzzy spatial relations in deformable models-application to brain MRI segmentation," *Pattern Recognition*, vol. 39, no. 8, pp. 1401–1414, 2006.

[76] I. Bloch, "Fuzzy relative position between objects in image processing: a morphological approach," *IEEE Transactions on Pattern Analysis and Machine Intelligence*, vol. 21, no. 7, pp. 657–664, 1999.

[77] I. Bloch, "Fuzzy spatial relationships for image processing and interpretation: a review," *Image and Vision Computing*, vol. 23, no. 2, pp. 89–110, 2005.

[78] L. D. Cohen and I. Cohen, "Finite-element methods for active contour models and balloons for 2-D and 3-D images," *IEEE Transactions on Pattern Analysis and Machine Intelligence*, vol. 15, no. 11, pp. 1131–1147, 1993.

[79] C. Xu and J. L. Prince, "Snakes, shapes, and gradient vector flow," *IEEE Transactions on Image Processing*, vol. 7, no. 3, pp. 359–369, 1998.

[80] A. Toprak and İ. Güler, "Impulse noise reduction in medical images with the use of switch mode fuzzy adaptive median filter," *Digital Signal Processing*, vol. 17, no. 4, pp. 711–723, 2007.

[81] I. Güler, A. Toprak, A. Demirhan, and R. Karakiş, "MR images restoration with the use of fuzzy filterhaving adaptive membership parameters," *Journal of Medical Systems*, vol. 32, no. 3, pp. 229–234, 2008.

[82] D. M. Bappy and I. Jeon, "Combination of hybrid median filter and total variation minimisation for medical X-ray image restoration," *IET Image Processing*, vol. 10, no. 4, pp. 261–271, 2016.

[83] H. Ullah, B. Ullah, L. Wu, F. Y. Abdalla, G. Ren, and Y. Zhao, "Multi-modality medical images fusion based on local-features fuzzy sets and novel sum-modified-laplacian in nonsubsampled shearlet transform domain," *Biomedical Signal Processing and Control*, vol. 57, Article ID 101724, 2020.

[84] I. Perfiljeva, "Fuzzy transforms," *Transactions on Rough Sets*, vol. 3135, pp. 63–81, 2004.

[85] X. Jin, G. Chen, J. Hou, Q. Jiang, D. Zhou, and S. Yao, "Multimodal sensor medical image fusion based on nonsubsampled shearlet transform and S-PCNNs in HSV space," *Signal Processing*, vol. 153, pp. 379–395, 2018.

[86] P. Lasagna and V. Kumar, "Feature-motivated simplified adaptive pcnn-based medical image fusion algorithm in nsst domain," *Journal of Digital Imaging*, vol. 29, pp. 73–85, 2016.

[87] J. Du, W. Li, and B. Xiao, "Anatomical-functional image fusion by information of interest in local laplacian filtering domain," *IEEE Transactions on Image Processing*, vol. 26, no. 12, pp. 5855–5866, 2017.

[88] L. Yang, B. L. Guo, and W. Ni, "Multimodality medical image fusion based on multiscale geometric analysis of contourlet transform," *Neurocomputing*, vol. 72, no. 1-3, pp. 203–211, 2008.

[89] P. Aspalli, P. Pattan, and D. P. Pattan, "Image registration and fusion using moving frame based decomposition framework algorithm," *International Journal of Innovative Technology and Exploring Engineering*, vol. 10, no. 5, pp. 57–63, 2021.

[90] A. Mohammed, K. Nisha, and P. Satshidevi, "A novel medical image fusion scheme employing sparse representation and dual pcnn in the nsct domain," in *Proceedings of the 2016 IEEE Region 10 Conference (TENCON)*, pp. 2147–2151, Singapore, November 2016.

[91] T. Venkat Narayana Rao and A. Govardhan, "Efficient segmentation and classification of mammogram images with fuzzy filtering," *Indian Journal of Science and Technology*, vol. 8, no. 15, 2015.

[92] S. K. Tiwari, N. Walia, H. Singh, and A. Sharma, "Effective analysis of lung infection using fuzzy rules," *International Journal of Bio-Science and Bio-Technology*, vol. 7, no. 6, pp. 85–96, 2015.

[93] P. G. Kumar, M. S. Kavitha, and B.-C. Ahn, "Automated detection of cancer associated genes using a combined fuzzy-rough-set-based f-information and water swirl algorithm of human gene expression data," *PLoS One*, vol. 11, Article ID e0167504, 2016.

[94] S. M. Harsha and J. Vajpai, "Fuzzy inference system for classification of electroencephalographic (eeg) data," in *Intelligent Human Computer Interaction (IHCI 2019)*Vol. 11886, Springer, Berlin, Germany, 2019.

[95] X.-H. Chang, J. H. Park, and P. Shi, "Fuzzy resilient energy-to-peak filtering for continuous-time nonlinear systems," *IEEE Transactions on Fuzzy Systems*, vol. 25, no. 6, pp. 1576–1588, 2017.

[96] X. Yin, W.-H. Ng, D. Abbott, B. Ferguson, and S. Hadjiloucas, "Application of auto regressive models of wavelet sub-bands for classifying terahertz pulse measurements," *Journal of Biological Systems*, vol. 15, no. 04, pp. 551–571, 2007.

[97] X.-X. Yin, W.-H. Ng, and D. Abbott, *P. Recognition and T. Reconstruction Of Terahertz Signals: Applications in Biomedical Engineering*, Springer-Verlag, Berlin Heidelberg, 2012.

[98] A. W.-C. Liew and H. Yan, "An adaptive spatial fuzzy clustering algorithm for 3-D MR image segmentation," *IEEE Transactions on Medical Imaging*, vol. 22, no. 9, pp. 1063–1075, 2003.

[99] L. Sun, J. He, X.-X. Yin et al., "An image segmentation framework for etrating tumours from breast magnetic resonance images," *Journal of Innovative Optical Health Sciences*, vol. 11, no. 4, 2018.

[100] X.-X. Yin, S. Hadjiloucas, Y. Zhang, M.-Y. Su, Y. Miao, and D. Abbott, "Pattern identification of biomedical images with time series: contrasting THz pulse imaging with DCE-MRIs," *Artificial Intelligence in Medicine*, vol. 67, pp. 1–23, 2016.

[101] X.-X. Yin, Y. Zhang, J. Cao, J.-L. Wu, and S. Hadjiloucas, "Exploring the complementarity of THz pulse imaging and DCE-MRIs: toward a unified multi-channel classification and a deep learning framework," *Computer Methods and Programs in Biomedicine*, vol. 137, pp. 87–114, 2016.

[102] X.-X. Yin, S. Hadjiloucas, J. H. Chen, J.-L. W. Y. Zhang, and M.-Y. Su, "Tensor based multichannel reconstruction for breast tumours identified from DCE-MRIs," *PLoS One*, vol. 12, no. 3, 2017.

[103] X.-X. Yin, S. Hadjiloucas, and Y. Zhang, *Pattern Classification of Medical Images: Computer Aided Diagnosis*, Springer-Verlag, Berlin Heidelberg, 2017.

[104] D. Pandey, X.-X. Yin, H. Wang, and Y. Zhang, "Accurate vessel segmentation using maximum entropy incorporating line detection and phase-preserving denoising," *Computer Vision and Image Understanding*, vol. 155, pp. 162–172, 2016.

[105] X. Yin, B. W. Ng, J. He, Y. Zhang, and D. Abbott, "Accurate image analysis of the retina using hessian matrix and binarisation of thresholded entropy with application of texture mapping," *PLoS One*, vol. 9, no. 4, Article ID e95943, 2014.

[106] Y. Cheng, Z. Jin, H. Chen, Y. Zhang, and X. Yin, "A fast and robust face recognition approach combining Gabor learned dictionaries and collaborative representation," *International Journal of Machine Learning and Cybernetics*, vol. 7, no. 1, pp. 47–52, 2016.

[107] A. ul Haq, X.-X. Yin, J. He, and Y. Zhang, "on space-time filtering framework for matching human actions across different viewpoints," *IEEE Transactions on Image Processing*, vol. 27, no. 3, pp. 1230–1242, 2018.

[108] S. S. Rahim, V. Palade, J. Shuttleworth, and C. Jayne, "Automatic screening and classification of diabetic retinopathy and maculopathy using fuzzy image processing," *Brain Informatics*, vol. 3, no. 4, pp. 249–267, 2016.

[109] J. Hu, C.-S. Wang, M. Wu, Y.-X. Du, Y. He, and J. She, "Removal of EOG and EMG artifacts from EEG using combination of functional link neural network and adaptive neural fuzzy inference system," *Neurocomputing*, vol. 151, pp. 278–287, 2015.

[110] P. Balaiah and Ilavennila, "Comparative evaluation of adaptive filter and neuro-fuzzy filter in artifacts removal from electroencephalogram signal," *American Journal of Application Science*, vol. 9, no. 10, pp. 1583–1593, 2012.

[111] I. Bloch, T. Géraud, and H. Maître, "Representation and fusion of heterogeneous fuzzy information in the 3D space for model-based structural recognition-Application to 3D brain imaging," *Artificial Intelligence*, vol. 148, no. 1-2, pp. 141–175, 2003.

[112] L. Xiao, C. Li, Z. Wu, and T. Wang, "An enhancement method for X-ray image via fuzzy noise removal and homomorphic filtering," *Neurocomputing*, vol. 195, pp. 56–64, 2016.

[113] J. J. J. Babu and G. F. Sudha, "An enhancement method for X-ray image via fuzzy noise removal and homomorphic filtering," *Neurocomputing*, vol. 195, pp. 56–64, 2016.

[114] K. Binaee and R. P. R. Hasanzadeh, "An ultrasound image enhancement method using local gradient based fuzzy similarity," *Biomedical Signal Processing and Control*, vol. 13, pp. 89–101, 2014.

Research Article

Automatic Segmentation of Magnetic Resonance Images of Severe Patients with Advanced Liver Cancer and the Molecular Mechanism of Emodin-Induced Apoptosis of HepG2 Cells under the Deep Learning

Haiyan Zhao,[1] Yuping Wang,[1] Chen He,[1] Jilin Yang,[1] Yaoming Shi,[2] and Xiaolin Zhu [1]

[1]*The Elderly of Treatment Department of Critical Medicine, The Frist Affiliated Hospital of Kunming Medical University, Kunming, Yunnan 650032, China*
[2]*Undergraduate Clinical Major, Haiyuan College of Kunming Medical University, Kunming, Yunnan 65003, China*

Correspondence should be addressed to Xiaolin Zhu; 2019213330@mail.chzu.edu.cn

To improve the accuracy of clinical diagnosis of severe patients with advanced liver cancer and enhance the effect of chemotherapy treatment, the U-Net model was optimized by introducing the batch normalization (BN) layer and the dropout layer, and the segmentation training and verification of the optimized model were realized by the magnetic resonance (MR) image data. Subsequently, HepG2 cells were taken as the research objects and treated with 0, 10, 20, 40, 60, 80, and 100 μmol/L emodin (EMO), respectively. The methyl thiazolyl tetrazolium (MTT) method was used to explore the changes in cell viability, the acridine orange (AO)/ethidium bromide (EB) and 4′,6-diamidino-2-phenylindole (DAPI) were used for staining, the Annexin V fluorescein isothiocyanate (FITC)/propidium iodide (PI) (Annexin V-FITC/PI) was adopted to detect the apoptosis after EMO treatment, and the Western blot (WB) method was used with the purpose of exploring the changes in protein expression levels of PARP, Bcl-2, and p53 in the cells after treatment. It was found that compared with the original U-Net model, the introduction of the BN layer and the dropout layer can improve the robustness of the U-Net model, and the optimized U-Net model had the highest dice similarity coefficient (DSC) (98.45%) and mean average precision (MAP) (0.88) for the liver tumor segmentation.

1. Introduction

Primary liver cancer is currently one of the common malignant tumors with high morbidity and mortality, which has seriously threatened the safety of human life [1]. Surgical treatment is currently the most direct and thorough method for liver treatment, but precise surgical treatment is required to preserve the integrity of the unaffected area of the liver to the greatest extent [2]. The prerequisite for doctors to perform accurate diagnosis and treatment of liver cancer is to accurately segment the lesion area from the patient's imaging treatment. The current manual segmentation method has the highest accuracy, but it will waste a lot of time and energy in the face of massive medical imaging data. In addition, the manual segmentation has the characteristics of non-repeatability and subjectivity [3, 4]. To improve the efficiency of medical image processing and realize the intelligence and repeatability of image segmentation, a large number of experts and scholars have introduced the intelligent algorithms to achieve this goal. At present, the algorithms commonly used for the image segmentation include the support vector machines (SVMs), convolutional neural networks (CNNs), and U-Net [5–7]. Among them, the U-Net model is mainly used for the segmentation of medical images and can fuse the image features of different scales, so it is widely used in the segmentation of medical images [8]. However, the depth of the original U-Net model is not enough to obtain a good network model through fast training. Therefore, to solve this problem, an improvement on the structure of the U-Net was explored in this study.

Surgical resection is limited to the treatment of patients with liver cancer in the early stage, but the patients with advanced liver cancer with the characteristics of fast development and easy metastasis can only inhibit the development of liver cancer through chemotherapy or radiotherapy [9]. Radiotherapy can cause vomiting and gastrointestinal mucosal damage in patients, and doxorubicin and other drugs commonly used in chemotherapy have certain toxicity, which can affect the growth of normal cells in the patient's body [10, 11]. Studies have proved that natural secondary metabolites derived from animals, plants, or microorganisms can reduce the toxic and side effects caused by radiotherapy or chemotherapy and have the advantages of high safety performance and resistance to drug resistance [12]. At present, EMO can intervene in the process of liver cancer, cervical cancer, prostate cancer, and other cancers. It mainly achieves alleviation of cancer disease process by blocking the cell cycle and inhibiting the cell proliferation [13, 14].

2. Methodology

2.1. Experimental Materials.
The MR imaging data related to the "advanced liver cancer" were obtained from The Cancer Imaging Archive, and the data provided by researchers of Harvard beamandrew machine learning and medical imaging on the GitHub were referred. As a result, a total of 1,526 MR images were obtained to construct the "MR Image Data Set of Advanced Liver Cancer."

2.2. Preprocessing of MR Image.
During the process of image data collection, there may be more interference in the image due to the changes in environment and magnetic field [15]. Therefore, to improve the effect of image segmentation, the images had to be normalized and standardized when inputting the MR images into the model.

The (0, 1) normalization method was adopted to process the image pixel matrix, and the mathematical expression of this method was given as follows:

$$x^{\sim} = \text{Factor} \cdot \frac{x - x_{\min}}{x_{\max} - x_{\min}}. \tag{1}$$

In the above equation, x was the pixel of input image, $x_{\max}$ represented the maximum value in the pixel matrix, $x_{\min}$ represented the minimum value in the pixel matrix, and Factor indicated the normalization coefficient. When it was normalized to (0, 1), then Factor = 1; when it was normalized to (0, 200), then the Factor = 200.

Z score was adopted for the standardization of the MR image, and the mathematical expression of this method was given as follows:

$$x' = \frac{x - \overline{x}}{\sigma}. \tag{2}$$

In the above equation, $\overline{x}$ represented the average value of the pixel matrix of the inputted image and σ represented the standard deviation of the pixel matrix of the inputted image.

The number of MR image data collected in this study was limited by time, cases, and other factors, and the use of deep learning technology for image segmentation required a large amount of data for model training, so it was hoped to expand the original MR samples in the form of data enhancement. The methods commonly used for image data enhancement include flip, random crop, color jittering, shift, scale, contract, noise, rotation, and reflection [16], and the Python was used for data enhancement of the MR images from the third-party database Augmentor.

2.3. Design and Improvement of U-Net.
U-Net was a network algorithm of the medical cell segmentation proposed by Olaf et al. in 2015. The basic structure of the network is shown in Figure 1. It can be seen that the original U-Net presented a structure similar to the "U," which contained a total of 23 convolutional layers, 4 downsampling operations, and 4 upsampling operations. Compared with the CNN, there was no fully connected layer in the U-Net. Each execution of downsampling included 2 convolution operations with a convolution kernel size of $3*3$ and 1 pooling operation with a size of $2*2$, while the upsampling operation only included 2 convolution operations with a convolution kernel size of $3*3$, and finally, a convolution layer with a convolution kernel size of $1*1$ was added to the U-Net.

Based on the original structure of U-Net, the BN layer and the dropout layer were added to improve the structure of the model, and the hyperparameters of the model were adjusted to improve the robustness of the model.

It can be observed from Figure 2(a) that when the traditional neural network was adopted for standardization, the sample data were standardized before the samples were inputted into the network, which reduced the difference among the inputted samples. From Figure 2(b), it can be known that the batch normalization [17] standardized the inputted data of each hidden layer based on the standardization results of traditional neural network. After the effect of activation function ReLU, the output of the first hidden layer was $L_1 = ReLU(W_{L1} + B_{L1})$. In the calculation of the hidden layer standardized by the batch normalization, it was necessary to process the matrix x of the input data using the linear transformation to obtain the input value q_1 in the hidden layer. Secondly, q_1 was standardized, and the average μ_y and standard deviation $\sqrt{\sigma_y^2 + \varepsilon}$ were subtracted to obtain the output value q_2. μ_y is referred to the average value of the selected batch, and $\mu_y = 1/m \sum_{i=0}^{m} W_{L_1 x_1}$. The standard deviation was also the standard deviation of a specific batch, and $\sigma_y^2 = 1/m \sum_{i=0}^{m} (W_{L_1 x_1} - \mu_y)^2$ to prevent errors when $\sigma_y^2 = 0$. The processed q_2 data showed a normal distribution characteristic, which reduced the expressive ability of the network model, so new parameters (m and B) had to be introduced. m and B were obtained by self-learning of the network after training, q_3 can be obtained after data q_2 were processed with the introduced parameters, and the output L_1 of the hidden layer was obtained using the activation function ReLU.

The basic structure parameters of the U-Net optimized in this study are shown in Table 1.
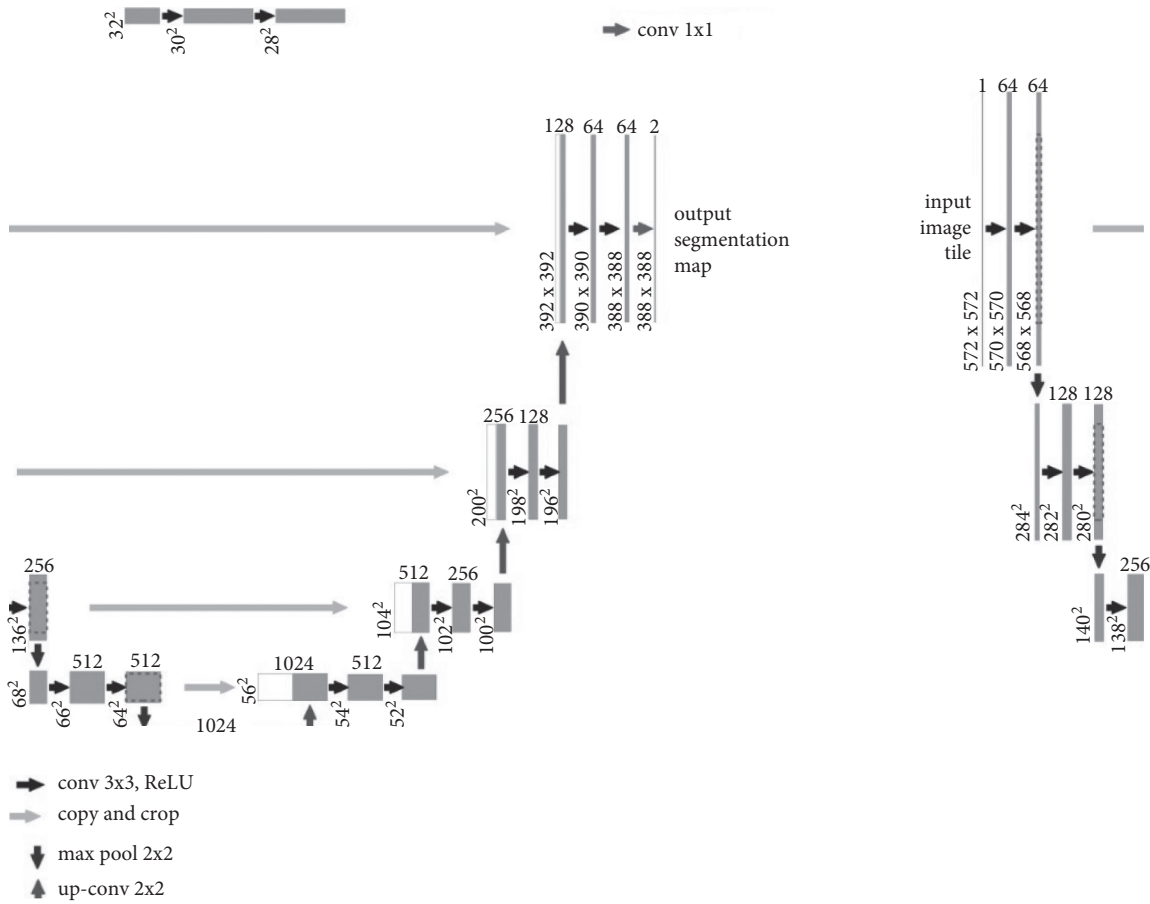
Figure 1: Basic structure of U-Net.

Finally, the U-Net model was built and tested under the Keras deep learning framework. The process of segmenting the MR image of liver cancer patients using the optimized U-Net model is shown in Figure 3.

2.4. Evaluation Indexes of Liver Tumor Segmentation Efficacy.

The DSC and recall and precision (R-P) were utilized to evaluate the segmentation efficacy of liver tumor by the optimized U-Net. Among them, DSC was used for evaluating the degree of overlap between the segmented tumor and the gold standard tumor. The closer it was to 1, the more similar the segmentation result was to the gold standard result. The calculation equation can be written as follows:

$$\text{DSC}(T, P) = \frac{2|T \cap P|}{|T| + |P|}. \tag{3}$$

In the above equation, T was the true value and P was the prediction value outputted by the model.

Recall was used to evaluate the correct rate of image classification. The closer it was to 1, the better the classification effect. The calculation equation was given as follows:

$$\text{recall} = \frac{TP}{TP + FN}. \tag{4}$$

In the above equation, TP is referred to the truth-positive value (both the classification result and the gold standard result were positive samples) and FN is referred to the false-negative value (the positive samples were predicted as negative samples).

Precision was to evaluate the error rate of wrong classification of the samples. The closer it was to 1, the better the classification effect, and it can be calculated with the following equation:

$$\text{precision} = \frac{TP}{TP + FP}. \tag{5}$$

In the above equation, the FP is referred to the false-positive value (the negative samples were predicated as the positive samples).

2.5. Test on Cell Viability of HepG2 after EMO Treatment.

Studies had shown that plants can selectively enrich the growth-promoting bacteria Stenotrophomonas through roots and then promote the accumulation of EMO in the roots (as shown in Figure 4) [18]. Studies had also shown that EMO can inhibit the proliferation of cancer cell through cell cycle arrest, autophagy, and apoptosis [19].

Based on this, the changes in cell viability by different concentrations of EMO (0 μmol/L, 10 μmol/L, 20 μmol/L, 40 μmol/L, 60 μmol/L, 80 μmol/L, and 100 μmol/L) effecting on HepG2 cells at the 0th, 12th, 24th, 26th, and 48th hour were compared. The activity of cell mitochondrial dehydrogenase was
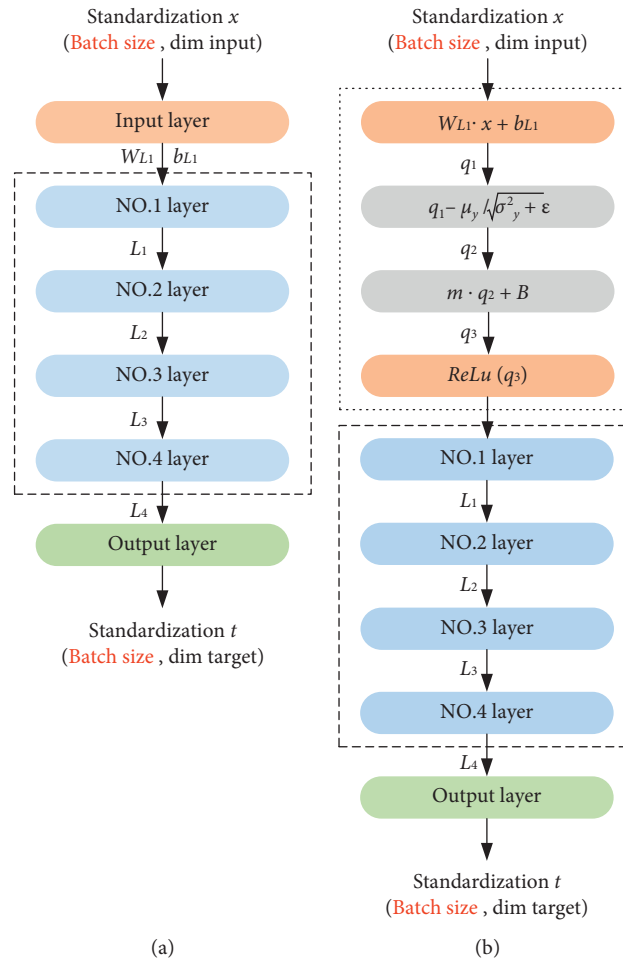
FIGURE 2: Normalization flows of traditional and batch.

tested by MTT. Firstly, the cells in the logarithmic growth phase were collected and inoculated in a 96-well plate after the cell density was adjusted to 1×10^4 for cultivation overnight; each well was supplemented with $10 \mu L$ of different concentrations of EMO (each concentration was added for 3 wells), respectively, and then incubated for 24 hours after mixing fully; the medium was discarded, and $100 \mu L$ of 5 mg/mL MTT was added to each well, shaken, and mixed at low speed for around 10 minutes; the absorbance of each well was detected at 560 nm wavelength with a microplate reader, and finally, the results were displayed by IC50 (the concentration at which cell viability was inhibited by 50%).

2.6. Test on Cell Morphology of HepG2 after EMO Treatment. After adjusting the cell density to 1×10^5, the cells were inoculated in a 12-well plate for cultivation overnight; each well was supplemented with $10 \mu L$ of $10 \mu mol/L$ (low concentration), $40 \mu mol/L$ (medium concentration), and $80 \mu mol/L$ (high concentration) EMO (each concentration was added for 3 wells), respectively, and then incubated for 24 hours after mixing fully. The morphologies of HepG2 cells treated with different concentrations of EMO and untreated (control group)

were observed with a light-induced microscope (Olympus, Japan), and related pictures should be taken.

2.7. Detection on Apoptosis of HepG2 after the EMO Treatment. AO combined with EB was adopted to stain the HepG2 in the control group, low concentration, medium concentration, and high concentration EMO treatment for 16 hours. The cells were rinsed with phosphate-buffered saline (PBS) twice before adding the dyes, and $50 \mu g/mL$ mixed dyes made of $100 \mu g/mL$ AO and $100 \mu g/mL$ EB at the ratio of 1 : 1 were added to each well, so that the cells were completely immersed in the solution, and then, they were immediately placed under a fluorescent inverted microscope (Olympus, Japan) to observe the luminous state of the cells, and related pictures should be taken.

The Annexin V-FITC/PI Cell Apoptosis Kit was used for the qualitative and quantitative analysis of the cells in the control group and the treatment groups with EMO with different concentrations. Firstly, the cells in different treatment groups were prepared to single-cell suspensions of 1×10^6 cells/mL with PBS, placed in a low-temperature centrifuge after adding 1 mL of the suspension, and centrifuged at 1,000 rpm for about 10 minutes at the

TABLE 1: Structure parameters of optimized U-Net model.

Layer no.	Structure
1	Batch_Nor 1
2-1	Conv 1–32
2-2	Conv 1–32
3	Maxpooling 1
4	Batch_Nor 2
5	Dropout (0.1)
6-1	Conv 2–64
6-2	Conv 2–64
7	Maxpooling 2
8	Batch_Nor 3
9	Dropout (0.1)
10-1	Conv 3–128
10-2	Conv 3–128
11	Maxpooling 3
12	Batch_Nor 4
13	Dropout (0.2)
14-1	Conv 4–256
14-2	Conv 4–256
15	Maxpooling 4
16	Batch_Nor 5
17	Dropout (0.2)
18-1	Conv 5–512
18-2	Conv 5–512
19	Maxpooling 5
20	Batch_Nor 6
21	Dropout (0.3)
22	Upsampling + merge 1
23	Batch_Nor 7
24	Dropout (0.2)
25-1	Conv 6–256
25-2	Conv 6–256
26	Upsampling + merge 2
27	Batch_Nor 8
28	Dropout (0.2)
29-1	Conv 7–128
29-2	Conv 7–128
30	Up-sampling + merge 3
31	Batch_Nor 9
32	Dropout (0.1)
33-1	Conv 8–64
33-2	Conv 8–64
34	Upsampling + merge 4
35	Batch_Nor 10
36	Dropout (0.1)
37-1	Conv 9–32
37-2	Conv 9–32
38	Conv 10-1

temperature of 4°C to collect the precipitate; the above steps were repeated for three times; the cells were resuspended with 500 μL binding solution and mixed fully after adding 10 μL of Annexin V-FITC reagent and 5 μL of PI reagent to react in a dark box at the room temperature lasting for 20 minutes; Annexin V-FITC and PI fluorescence were detected with a flow cytometer (Thermo Fisher Scientific, USA) at the wavelengths of 488 nm–630 nm, respectively.

2.8. Detection on Levels of Related Proteins in HepG2 after Treatment with EMO. The radio-immunoprecipitation assay
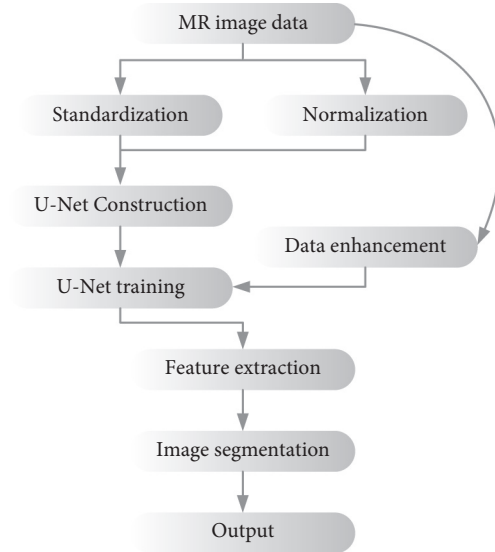

FIGURE 3: Process of segmenting the MR image of liver cancer patients using the optimized U-Net network.
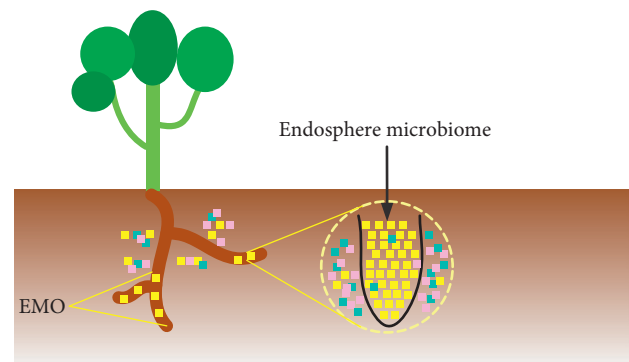

FIGURE 4: Accumulation of EMO in plant roots.

(RIPA) cell lysate was used for cell lysis on ice, and then, the cells were centrifuged, and the cell protein supernatant was collected. The protein concentration was detected using the bicinchoninic acid (BCA) protein quantification kit. The separate gels and concentrated gels of different concentrations were prepared according to the molecular weights of the target protein and up-sampled in the sample holes, and then, the electrophoresis was performed at 80 V and then 120 V, respectively, until the bromophenol blue dye solution was 1 cm from the bottom of the gel. The gels were cut and transferred with polyvinylidene fluoride (PVDF) membrane. The transferred PVDF membrane was placed in a blocking solution for 60 minutes and rinsed with the blocking solution three times and then incubated with the poly ADP-ribose polymerase (PARP), Bcl-2, and p53 primary antibody overnight at a temperature of 4°C. It was rinsed with the blocking solution another three times and then incubated with corresponding secondary antibody for around 120 min at the condition of room temperature; the enhanced chemiluminescence (ECL) color developing solution was supplemented to develop in the gel imaging system (Bio-
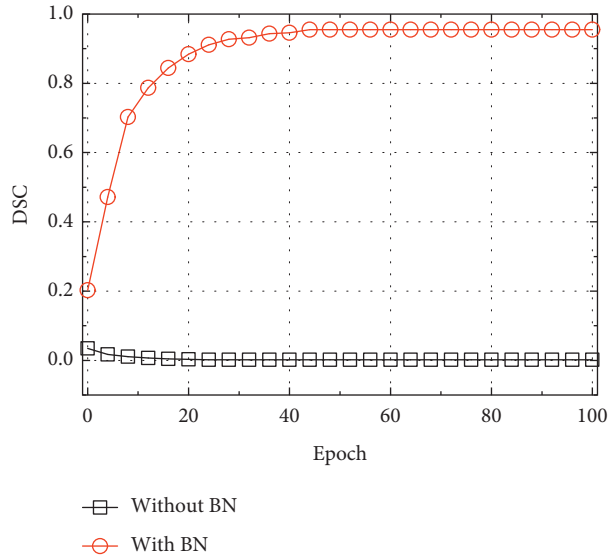
FIGURE 5: Impacts of the BN layer on test results of the U-Net.
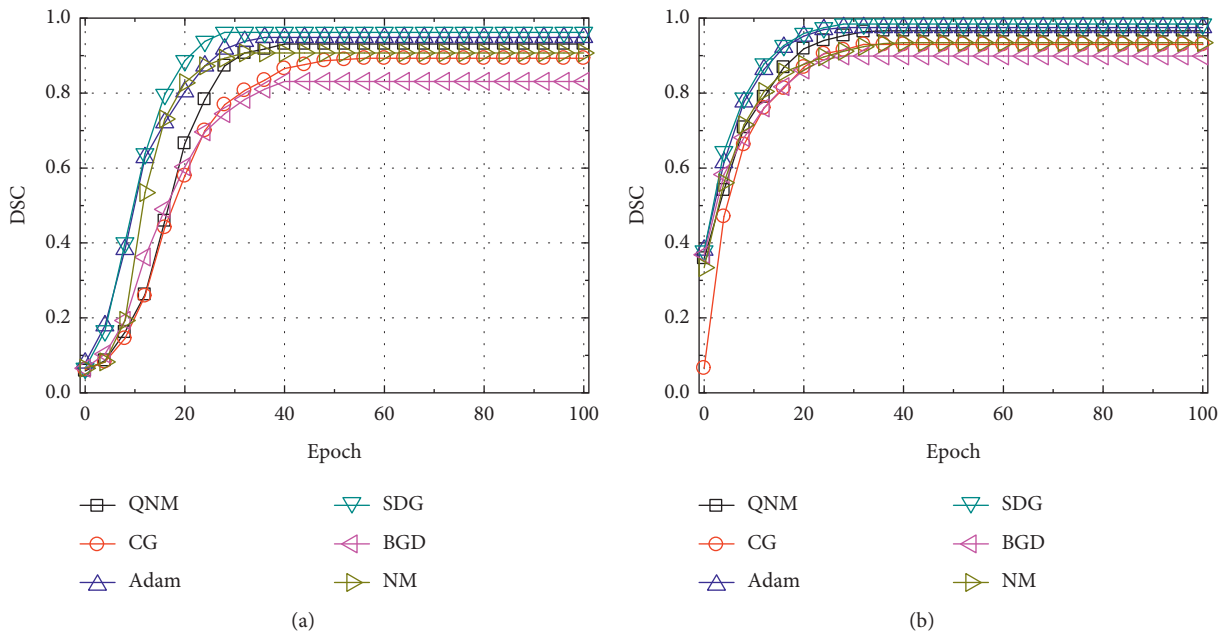

(a)

(b)

FIGURE 6: Impacts of dropout layer optimized by various algorithms on the test results of U-Net model.

Rad, USA). Quantity One was used for image acquisition and gray value analysis.

2.9. Statistical Analysis. GraphPad was used for data processing, and the one-way ANOVA process in SPSS 19.0 was used for analysis. The experimental data of the mechanism of EMO on the apoptosis of HepG2 cells were all expressed as mean ± standard deviation, and Duncan's multiple comparisons were used to analyze the differences between groups. It was considered that $P < 0.05$ indicated that the difference was statistically significant, $P < 0.05$ indicated

there was a significant difference, and $P < 0.01$ indicated there was an obviously great difference.

3. Results and Discussion

3.1. Performance Test of Optimized U-Net. The performance of the U-Net model with and without the BN layer was compared, and the results are given in Figure 5. It can be seen that as the number of training increased, the DSC value of the U-Net model without the BN layer showed a decreasing trend, indicating that the model training was not successful. This may be because the U-Net model used
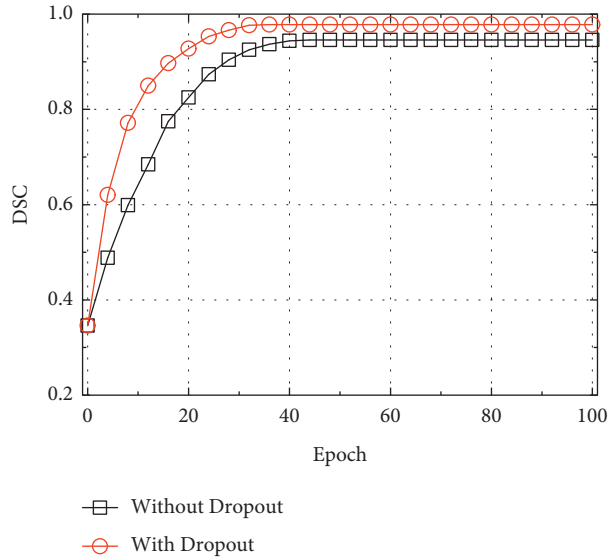
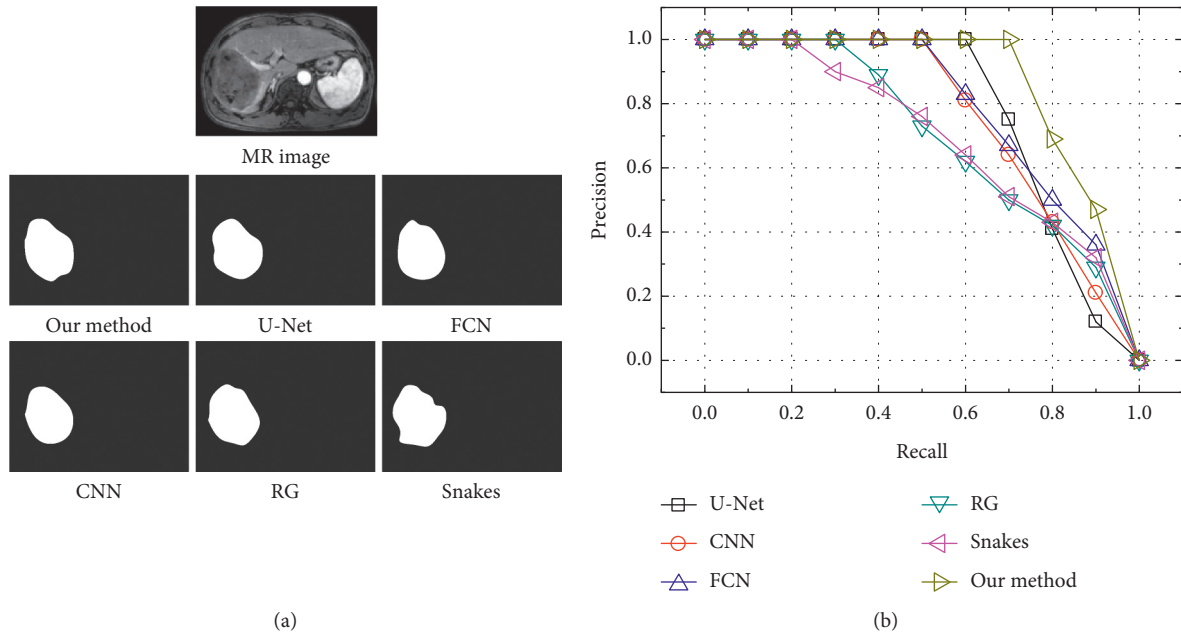FIGURE 7: Test results of U-Net model before and after the data enhancement.

(a)

(b)

FIGURE 8: Analysis on segmentation efficacy of liver tumor with different models.

the random parameter initialization. Similar to other re-search results, adding BN layer to FCN model can improve the efficiency and accuracy of brain image segmentation [20].

The test results of U-Net adding with and without the dropout layer were compared optimized by the batch gradient descent (BGD), stochastic gradient descent (SGD), Newton's method (NM), quasi-newton method (QNM), conjugate gradient (CG), and Adam optimization algorithms, and the results were given as below. It can be seen from Figures 6(a) and 6(b) that the U-Net model optimized by SGD had the fastest convergence speed and the highest DSC value after stability regardless of whether a dropout layer was added to

the U-Net model. Taking the result of SGD optimization as an example, it was found based on the comparison that the test result of the U-Net model with the dropout layer was re-markably better than the model without the dropout layer, and the DCS value was increased by about 2.24%. It shows that adding a dropout layer can prevent the model from overfitting or generalization, and it also improves the seg-mentation ability and robustness of the model [21].

Finally, the changes in training DSC value of the im-proved U-Net model before and after the enhancement of the MR image data were compared. It can be observed from Figure 7 that the convergence speed of the model after the data enhancement was faster than that before the data
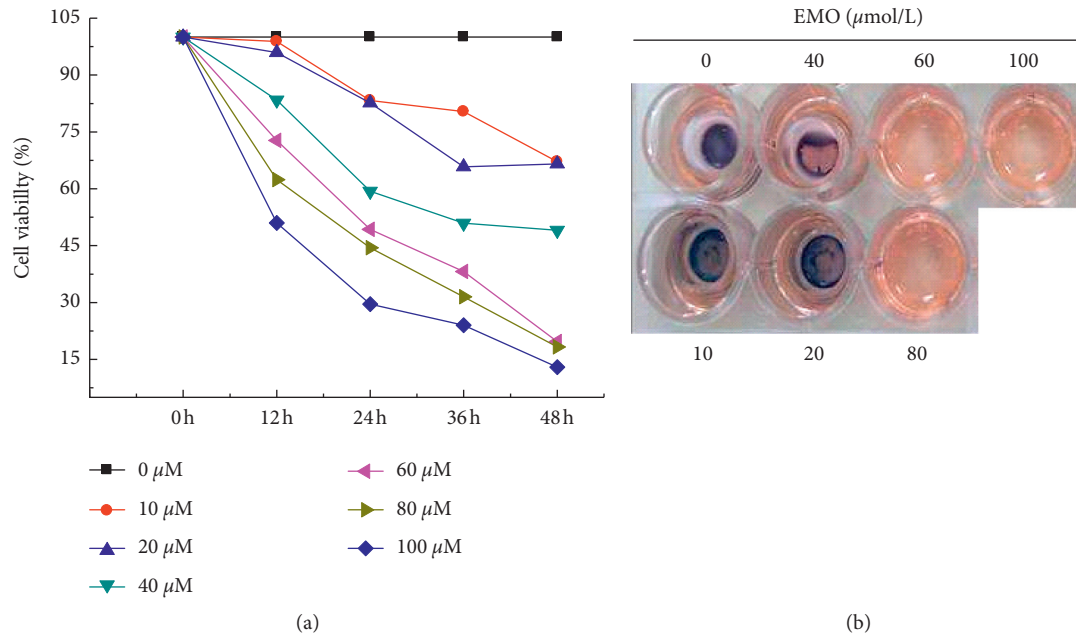
(a)　　　　　　　　　　　　　　　　　　　　　　　(b)

Figure 9: Impacts of different concentrations of EMO on cell viability of HepG2.
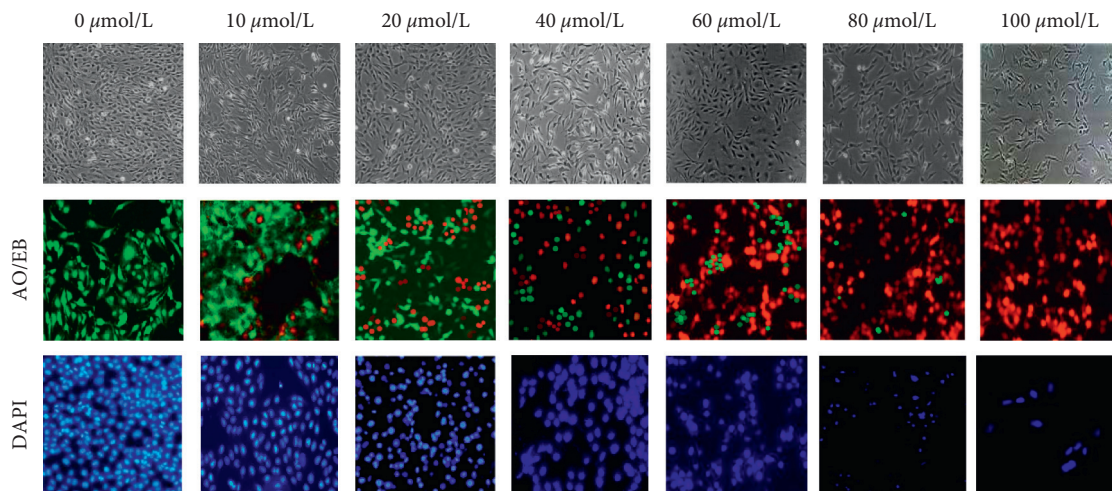

Figure 10: Morphology and staining results of HepG2 after being treated with EMO in different concentrations.

enhancement greatly, and with the gradual increase in the number of iterations, the model became stable gradually. When the maximum number of iterations was reached, the DSC verification result of the model after data enhancement was 97.8%, while the DSC verification result of the model before the data enhancement was 94.55%, so it increased by 3.25%.

3.2. Segmentation Efficacy of MR Liver Tumor Based on the Optimized U-Net Model.
The application effects in liver tumor segmentation of original U-Net, convolutional neural network (CNN), FCN, regional growth (RG), and Snakes were compared with the effect of the optimized U-Net algorithm in this study, and the results are shown in Figure 8. It can be seen from Figure 9(a) that the segmentation efficacy of U-Net, CNN, FCN, and the improved U-Net model was similar to the gold standard segmentation

efficacy, while that of RG was excessively segmented when the distinction between liver tumors and surrounding tissues was not high. Under the condition of uneven grayscale distribution of MR images and uneven surface of the tumor, under segmentation could be found for the Snakes. The segmentation efficacies of different models were quantitatively compared, and recall and precision values were used to draw the P-R curve to obtain the area under the PR curve mAP. From Figure 9(b), it can be seen that the improved U-Net model had the highest mAP value (0.88), followed by the original U-Net model (0.74), while the Snakes model had the smallest mAP value (0.53).

3.3. Impacts of EMO on Cell Viability and Proliferation of HepG2.
The MTT was used to determine the effect of different concentrations of EMO on the viability of HepG2

cells. It can be seen from Figure 9(a) that with the gradual increase in treatment time, the viability of HepG2 cells gradually decreased after treatment with different concentrations of EMO. It meant that the higher the EMO concentration, the lower the viability of HepG2 cells. The blue-purple formazan crystal staining was adopted to observe the changes in the number of HepG2 viable cells after treatment with different concentrations of EMO. It can be known from Figure 9(b) that the formation of formazan crystals was proportional to the number of viable cells. With the gradual increase in EMO concentration, the amount of formazan crystal gradually decreased, which was consistent with the test results of cell viability.

3.4. Impacts of EMO on Morphology and Staining Results of HepG2. First, the changes in cell morphology, AO/EB, and DAPI staining results of HepG2 cells treated with different concentrations of EMO were observed under a microscope. The results are shown in Figure 10. It can be seen that the HepG2 cells treated with 0μmol/L EMO were tightly connected and exhibited the irregular spindle shapes. With the increasing concentration of EMO, the cell outline became blurred, most of the cells came off, and the number of adherent cells decreased, similar to the characteristics of apoptosis. The AO/EB was used for cell staining, and it can be seen that as the concentration of EMO increased, the proportion of green fluorescence in HepG2 cells gradually decreased, while the proportion of orange-red fluorescence gradually increased; when the EMO concentration reached 100μmol/L, HepG2 cells all became red. The results of DAPI staining showed that with the gradual increase in EMO concentration, the blue fluorescence in HepG2 cells gradually decreased, showing a dose-dependent manner.

4. Conclusion

To improve the effect of deep learning algorithm in tumor segmentation in images and to explore the molecular mechanism of the impacts of EMO on liver cell apoptosis, the U-Net model was optimized in this study to segment the MR images of liver cancer patients. It was found that the improved U-Net model can improve the efficiency and robustness of tumor segmentation, and the segmentation effect was significantly higher than other advanced models.

Data Availability

The dataset used in this study is available from the corresponding author upon request.

Conflicts of Interest

The authors declare that they have no conflicts of interest regarding this work.

Authors' Contributions

Haiyan Zhao and Yuping Wang made equal contributions to the manuscript. They worked together.

References

[1] N. M. Niehoff, E. C. Zabor, J. Satagopan et al., "Prediagnostic serum polychlorinated biphenyl concentrations and primary liver cancer: a case-control study nested within two prospective cohorts," *Environmental Research*, vol. 187, Article ID 109690, 2020.

[2] R. Mehta, A. Ejaz, J. M. Hyer et al., "The impact of dedicated cancer centers on outcomes among medicare beneficiaries undergoing liver and pancreatic cancer surgery," *Annals of Surgical Oncology*, vol. 26, no. 12, pp. 4083–4090, 2019.

[3] L. A. Orci, G. Oldani, S. Lacotte et al., "Dynamic volume Assessment of hepatocellular carcinoma in rat livers using a clinical 3T MRI and novel segmentation," *Journal of Investigative Surgery*, vol. 31, no. 1, pp. 44–53, 2018.

[4] H. Sang, S. Choi, L. Soo et al., "LI-RADS classification and prognosis of primary liver cancers at gadoxetic acid-enhanced MRI," *Radiology*, vol. 290, no. 2, pp. 388–397, 2018.

[5] J. Chen and S. Zhang, "Segmentation of sonar image on seafloor sediments based on multiclass SVM," *Journal of Coastal Research*, vol. 83, no. 1, pp. 597–602, 2018.

[6] J. Dolz, I. B. Ayed, J. Yuan, and C. Desrosiers, "HyperDense-Net: a hyper-densely connected CNN for multi-modal image segmentation," *IEEE Transactions on Medical Imaging*, vol. 38, no. 5, pp. 1116–1126, 2018.

[7] U. Kamal, T. I. Tonmoy, S. Das, and M. K. Hasan, "Automatic traffic sign detection and recognition using SegU-net and a modified tversky loss function with L1-constraint," *IEEE Transactions on Intelligent Transportation Systems*, vol. 21, no. 4, pp. 1467–1479, 2020.

[8] R. M. Rad, P. Saeedi, J. Au, and J. Havelock, "Trophectoderm segmentation in human embryo images via inceptioned U-net," *Medical Image Analysis*, vol. 62, Article ID 101612, 2020.

[9] K. Nishikimi, S. Tate, A. Matsuoka, and M Shozu, "Resection of a metastatic bulky subphrenic tumor for the treatment of advanced ovarian cancer using liver mobilization and the Pringle maneuver," *Gynecologic Oncology*, vol. 151, no. 1, pp. 176-177, 2018.

[10] Z. W. Lim, V. B. Varma, R. V. Ramanujan, and A. Miserez, "Magnetically responsive peptide coacervates for dual hyperthermia and chemotherapy treatments of liver cancer," *Acta Biomaterialia*, vol. 110, pp. 221–230, 2020.

[11] E. Simoneau and J.-N. Vauthey, "Progression of colorectal cancer liver metastasis after chemotherapy: a new test of time?" *Annals of Surgical Oncology*, vol. 25, no. 6, pp. 1469-1470, 2018.

[12] J. Mann, "Natural products in cancer chemotherapy: past, present and future," *Nature Reviews Cancer*, vol. 2, no. 2, pp. 143–148, 2002.

[13] J. Gu, C.-f. Cui, L. Yang, L. Wang, and X.-h. Jiang, "Emodin inhibits colon cancer cell invasion and migration by suppressing epithelial-mtwcp," *Oncology Research Featuring Preclinical and Clinical Cancer Therapeutics*, vol. 27, no. 2, pp. 193–202, 2019.

[14] I. T. Saunders, N. Kapur, H. Mir, and S. Singh, "Abstract 312: Emodin inhibits colon cancer by modulating apoptotic and cell survival signals," *Cancer Research*, vol. 78, no. 13, p. 312, 2018.

[15] E. T. Tan, C. J. Hardy, Y. Shu, A. GuidonIn, and J. Huston, "Reduced acoustic noise in diffusion tensor imaging on a compact MRI system," *Magnetic Resonance in Medicine*, vol. 79, no. 6, pp. 2902–2911, 2018.

[16] K. Kim, S. Kim, and K. S. Kim, "Effective image enhancement techniques for fog-affected indoor and outdoor images," *IET Image Processing*, vol. 12, no. 4, pp. 465–471, 2018.

[17] W. Holger, J. Patrik, S. Anders, L.-P. Zelmina, O. Bjrn, and N. Sven, "Batch-normalization of cerebellar and medulloblastoma gene expression datasets utilizing empirically defined negative control genes," *Bioinformatics*, vol. 18, p. 18, 2019.

[18] T. Chen, J. Gu, H. Wang et al., "Semi-preparative scale separation of Emodin from plant extract by using molecularly imprinted polymer as stationary phase," *Chromatographia*, vol. 77, no. 13-14, pp. 893–899, 2014.

[19] T. Ian, H. Saunders, K. Neeraj, and S. Singh, "Emodin inhibits colon cancer by altering BCL-2 family proteins and cell survival pathways," *Cancer Cell International*, vol. 19, p. 98, 2019.

[20] J. Bai, J. Wu, R. Tang et al., "Emodin, a natural anthraquinone, suppresses liver cancer in vitro and in vivo by regulating VEGFR2 and miR-34a," *Investigational New Drugs*, vol. 38, no. 2, pp. 229–245, 2019.

[21] Y. Hiasa, Y. Otake, M. Takao, T. Ogawa, N. Sugano, and Y. Sato, "Automated muscle segmentation from clinical CT using bayesian U-net for personalization of a musculoskeletal model," *IEEE Transactions on Medical Imaging*, vol. 39, no. 4, pp. 1030–1040, 2019.